

# **Characterisation and Field Deployment of a Novel Quantitative Time-of-Flight Aerosol Mass Spectrometer (ToF-AMS)**

Dissertation  
zur Erlangung des Grades  
„Doktor der Naturwissenschaften“  
am Fachbereich Physik, Mathematik und Informatik  
der Johannes Gutenberg-Universität  
in Mainz

vorgelegt von

Silke S. Hings  
geboren in Mainz

Mainz, den 24. November 2006



# Contents

<b>1</b>	<b>Introduction .....</b>	<b>1</b>
1.1	The Atmospheric Aerosol.....	1
1.2	Measurement of Atmospheric Aerosols .....	5
1.2.1	Online Aerosol Mass Spectrometry .....	5
1.3	Objectives of this Work.....	13
<b>2</b>	<b>The Time-of-Flight Aerosol Mass Spectrometer – Set-up and Operation .....</b>	<b>15</b>
2.1	Set-up.....	15
2.1.1	Aerosol Inlet and Sampling Chamber .....	17
2.1.2	Particle Sizing Chamber.....	19
2.1.3	Particle Evaporation and Ionisation Chamber.....	20
2.1.4	Detection and Chemical Analysis Chamber.....	21
2.2	Modes of Operation .....	22
2.3	Differences to Q-AMS Instruments.....	24
<b>3</b>	<b>ToF-AMS Data Analysis and Characterisation.....</b>	<b>25</b>
3.1	Conversion of Raw Mass Spectra into Unit Resolution Spectra .....	27
3.1.1	I-ToF Calibration.....	28
3.1.2	Mass Resolving Power .....	29
3.1.3	Peak Integration.....	30
3.2	Conversion of Signal Intensity into Mass Concentrations .....	33
3.2.1	Duty Cycle Correction.....	35
3.2.2	Inlet Flow and Airbeam Correction.....	37
3.2.3	IE Calibration .....	43
3.3	Characterisation of Size Distribution Measurements .....	54
3.3.1	Size Calibration .....	54
3.3.2	Pressure-dependency of the Size Calibration.....	61
3.3.3	Dependency on Vaporiser Temperature .....	65
3.4	Mass Concentration Detection Limits .....	68
3.4.1	Definition.....	68

3.4.2 Measurement of AMS Detection Limits .....	68
3.4.3 Filter Measurements.....	70
3.4.4 Measurement at Elevated Mass Concentrations.....	75
3.4.5 Background Perturbation Experiments .....	79
3.4.6 Reduction of the Organics-related Detection Limits.....	81
3.5 Size-dependent Mass Spectra.....	84
3.6 Data Analysis Software .....	88
<b>4 Field Deployment of the ToF-AMS.....</b>	<b>91</b>
4.1 PMTACS-NY 2004 – First ToF-AMS Field Deployment.....	91
4.2 FACE-2004 .....	101
4.3 HNY 2005 .....	107
<b>5 Conclusions and Future Work .....</b>	<b>115</b>
<b>6 Appendix .....</b>	<b>119</b>
6.1 ToF-AMS Data Analysis Software .....	119
6.2 List of Figures .....	121
6.3 List of Tables.....	127
6.4 List of Symbols .....	129
6.5 List of Abbreviations.....	133
6.6 Publications Originating from this Work .....	135
<b>7 References .....</b>	<b>137</b>

# 1 Introduction

## 1.1 The Atmospheric Aerosol

The term “aerosol” was introduced more than 80 years ago as an analogy to the term hydrosol (a stable liquid suspension of solid particles; Hinds, 1999). It is defined as a suspension of solid or liquid particles in a gas and it includes a wide range of phenomena like dust, fume, mist, fog, haze, smoke and smog (Seinfeld and Pandis, 1998). Atmospheric aerosol particles cover a wide size range from a few nanometres (nm) to tens of micrometres ( $\mu\text{m}$ ) in diameter. They are either directly emitted into the atmosphere (primary particles) or formed there by the oxidation of precursor gases (secondary particles), where the resulting oxidation products nucleate to form new particles or condense on pre-existing ones. Aerosol particles are removed from the atmosphere either by deposition at the Earth’s surface (dry deposition) or by incorporation into cloud droplets during the formation of precipitation (wet deposition). Tropospheric aerosol particles vary widely in their composition and concentration over the Earth, because wet and dry deposition lead to relatively short residence times in the troposphere and because the geographical distribution of particle sources is highly non-uniform. While the lifetimes of atmospheric trace gases range from less than a second to a century or more, the residence times of particles in the troposphere vary from a few days to a few weeks only (Seinfeld and Pandis, 1998).

Atmospheric aerosols have significant impacts on our environment on a local, regional and global scale. Locally, vehicular emissions, wood burning fires and industrial processes cause urban air pollution (Fenger, 1999; Mayer, 1999), which is related to influences on human health (e.g. Wichmann et al., 2000; Samet et al., 2000; Dockery et al., 1993); on a regional scale, aerosols can be transported from areas of high emissions to relatively clean remote areas, whereas globally aerosols have the potential to significantly influence our entire planet through their role in heterogeneous chemistry in the troposphere and stratosphere (Ravishankara, 1997; Finlayson-Pitts and Pitts, 2000; Warneck, 1999) and through their effect on the Earth’s climate as they scatter sunlight and serve as condensation nuclei for the formation of cloud droplets (Charlson et al., 1992; Penner et al., 2001; Ramanathan et al., 2001). The radiative effect of aerosols causes the largest uncertainty in global climate predictions to quantify the climate forcing due to man-made changes in the composition of the atmosphere.

In order to better quantify all these effects, a better understanding of the formation, composition and transformation of atmospheric aerosols is of critical importance.

### Aerosol Properties

Atmospheric particles are usually referred to as having a diameter, implying they are spherical. However, aerosol particles have widely variable shapes for which geometrical diameters are often not meaningful. Expressing the size of such particles is essential since many important properties of the particles, such as volume, mass, and velocity, depend on their size (Hinds, 1999). In practice, the size of non-spherical particles is expressed in terms of an equivalent diameter that depends on a physical property. An equivalent diameter is defined as the diameter of the sphere that would have the same value of a particular physical

property as that of the non-spherical particle. For the definitions of the different types of equivalent diameters the reader is directed to Hinds (1999). It is important to note that various types of instrumentation report different measures of the particle diameter, depending on the employed methodology. For this reason, a universal measure of aerosol particle size does not exist. Therefore the sizing definition will be specified for particle diameters reported in this thesis. The diameters of atmospheric aerosol particles span over more than four orders of magnitude, from a few nanometres to tens of micrometres. Atmospheric aerosols are classified into separate modes according to their size, formation process, and atmospheric age:

Particles with diameters larger than 1  $\mu\text{m}$  are referred to the coarse mode. They are mainly produced by mechanical processes and directly introduced into the atmosphere from anthropogenic as well as natural sources. Due to their relatively large size, coarse mode particles settle out of the atmosphere in short time by sedimentation.

Particles with diameters between 0.1 and 1  $\mu\text{m}$  belong to the accumulation mode. They represent a region of particle growth, mainly due to the coagulation of particles with diameters smaller than 0.1  $\mu\text{m}$  and from condensation of vapours onto existing particles, causing them to grow into this range. In addition, they are introduced into the atmosphere directly, mainly through incomplete combustion of wood, oil, coal, gasoline and other fuels. As the removal mechanisms are least efficient in this regime, particles accumulate there until they are mainly lost through rain or other forms of precipitation (wet deposition).

Particles with diameters between 0.01 and 0.1  $\mu\text{m}$  are identified as Aitken mode particles. They are formed from gas-to-particle conversion or from the condensation of hot vapours during combustion processes. Aitken mode particles act as condensation nuclei of low-vapour pressure gaseous species, causing them to grow into the accumulation mode. Their lifetime is short, as they are lost principally by evaporation or coagulation with larger particles.

Particles with diameters smaller than 0.01  $\mu\text{m}$  are called nucleation mode particles. They are thought to be generated by gas-to-particle conversion processes which are not yet well understood on a molecular level. Ultrafine particles are observed in bursts of very large numbers in the presence of either biogenic or anthropogenic emissions under favourable local conditions in many different environments including costal zones (O'Dowd et al., 2002) and forests (Kulmala et al., 2004). Due to their rapid coagulation or random impaction onto surfaces, the lifetime of ultrafine particles is very short, sometimes in the order of minutes.

The exact size ranges of these modes vary in the literature, but the definitions given previously will be used throughout this thesis.

An illustration of the number, size and volume distributions for a typical urban model aerosol is shown in Figure 1.1, showing the different modes described above (except the ultrafine particle mode).

Aerosol concentrations are most commonly reported in terms of mass or number of particles in a unit volume of aerosol. Common units used are  $\mu\text{g m}^{-3}$  and number  $\text{cm}^{-3}$ .

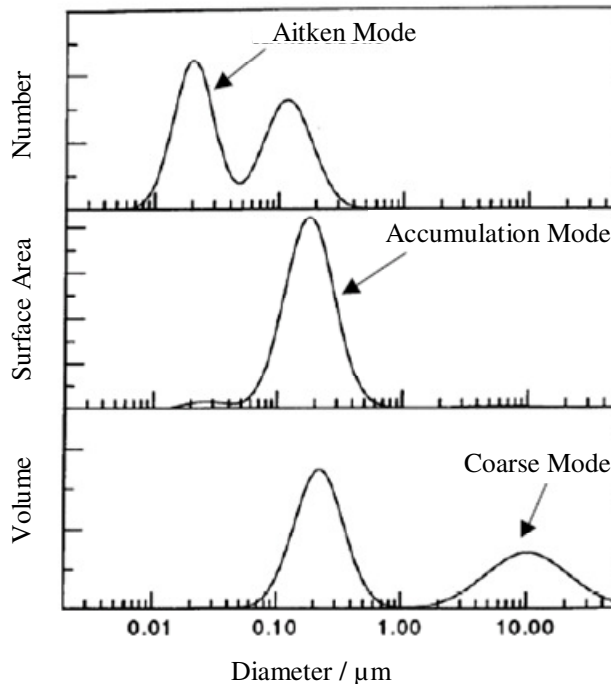


Figure 1.1: Illustration of number, surface area and volume distributions of a typical urban model aerosol (Seinfeld and Pandis, 1998).

### Aerosol Chemical Composition

Many effects of atmospheric aerosol particles depend on their chemical composition. Generally, atmospheric aerosol particles are composed of a mixture of species from a number of different sources. The mixing state (i.e. how all components are distributed among the particles) of these components is an important property of atmospheric aerosols. Particles are externally mixed when they arise from different sources and the individual particles have different chemical composition; they are internally mixed when all particles of a given size contain uniform mixture of all components.

Atmospheric aerosols are generally composed of variable amounts of sulphate, nitrate, ammonium, sodium, chloride, trace metals, crustal elements, water and carbonaceous material. The sulphate components are predominantly derived from atmospheric oxidation of anthropogenic (sulphur dioxide,  $\text{SO}_2$ ) and natural (dimethyl sulphide, DMS) sulphur-containing compounds. Nitrate is formed mainly from the oxidation of atmospheric nitrogen dioxide ( $\text{NO}_2$ ). Sulphate and nitrate are initially formed as sulphuric ( $\text{H}_2\text{SO}_4$ ) and nitric acid ( $\text{HNO}_3$ ) but are progressively neutralised by atmospheric ammonia forming the corresponding salts. Chlorides also enter atmospheric particles as a result of ammonia neutralisation of hydrochloric acid (HCl) vapour, which is emitted from sources like incinerators and power stations or from the chemical decomposition of chlorofluoro hydrocarbons (CFC). However, the main source for atmospheric chlorides is sea spray even at locations hundreds of miles from the coast. Crustal materials arise from soil dust and windblown materials. They vary strongly in their composition according to local geology and surface conditions and reside mainly in the coarse and accumulation mode particle fraction. The carbonaceous aerosol fraction contains both elemental and organic carbon. Elemental carbon (EC) is also called black carbon, graphitic carbon, or soot, and is emitted directly into the atmosphere from combustion processes. Organic carbon (OC) is either directly emitted into the atmosphere by biomass burning and combustion processes, or

introduced by secondary organic aerosol (SOA) formation. SOA formation occurs when volatile organic compounds undergo atmospheric oxidation reactions, forming products having low enough volatilities to form aerosol particles via either nucleation or gas-to-particle partitioning to pre-existing particles (Odum et al., 1996; Hoffmann et al., 1997; Kamens et al., 1999; Kamens and Jaoui, 2001). Volatile organic compounds (VOC) are emitted into the atmosphere from anthropogenic and biogenic sources (Went, 1960; Odum et al., 1996; Seinfeld and Pandis, 1998; Kleindienst et al., 1999; Aschmann et al., 2002).

Understanding the composition of atmospheric aerosol particles is necessary for identifying their sources and predicting their effect on various atmospheric processes as well as health related issues.

## 1.2 Measurement of Atmospheric Aerosols

The ideal instrument for the measurement of atmospheric aerosol particles should be mobile, robust and reliable; it should measure in real time with high temporal and spatial resolution and it should have low detection limits; it should provide unbiased, precise, correct and repeatable measurements of number and mass concentrations, size distributions and the chemical composition of atmospheric aerosols, as well as their mechanical, optical, biological and toxicological properties. It is obvious, that such a single instrument does not and will probably never exist. In practice, a complementary collection of different instruments is used for physical and chemical measurements of atmospheric aerosols, which have been recently reviewed in a number of publications (Chow, 1995; Spurny, 1999; McMurry, 2000).

### 1.2.1 Online Aerosol Mass Spectrometry

While aerosol scientists have developed a large number of techniques for the measurement of the physical properties of aerosols, it is now obvious that future progress in understanding aerosol properties, processes and impact will require the development of new techniques for particle chemical analysis, which are also capable of determining information about size, shape, optical properties and elemental and molecular composition of each particle. Over the past decade aerosol mass spectrometry has gained considerable interest as a means of correlating the size and chemical composition of individual particles or small particle ensembles in real time.

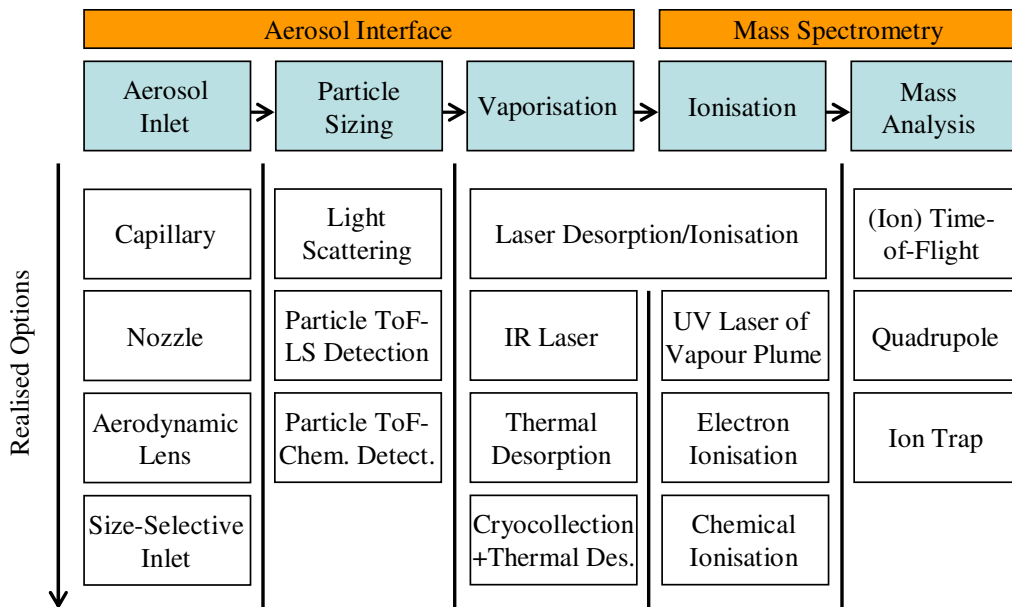


Figure 1.2: Conceptual schematic of an online aerosol mass spectrometer (after Jimenez, 2002)

The basic principle of an online aerosol mass spectrometer is to introduce airborne particles into the instrument, vaporise and ionise the material and then analyse the ions produced using mass spectrometry. Sampling artefacts are greatly reduced and the time required to characterise the aerosol is only limited by the amount of time needed to analyse a statistically significant number of particles (typically in the order of minutes). A large

number of techniques have been implemented in the development of various aerosol mass spectrometers. However, the basic concept of each of these instruments can be classified into five discrete stages: sample introduction, aerosol particle sizing, vaporisation, ionisation and mass spectrometry. Figure 1.2 is a conceptual schematic of an aerosol mass spectrometer, including different techniques that may be used for the individual stages. Some of these will be further described in the next section.

For a comprehensive history and review of the majority of instruments that use these principles, the reader is directed to Suess and Prather (1999) which covers all major developments until the end of the 20<sup>th</sup> century, and to Johnston (2000), Noble and Prather (2000) and Sipin et al. (2003).

### Inlet Technology

Random collisions with gas molecules can prevent ions from an ion source from being detected. Mass spectrometers must therefore be operated at high or ultra-high vacuum ( $10^{-1}$  –  $10^{-6}$  Pa). A key feature of an inlet system is therefore to transfer particles from ambient pressure into the vacuum system of the mass spectrometer. It is also desirable that transport losses are small over a wide particle size range and that the chemical characteristics of the particles are not changed. In addition, particles need to be focused into a highly collimated beam to generate an aerosol beam with high particle number density. For this purpose, a variety of inlets can be used (Drewnick, 2003). The simplest form of an aerosol inlet is a nozzle, which can also be used as a size-selective inlet. The particle size for which the transmission efficiency is optimal depends on the pressure downstream the nozzle. Particles are only weakly focused. The transmission of particles through a capillary is nearly constant over a large particle size range, but particles are also only weakly focused. In an aerodynamic lens the particles are drawn through a series of concentric apertures with successively decreasing diameters, causing the gas streamlines to repeatedly compress and expand. As result the particle streamlines converge on the axis of the lens and the particles form a tightly collimated beam when they are accelerated through the final nozzle into the vacuum. The main advantage of aerodynamic lenses is the effective focusing of particles over a wide range of sizes into a narrow beam with low divergence (e.g. Liu et al., 1995a and b; Zhang et al., 2002 and 2004).

### Sizing Techniques

After the particles are introduced into the instrument and a particle beam is formed, the particles can be sized with the help of two different methods. For optical particle sizing the intensity of scattered light of the particles is measured as they pass a single laser beam (Murphy and Thomson, 1995). The light scattering intensity increases with increasing particle size. Here, the optical diameter of the particles is measured. Disadvantages of this method are the quite low resolution (in diameter space) and the dependency on the optical properties of the particles. In addition, the minimum particle size that can be detected is quite large. For aerodynamic particle sizing the particle velocity is determined from the flight time of the particles measured between two fixed points (Prather et al., 1994; Gard et al., 1997; Jayne et al., 2000). Here, the particle velocity decreases with increasing particle diameter, and the aerodynamic diameter of the particles is determined.

## Vaporisation and Ionisation Techniques

For the vaporisation of the particles, either thermal or laser desorption can be used. For the former the aerosol beam is directed onto a hot surface (several 100 °C) where the particles flash-vaporise. This method can be used in combination with continuous ionisation and mass spectrometry. Using the latter technique, the particles are hit by an intensive laser pulse and are therefore vaporised. This method is especially used for single particle analysis.

Ionisation methods include laser desorption/ionisation (LDI), where the particles are both vaporised and ionised simultaneously by a single high-powered UV laser pulse, ionisation by a UV laser pulse after evaporation of the particles by another laser, electron impact ionisation and chemical ionisation. During electron impact ionisation the gas is exposed to a flux of electrons produced from a hot filament and accelerated to a given kinetic energy (typically  $E_{kin} = 70$  eV). These electrons strike the neutral molecules and transfer enough energy to cause them to lose one or more of their own electrons, creating positive ions. Due to the high energies deposited in the molecules, molecular bonds are frequently broken during the ionisation process, leading to high fragmentation of the molecules. However, different chemical species create highly reproducible fragmentation patterns that can be used for identification (McLafferty and Turecek, 1993). Chemical ionisation introduces less fragmentation in the analysed molecules, making it particularly useful for the identification and quantification of organic species. However, as it is selective, only a fraction of the particulate mass will be accounted for.

## Mass Spectrometers

After the particles are vaporised and the resulting vapour molecules are ionised, the ions are guided into a mass spectrometer. The basic principle of a mass spectrometer is to separate ions according to their mass-to-charge ratios ( $m/z$ )<sup>1</sup> and count them. Two kinds of mass spectrometers can be distinguished: continuous working mass spectrometers, where the individual mass-to-charge ratios are scanned to obtain a whole mass spectrum, and pulsed mass spectrometers, where all  $m/z$  are analysed simultaneously. The first mass spectrometer that was presented by Dempster (1918) was a magnetic sector mass spectrometer, where ions are accelerated and focused using electric fields and their paths are bent with transverse magnetic fields. The velocities and therefore the deflected trajectories of the ions are dependent on their mass-to-charge ratios, because the ions are accelerated over a specific electrical potential. Using a fixed detector like an electrometer, the ions are filtered according to their  $m/z$  prior to counting. The whole mass range is scanned by varying the electric or magnetic field strengths at a given geometry. Magnetic sector mass spectrometers are not favoured in most current designs of aerosol mass spectrometers because of their bulk, but due to the capability of very high mass resolving powers they are often used in other laboratory applications where mass measurements of fractions of amu are needed (e.g. for the identification of specific elements).

A more recent design of a mass spectrometer is the quadrupole mass spectrometer which was introduced by Paul and Steinwedel (1953). It consists of four cylindrical parallel rods. A voltage is applied between two opposing rods, consisting of AC and DC components. The

<sup>1</sup> Note, that  $m$  is the mass of the ion relative to the standard atomic mass (defined as one twelfth of the rest mass of a  $^{12}\text{C}$  atom, or  $1.6606 \cdot 10^{-27}$  kg) and  $z$  is the charge relative to  $e$ , the elementary charge ( $1.602 \cdot 10^{-19}$  C).  $m/z$  is here treated as being dimensionless, although atomic mass units (amu or u), Daltons (Da) and Thompsons (Th) are used as units for the same quantity elsewhere in the literature.

voltages can be set in a way that only ions of a specific  $m/z$  can pass the analyser on stable trajectories. Ions of all other  $m/z$  adopt trajectories with oscillations larger than the spacing of the rods, causing them to strike the rods, become neutralised and cannot be detected. A whole mass spectrum is scanned by variation of the alternating electric field. Near the end of the rods the ions are extracted using additional electric fields and detected by electrometers or electron multipliers. Because quadrupole mass spectrometers are easy to handle, compact and robust they are well suited for field instrumentation. However, as the mass spectrum needs to be scanned within typically several hundred milliseconds, a quadrupole mass spectrometer is not applicable for single particle analysis. In addition, it has a low duty cycle, limited mass range and limited mass resolving power<sup>2</sup>.

Ion trap mass spectrometers are similar to quadrupole instruments, but here a high frequency field is applied three-dimensionally using a system of two end cap electrodes either side of a ring electrode. The voltages can be set to capture and hold all ions and then be changed to selectively release ions according to their  $m/z$ . Therefore an ion trap mass spectrometer is capable of delivering a complete mass spectrum of a single ionisation event. While ion trap mass spectrometers are very compact and the possibility of tandem mass spectrometry is given, they are also very expensive, have only moderate mass resolving power and a limited dynamic range.

Another type of mass spectrometer is the time-of-flight mass spectrometer. Its basic principle (see Figure 1.3) is to accelerate ions in an electric field and measure their flight times (i.e. the ion time-of-flight) they need to pass a flight path of a certain length.

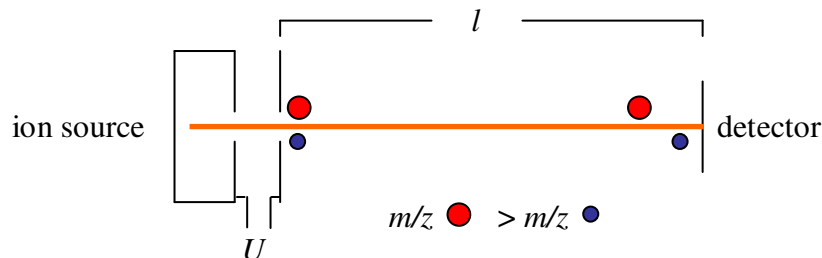


Figure 1.3: Schematic of a linear time-of-flight mass spectrometer.

The higher the mass of the ions, the less they are accelerated. Due to the acceleration in the electric field, their kinetic energy  $E_{kin}$  is equal to the energy  $E_{el}$  obtained by passing the potential gradient  $U$ :

$$E_{kin} = \frac{1}{2} \cdot m_{ion} v_{ion}^2 = E_{el} = q \cdot U \quad (1.1)$$

with  $m_{ion}$  the mass of the ion,  $v_{ion}$  the velocity of the ion and  $q = z \cdot e$  the electric charge of the ion,  $z$  the number of net elementary charges in the ion and  $e$  the elementary charge. With the velocity  $v_{ion}$  equal to the flight path  $l$  divided by the flight time  $t_{ion}$  of the ions,  $t_{ion}$  is proportional to the square root of the  $m/z$  of the ion:

<sup>2</sup> In time-of-flight mass spectrometry, the mass resolving power  $R$  of an instrument is an important measure of instrument performance. It is the ability to separate ions of similar flight times but different  $m/z$  into separate signals and can be expressed as the  $m/z$  divided by the full width at half maximum (FWHM) of a peak at this particular  $m/z$  (see section 3.1.2).

$$t_{ion} = \sqrt{\frac{m_{ion}}{z} \cdot \frac{1}{2eU}} \cdot l \propto \sqrt{\frac{m}{z}} \quad (1.2)$$

A time-of-flight mass spectrometer is capable of acquiring a complete mass spectrum for a single ionisation event and can therefore be used for single particle analysis. In addition, practically all ions that leave the ion source reach the detector, resulting in very low detection limits and very large mass range. However, the spatial and velocity distributions of the ions prior to the acceleration, the length of the initial ion pulse and the length of the flight path cause the mass resolving power to be relatively low.

In order to increase the mass resolving power of time-of-flight mass spectrometers, reflectrons are used (Figure 1.4), where the ions need to pass an inverted electric field until they change their direction and are accelerated onto the detector. Faster ions penetrate deeper into the electric counter field and therefore have to travel a longer flight path than slower ions. As a result, all ions of a particular  $m/z$  reach the detector simultaneously independent on their initial velocity. With this configuration, a time-of-flight mass spectrometer can reach mass resolving powers up to 10000.

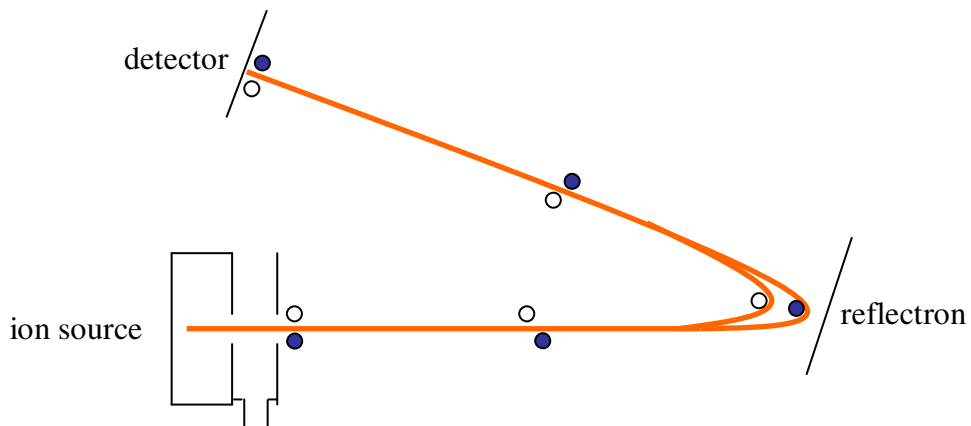


Figure 1.4: Schematic of a reflectron time-of-flight mass spectrometer.

In time-of-flight mass spectrometry, microchannel plate (MCP) detectors are used, which consist of a thin (0.5 mm) glass plate with a diameter between 2-4 cm, including a high number of parallel channels (diameters between 2-20  $\mu\text{m}$ ) which work as electron multipliers with very high time resolution (Wiza, 1979).

### Thermal Evaporation-Based Aerosol Mass Spectrometers

The first example of an aerosol mass spectrometer was introduced by Davis (1973). The aerosol particles were introduced through a steel capillary and a thin wall pinhole and analysed by a surface ionisation magnetic sector mass spectrometer. Through impaction on a surface heated up to  $\sim 1700^\circ\text{C}$  the particles evaporated to neutral and ionic species.

Other surface ionisation instruments have been developed over years, some of them using quadrupole mass spectrometers (e.g. Myers and Fite, 1975; Jäglid et al., 1996; Davidsson et al., 2002; Svane et al., 2004). However, one major problem of surface ionisation methods is the limitation to species with ionisation potentials below the work function of the heated surface ( $\sim 8$  eV), which are typically alkali and alkali earth metals. In addition, interactions between the heated surface and the particle components can occur.

These problems were overcome by separating the vaporisation and ionisation steps using thermal desorption of the particles upon impaction on a surface heated to lower temperatures and ionising the resulting neutral gas molecules by electron impact (EI). Examples for aerosol mass spectrometers using these techniques are the Chemical Analysis of Aerosols in Real Time (CAART; Allen and Gould, 1981) and Particle Analysis by Quadrupole Mass Spectrometry (PAMS; Sinha et al., 1982), both using a quadrupole mass spectrometer as analyser. Another example for an instrument that employs these principles is the Thermal Desorption Particle Beam Mass Spectrometer (TDPBMS), developed to investigate secondary organic aerosol formation (Tobias and Ziemann, 1999; Tobias et al., 2000).

In addition to electron impact ionisation and quadrupole mass spectrometry, other techniques have been used in thermal desorption-based aerosol mass spectrometers. One example is the Atmospheric Pressure Chemical Ionisation Mass Spectrometer (APCI-MS; Hoffmann et al., 2002) which uses an ion trap mass spectrometer as analyser.

All aerosol mass spectrometers described so far do not include a direct method of quantifying the size of the particles being studied. The Quadrupole Aerosol Mass Spectrometer (Q-AMS) developed by Jayne et al. (2000) also uses thermal desorption and electron impact ionisation, which makes it capable of quantifying most chemical substances found in sub-micrometre sized aerosol particles. Additionally, the Q-AMS is capable of measuring mass size distributions of the chemical species in the aerosol by chopping the particle beam and measuring the time-resolved ion signal intensity of the particle vapour. This technique will be described in more detail in chapter 2.

Over the years, thermal desorption-based aerosol mass spectrometers have provided valuable information on the chemical composition of aerosol particles. However, they do have intrinsic problems. Firstly, like magnetic sector instruments, quadrupole mass spectrometers are only capable of studying one  $m/z$  at a time, which means that only one aspect of the chemical composition of a single particle can be investigated. While the instrument can probe the overall chemical nature of the aerosol as a whole, it cannot directly deliver information on the mixing state of the particles and it is not suitable for single particle analysis. Secondly, thermal desorption is limited by the volatility of the chemical components of the aerosol particles under analysis. While components like ammonium nitrate, ammonium sulphate or organic compounds can be readily vaporised upon impaction on the heated surface, refractory substances such as elemental carbon, sea salt or crustal material can not. As result, these instruments are not suitable for the analysis of such aerosol components.

To address these issues, much of the effort in the area of aerosol mass spectrometry has been concentrated in the last decade or so on the development of laser-based instrumentation.

### Laser-based Aerosol Mass Spectrometers

The first aerosol mass spectrometer combining the laser desorption/ionisation (LDI) technique with a highly improved method for particle sizing was developed by Sinha (1984). Two continuous He:Ne lasers were used to measure the particle velocities and a third laser, a high-energy pulsed Nd:YAG laser was used for the desorption and ionisation of individual particles. The resulting ions were analysed by a quadrupole mass spectrometer.

McKeown et al. (1991) were the first who used the LDI technique in combination with a time-of-flight mass spectrometer. As described above, a major advantage of this kind of

mass spectrometer is that ions of all  $m/z$  are detected without the need to scan and therefore a complete mass spectrum can be obtained from only a single particle. Other examples of such instruments are the Rapid Single Particle Mass Spectrometry (RSMS; Carson et al., 1995; Carson et al., 1997; Lake et al., 2003), the Particle Blaster (Reents et al., 1995; Reents and Ge, 2000), the Particle Analysis by Laser Mass Spectrometry (PALMS; Murphy and Thomson, 1995; Thomson et al., 2000), the Single Particle Laser Ablation Time-of-Flight Mass Spectrometer (SPLAT; Ettner-Mahl, 2006), and the Aerosol Time Of Flight Mass Spectrometer (ATOFMS; Prather et al., 1994; Gard et al., 1997) which is sold commercially by TSI as model 3800.

One advantage of LDI aerosol mass spectrometry is that two mass spectrometers can be used in parallel, configured to extract ions with opposite polarities from the desorption region (Hinz et al., 1996). This means that positive and negative mass spectra for individual particles can be captured simultaneously, increasing the amount of information obtained.

Laser-based aerosol mass spectrometers are proving to be powerful and unique tools with a large number of applications (Suess and Prather, 1999). However, while qualitative information on the chemical composition of aerosols can be obtained, providing quantitative data with LDI represents an intrinsic problem. On the one hand, LDI methods that employ high laser fluence (laser power density) can produce extensive fragmentation of molecules and quantitative information on the elementary composition can therefore be obtained (Reents and Schabel, 2001), although information on the molecular structure cannot be obtained. On the other hand, when employing lower fluences, less fragmentation occurs, allowing more chemical information to be obtained. At the same time the particle components are not necessarily fully vaporised or ionised by the laser pulse and are therefore detected with varying efficiency depending on the particle's size and chemical composition. Furthermore, incomplete vaporisation makes ionisation more sensitive to species present on the surface than those in the core (Allen et al., 2000; Kane and Johnston, 2000). In addition, individual chemical components can interact with each other during the desorption and ionisation process, resulting in an uneven distribution of charges between the fragments. This is known as 'matrix effect' (Reilly et al., 2000). Finally, spectral intensities depend not only on the laser power density absorbed by the molecules, but also on the instrument sensitivity to specific species. This in turn depends on the absorption characteristics of the individual species present in the sample under study (Gross et al., 2000).

One approach to improve the quantification abilities of laser-based instruments is the introduction of the two-step laser method, which decouples the desorption and ionisation processes by using two separate, weaker lasers (Morrical et al., 1998). This method appears to produce promising results and has been further investigated, improved and implemented by Cabalo et al. (2000). However, it has so far not been used in the field.

Until now, various types of aerosol mass spectrometers have been deployed under a wide range of measurement conditions and atmospheric situations. Those conditions range from clean background situations (Hinz et al., 2005; Drewnick et al., 2006), and aircraft measurements in the upper troposphere (Schneider et al., 2006a) and the lower stratosphere (Murphy and Thomson, 2000), to measurements of high mass concentrations in vehicle exhausts (Schneider et al., 2005; Schneider et al., 2006b) and fireworks events (Drewnick et al., 2006).

The review of the thermal desorption- and laser-based aerosol mass spectrometry instruments presented in this chapter demonstrates the complementary nature of these instruments - and that an ‘ideal’ single instrument is not (yet) available. Different types of aerosol mass spectrometers have different capabilities and limitations. Aerosol mass spectrometers employing thermal desorption and electron impact ionisation for example provide quantitative chemical information on aerosol particles, but refractory particle components like sea salt or metals cannot be analysed. Due to this reason, those instruments are usually set up to analyse particles with diameters below 1 µm. On the other hand, aerosol mass spectrometers using LDI can analyse single particles, giving direct information about the mixing state of the particles, and are capable of analysing refractory aerosol components. However, providing quantitative information with LDI represents an intrinsic problem.

Summarising, this shows that the systematic characteristion of instruments is crucial to understand their limitations and capabilities.

## 1.3 Objectives of this Work

In the beginning of this PhD work, the Aerodyne Time-of-Flight Aerosol Mass Spectrometer (ToF-AMS) was set up during a field campaign in New York City for the first time. This was done in collaboration with Aerodyne Research Incorporated (Billerica, MN, USA), Tofwerk (Thun, Switzerland), and the University of Colorado (Boulder, CO, USA). The ToF-AMS is based on the well-known Aerodyne Quadrupole Aerosol Mass Spectrometer (Q-AMS; Jayne et al., 2000), and it uses the same sizing, evaporation and ionisation techniques. However, instead of a quadrupole mass spectrometer, a time-of-flight mass spectrometer is used to analyse the ions.

The major objective of this work was to characterise the ToF-AMS in the laboratory as well as during field campaigns and to compare it to the Q-AMS to show its capabilities and limitations. In addition, the development of data analysis strategies and the implementation of these into a user-friendly and automated data analysis software was another major part of this work.

In chapter 2, the ToF-AMS, its hardware and its operation will be described and its major differences to the Q-AMS will be outlined. Chapter 3 will then give detailed explanations on the data analysis tools that were developed to obtain meaningful and quantitative data from the instrument, as well as on the calibrations that are needed during or before data collection in order to apply these tools correctly. Many of these tools are the results of systematic instrument characterisation experiments. In addition, the results from detailed measurements of mass concentration detection limits of both the ToF-AMS and a Q-AMS will be presented, as well as the capability of the ToF-AMS to derive size-dependent information on all  $m/z$  simultaneously. Finally, the implementation of the described data analysis strategies into a user-friendly data analysis software is presented. In the last chapter (chapter 4), the field deployment of the ToF-AMS during three different field campaigns in situations of urban pollution and background conditions will be described and its capability as a tool for quantitative measurements of the chemical composition as well as chemically resolved size distributions of the atmospheric aerosol will be validated.



## 2 The Time-of-Flight Aerosol Mass Spectrometer – Set-up and Operation

The Time-of-Flight Aerosol Mass Spectrometer (hereafter referred to as “ToF-AMS”) introduced by Drewnick et al. (2005) and developed by Aerodyne Research Incorporated (Billerica, MN, USA) can provide quantitative data on both the non-refractory chemical species present in aerosol particles as well as the size of the particles. It is a combination of the well-characterised quadrupole mass spectrometer-based Aerodyne Aerosol Mass Spectrometer (“Q-AMS”) aerosol sampling, sizing and evaporation/ionisation technology (e.g., Jayne et al. 2000; Jimenez et al. 2003a) and a compact orthogonal extraction time-of-flight mass spectrometer (Tofwerk, Thun, Switzerland; e.g. Steiner et al., 2001).

A picture and a schematic of the ToF-AMS are shown in Figure 2.1 and Figure 2.2, respectively. The aerosol is introduced into the ToF-AMS through a critical orifice and an aerodynamic lens assembly (Zhang et al., 2002; Zhang et al., 2004a) which focuses aerosol particles in the size range 40 – 600 nm with an efficiency of almost 100 % into a narrow beam. The last aperture of the aerodynamic lens works as a critical orifice. Here the particles are accelerated to a size-dependent terminal velocity upon gas expansion into the vacuum chamber. After passing the sampling chamber, the particle beam is directed through a skimmer into the particle sizing chamber, while most of the surrounding gas is pumped away. At the front end of the particle sizing chamber the particle beam can be modulated by a mechanical chopper for particle size measurements. Aerodynamic particle size information can be obtained from the measured particle flight time from the chopper to the vaporiser after calibration with particles of known size, density and shape.

After travelling through the particle sizing chamber the particle beam passes another aperture and impacts onto the vaporiser, a porous tungsten surface, typically heated up to a temperature between 400 and 700 °C. Upon impaction onto this surface the non-refractory aerosol components flash-vaporise and the resulting vapour molecules are ionised by electron impact ( $E_{kin} = 70$  eV). The resulting positive ions are transferred into the extractor of the time-of-flight mass spectrometer and accelerated orthogonally to their flight direction into the flight tube of the mass spectrometer by a pulsed electrical field (pulsing frequency ~76.9 kHz).

This chapter describes the individual components of the ToF-AMS, its principles and modes of operation.

### 2.1 Set-up

The Time-of-Flight Aerosol Mass Spectrometer is mounted in a single mobile rack which integrates the vacuum system, the mass spectrometer and the instrument electronics including the data acquisition system. The dimensions of the rack are 104 x 61 x 124 cm and the weight of the ToF-AMS is about 200 kg. A picture of the ToF-AMS used during this work is shown in Figure 2.1

The ToF-AMS vacuum system consists of four individual differentially pumped chambers: the aerosol sampling chamber, the particle sizing chamber, the particle evaporation and

ionisation chamber and the chemical analysis and detection chamber. A basic schematic of the ToF-AMS is shown in Figure 2.2.

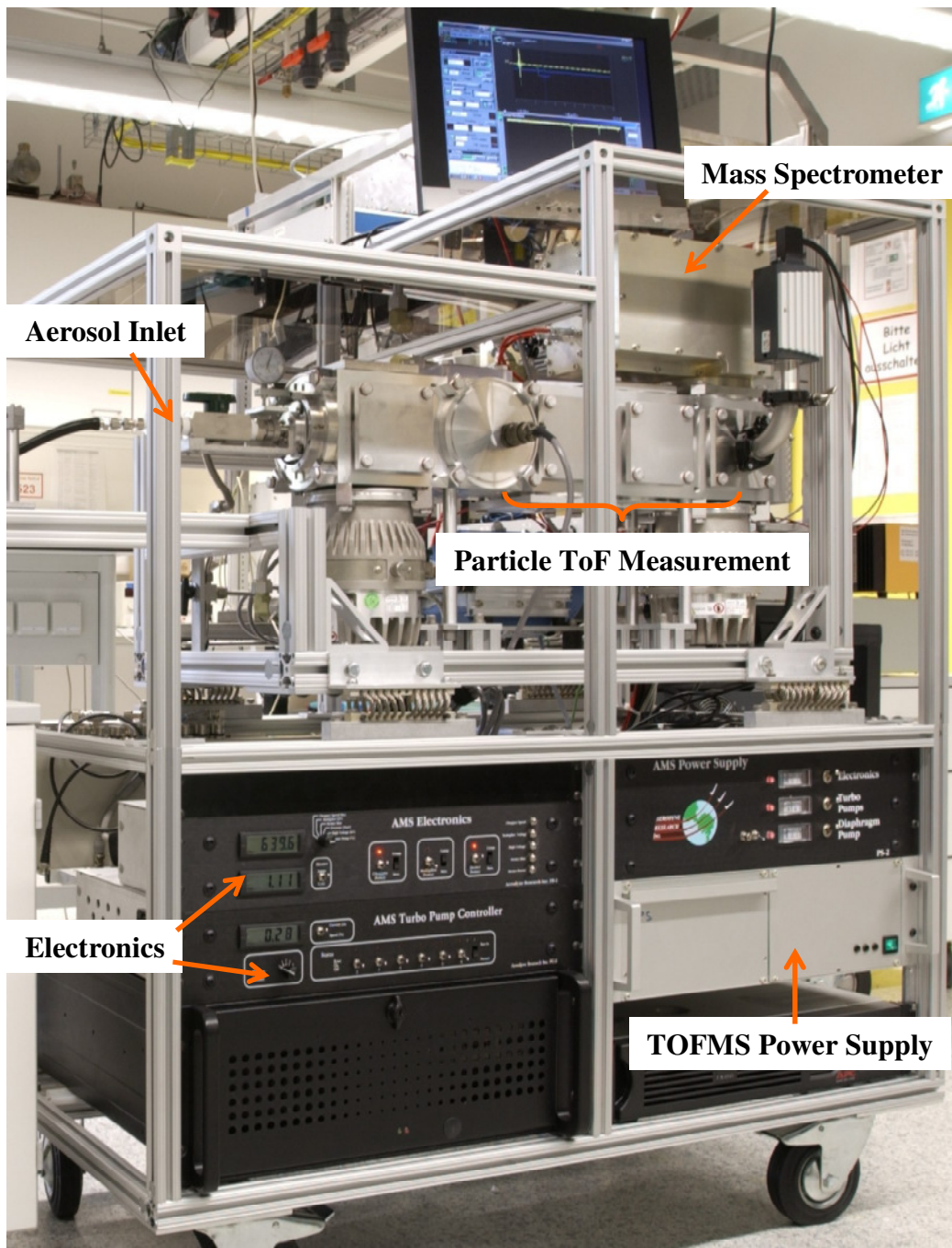


Figure 2.1: A picture of the mobile Time-of-Flight Aerosol Mass Spectrometer (ToF-AMS) used during this work in its configuration for field deployment.

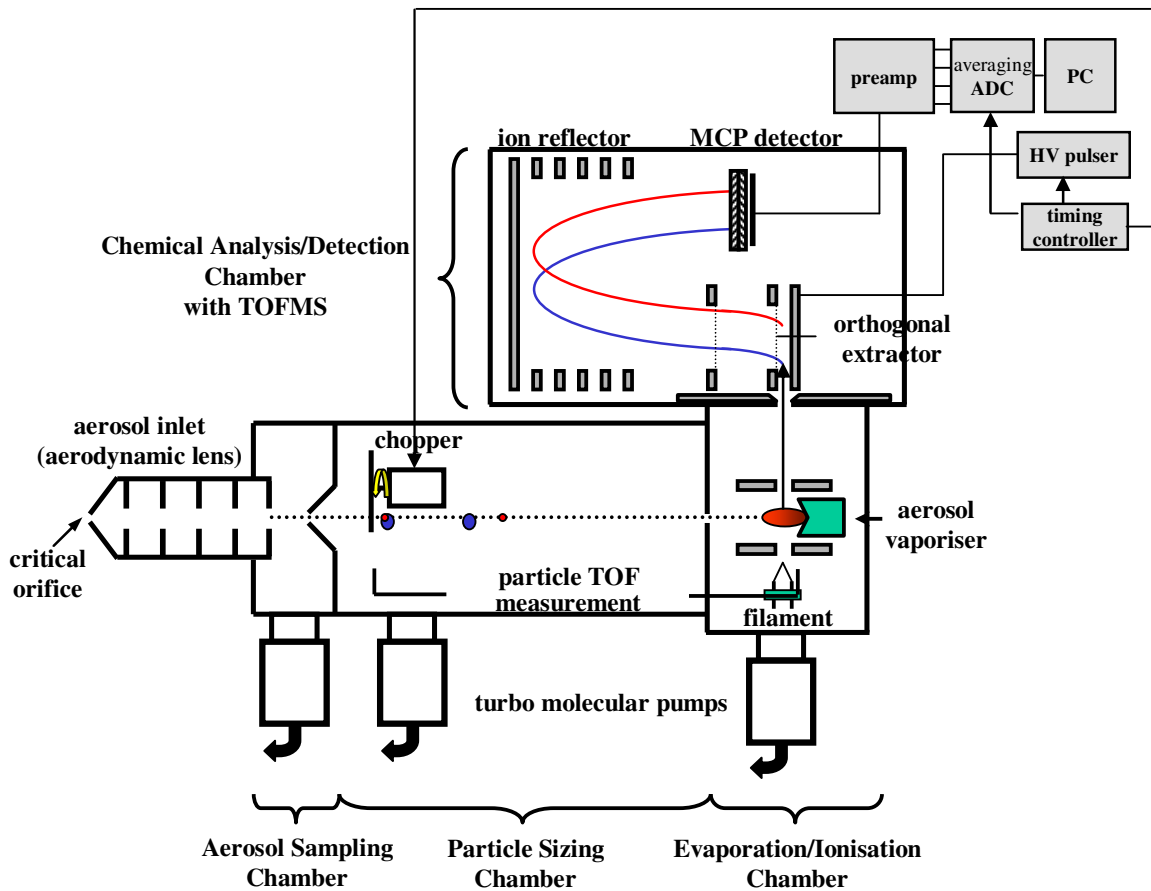


Figure 2.2: Schematic of the Time-of-Flight Aerosol Mass Spectrometer (ToF-AMS).

The power consumption of the ToF-AMS under sampling conditions is about 600 W, with 1/3 of this power used by the instrument electronics and the data acquisition computer. The remaining power is used by the vacuum system.

### 2.1.1 Aerosol Inlet and Sampling Chamber

The aerosol is introduced into the instrument through a critical orifice with 100 µm inner diameter at a volumetric inlet flow rate of  $1.4 \text{ cm}^3 \text{ s}^{-1}$ . The particle beam is then accelerated through an aerodynamic lens system similar to that introduced by Liu et al. (1995a) and Liu et al. (1995b) and developed further by Zhang et al. (2002) and Zhang et al. (2004a). The aerodynamic lens consists of a cylindrical tube of 10 mm inner diameter and 300 mm length, containing 6 apertures. The inner diameters of the apertures are gradually reduced from 5 mm to 3 mm. The apertures are thin plates (0.5 mm) except from the first and the last ones, which are cylinders of 10 mm length. The chamber pressure downstream the last aperture (nozzle) is maintained below 0.1 Pa using a 280 l/s turbo molecular pump (Varian V-301NAV) backed by a diaphragm pump (Vacuubrand MD1-Vario), while the pressure upstream the nozzle (inside the aerodynamic lens) is ~180 Pa at standard ambient pressure. The set-up of the aerodynamic lens leads to a series of contractions and expansions in the air streamlines. Because of the particles' larger inertia compared to the gas molecules, the particle trajectories deviate from the gas streamlines. Particles with high enough inertia are partially carried across the diverging gas streamlines, keeping them close to the horizontal axis of the aerodynamic lens, resulting in a narrow collimated particle beam. The

performance of the aerodynamic lens was simulated by Jayne et al. (2000), using a computational fluid dynamics software (FLUENT; Fluent Inc., Lebanon, NH, USA). This resulted in particle trajectories inside the lens, lens transmission efficiency and size-dependent particle velocities. Figure 2.3 illustrates the simulated particle trajectories for spherical particles with  $1 \text{ g cm}^{-3}$  density and 100 nm diameter.

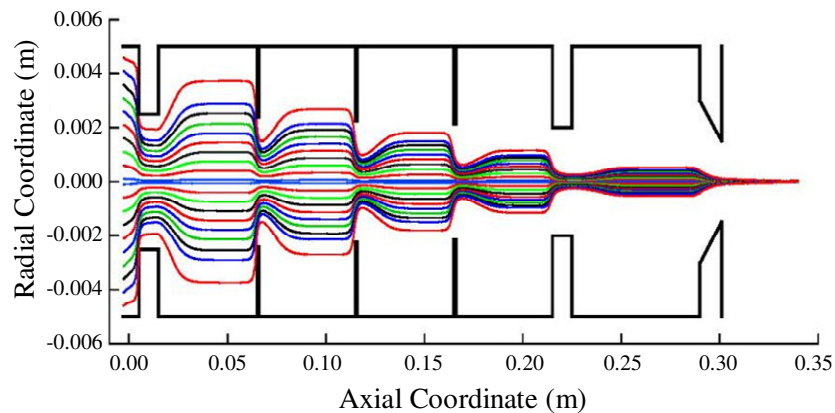


Figure 2.3: FLUENT simulation results illustrating the particle trajectories of 100 nm diameter spheres inside the aerodynamic lens (Jayne et al., 2000). The critical orifice is upstream the first aperture.

According to the fluid dynamics calculations the transmission and focusing efficiency of the lens was determined to be ~100 % for particles with diameters between approximately 40 and 600 nm (Figure 2.4, Worsnop, 2003). Below the lower cut-off the transmission efficiency decreases sharply because small particles have too little inertia to be focused aerodynamically and therefore follow the gas streamlines. At the upper cut-off the transmission efficiency gradually decreases with increasing particle diameter because large particles are mostly lost through impaction onto the critical orifice or on the first lens stage.

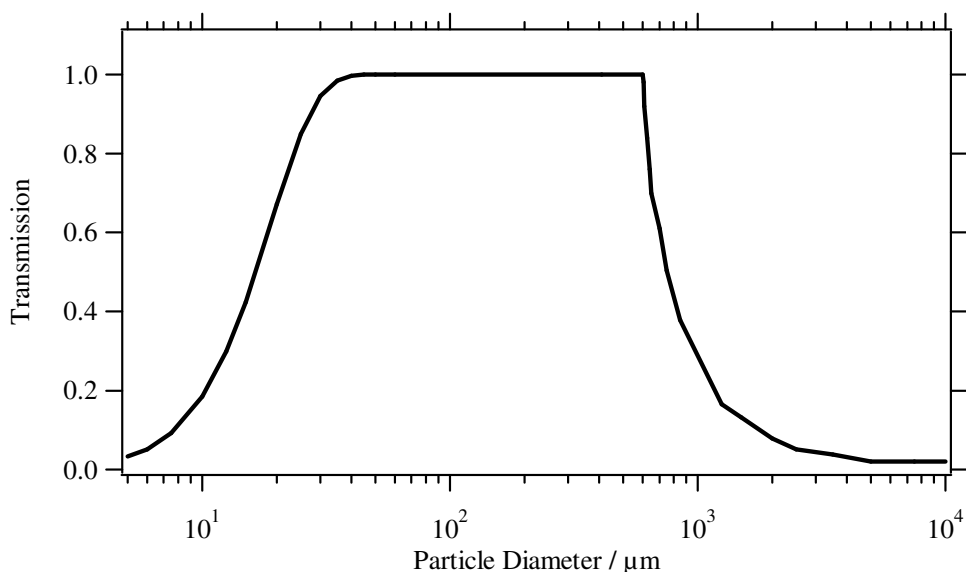


Figure 2.4: Size-dependent transmission efficiency of the aerodynamic lens (Worsnop, 2003).

After being focused by the aerodynamic lens, the particles are accelerated through the nozzle into the vacuum chamber by a supersonic expansion. The resulting particle beam width is mainly determined by Brownian motion and lift forces on the particles during the nozzle expansion (Liu et al., 1995a and Liu et al., 1995b). Brownian motion is caused by random collisions of air molecules with the particles, resulting in particle beam divergence and broadening of the beam profile. Lift forces are forces directed orthogonally to the main flow direction. They only affect non-spherical particles and lead to a beam broadening. It is difficult to quantify the effect of lift forces on arbitrarily shaped particles, because it depends on the geometry and orientation of the particles. Measurements show that beam width at the vaporiser is smaller than 1 mm, depending on the particle size and shape (Huffman et al., 2005).

### 2.1.2 Particle Sizing Chamber

The aerodynamic lens is aligned so that particles are directed through a 1 mm diameter skimmer cone into the particle sizing chamber. The skimmer is used to improve the vacuum and to remove most of the surrounding gas. The pressure inside the chamber is maintained at  $\sim 10^{-3}$  Pa by a 70 l/s turbo molecular pump (Varian V-70LP). This pump, as well as the other turbo molecular pumps, is backed by the inlet turbo molecular pump so that only a single roughing pump is needed for the whole system. At the front end of the chamber the particle beam passes the particle chopper, a metallic rotating disk (50 mm diameter, 0.2 mm thick) with two radial slits positioned 180 degrees apart. The chopper can be moved perpendicular to the particle flight direction by a servo motor to three different positions: in the “open” position the chopper is moved out of the beam, allowing it to completely pass through; in the “blocked” position the chopper is moved into the beam to completely block it; and in the “chopped” position the chopper lets small pulses of material through at a user-definable frequency of 100-120 cycles per second. The chopper position used depends on the mode the ToF-AMS is operated in (see later section of this chapter).

During the supersonic expansion of the particle-laden air on exiting the aerodynamic lens, small particles are accelerated to higher velocities than large particles, resulting in a size-dependent particle velocity distribution. The size of the particles can therefore be determined from the flight time the particles need to cover the distance between the particle chopper and the detection region ( $l_c = 395$  mm). For this reason the chopper is coupled to an optical sensor to define the start of the particle time-of-flight (PToF) cycle and to synchronise the time-resolved particle detection using the mass spectrometer. The PToF measurement relies on the fast particle vaporisation and detection (of the order of microseconds) compared to the particle flight times (in the order of milliseconds). The measured particle velocities can be converted into particle diameters using a curve derived during a calibration with particles of known size, density and shape. This calibration will be described in detail in section 3.4.1.

Since the aerodynamic diameter  $d_a$ , as it is defined for example by Hinds (1999), is not valid to describe the aerodynamic characteristics of particles in the free molecular flow regime (where the mean free path of the particles is larger than their diameter; this is the flow regime found in the aerodynamic lens), the vacuum-aerodynamic diameter was introduced by Jimenez et al. (2003b) for AMS measurements. It can be defined as follows:

The vacuum-aerodynamic (equivalent) diameter  $d_{va}$  is the diameter of a spherical particle of standard density (1 g cm<sup>-3</sup>) that obtains the same

velocity in an acceleration by expansion of the carrier gas *in the free molecular flow regime* as the particle under investigation

The relationship between the vacuum aerodynamic diameter  $d_{va}$  and the volume-equivalent diameter  $d_{ve}$  is given by Equation (2.1) (DeCarlo et al., 2004):

$$d_{va} = \frac{\rho_p}{\rho_0} \cdot \frac{d_{ve}}{\chi_v} \quad (2.1)$$

Where  $\rho_p$  is the particle density in  $\text{g cm}^{-3}$ ,  $\rho_0$  the standard density ( $1 \text{ g cm}^{-3}$ ) and  $\chi_v$  the dynamic shape factor in the free molecular regime limit.

The size-dependent results in this thesis will be mostly reported in terms of the vacuum aerodynamic diameter. However, other diameters like the geometric particle diameter  $d_p$  and the electrical mobility diameter  $d_{mob}$  will also be used (see Appendix 6.4, List of Symbols).

### 2.1.3 Particle Evaporation and Ionisation Chamber

The particle evaporation and ionisation chamber is separated from the particle sizing chamber by a 3.8 mm inner diameter aperture and is differentially pumped by another 70 l/s and a 280 l/s turbo molecular pump which maintain the pressure at approximately  $2 \cdot 10^{-5} \text{ Pa}$ . The focused particle beam is directed into the chamber and impacts onto the vaporiser located at the downstream end inside a commercial compact cross beam electron impact ion source (Inficon, East Syracuse, NY, USA; see Figure 2.5).

The vaporiser has a diameter of 3.8 mm and is custom-built from porous tungsten (~20 % void volume, ~100-200  $\mu\text{m}$  pore sizes). At the front end, where the particles impact, the vaporiser has an inverted cone shape with a 60-degree included angle. It is brazed onto a molybdenum heater body, containing an embedded resistive wire potted in ceramic and is heated conductively. The vaporiser temperature is measured by a micro thermocouple attached to the vaporiser and can be adjusted in a range between 200 °C (limited by radiative heating from the electron emitting filament) and 1000 °C.

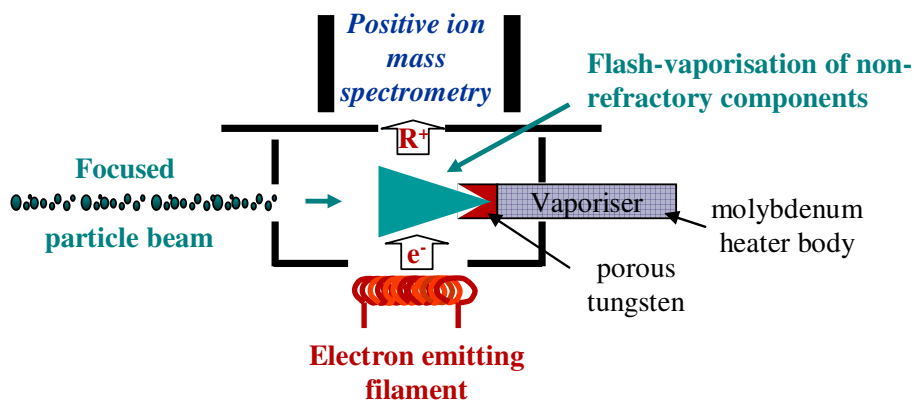


Figure 2.5: Schematic of the evaporation and ionisation sub-chamber (Aerodyne Research, Inc.).

Crucial to this design is mounting the vaporiser in the centre of the ioniser so that essentially every molecule that leaves the vaporiser passes through the ionisation volume that is imaged into the mass spectrometer. It is also necessary to apply a voltage bias to the vaporiser to

“retune” the distorted electric field caused by placing the vaporiser inside the ioniser. This bias lies typically within several volts of the ionisation chamber voltage.

Upon impaction onto the vaporiser, the non-refractory fraction of the aerosol particles flash-vaporise. The term “non-refractory” is defined operationally as those species which flash-vaporise at the vaporiser temperature under vacuum conditions. The resulting vapour molecules are ionised by 70 eV electrons emitted from a tungsten filament located to the side of the ion source. The positive ions are extracted from the ion source via a lens at a potential of approximately -100 V and are focused into a beam with the help of an Einzel lens.

#### 2.1.4 Detection and Chemical Analysis Chamber

From the ion source the ions are transferred 96 mm to the orthogonal time-of-flight extractor through electrostatic lenses, designed to keep the ion loss as small as possible, and enter the time-of-flight mass spectrometer (TOFMS) through a hole of approximately 6 mm diameter. The mass spectrometer is housed in the chemical analysis and detection chamber, pumped by another Varian 70 l/s turbo molecular pump. The open area of the ion extractor is 46 mm in length and matches the active area of the micro channel plate (MCP) detector. The ions drift through the extractor with a kinetic energy of 50 eV before they are orthogonally extracted into the ion time-of-flight (I-TOF) region of the mass spectrometer by a pulsed high voltage. The extraction period is typically 13  $\mu$ s, generating 76923 complete mass spectra per second. One mass spectrum typically consists of in the order of 10000 points, with one point representing an ion flight time of 1 ns. Together with the TOFMS voltage settings, the number of points per mass spectrum determines the maximum possible  $m/z$  that can be measured. During this work, the maximum  $m/z$  measured was typically in the order of 310. The TOFMS is equipped with a two-stage gridded ion reflector, resulting in an effective ion flight path of 430 mm. After post acceleration the ions are collected by a 40 mm Chevron stack MCP detector (Burle Technologies, Inc., Sturbridge, USA), and the MCP output signal is detected in two channels of a high speed (1 GHz) 8-bit analogue-to-digital conversion data acquisition card (AP240, Acqiris, Geneva, Switzerland) in parallel. One of the channels records the mass spectral signal with an amplification of 11 (Amplifier Model ACA-2-21-N, Becker & Hickel GmbH, Germany), while the second channel works without any amplification in order to extend the dynamic range. The AP240 allows the user to set a minimum signal intensity, below which all signals are discarded (“data acquisition threshold”). This thresholding aims to eliminate electronic noise from the mass spectra, without discarding signal intensity originating from ions. The data is transferred from the acquisition card, processed and stored to disk by a custom-written logging software (Jimenez Laboratory, University of Colorado at Boulder, USA and Aerodyne Research Incorporated, Billerica, USA). For high duty cycle spectrum acquisition, the collected raw spectra are averaged on the data acquisition card in real-time before transfer to the CPU every few seconds.

## 2.2 Modes of Operation

The ToF-AMS can be operated in three different modes of operation, controlled by the data acquisition software, providing different information about the measured aerosol particles.

The MS or *mass spectrum mode* is used to collect average mass spectra of the non-refractory aerosol components for an ensemble of particles. The particle chopper is alternately moved into the open and blocked positions. In the beam open position, mass spectra of the non-refractory aerosol components for an ensemble of particles are recorded together with a fraction of the air surrounding the particles and the instrument background. Measuring with the beam blocked gives the background signal due to residual air and vapour molecules. By subtracting the background signal from the mass spectrum measured in the beam open position, mass spectra of the non-refractory aerosol components with a fraction of the surrounding air (the so-called “airbeam”) only are obtained. The vapours evolving from the particles are continuously ionised and the resulting ions are continuously guided into the extractor of the TOFMS. Quantitative mass concentrations in  $\mu\text{g}$  of particulate material per  $\text{m}^3$  of ambient air can be obtained for all ionised elements, molecules and molecule fragments. From this, quantitative ambient mass concentrations of various chemical species (in  $\mu\text{g m}^{-3}$ ) can be derived. Particle size measurements are not conducted in MS mode.

The PToF or *particle time-of-flight mode* is used to collect average size distribution data for all non-refractory aerosol components in an ensemble of particles. This mode of operation is based on the fact that the aerosol particles gain a velocity distribution as they are accelerated from the aerodynamic lens into the vacuum chamber which is dependent on their size, density and shape. The particle beam is chopped by the particle chopper at a user-selectable frequency in the range of 80-130 Hz. Aerosol particles can only pass through when one of the chopper disc slits is in line with the particle beam. An optical sensor positioned on the chopper mount senses when a slit is in the position where the particle beam is allowed to pass. Starting at this point, the MCP response (complete mass spectra) as a function of time is recorded. The delay between the particle beam passing the chopper and the ion detection in the mass spectrometer is the particle flight time through the system. This is possible since the time scale for evaporation, ionisation and mass spectrometric analysis is short ( $\sim 50 \mu\text{s}$ ) compared to the flight time of the particles from the chopper to the vaporiser ( $\sim 2-5 \text{ ms}$ , depending on the particle size). The TOFMS is pulsed continuously at 76.9 kHz, producing a complete mass spectrum every  $13 \mu\text{s}$ . During typically  $200 \mu\text{s}$  in the beginning of each chopper cycle, no data are collected from the mass spectrometer, since no particles or gases will obtain a velocity high enough to reach the vaporiser within this time. After this data delay, typically 520 mass spectra are recorded as a function of time during each chopper cycle. Before transfer of the data into the PC, the spectra of every point in the chopper cycle (for every particle time-of-flight) are individually averaged over typically 300 chopper cycles on the data acquisition card. Due to limited on-board memory two consecutive mass spectra are co-added into a separate segment of the memory on the data acquisition card, so that the effective time resolution then is  $26 \mu\text{s}$  and the size distribution is divided into 260 size bins. The data obtained in this mode can be transformed into mass distributions of various species as a function of their vacuum aerodynamic diameter after applying the appropriate calibrations as will be discussed in chapter 3.

The SPToF or *single particle time-of-flight mode* is used to collect size-dependent single particle information. In this mode the ToF-AMS is operated in the same way as in the PToF mode, but without averaging of chopper cycles on the data acquisition card. In this mode, for particles large enough to supply sufficient mass, individual quantitative particle chemical composition information can be obtained. This exceeds the capability of the to-date laser ablation instruments. The SPToF mode will not be discussed in more detail, as it was not further characterised during this work. The exploration of the potential inherent here needs a large amount of additional work.

## 2.3 Differences to Q-AMS Instruments

As already mentioned in chapter 1, the ToF-AMS is a further development of the Aerodyne Aerosol Mass Spectrometer (Q-AMS) designed by Aerodyne Research Incorporated (Billerica, USA) and introduced by Jayne et al. (2000). Other than the ToF-AMS, the Q-AMS uses a quadrupole mass spectrometer (QMS) to perform the analysis and a secondary electron multiplier to detect the ions. The main difference between the two instruments is that in the Q-AMS ions of only one  $m/z$  can be studied at any one time, while in the ToF-AMS a whole mass spectrum is achieved for every pulse of the orthogonal extractor. In MS mode, the QMS continuously scans from  $m/z$  0 to 300 at a rate of 1000 per second. The logging and control software of the Q-AMS records the multiplier signal as a function of  $m/z$ , generating complete mass spectra. In the PToF mode, the QMS is set to a selection of single  $m/z$  at a user-definable rate, resulting in size-resolved information for only a few  $m/z$ . Due to the need to scan in order to obtain a whole mass spectrum, the Q-AMS duty cycle is much lower than the duty cycle of the ToF-AMS, and size distributions can only be obtained for a few  $m/z$  and not for all  $m/z$  simultaneously as in the ToF-AMS.

In the following, the terms “Q-AMS” and “ToF-AMS” will be used, when only the specific instrument is meant, and “AMS” if the given information is true for all types of Aerodyne Aerosol Mass Spectrometers.

### 3 ToF-AMS Data Analysis and Characterisation

The first two chapters provided the background necessary to understand the development of data analysis procedures and characterisation of the ToF-AMS. It was illustrated why the development of an instrument like the ToF-AMS is important and why it is essential to thoroughly characterise it. In addition, the hardware set-up and the operation of the ToF-AMS was explained.

In other words, we are now at the point where we have ToF-AMS raw data obtained during the operation of the ToF-AMS in both MS and PToF mode.

This chapter will describe how ToF-AMS raw data are analysed and which calibrations are needed to obtain meaningful results. Some parts of the ToF-AMS data processing builds on procedures developed for the Q-AMS (e.g. Allan et al., 2003a; Allan et al., 2003b). However, a complete explanation of all procedures needed to analyse ToF-AMS data will be given and all steps that are different from the Q-AMS data analysis will be discussed and characterised in more detail.

Figure 3.1 is a flow chart of the ToF-AMS data analysis procedures that can also be seen as a guide through chapter 3. In the black-bordered boxes the format of the data of each processing stage is shown, starting with the raw mass spectra as they are stored to disk by the data acquisition software. Everything that is written in the middle column of the flow chart is valid for both MS and PToF mode data, while the steps in the left column are only applied to MS mode data, the steps in the right column only to PToF mode data. The light blue shaded boxes show corrections and calibrations which have to be applied to the data during the various processing steps. As outline for chapter 3, it is indicated in dark green in which section of the chapter the different information can be found. Lastly, text written in bold black signalises all steps of the data processing procedure which have been further investigated as part of this work or are results of characterisation experiments performed during this work.

Section 3.1 describes the conversion of raw mass spectra into spectra of unit resolution in  $m/z$  space (“unit resolution spectra”). In section 3.2 it is explained how the measured signal intensity is converted into mass concentrations of aerosol species. All procedures described in these two chapters are applied to MS mode as well as to PToF mode data. Section 3.3 addresses the further processing of PToF mode data to derive aerosol mass size distributions. Section 3.4 is about mass concentration detection limits, experimentally determined for various measurement conditions, and compared to Q-AMS limits of detection. One of the features of the ToF-AMS, the capability to obtain size-dependent mass spectra, is discussed in section 3.5. The last section of this chapter, 3.6, deals with the implementation of the described data analysis strategies into a user-friendly data analysis software.

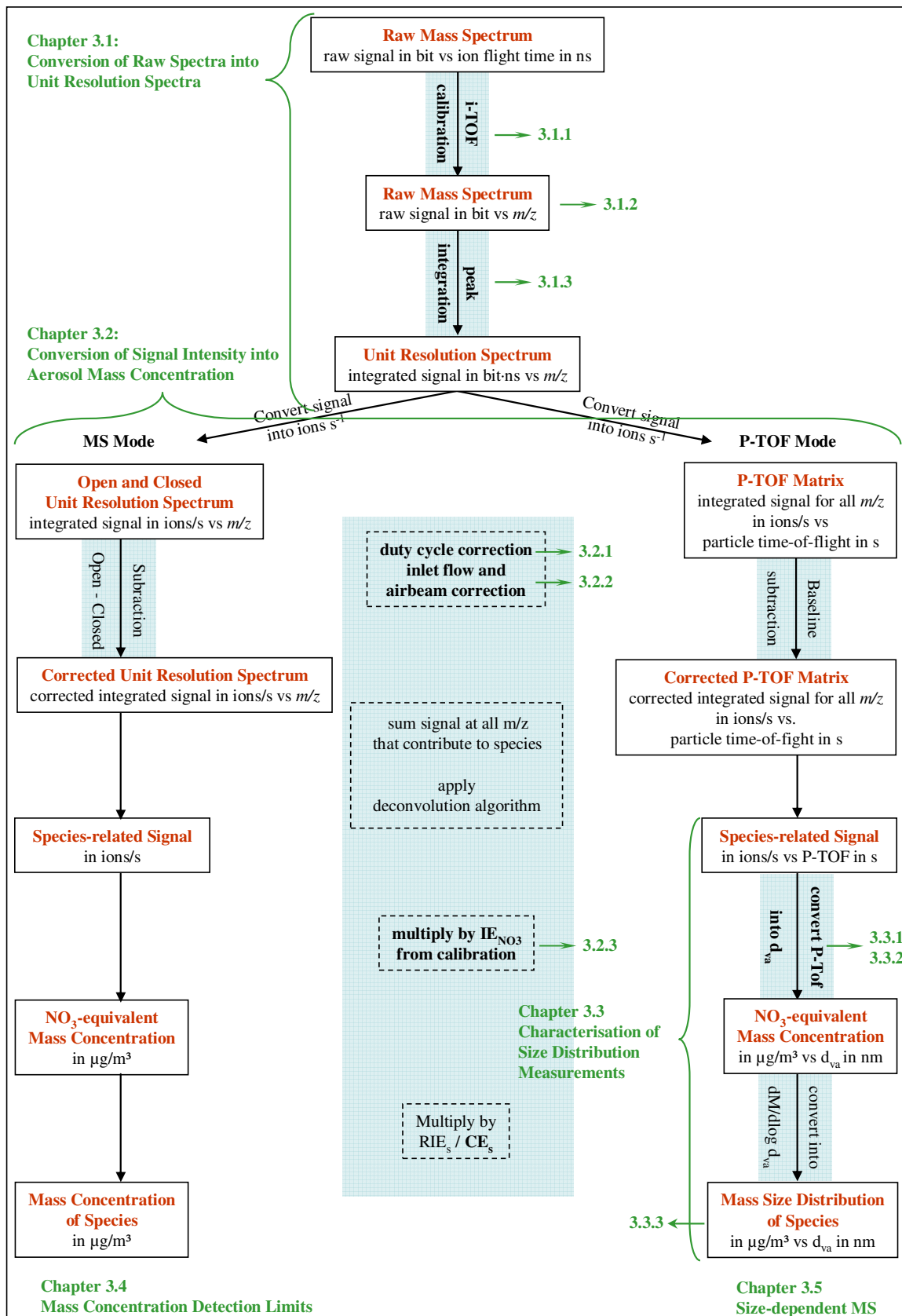


Figure 3.1: Flow chart of ToF-AMS data analysis and processing. For details see text.

### 3.1 Conversion of Raw Mass Spectra into Unit Resolution Spectra

Both modes of operation provide averaged raw mass spectra, given as the measured signal in bits (between 0 and 255) as a function of the ion flight time (Figure 3.2). In MS mode, a mass spectrum averaged for a user-selectable interval (“saving interval”) is stored to disk as one 1-dimensional array per saving interval. Together with the TOFMS voltage settings the number of points (one point equals 1 ns) in the array determines the maximum possible  $m/z$  that can be measured and can be set via the data acquisition software. During this work, it was typically set to a value in the order of 10000 points, resulting in a maximum  $m/z$  of approximately 310.

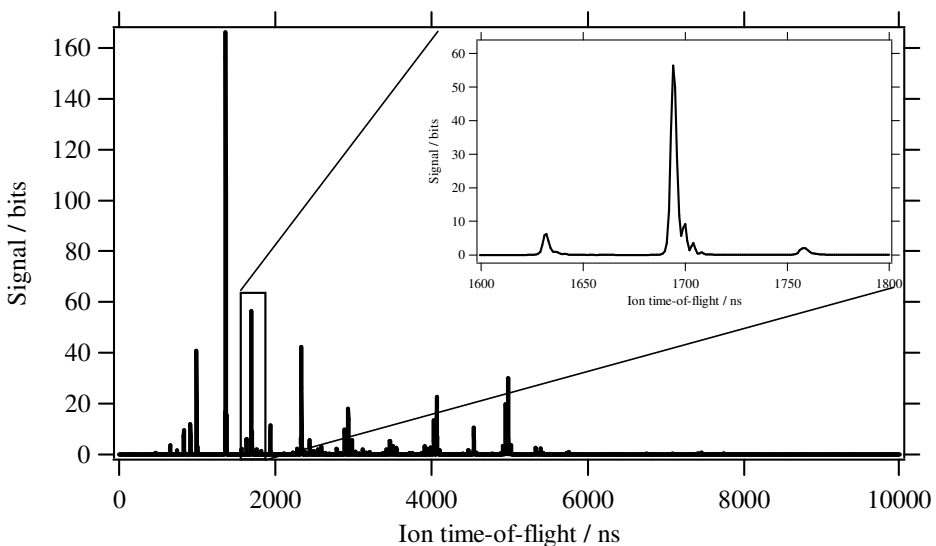


Figure 3.2: Averaged raw mass spectrum as it is acquired with the ToF-AMS.

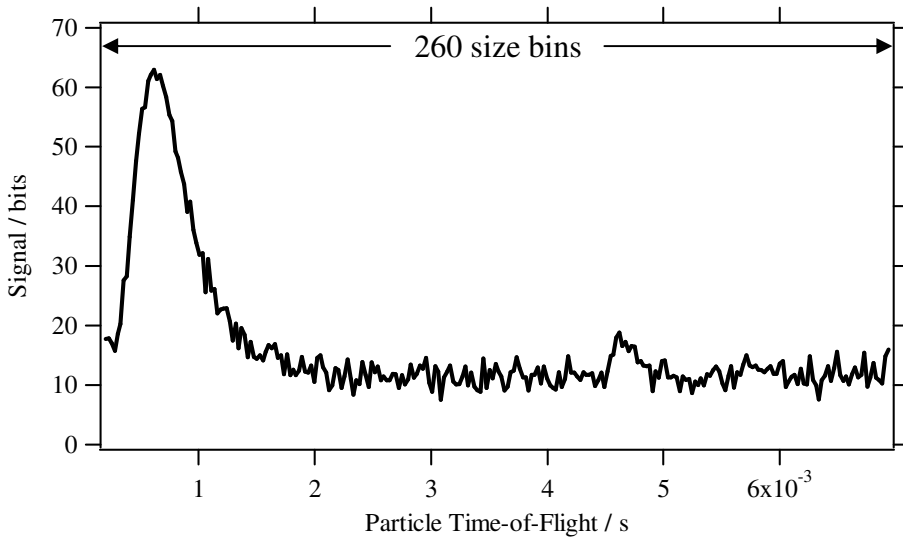


Figure 3.3: PToF distribution as it is acquired in PToF mode. Shown is one column of the 2-dimensional PToF array, containing the measured signal as a function of particle flight time for one specific ion flight time (1742 ns, corresponding to  $m/z$  28).

In PToF mode, complete mass spectra are measured as a function of the particle flight time, resulting in one 2-dimensional array stored to disk once per saving interval. This array contains average mass spectra in the rows (again 8892 points per row) and particle flight time distributions (i.e., the measured signal as a function of the particle flight time) for every ion time-of-flight in the columns (Figure 3.3). Under standard operating conditions, one column contains 260 points representing 260 different particle diameters. However, this number can change if a different number of mass spectra is taken during one chopper cycle. This value can also be set via the data acquisition software.

### 3.1.1 I-ToF Calibration

In order to be able to calculate the signal that is produced by ions of one particular  $m/z$ , it is necessary to convert the raw mass spectra into spectra of unit resolution in  $m/z$  space, or in other words to determine the signal that corresponds to each individual  $m/z$ .

For this purpose the flight time of an ion needs to be converted into its  $m/z$ . In the extractor of the TOFMS the ions are accelerated to a velocity  $v_{ion}$  by the flight tube voltage  $U_{ion}$  according to Equation (3.1).

$$q \cdot U_{ion} = \frac{1}{2} m_{ion} \cdot v_{ion}^2 \Rightarrow v = \frac{s_{ion}}{t_{ion}} = \sqrt{\frac{2 q U_{ion}}{m_{ion}}} \quad (3.1)$$

where  $t_{ion}$  is the flight time of the ions in the TOFMS,  $s_{ion}$  the effective drift length of the TOFMS (430 mm),  $m_{ion}$  the mass of the ion,  $q = z \cdot e$  the electric charge of the ion,  $z$  the number of net elementary charges in the ion and  $e$  the elementary charge. According to Equation (3.1) the flight time of each ion is proportional to the square root of its  $m/z$ . This results in Equation (3.2), the I-TOF calibration equation for the TOFMS.

$$\sqrt{\frac{m}{z}} = a \cdot t_{ion} + b \quad (3.2)$$

where  $a$  and  $b$  are calibration constants. Those are determined by plotting the square roots of the exact  $m/z$  of a number of prominent peaks in the mass spectrum versus their ion flight times (determined as the position of the peak maximum) and fitting a linear regression to these points. The peaks used for this calibration are typically  $\text{N}^+$  ( $m/z$  14.0031),  $\text{N}_2^+$  ( $m/z$  28.0061),  $\text{O}_2^+$  ( $m/z$  31.9898),  $\text{Ar}^+$  ( $m/z$  39.962) and  $\text{W}^+$  ( $m/z$  183.951), which are usually easy to recognise within a mass spectrum. As the ion flight time through the mass spectrometer is dependent on the applied voltages, and these may drift with changing ambient temperature, an I-TOF calibration should be performed for each mass spectrum individually, especially when performing measurements under changing temperature conditions.

In order to check the quality of the calibration, from a set of 800 mass spectra, recorded in MS mode and representing a 5-minute average each, every mass spectrum was analysed in more detail. This analysis shows that the linearity of the I-TOF calibration is extremely good for all spectra: the Pearson's  $r^2$  is greater than 0.9999995 for all I-TOF calibrations.

Applying an I-TOF calibration to the raw data results in raw mass spectra expressed as the signal intensity in bits as a function of  $m/z$ .

### 3.1.2 Mass Resolving Power

In time-of-flight mass spectrometry, the mass resolving power  $R$  of an instrument is an important quality measure of instrument performance. It is the ability to separate ions of similar flight times but different  $m/z$  into separate signals and can be expressed as the  $m/z$  divided by the full width at half maximum (FWHM) of a peak at this particular  $m/z$  (Equation (3.3)).

$$R = \frac{m/z}{\Delta m/z} \quad (3.3)$$

where  $\Delta m/z$  is the FWHM of the peak.

To determine the  $m/z$ -dependency of the mass resolving power of the used mass spectrometer, it is necessary to acquire a mass spectrum containing peaks at almost all  $m/z$  of interest (up to the maximum  $m/z$  that can be measured with the used timing scheme). For this purpose, a suspension of polystyrene latex (PSL) spheres ( $d_p = 300 \text{ nm} \pm 6 \text{ nm}$ ) in water was nebulised by a Constant Output Atomizer (Model 3076, TSI Incorporated, Shoreview, MN, USA; TSI Incorporated, 2005) to generate an aerosol containing a high number and mass concentration of PSL particles. The droplets were subsequently dried using a diffusion dryer (Model 3062, TSI Incorporated, Shoreview, MN, USA) filled with silica gel before the resulting PSL particles were introduced into a Condensation Particle Counter (CPC, Model 3025, TSI Incorporated, Shoreview, MN, USA; TSI Incorporated, 2002) and the ToF-AMS in parallel. The CPC was used to check the aerosol number concentration and the ToF-AMS was set to MS mode with a 5-minute saving interval.

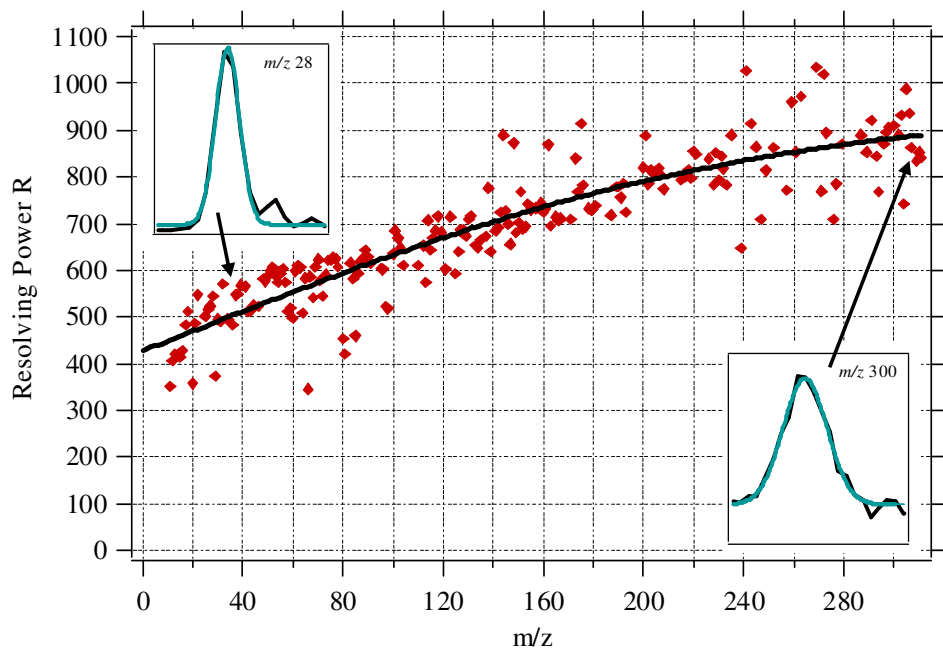


Figure 3.4: Mass resolving power  $R$  of the time-of-flight mass spectrometer used during this work as a function of  $m/z$ . The inserts show two different peaks in the beginning and in the end of the raw mass spectrum (black) and the resulting Gaussian fits (green).

To determine the mass resolving power  $R$  as a function of  $m/z$ , a Gaussian function was fitted (using IGOR Pro 5.04, Wavemetrics Inc., Lake Oswego, OR, USA) to every single peak in the mass spectrum measured in the chopper open position and the FWHM of the peaks was calculated from the fit parameters according to Equation (3.4).

$$\Delta m = \sigma \cdot \sqrt{4 \cdot \ln(2)} \quad (3.4)$$

with  $\sigma$  the width parameter of the Gaussian fit. The results are shown in Figure 3.4. The mass resolving power is a function of  $m/z$  with  $R \approx 500$  at  $m/z$  28 and  $R \approx 900$  at  $m/z$  300. For the used Tofwerk TOFMS the  $m/z$ -dependency can be approximated by Equation (3.5) (Tofwerk, Thun, Switzerland):

$$R(m/z) = \frac{-R_0}{1 + e^{(m/z - m_0)/d_m}} + R_0 \quad (3.5)$$

with  $R_0$  the maximum mass resolving power achieved with the used TOFMS,  $m_0$  the  $m/z$  at which the resolving power is  $R_0/2$  and  $d_m$  a slope parameter.

For the TOFMS used during this work, the following parameters were determined:

$$\begin{aligned} R_0 &= 964 \\ m_0 &= 26 \\ d_m &= 114.5 \end{aligned}$$

This mass resolving power gives a resolution of 0.3  $m/z$  at  $m/z$  300 and of  $< 0.1 m/z$  at  $m/z$  28, which, however, is not sufficient for the separation of for example CO<sub>2</sub> and C<sub>3</sub>H<sub>8</sub>, both fragments at  $m/z$  44.

### 3.1.3 Peak Integration

In a time-of-flight mass spectrometer peak area is the physically meaningful value for defining the signal intensity corresponding to a particular  $m/z$ . In other words, extracting a unit resolution spectrum from a ToF-AMS raw mass spectrum is equivalent to assigning the total peak area (which extends over several  $m/z$  points in the raw data) to the one  $m/z$  value corresponding to the peak maximum. For this purpose, the borders within which the peaks are to be integrated need to be defined. There are various possibilities of defining the peak integration borders:

- 1) Fixed borders around the peak maximum (e.g. -0.2 to +0.3  $m/z$ ).

This usually results in an integration interval that is broader than the actual peak so that some of the signal not corresponding to the peak will be integrated as well. As the signal between two peaks is only determined by the MS baseline (see below) which can be subtracted from the signal, this is not significant.

This method works properly approximately up to  $m/z$  200. Because the peak width increases with increasing  $m/z$ , the fixed borders become too narrow after this value.

- 2) Variable borders around the peak maximum, defining the borders in a way that the integration interval becomes broader with increasing  $m/z$ .

As the  $m/z$ -dependent mass resolving power (and therefore the peak width) is not

equal for every mass spectrometer, these borders need to be defined for every instrument individually.

- 3) Variable borders around the peak maximum, dependent on the mass resolving power of the TOFMS, in order to match the total peak width of all peaks.

The borders before the peak,  $b_l$ , and after the peak,  $b_h$  are defined as

$$\begin{aligned} b_l &= m_p \cdot \left(1 - \frac{1}{2 \cdot R}\right) \\ b_h &= m_p \cdot \left(1 + \frac{1}{2 \cdot R}\right) \end{aligned} \quad (3.6)$$

where  $m_p$  is the  $m/z$  value at the peak maximum. Here again, the integration borders are different for different instruments, as the  $m/z$ -dependency of the mass resolving power might be different.

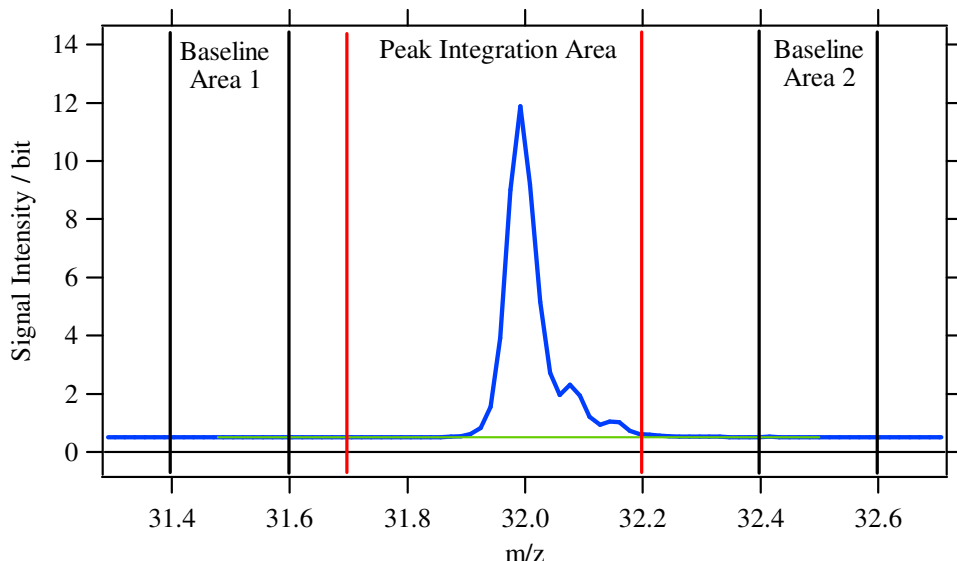


Figure 3.5: Illustration of the peak integration process. The MS baseline (green line) is calculated by linearly interpolating between the averages of the baseline areas before (Baseline Area 1) and after the peak (Baseline Area 2) and subtracted from every point within the integration interval. The total signal corresponding to a particular  $m/z$  is given as the sum of all points within the integration interval (Peak Integration Area).

As a mass spectrum usually has a baseline (“MS baseline”) different from zero (mainly due to a background of scattered ions), it is necessary to subtract this baseline from every point of a peak before integration. Because this baseline is not constant over the whole mass spectrum, two baseline regions are defined for each peak, one before and one after the peak. The baseline of a particular peak is then calculated by linearly interpolating between the averages of the baseline areas before ( $b_l$ ) and after ( $b_h$ ) the peak. After subtraction of the corresponding MS baseline value from every point  $i$  within the integration interval, all points are summed up to give the total signal  $I_{tot}$  corresponding to a particular  $m/z$  (Equation (3.7)).

$$I_{tot} = \sum_i \left( I_i - \frac{b_{1,i} + b_{2,i}}{2} \right) \quad (3.7)$$

The peak integration process is illustrated in Figure 3.5.

During this work, if not otherwise noted, method 1), the fixed borders around the peak maximum, was used for determining the integration area for the peak integration of MS mode data, and the MS baseline was subtracted. The PToF mode raw data were integrated by the data acquisition software using method 3) and the unit resolution spectra were saved in order to save disk space.

After having integrated all peaks in a mass spectrum one gets a unit resolution spectrum in units of bits·ns as a function of  $m/z$ .

## 3.2 Conversion of Signal Intensity into Mass Concentrations

The conversion of the measured signal intensity into mass concentrations is generally the same for both MS mode as well as PToF mode data and for all Aerodyne AMS instruments. The mass concentrations of the various species are calculated from the integrated signal of the unit resolution spectra. Therefore the procedure will be explained mainly on the basis of the MS mode data, though it is the same for the PToF mode data with the exception that those data also contain size-dependent information. The extraction of this additional information will be discussed in section 3.3.

### Conversion of Signal into Ions s<sup>-1</sup>

In a first step it is necessary to convert the signal intensity given in bits·ns into ion s<sup>-1</sup>. To be able to do this one needs to know the signal intensity of a single ion, which is determined during a calibration procedure included in the data acquisition software. During this procedure unthresholded raw data are acquired and the mean area of all single ion events is determined (for further information about this procedure see <http://cires.colorado.edu/jimenez-group/ToFAMSResources/ToFManual/acquisition.html#Threshold>). The single ion signal intensity *SI* is given in bits·ns. The measured signal intensity can be converted from bits·ns into ions s<sup>-1</sup> according to Equations (3.8) and (3.9).

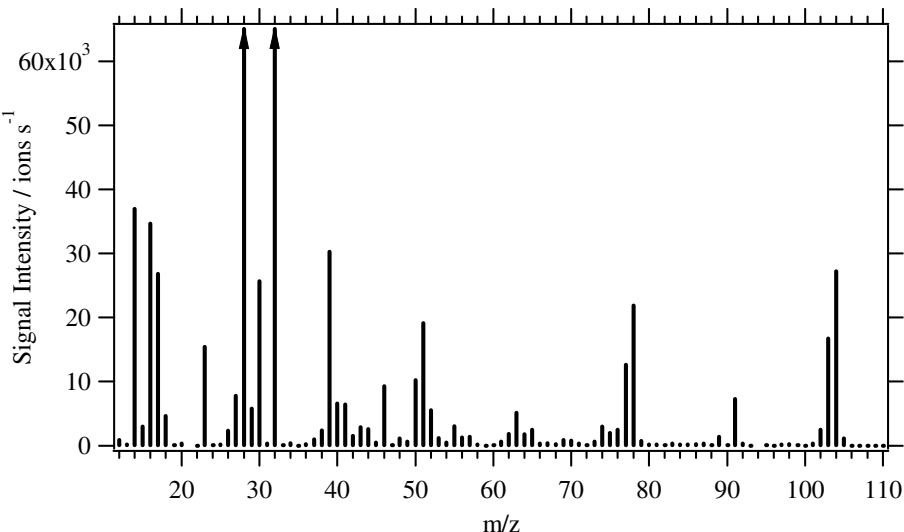


Figure 3.6: Unit resolution spectrum of laboratory-generated PSL particles in ions s<sup>-1</sup> as a function of *m/z*. The height of the sticks corresponds to the total integrated signal intensity of the individual *m/z*.

$$\text{MS mode: } I_{MS,ions} = \frac{I_{MS,bits}}{SI} \cdot f_{pulse} \quad (3.8)$$

$$\text{PToF mode: } I_{P-TOF,ions} = \frac{I_{P-TOF,bits}}{SI} \cdot f_{chopper} \cdot \frac{n_{coadds}}{D_{chopper}} \quad (3.9)$$

with  $I_{MS}$  and  $I_{PToF}$  the signal intensities measured in MS mode and PToF mode, respectively; the indices *bits* and *ions* stand for the units bits·ns and ions s<sup>-1</sup>, respectively;  $f_{pulse}$  is the

pulsing frequency of the mass spectrometer,  $f_{chopper}$  is the frequency at which the particle beam is chopped,  $n_{coadds}$  the number of spectra that are coadded and  $D_{chopper}$  the chopper duty cycle in PToF mode (1 % for the chopper used during this work).

This conversion results in unit resolution spectra in ions  $\text{s}^{-1}$  as a function of  $m/z$  as shown for example in Figure 3.6.

In MS mode, for every saving interval two averaged mass spectra are saved; one spectrum containing the average of all mass spectra taken in the chopper open position (which gives the average mass spectrum of the aerosol together with the instrument background), and one mass spectrum containing the average of all mass spectra measured in the beam blocked position (giving the average mass spectrum of the instrument background only). Through subtraction of the beam blocked spectrum from the beam open spectrum, one derives the average mass spectrum of the aerosol beam without the instrument background (“difference spectrum”). This procedure is equivalent to subtracting the blank signal from the measured signal in standard analytical methods.

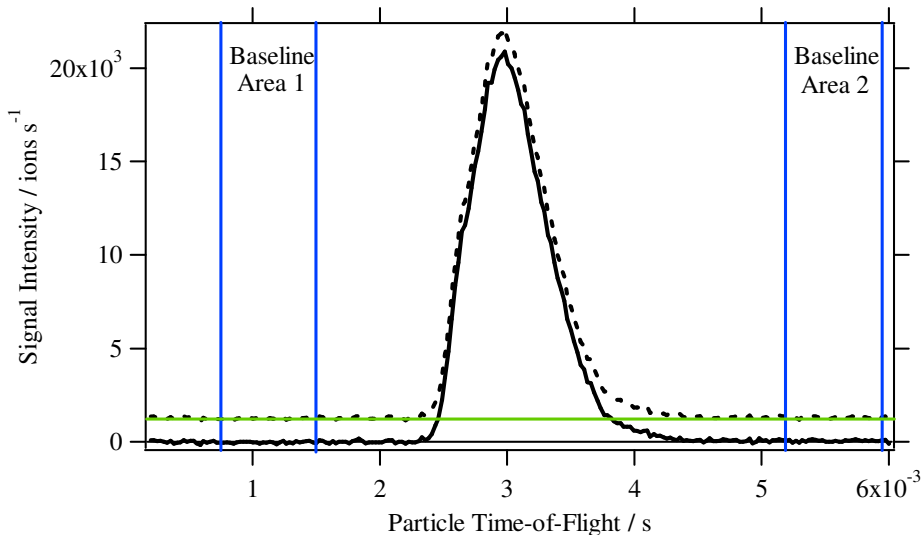


Figure 3.7: Illustration of the PToF baseline subtraction for an individual  $m/z$ . The baseline (green line) is calculated as the linear interpolation between the averages of the two baseline areas (Baseline Area 1 in the beginning of the PToF cycle; Baseline Area 2 in the end of the PToF cycle). The dotted and solid curves show the PToF distribution before and after PToF baseline subtraction, respectively.

For PToF mode data, as there is no individual background measurement, this is derived by subtracting the “PToF baseline” from the PToF distributions of all  $m/z$  after integration of the raw data. As can be seen in Figure 3.7, the PToF distributions have a baseline that is non-zero (i.e. the PToF signal of particle flight times where no particle or gas signal is expected is non-zero). In order to subtract this PToF baseline, two baseline regions are defined: one in the beginning of the PToF cycle<sup>1</sup> and one in the end, at particle flight times where no particle-caused signal will occur. Similar to the MS baseline subtraction (see section 3.1.3) the PToF baseline is linearly interpolated between the averages of the two baseline areas and

<sup>1</sup> The shown distribution represents one PToF (or chopper) cycle, consisting of 260 points, resulting from 520 spectra acquired during the chopper cycle and coadding of two adjacent spectra.

subtracted from every point in the PToF distribution. This is done for the PToF distributions of every single  $m/z$  individually. For  $m/z$  at which gas phase signal occurs at small flight times (e.g.  $m/z$  14, 16, 28 and 32), only baseline area 2 is used for calculation of the PToF baseline.

After having calculated the average aerosol unit resolution mass spectrum in  $\text{ions s}^{-1}$  as a function of  $m/z$  several corrections need to be applied to the spectrum before calculating the aerosol mass concentrations.

### 3.2.1 Duty Cycle Correction

The fraction of ions that are used for mass spectrometric analysis and are captured by the detector of those that are generated in the ion source from the particle vapour is called the ion duty cycle  $D_{ion}$  of the TOFMS. In the TOFMS it is limited by the effect of “overshooting” of ions in the orthogonal extractor (see Figure 3.8), which means that ions are lost for the analysis because they cross the whole extractor before they are extracted into the TOFMS.

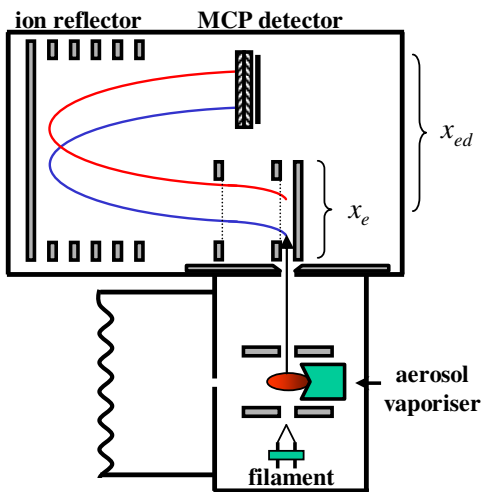


Figure 3.8: Schematic of the vaporisation/ionisation chamber and the TOFMS.

The duty cycle  $D_{ion,overshoot}$  due to overshooting of ions is defined by the instrument geometry and is given by Equation (3.10).

$$D_{ion,overshoot} = \frac{x_e}{x_{ion}} \quad (3.10)$$

where  $x_e$  is the length of the orthogonal extractor and  $x_{ion}$  is the distance travelled by ions during the time between two extraction pulses  $T_{pulse}$ . With Equation (3.11)

$$\begin{aligned} x_{ion} &= v_{ion} \cdot T_{pulse} \\ &= \sqrt{\frac{2qU_{ion}}{m_{ion}}} \cdot T_{pulse} \end{aligned} \quad (3.11)$$

this results in Equation (3.12):

$$D_{ion,overshoot} = \frac{x_e}{T_{pulse}} \cdot \sqrt{\frac{m_{ion}}{q}} \cdot \sqrt{\frac{1}{2U_{ion}}} \quad (3.12)$$

where again  $v_{ion}$  is the ion velocity,  $q$  the charge of the ion,  $m_{ion}$  the ion mass and  $U_{ion}$  the ionisation chamber voltage.

For a given extraction length  $x_e$  and pulsing time  $T_{pulse}$  the ion duty cycle caused by overshooting is dependent on the ionisation chamber voltage (which gives the primary ion beam energy) and the  $m/z$  of the ion. The maximum  $m/z$  that can be detected with the TOFMS within each individual pulse cycle is determined by the time  $T_{pulse}$  between two pulses. If  $T_{pulse}$  is greater than or equal to the flight time  $t_{ed}$  (Equation (3.13)) an ion of a certain  $m/z$  needs to cover the distance  $x_{ed}$  between the centres of the extractor and the detector, the ion can be detected.

$$t_{ed} = \frac{x_{ed}}{v_{ion}} = x_{ed} \cdot \sqrt{\frac{m_{ion}}{2qU_{ion}}} \quad (3.13)$$

The maximum achievable ion duty cycle for a certain  $m/z$  is reached when  $T_{pulse}$  is equal to  $t_{ed}$  for this  $m/z$ :

$$\begin{aligned} D_{ion,overshoot,max} &= D_{ion,overshoot}(T_{pulse} \equiv t_{ed}) \\ &= \frac{x_e}{x_{ed}} \cdot \sqrt{\frac{2qU_{ion}}{m_{ion}}} \cdot \sqrt{\frac{m_{ion}}{2qU_{ion}}} \\ &= \frac{x_e}{x_{ed}} \end{aligned} \quad (3.14)$$

Equation (3.14) shows that the maximum possible ion duty cycle of the TOFMS is determined only by the geometry of the mass spectrometer. It is 57 % for the mass spectrometer used here, i.e. 57 % of the ions produced inside the particle evaporation and ionisation region are captured by the detector.

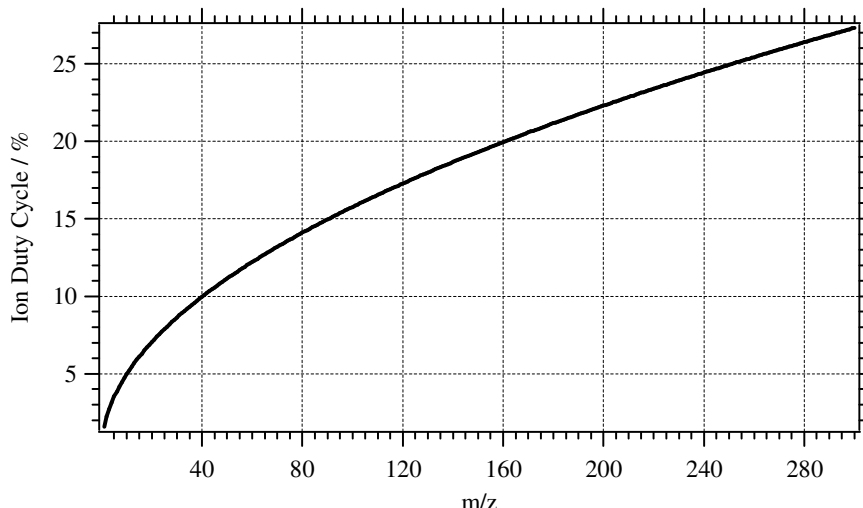


Figure 3.9: Overall ion duty cycle  $D_{ion,overall,MS}$  of the ToF-AMS in MS mode according to Equation (3.15).

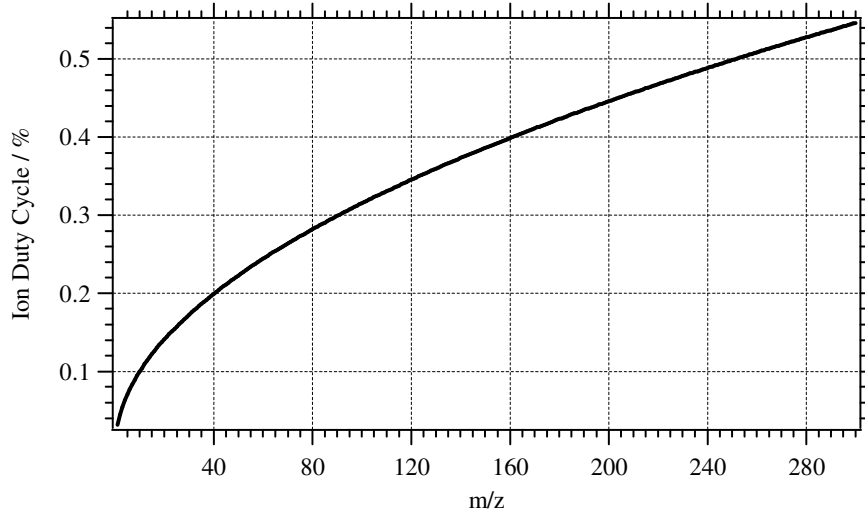


Figure 3.10: Overall ion duty cycle  $D_{ion,overall,PToF}$  of the ToF-AMS in PToF mode according to Equation (3.15).

In order to calculate the overall ToF-AMS duty cycles  $D_{ion,overall,MS}$  and  $D_{ion,overall,PToR}$  for MS or PToF mode analysis, respectively, one has to include the chopper duty cycle into the calculations to account for the fraction of particles collected by the instrument that is used for analysis. In the MS mode, the duty cycle of the chopper  $D_{chopper}$  is 50 %, since it is in open or blocked position for 50 % of the time (neglecting the time the chopper needs to move into the open or blocked position). In PToF mode the chopper lets the aerosol beam through for 1 % of the time, resulting in a chopper duty cycle  $D_{chopper}$  of 1 %. Therefore:

$$\begin{aligned} D_{ion,overall,MS} &= D_{chopper,MS} \cdot D_{ion,overshoot} = 50\% \cdot D_{ion,overshoot} \\ D_{ion,overall,P-TOF} &= D_{chopper,PToF} \cdot D_{ion,overshoot} = 1\% \cdot D_{ion,overshoot} \end{aligned} \quad (3.15)$$

The ion duty cycles of MS and PToF mode for an ion chamber voltage  $U_{ion}$  of 47.5 eV and an pulsing time  $T_{pulse}$  of 13  $\mu$ s are given in Figure 3.9 (MS mode) and Figure 3.10 (PToF mode) as a function of  $m/z$ .

The measured signals from MS and PToF mode need to be corrected for this  $m/z$ -dependency of the ion duty cycle. This can be done by normalising the signal to one particular  $m/z$  (usually  $m/z$  28) according to Equation (3.16), as long as the calibration measurements (described in the following section) are also normalised to this  $m/z$ .

$$I_{corr}(m/z) = I(m/z) \cdot \sqrt{\frac{m/z_{norm}}{m/z}} \quad (3.16)$$

After having applied the duty cycle correction the data are given in corrected signal intensity in ions  $s^{-1}$  as a function of  $m/z$ .

### 3.2.2 Inlet Flow and Airbeam Correction

The volumetric inlet flow rate  $Q_{in}$  and the mass flow rate  $\dot{m}_{in}$  through a critical orifice can be expressed according to Equations (3.17) and (3.18) (Baron & Willeke, 2001 (Equation 21-7)).

$$Q_{in} = 0.58 \cdot k_d \cdot A \cdot \sqrt{\frac{\gamma \cdot p_{up}}{\rho_{air}}} \quad (3.17)$$

$$\dot{m}_{in} = 0.58 \cdot k_d \cdot A \cdot \sqrt{\gamma \cdot p_{up} \cdot \rho_{air}} \quad (3.18)$$

where  $k_d$  is the discharge coefficient,  $A$  the orifice area,  $\gamma$  the ratio of specific heats (1.4 for air),  $p_{up}$  the pressure upstream the orifice and  $\rho_{air}$  the density of air at  $p_{up}$ . Using the ideal gas law, this can be converted into

$$Q_{in} = 0.58 \cdot k_d \cdot A \cdot \sqrt{\frac{\gamma \cdot R T_{air}}{M_{air}}} \quad (3.19)$$

$$\dot{m}_{in} = 0.58 \cdot k_d \cdot A \cdot \sqrt{\frac{\gamma \cdot M_{air}}{R T_{air}}} \cdot p_{up} \quad (3.20)$$

where  $M_{air}$  is the molecular weight of air,  $R$  is the universal gas constant and  $T_{air}$  is the air temperature.

For a given temperature  $T_{air}$ , the volumetric inlet flow rate  $Q_{in}$  is only dependent on the orifice area, while the mass flow rate  $\dot{m}_{in}$  is as well dependent on the pressure  $p_{up}$  in front of the critical orifice. Furthermore, again using the ideal gas law, the following relationship between  $Q_{in}$  and  $\dot{m}_{in}$  is given:

$$\dot{m}_{in} \propto Q_{in} \cdot p_{up} \quad (3.21)$$

During ToF-AMS measurements a change in  $p_{up}$  is equal to a change in the ambient pressure, while a change in the orifice area  $A$  can be caused by clogging of the critical orifice. The volumetric flow rate  $Q_{in}$  into the ToF-AMS is continuously monitored via a measurement of the pressure  $p_{lens}$  inside the aerodynamic lens behind the inlet orifice after calibration with a bubble flow meter (Gillian Gilibrator-2, Sensidyne, Clearwater, FL, USA). The pressure  $p_{lens}$  is measured with a Baratron pressure gauge (MKS Instruments, Wilmington, MA, USA) which supplies a voltage in the range 1-10 V directly proportional to the pressure in Torr (resulting in a measured pressure range of 133-1333 Pa). For the inlet flow calibration the critical orifice is exchanged with a needle valve to simulate a range of effective areas of the critical orifice. Then the volumetric flow rate  $Q_{in}$  and the corresponding lens pressure  $p_{lens}$  are measured with a bubble flow meter and a pressure gauge, respectively, for a number of different needle valve settings. The volumetric flow rate can then directly be related to the lens pressure according to Equation (3.22).

$$Q_{in} = a + b \cdot p_{lens} \quad (3.22)$$

where  $a$  and  $b$  are calibration parameters. As  $p_{lens}$  is a measure of the mass flow rate into the instrument and is therefore not only dependent on the critical orifice area  $A$  but also on the upstream pressure  $p_{up}$ , this calibration is only valid for the upstream pressure  $p_{up}$  at which it was performed. For this reason, a pressure-dependent inlet flow calibration was performed. The calibration experiment set-up is shown in Figure 3.11 and Figure 3.12.

In this calibration set-up the inlet system was operated using the regular 100 µm ID critical orifice. In order to control the pressure  $p_{up}$  upstream the critical orifice, a needle valve was mounted in front of the orifice. The volumetric flow rate  $Q_{meas}$  through the needle valve was measured at ambient pressure  $p_{amb}$  with the bubble flow meter. The pressure  $p_{up}$  was measured with a Baratron pressure gauge with a range of 1-1000 Torr (equal to 1.33-1333 hPa), the pressure  $p_{lens}$  inside the aerodynamic lens was measured with a pressure gauge with a range of 1-10 Torr (133-1333 Pa); the ambient pressure  $p_{amb}$  was taken from measurements of the meteorological station of the university of Mainz, located in ~200 m distance from the laboratory.

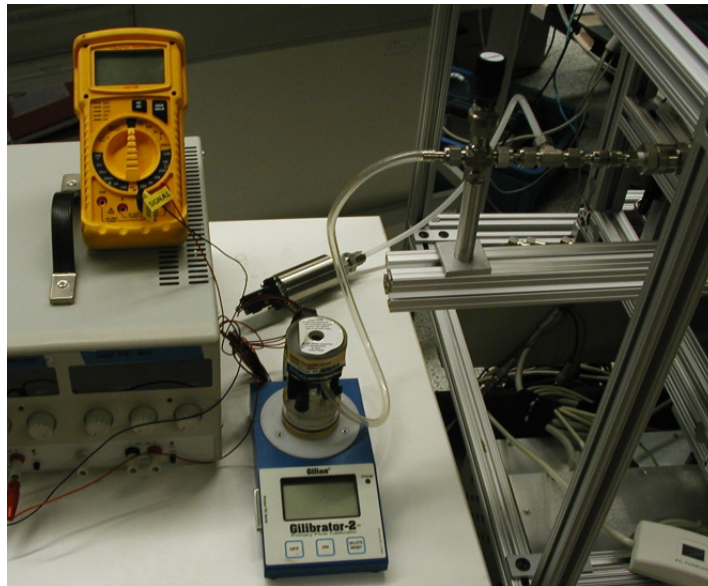


Figure 3.11: A picture of the inlet flow calibration set-up.

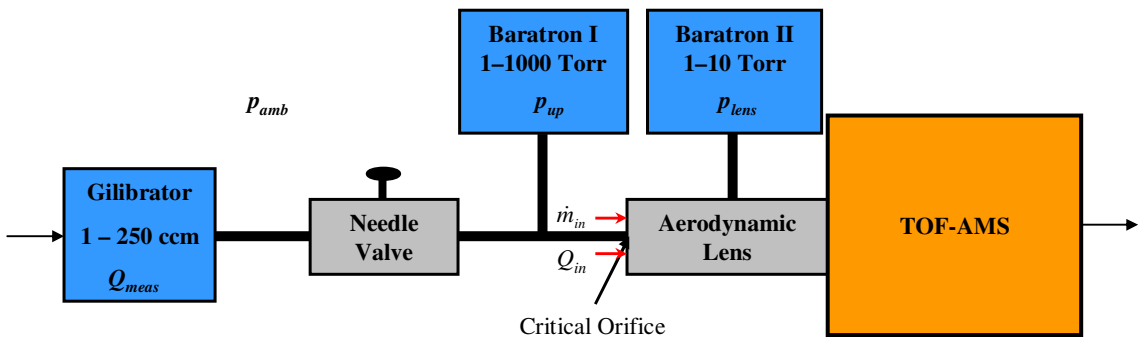


Figure 3.12: Schematical set-up of the pressure-dependent inlet flow calibration.

Because the bubble flow meter measures the volumetric flow rate  $Q_{meas}$  at ambient pressure  $p_{amb}$ , the volumetric flow rate  $Q_{in}$  into the ToF-AMS at pressure  $p_{up}$  needs to be calculated from the measured flow rate  $Q_{meas}$  and the pressure ratio  $p_{amb}/p_{up}$  according to Equation (3.23).

$$Q_{in} = \frac{P_{amb}}{P_{up}} \cdot Q_{meas} \quad (3.23)$$

Using Equation (3.21), the mass flow rate into the ToF-AMS can be directly related to the measured inlet flow rate  $Q_{meas}$ :

$$\dot{m}_{in} \propto p_{amb} \cdot Q_{meas} \quad (3.24)$$

With the help of this calibration the pressure-dependency of both the volumetric and the mass flow rate into the ToF-AMS can be determined.

Shown in Figure 3.13 is the measured lens pressure  $p_{lens}$  as a function of the upstream pressure  $p_{up}$ . From ambient pressure down to about 300 hPa upstream pressure the lens pressure decreases linearly with the upstream pressure, but for upstream pressures smaller than 300 hPa the relationship is no longer linear and the lens pressure decreases faster than the upstream pressure. The measured volumetric and mass flow rates are shown in Figure 3.14 as a function of upstream pressure and in Figure 3.15 as a function of lens pressure. Parameterisations of the pressure-dependencies of the volumetric flow rate are given in Equations (3.25) and (3.26).

$$Q_{in} [\text{cm}^3 \text{s}^{-1}] = 1.364 [\text{cm}^3 \text{s}^{-1}] + 4.91 \cdot 10^{-5} [\text{cm}^3 \text{s}^{-1} \text{hPa}^{-1}] \cdot p_{up} [\text{hPa}] \quad \text{for } p_{up} > 300 \text{ hPa} \quad (3.25)$$

$$Q_{in} [\text{cm}^3 \text{s}^{-1}] = 1.354 [\text{cm}^3 \text{s}^{-1}] + 0.033 [\text{cm}^3 \text{s}^{-1} \text{hPa}^{-1}] \cdot p_{lens} [\text{hPa}] \quad \text{for } p_{lens} > 0.7 \text{ hPa} \quad (3.26)$$

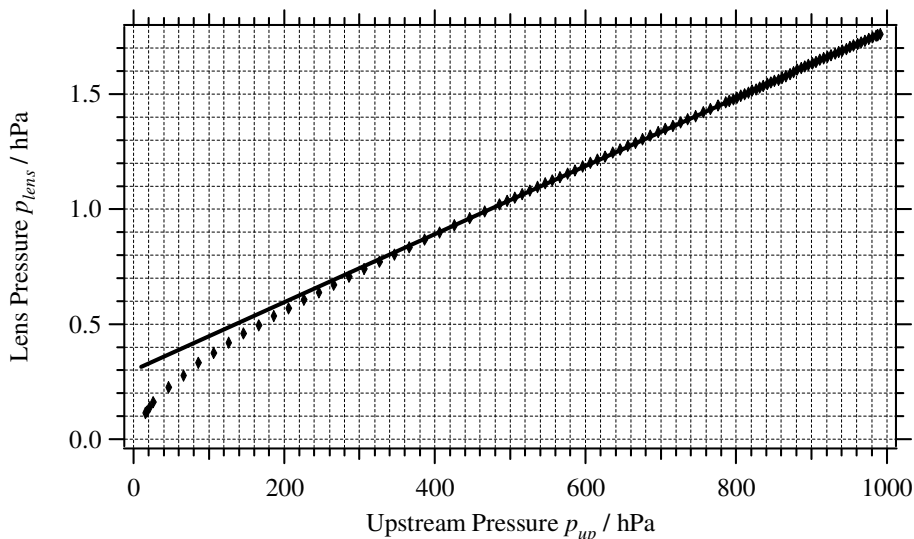


Figure 3.13: The measured pressure inside the aerodynamic lens as a function of the upstream pressure in front of the critical orifice (dotted). The solid line represents a linear regression through the points above 300 hPa upstream pressure.

In summary, the difference in the volumetric flow rate during a pressure change in  $p_{up}$  from 975 hPa to 1025 hPa (which can occur during ambient measurements) would be smaller than 0.2 %, the difference in  $Q_{in}$  for a pressure change from 1025 hPa to 300 hPa would be 2.5 %. In other words, considering  $Q_{in}$  to be constant for all ambient pressures (as expected from Equation (3.43)) that occur during ground-based measurements does not result in significant errors. At lower pressures like for example during air plane measurements, a correction is readily available.

Nevertheless, during a measurement over a long time or during measurements with high aerosol mass concentrations, the effect of clogging of the critical orifice can occur, causing the volumetric and the mass flow rate to decrease. The measured signal then needs to be corrected for this effect. Additionally, over the time of such a measurement a deterioration of the MCP detector performance as a result of charge flown through the MCP occurs, reducing the magnitude of the signal generated per ion. This causes an artificial decrease in the measured signal that also needs to be corrected for.

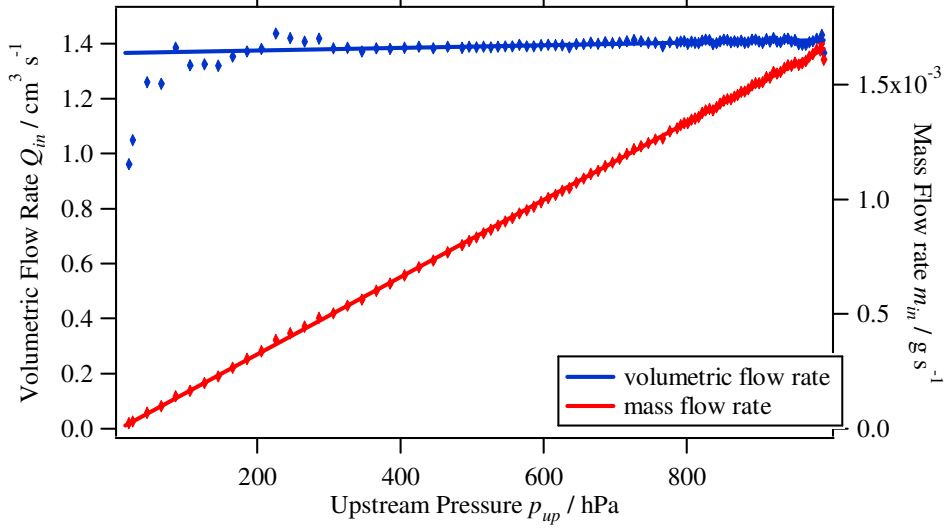


Figure 3.14: Volumetric (blue) and mass (red) flow rate into the ToF-AMS as a function of the upstream pressure in front of the critical orifice. The measured values are indicated by the dotted lines, the solid lines represent the linear regression through the measured values down to 300 hPa  $p_{up}$ .

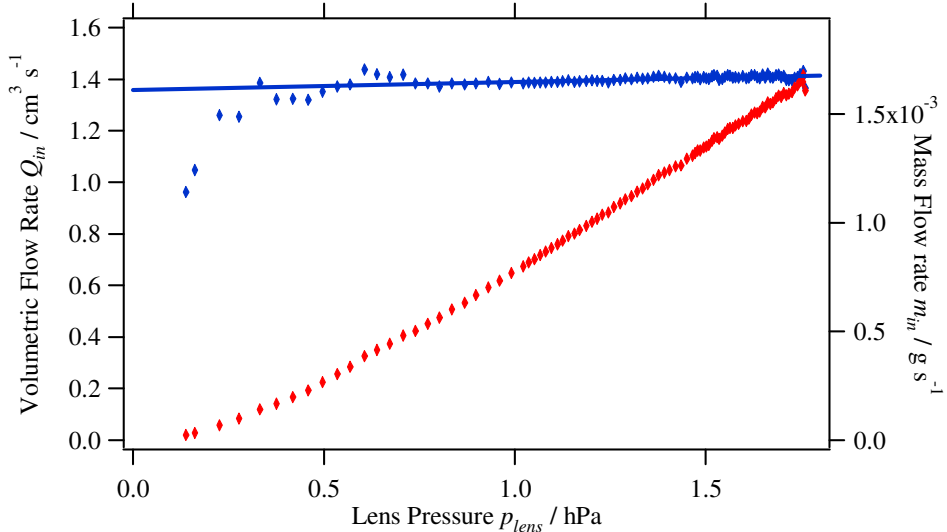


Figure 3.15: Volumetric (blue) and mass (red) flow rate into the ToF-AMS as a function of the lens pressure. The measured values are indicated by the dotted lines, the solid line represents the linear regression through the measured values down to 0.7 hPa  $p_{lens}$ .

Because to a first approximation the relative degradation in the signal should be equal for all species (for exceptions see Chapter 4.2), it is possible to use the signal generated by air molecules ( $N_2^+$  ( $m/z$  28) and  $O_2^+$  ( $m/z$  32)), the so-called airbeam signal  $AB$  as a measure for the MCP detector performance. If the amplification of the ion signal did not decrease, the airbeam signal would be constant, since the air concentration is constant. Unfortunately, a change in mass flow rate, caused by a change in the upstream pressure, would also cause a change in the magnitude of the airbeam signal.

This means that the measured signal  $I$  needs to be corrected for changes in the airbeam signal that are caused by a decay in the MCP detector performance and for changes in the mass and volumetric inlet flow rates that are caused by clogging of the critical orifice. It must not be corrected for changes in the mass flow rate that are caused by changes in the upstream pressure. This correction can be applied in four subsequent steps, which are illustrated in Figure 3.16.

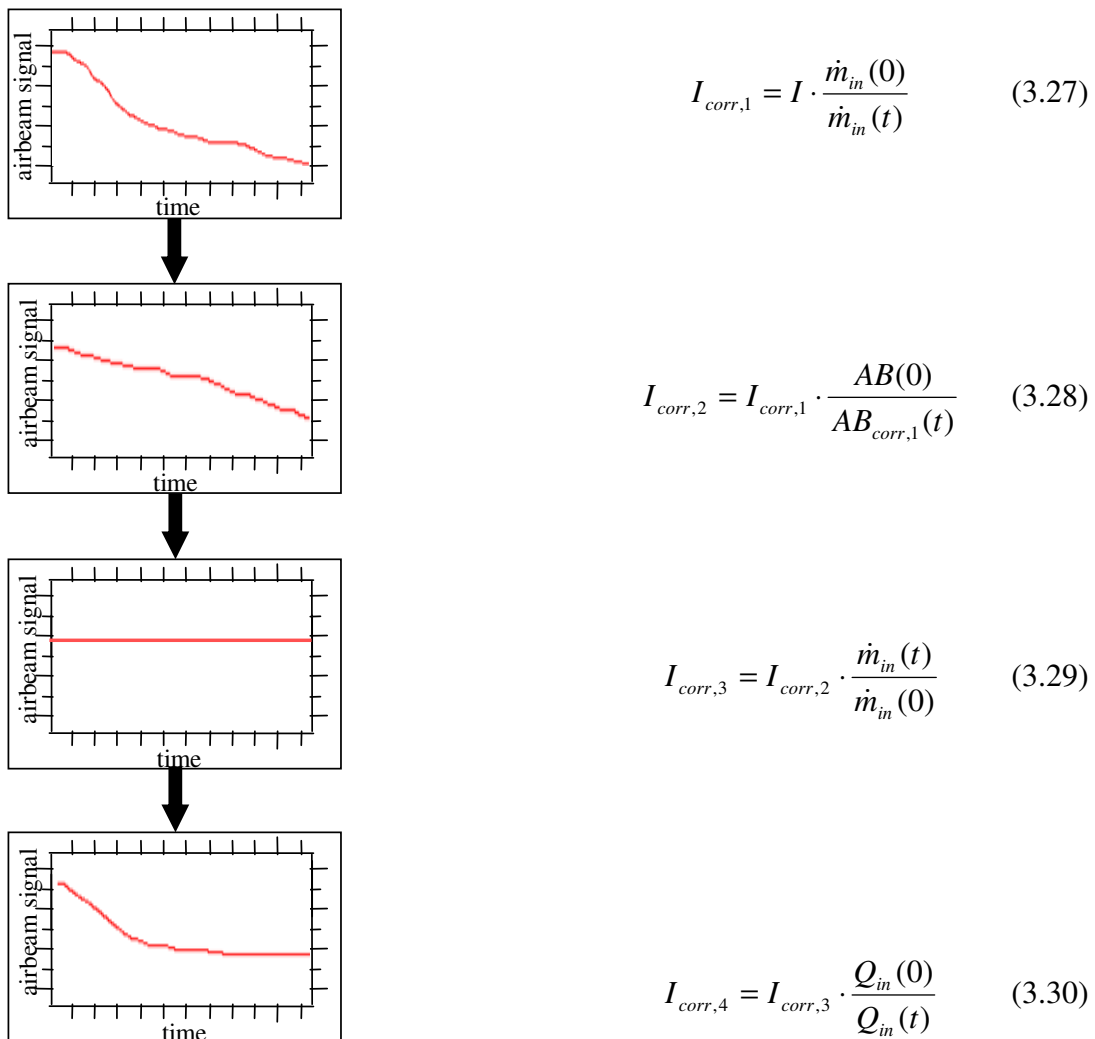


Figure 3.16: Illustration of the signal correction to account for a decay in the MCP detector performance and clogging of the critical orifice. See text for details.

In step one (Equation (3.27)) the at time  $t$  measured signal  $I(t)$  (for all  $m/z$ ) is normalised to a constant mass flow rate  $\dot{m}_{in}$  which is constantly monitored by measuring the lens pressure. This is done to exclude a change in  $AB$  caused by a change in  $\dot{m}_{in}$ . In step two (3.28) the corrected signal from step one (including the  $AB$  signal) is normalised to the airbeam signal at time  $t = 0$  to obtain constant airbeam signal  $AB$ . This corrects for a decay in the MCP detector performance. Step three (3.29) is the inverse of step two and is done to reconstruct the signal dependency on the actual mass flow rate. Finally, step four (3.30) normalises to the constant volumetric flow rate to correct for changes caused by clogging of the critical orifice. For this purpose,  $Q_{in}(t)$  can be calculated from the measured inlet flow rate  $Q_{meas}$ , the pressure inside the lens  $p_{lens}$  and the ambient pressure  $p_{amb}$  according to Equation (3.32). Therefore it is necessary to also monitor the ambient pressure  $p_{amb}$  during measurements.

$$Q_{in}(t) = Q_{meas}(t) \cdot \frac{p_{amb}(t)}{p_{lens}(t)} \quad (3.31)$$

The magnitude of the inlet flow and airbeam correction is dominated by the deterioration of the MCP detector performance, which can be quantified from the decrease in the airbeam signal. During this work, an average decrease in the airbeam signal of approximately 5 % during one week of operation was observed. The additional correction due to clogging of the critical orifice strongly depends on the measurement conditions (e.g. aerosol mass concentration and composition).

After having applied the duty cycle correction and the airbeam and inlet flow corrections as described in the previous sections, the data measured are still unit resolution spectra in units of (integrated and corrected) signal in ions  $s^{-1}$  as a function of  $m/z$ .

### 3.2.3 IE Calibration

#### Conversion of Unit Resolution Spectra into Mass Concentrations of Various Species

The thermal vaporisation and 70 eV electron impact ionisation of a certain chemical species in the AMS leads to a specific number of  $m/z$  peaks in the mass spectrum, with a characteristic fragmentation pattern for that species. For example, nitrate fragments appear mainly at  $m/z$  30 ( $\text{NO}^+$ ) and 46 ( $\text{NO}_2^+$ ), sulphuric acid produces major peaks at  $m/z$  48 ( $\text{SO}^+$ ), 64 ( $\text{SO}_2^+$ ) and 80 ( $\text{SO}_4^+$ ). The summation of all signal intensities at all  $m/z$  that correspond to a specific species  $s$  gives the total species signal intensity  $I_s$ . Application of the deconvolution algorithm described in Allan et al. (2004) corrects for the fact that some  $m/z$  contain interfering signals from several species. This is identical for all Aerodyne AMS instruments, since the fragmentation of the various species is a result of the vaporisation and 70 eV electron impact ionisation process, and is not influenced by the different ion detection methods used in the Aerosol Mass Spectrometers. The mass concentration  $C_s$  of a chemical species  $s$  (in  $\mu\text{g}$  of particulate mass per  $\text{m}^3$  of air) can be calculated from the species signal intensities after Equation (6) from Jimenez et al. (2003a) as follows:

$$C_s = RIE_s \cdot \frac{\sum_f I_{sf}}{N_A Q_{in}} \cdot \frac{MW_{NO_3}}{IE_{NO_3}} \cdot 10^{12} \quad (3.32)$$

with  $\sum_f I_{sf}$  the total signal intensity (in ions s<sup>-1</sup>) of species  $s$  summed over all fragments  $f$ ,  $MW_{NO_3}$  the molecular weight of nitrate (62 g mol<sup>-1</sup>),  $IE_{NO_3}$  the calibrated ionisation and transmission efficiency of nitrate,  $N_A$  Avogadro's number ( $6.02 \cdot 10^{23}$  mole<sup>-1</sup>),  $Q_{in}$  the volumetric aerosol flow rate into the instrument (in cm<sup>3</sup>s<sup>-1</sup>), and  $RIE_s$  the relative ionisation and transmission efficiency of species  $s$ , a factor which corrects for differences in the ionisation and transmission efficiencies ( $IE$ ) of different species with respect to the measured  $IE_{NO_3}$ . The  $RIE$  values typically used for AMS measurements are 1.15 for sulphate, 4 for ammonium, 1.4 for organics and 1.3 for chloride. Those values are typically used for AMS mass concentration calculations and are based on calibrations from laboratory generated aerosol (e.g. Alfarra *et al.*, 2004). Ammonium nitrate is used as the primary calibration species, because its ionisation efficiency, density and shape are well known and because ammonium nitrate does not leave much residue to interfere with subsequent measurements. Ammonium nitrate vaporises with close to 100 % efficiency, so that the ionisation efficiency of NO<sub>3</sub><sup>+</sup> can be quantitatively measured. In addition, ammonium nitrate particles are well focused by the aerodynamic lens, so that all the particles can be detected (Aerodyne Research Incorporated, 2005).

As shown in Equation (3.32), for calculating the mass concentrations of all species the ionisation efficiency of nitrate,  $IE_{NO_3}$ , and the species' ionisation efficiencies relative to the one of the calibration species are needed. The ionisation efficiency is defined as the number of ions detected per molecule of species  $s$  that is introduced into the instrument. For calibration purposes the ionisation efficiency is expressed as the number of ions per particle ( $IPP$ ) introduced into the AMS divided by the number of molecules per particle ( $MPP$ ).

In order to determine the  $IE_{NO_3}$ , an ionisation efficiency calibration (IE calibration) needs to be performed. For this calibration ammonium nitrate particles are generated by nebulising (Constant Output Atomizer Model 3076, TSI Inc.) a solution of NH<sub>4</sub>NO<sub>3</sub> in water and subsequently drying them with the help of a diffusion dryer (Model 3062, TSI Inc.). The particles are then size-selected by an Electrostatic Classifier (Model 3080, TSI Inc.; TSI Incorporated, 2006) and directed to a CPC (Model 3025, TSI Inc.) and the ToF-AMS in parallel. In order to minimise particle losses, the inlet lines must be kept short and should have equal length for the ToF-AMS and the CPC. During this work, the particle concentration was measured with the CPC and mass spectra as well as size distribution data were measured with the ToF-AMS for an averaging interval of 2 minutes (for this purpose the ToF-AMS was set to a general alternation mode, switching between MS and PToF mode every 10 seconds). This was done on a regular basis several times during this work. One of these calibrations, done for three different particle sizes (electrical mobility diameters  $d_{mob} = 250, 350$  and 400 nm) and various particle number concentrations, will be discussed in more detail now.

Knowing the size of the particles introduced into the instrument, the number of NO<sub>3</sub> molecules per particle can be determined using Equation (3.33).

$$MPP = \frac{N_A \cdot \rho_{NH_4NO_3} \cdot f_{NO_3} \cdot \pi/6 \cdot d_{mob}^3 \cdot S}{MW_{NO_3}} \quad (3.33)$$

where  $d_{mob}$  is the electrical mobility diameter of the calibration particles,  $\rho_{NH_4NO_3}$  is the density of ammonium nitrate,  $S$  is a correction factor that corrects for the actual particle density and shape (DeCarlo *et al.* 2004; see chapter 3.3.1 for details),  $f_{NO_3}$  is the fraction of

$\text{NO}_3$  mass in  $\text{NH}_4\text{NO}_3$ ,  $MW_{\text{NO}_3}$  is the molecular weight of nitrate and  $N_A$  is Avogadro's number.

The number of ions per particle can directly be determined from the measured nitrate signal  $I_{\text{NO}_3}$  (in  $\text{ions s}^{-1}$ ) after it has been corrected for ion duty cycle, MCP detector decay and clogging of the critical orifice as described in the previous sections, the particle number concentration  $N_{\text{CPC}}$  (in particles  $\text{cm}^{-3}$ ) and the volumetric inlet flow rate  $Q_{\text{in}}$  (in  $\text{cm}^3 \text{s}^{-1}$ ):

$$\text{IPP} = \frac{I_{\text{NO}_3}}{N_{\text{CPC}} \cdot Q_{\text{in}}} \quad (3.34)$$

### Doubly-charged Particle Correction

As the particles are size-selected with a DMA, doubly-charged particles which have the same electrical mobility diameter but a larger geometric and vacuum-aerodynamic diameter might be introduced into the instrument (for details see TSI Incorporated, 2006). Since we only want to consider signal from singly-charged particles, this effect results in a too high nitrate signal  $I_{\text{NO}_3}$  determined in MS mode as well as in a too high number concentration  $N_{\text{CPC}}$  measured with the CPC. It can be corrected for by applying correction factors to the measured  $I_{\text{NO}_3}$  and  $N_{\text{CPC}}$ , which can be determined from the measured PToF distributions. Figure 3.17 shows a PToF distribution (measured signal at  $m/z$  30 ( $\text{NO}_2^+$ ) as a function of  $d_{\text{va}}$ ) obtained during the IE calibration with 250 nm electrical mobility diameter particles. The part of the distribution that corresponds to doubly-charged particles is indicated in red, while the grey shaded area under the distribution gives the signal of the singly-charged particles.

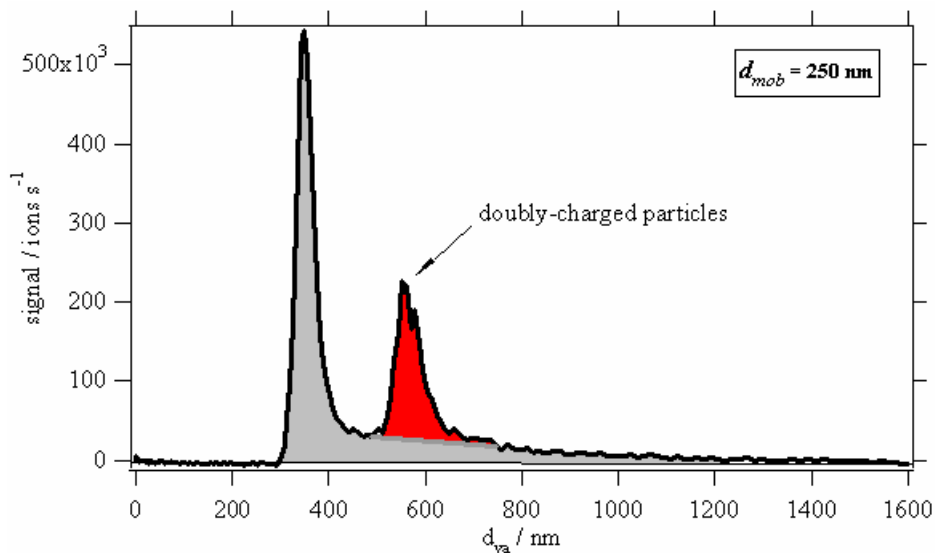


Figure 3.17: PToF distribution measured during an IE calibration using ammonium nitrate particles with  $d_{\text{mob}} = 250 \text{ nm}$ . The part of the distribution that corresponds to doubly-charged particles is drawn in red, the grey shaded area gives the signal that corresponds to singly-charged particles. Note, that there is still non-zero signal from singly-charged particles at high  $d_{\text{va}}$  due to slow evaporation of the particles.

The correction factor  $\text{Corr}_I$  that needs to be applied to account only for the nitrate signal from singly-charged particles measured in MS mode can be calculated from the

corresponding PToF distribution as the ratio between the signal corresponding to the singly-charged particles,  $I_{NO_3}$  (singly) (grey area), and the total signal,  $I_{NO_3}$  (total) (grey and red area) (Equation (3.35)).

$$Corr_I = \frac{I_{NO_3}(\text{singly})}{I_{NO_3}(\text{total})} \quad (3.35)$$

The correction factor  $Corr_N$  that needs to be applied to the measured CPC particle number concentration  $N_{CPC}$  is given by Equation (3.36).

$$Corr_N = \frac{N_{CPC}(\text{singly})}{N_{CPC}(\text{total})} \quad (3.36)$$

In general, the particle number concentration  $N$  can be determined from the mass concentration of the particles  $C$ , the volume equivalent diameter of the particles  $d_{ve}$  and the particle density  $\rho_p$  according to Equation (3.37).

$$N = \frac{C}{\frac{\pi}{6} \cdot d_{ve}^3 \cdot \rho_p} \quad (3.37)$$

For a given particle size the mass concentration of the calibration particles  $C_{CPC}$  is directly proportional to the nitrate mass concentration  $C_{NO_3}$ . According to Equation (3.32),  $C_{NO_3}$  is proportional to the total nitrate signal  $I_{NO_3}$  measured with the ToF-AMS in MS mode:

$$C_{CPC} \propto C_{NO_3} \propto I_{NO_3} \quad (3.38)$$

Combining Equations (3.37) and (3.38), the relationship between the measured particle number concentration  $N_{CPC}$  and the nitrate signal is given by Equation (3.39).

$$N_{CPC} \propto \frac{I_{NO_3}}{d_{ve}^3} \quad (3.39)$$

Introducing this relationship into Equation (3.36),  $Corr_N$  can be calculated as follows:

$$Corr_N = \frac{\frac{I_{NO_3}(\text{singly})}{d_{ve}^3(\text{singly})}}{\frac{I_{NO_3}(\text{singly})}{d_{ve}^3(\text{singly})} + \frac{I_{NO_3}(\text{doubly})}{d_{ve}^3(\text{doubly})}} \quad (3.40)$$

The *IPP* (Equation (3.34)) are therefore given as:

$$\begin{aligned}
 IPP &= \frac{I_{NO_3,MS}}{N_{CPC} \cdot Q_{in}} \cdot \frac{Corr_I}{Corr_N} \\
 &= \frac{I_{NO_3,MS}}{N_{CPC} \cdot Q_{in}} \cdot \left( Corr_I + (1 - Corr_I) \cdot \frac{d_{ve}^3(\text{singly})}{d_{ve}^3(\text{doubly})} \right)
 \end{aligned} \tag{3.41}$$

With the following relationship between the vacuum aerodynamic diameter  $d_{va}$  and the volume equivalent diameter  $d_{ve}$  (Equation (3.42), DeCarlo et al., 2004)

$$d_{va} = \frac{\rho_p}{\rho_0} \cdot \frac{d_{ve}}{\chi_v} \Rightarrow \frac{d_{ve}^3(\text{singly})}{d_{ve}^3(\text{doubly})} = \frac{d_{va}^3(\text{singly})}{d_{va}^3(\text{doubly})} \tag{3.42}$$

the volume equivalent diameter in Equation (3.41) can be replaced by the vacuum aerodynamic diameter.

In other words, doubly-charged particle corrections for both the nitrate signal measured in the ToF-AMS MS mode and the particle number concentration measured with a CPC can be determined from the corresponding PToF distributions measured in the ToF-AMS PToF mode.

For the IE calibrations performed during this work, this was done manually by calculating  $I_{NO_3}$  (total) and  $I_{NO_3}$  (doubly) from the corresponding area under the PToF distributions ( $m/z$  30) of every calibration point;  $I_{NO_3}$  (singly) was calculated by subtracting  $I_{NO_3}$  (doubly) from  $I_{NO_3}$  (total). The vacuum aerodynamic diameters of the singly and doubly-charged particles were determined visually from the PToF distributions (for details concerning the conversion of particle flight times into  $d_{va}$ , see section 3.3.1). For the calibrations performed during this work, the doubly-charged particle correction was on average in the order of 17 % for particles with electrical mobility diameters of  $d_{mob} = 250$  nm and in the order of 4 % for  $d_{mob} = 350$  nm; for particles with  $d_{mob} = 400$  nm no doubly-charged particles were measured.

### Uncertainties of the IE Calibration

The uncertainties of the IE calibration arise from the uncertainty in the determination of the  $IPP$  and the  $MPP$ , which again are a combination of various factors. In the following, the various uncertainties and errors that determine the overall uncertainty of  $IPP$  and  $MPP$  and consequently of  $IE_{NO_3}$  are listed and discussed:

- Uncertainty in the determination of  $IPP$ :

- Statistical error of  $I_{NO_3}$

The distribution of the number of detected ions in the mass spectrum can be modelled as a Poisson distribution. For calculation of the error of the measured signal it must also be taken into account that the signal of a single ion is not a constant but arises from a Gaussian distribution of pulse areas or intensities. In this simplified approach the distribution width of single ion intensities is accounted for by multiplying the width of the Poisson distribution with a constant factor of  $\alpha = 1.2$ , which was determined from single-ion measurements with the Q-AMS (Allan et al., 2003a). Therefore, the (statistical) error of any signal  $I$ , in ions per second, is given by Equation (3.43).

$$\Delta I = \alpha \cdot \frac{\sqrt{I}}{\sqrt{t_s}} \quad (3.43)$$

with  $t_s$  the total time in seconds spent sampling the particular  $m/z$  channel associated with signal  $I$ , during the data acquisition interval.  $t_s$  is equal to the time spent measuring the signal in MS mode times the duty cycle of ion extraction of the TOFMS (Drewnick et al., 2005).

As the signal  $I_d$  of the aerosol particles (“difference” signal) is the difference between the signal  $I_o$  measured in beam open position and the signal  $I_b$  measured in beam blocked position, the statistical error of the difference signal is given as:

$$\Delta I_d = \alpha \cdot \frac{\sqrt{I_o + I_b}}{\sqrt{t_s}} \quad (3.44)$$

The total nitrate signal  $I_{NO_3}$  is the sum of all signals  $I_d$  at all nitrate fragments  $f$ . Therefore the statistical error of  $I_{NO_3}$  can be calculated according to Equation (3.45).

$$\Delta I_{NO_3} = \sqrt{\sum_f (\Delta I_{d,f})^2} \quad (3.45)$$

- Uncertainty in the conversion of the signal  $I_{NO_3}$  from bits·ns into ions  $s^{-1}$   
This uncertainty is due to the uncertainty in the determination of the single ion signal strength  $SI$ . It does not need to be taken into account here, because it cancels out when aerosol mass concentrations are calculated.
- Additional uncertainties in  $I_{NO_3}$   
Additional uncertainties are caused by fluctuations of the voltages and the filament current, and by particle losses in the instrument. They are estimated to be in the order of  $\pm 2\%$ .
- Uncertainty in the particle number concentration  $N_{CPC}$   
The particle number concentration is determined by averaging of the CPC readings within an interval of 2 minutes. Uncertainties are caused by particle losses inside the inlet lines of CPC and ToF-AMS and by uncertainties in the absolute calibration of the CPC. These uncertainties are estimated to be  $\pm 5\%$ .
- Uncertainty due to the doubly-charged particle correction  
This uncertainty is dependent on the particle size and is very hard to quantify. It is estimated to be below  $\pm 5\%$  for the calibrations performed here.
- Uncertainty in the determination of  $MPP$ 
  - Uncertainty in the selected particle size  
The DMA selects particles within a small range of electrical mobilities. Thus, the selected aerosol is not exactly mono-disperse and the particle diameter is determined as the maximum of the resulting size distribution. It is dependent on the voltage of the inner electrode and on the sheath flow. The overall uncertainty in the selected particle diameter  $d_{mob}$  is estimated to  $\pm 3\%$ , resulting in an uncertainty of  $MPP$  of  $9\%$ .

- Uncertainty in the particle density

Differences of the actual particle density to the density of the bulk material are corrected for by multiplying with the Jayne shape factor  $S$ , which is determined by calibration with particles of known size, density and shape (see Chapter 3.3.1). The density of laboratory-generated ammonium nitrate particles is typically in the order of 20 % less than the density of the bulk material.

The resulting uncertainties of the IE calibration will be given in the following section.

## Results

As already mentioned before, IE calibrations have been performed with dried ammonium nitrate particles of three different diameters ( $d_{mob} = 250, 350$  and  $400$  nm) and for various particle number concentrations ( $340\text{-}8600\text{ cm}^{-3}$  for  $d_{mob} = 250$  nm;  $20\text{-}4700\text{ cm}^{-3}$  for  $d_{mob} = 350$  nm;  $15\text{-}3700\text{ cm}^{-3}$  for  $d_{mob} = 400$  nm). This was done to study the consistency and limiting factors of the IE calibration and to check if the developed doubly-charged particle correction procedure works properly. In order to visualise the results of the performed IE calibrations, the measured ions per second introduced into the instrument (i.e. the  $I_{NO_3}$ ) are plotted versus the molecules per second introduced into the instrument (i.e.  $MPP$  multiplied by  $N$  and  $Q_{in}$ ). The  $IE_{NO_3}$  is then given as the slope of a linear regression through the points (Equation (3.46)).

$$\text{ions per second} = IE_{NO_3} \cdot \text{molecules per second} \quad (3.46)$$

The results of the three different IE calibrations are shown in Figure 3.18 ( $d_{mob} = 250$  nm), Figure 3.19 ( $d_{mob} = 350$  nm) and Figure 3.20 ( $d_{mob} = 400$  nm).

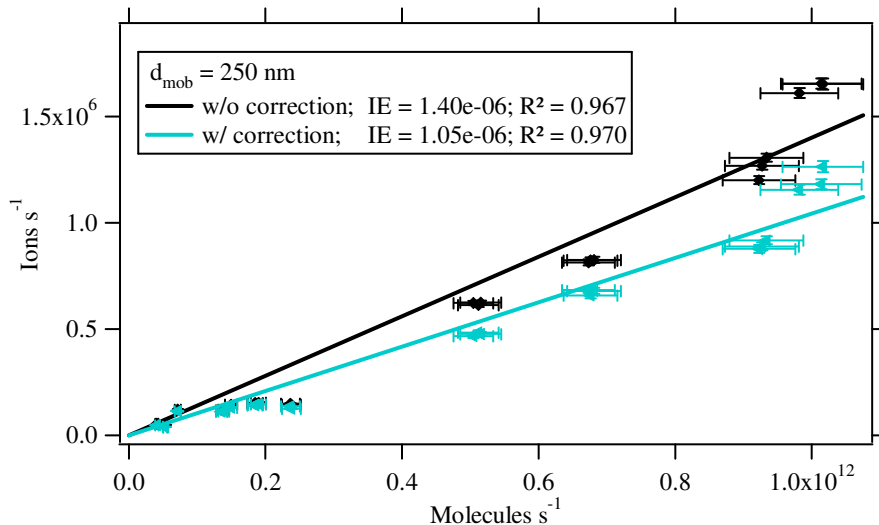


Figure 3.18: IE calibration with ammonium nitrate particles ( $d_{mob} = 250$  nm), without (black) and with (blue) correction for doubly-charged particles. The solid lines represent linear regressions through the measured values, the error bars are calculated from the uncertainties given in the last section.

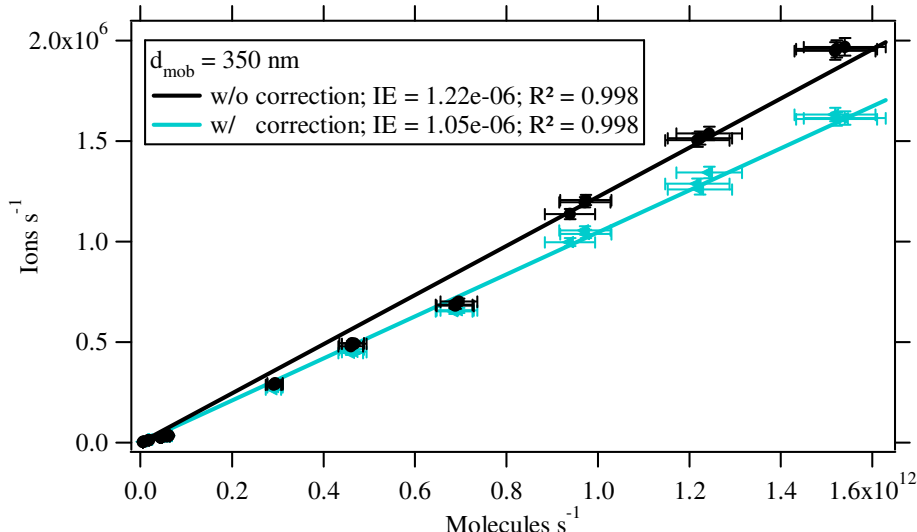


Figure 3.19: IE calibration with ammonium nitrate particles ( $d_{mob} = 350$  nm), without (black) and with (blue) correction for doubly-charged particles. The solid lines represent linear regressions through the measured values, the error bars are calculated from the uncertainties given in the last section.

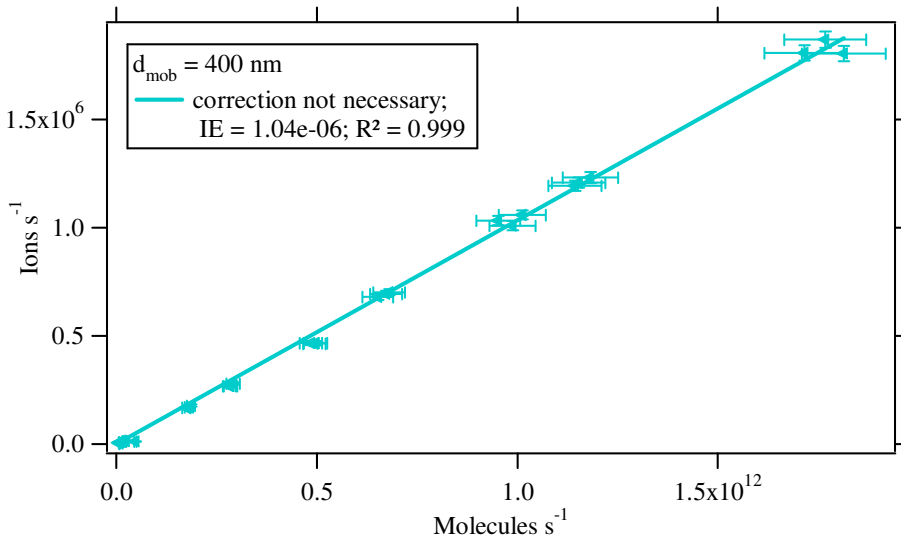


Figure 3.20: IE calibration with ammonium nitrate particles ( $d_{mob} = 400$  nm). A correction for doubly-charged particles was not necessary. The solid line represents a linear regression through the measured values, the error bars are calculated from the uncertainties given in the last section.

The results of the calibrations without including the doubly-charged particle corrections are shown in black and the ones including these corrections are shown in blue. The effect of doubly-charged particles is highest for the particles with  $d_{mob} = 250$  nm and decreases with increasing diameter. This is due to the size distribution of the particles that leave the atomiser, where only few particles are found at large particle sizes. For the 400 nm diameter particles no doubly-charged particles were found, and it was not necessary to apply a correction at all. In addition, the scattering of the data points around the calibration line is highest for the 250 nm diameter particles with a correlation coefficient of  $R^2 = 0.969$ . The correlation coefficients for the other calibrations are  $R^2 = 0.998$  and  $R^2 = 0.999$  for  $d_{mob} =$

350 nm and 400 nm, respectively. The  $IE_{NO_3}$  determined during the three calibrations is nearly identical with  $IE_{NO_3} = 1.05 \cdot 10^{-6}$  for the calibrations with  $d_{mob} = 250$  and 350 nm and  $IE_{NO_3} = 1.04 \cdot 10^{-6}$  for the calibration with  $d_{mob} = 400$  nm. The error bars in Figure 3.18 to Figure 3.20 represent the uncertainties of the calibration as described in the previous section. The resulting uncertainties in the determined  $IE_{NO_3}$  are in the order of 9 to 10 % for all three calibrations. The results of the IE calibrations are also given in Table 3.1.

Summarising, the results shown here indicate that the IE calibration procedure performed in MS mode, with the help of an external CPC to count the particles, works very well as long as a correction factor for doubly-charged particles is applied correctly. This correction factor can be obtained from the PToF distributions acquired at the same time as the mass spectra. For this purpose the ToF-AMS can be set to general alternation mode, switching between MS and PToF mode every few seconds.

It was found that – under the conditions during these calibrations - the effect of doubly-charged particles did not play a role for the calibration with 400 nm electrical mobility diameter particles. Therefore it is recommended to perform IE calibrations with ammonium nitrate particles of this size. Nevertheless, when the size distribution of the calibration particles exiting the atomiser is shifted to larger particle diameters, the effect of doubly-charged particles might also play a role for the 400 nm calibration particles. Therefore, PToF distributions should always be acquired during an IE calibration in order to be able to correct for doubly-charged particles if necessary.

<b><math>d_{mob}</math></b>	<b><math>IE_{NO_3}</math></b>	<b>Relative Uncertainty</b>
<b>250</b>	$1.05 \cdot 10^{-6} \pm 1.03 \cdot 10^{-7}$	10 %
<b>350</b>	$1.05 \cdot 10^{-6} \pm 9.66 \cdot 10^{-8}$	9 %
<b>400</b>	$1.04 \cdot 10^{-6} \pm 9.87 \cdot 10^{-8}$	10 %

Table 3.1:  $IE_{NO_3}$  values derived from calibrations with ammonium nitrate particles of three different mobility diameters  $d_{mob}$ .

### IE Calibration Procedure in the Q-AMS

As within the scope of this work ToF-AMS data will be compared to Q-AMS data, the differences in the IE calibration procedures of the two instruments will be discussed shortly. In the Q-AMS, an IE calibration can be performed without the use of a CPC, because the data acquisition and logging software is capable of detecting and counting single particles as pulses in the detected signal in PToF mode. Before logging, the software blocks the aerosol beam and measures the maximum instantaneous signal level (due to background gases and electronic noise), which it bases a threshold voltage on. During sampling, any pulses above this threshold are counted as single particles. The vacuum aerodynamic diameter of the single particle can be derived from its time-of-flight and the total amount of ions detected from the particle by integrating the pulse. The probability that a particle will be successfully detected and counted is based on the mass of the particle and the amount of background at the  $m/z$  being monitored. Generally speaking, only particles with a  $d_{va}$  greater than about 200 nm are counted reliably, also this varies with the chemical species being studied and its background partial pressure in the detection region. Therefore a Q-AMS IE calibration is performed in PToF mode rather than in MS mode. For this purpose, the QMS is set to

measure alternately  $m/z$  30 and 46, which are the major nitrate fragmentation peaks. The nitrate signal  $I_{NO_3}$  is calculated from the average integrated signal pulses produced by single particles at  $m/z$  30 and 46. Multiply-charged particles are eliminated from this calibration analysis by ignoring particles with a time-of-flight greater than a threshold value which is user-selectable.

Since the  $I_{NO_3}$  is calculated from the signal in a limited  $d_{va}$ -range only, in contrary to the IE calibration analysis described for the ToF-AMS, this procedure does not account for slow evaporation of the calibration particles (see Figure 3.17). Thus, the calculated  $I_{NO_3}$  is too small resulting in a too small  $IE_{NO_3}$ .

Additionally, the Q-AMS IE calibration is performed using only the two most prominent nitrate fragments ( $m/z$  30 and 46). Laboratory work has shown that these signals account for about 90 % of the total nitrate ion signal from ammonium nitrate (Hogrefe et al., 2004). Therefore the actual nitrate ionisation efficiency can be determined from the  $IE_{NO_3}$  determined during a Q-AMS IE calibration by multiplying with a factor of 1.1. To simplify matters, this is usually done by applying a  $RIE$  value of 1.1 for nitrate, when calculating aerosol mass concentrations.

### **IE Calibration in the ToF-AMS SPToF mode**

Instead of performing an IE calibration in MS mode, where a CPC is necessary to determine the particle number concentration, an IE calibration can also be performed using the SPToF mode of the ToF-AMS (see chapter 2). Here single particle data are acquired and filtered before saving to disk, so that only files containing particle information are stored. The filtering is done by the data acquisition software as follows: if signals at  $m/z$  corresponding to the selected species (in this case nitrate) are above a software defined threshold, a single particle file is stored. This means that the number of saved files equals the number of the detected particles. To exclude doubly-charged particles from the analysis, files are ignored where the peak of the particle signal is not within the  $d_{va}$  range of the singly-charged particles. The  $I_{NO_3}$  is then calculated from the signal of the singly-charged particles only, including signal due to slow evaporation of particles. As in the Q-AMS IE calibration analysis, also in this procedure only  $m/z$  30 and 46 are used for analysis. Therefore the obtained  $IE_{NO_3}$  must be multiplied by a factor of 1.1, which is usually done by applying a  $RIE$  of 1.1 to nitrate when calculating mass concentrations.

An IE calibration performed in SPToF mode probably is the most reliable IE calibration procedure that can be done for the ToF-AMS, because there is no need for an external particle counter, and because multiply-charged particles can be easily excluded from the analysis without introducing additional uncertainty. Nevertheless, as the SPToF mode has not been available for most parts of this work and is still being tested, the IE calibration procedure using MS and PToF mode data (as described before) was developed during this work.

### **Calculation of Species' Mass Concentrations**

After multiplying the species-related signal by the  $IE_{NO_3}$  obtained from the IE calibration, the data have the format of “nitrate-equivalent” mass concentrations in  $\mu\text{g m}^{-3}$ . These nitrate-equivalent mass concentrations can be converted into ‘real’ mass concentrations of a species, if the relative ionisation efficiency  $RIE_s$  of the species  $s$  is known. Since the ionisation efficiency is different for different species, the  $RIE_s$  can be seen as a correction factor to the ionisation efficiency of the calibration species. The  $RIE_s$  of various species have been

determined during laboratory measurements (Alfarra et al., 2004; Hogrefe et al., 2004). Typical values used for AMS measurements are  $RIE_{SO_4} = 1.2$ ,  $RIE_{Org} = 1.4$ ,  $RIE_{Chl} = 1.3$  and  $RIE_{NH_4} = 4$ . Several studies show that the AMS underestimates ambient aerosol mass concentrations by a constant factor (DeCarlo et al., 2004). This is likely due to particle bounce from the vaporiser surface and needs to be corrected for by applying an additional correction factor, the collection efficiency (*CE*) factor (e.g. Drewnick et al., 2005). The *CE* is defined as the number of detected particles divided by the number of particles passing through the inlet. It has been shown that a collection efficiency of  $CE = 0.5$  is a good estimate for most ambient data. Nevertheless, at high relative humidities or for liquid particles particle bounce can be reduced, resulting in a  $CE > 0.5$ . In addition, the *CE* can be different for different chemical species, if the particles are not internally mixed (Weimer et al., 2005). It should, if possible, always be verified with the help of other quantitative techniques.

As mentioned before, if during a Q-AMS IE calibration slow evaporation of particles occurs, the obtained  $IE_{NO_3}$  will be smaller than the actual  $IE_{NO_3}$ . This effect is typically included in the collection efficiency factor obtained from the comparison of AMS data with data from other instruments. However, as in the ToF-AMS IE calibration the effect of slow evaporation is included, it does not need to be included in the *CE*, resulting in a lower ToF-AMS *CE* compared to the *CE* derived from Q-AMS measurements. When comparing mass concentrations measured with the ToF-AMS to those measured with a Q-AMS, this needs to be taken into account.

### 3.3 Characterisation of Size Distribution Measurements

The conversion of the signal from raw mass spectra measured in PToF mode into mass concentrations is exactly the same as for the MS mode data. The only exception is that the PToF data are acquired as a function of the particle flight time, which can be converted into particle vacuum aerodynamic diameter. Up to here, the PToF raw data arrays have been converted into species-related signal in ions  $s^{-1}$  as a function of particle flight time  $t_p$ . In the following, the conversion of the particle flight time into particle vacuum aerodynamic diameter will be described. In addition, the dependencies of the size distribution measurements on the ambient pressure and on the vaporiser temperature will be discussed.

#### 3.3.1 Size Calibration

As already mentioned in Chapter 2, the supersonic expansion of the particle-laden air on exiting the aerodynamic lens results in a size-dependent particle velocity distribution. Due to their lower inertia, small particles are accelerated to higher velocities than large particles, which makes it possible to derive the vacuum-aerodynamic diameter of the particles from the measured particle velocity.

In order to explain this dependency of the particle diameter on the particle velocity, one can use a very simplified approach:

The flow conditions in the AMS inlet are laminar, therefore the drag force  $F_D$  onto the particles can be described by Stokes' Law:

$$F_D = \frac{3\pi \cdot \eta_{air} \cdot \Delta v \cdot d_p}{C_c} \quad (3.47)$$

where  $\eta_{air}$  is the viscosity of air,  $\Delta v$  is the relative velocity of gas and particle,  $d_p$  the particle diameter and  $C_c$  the Cunningham slip correction factor.  $C_c$  can be parameterised (for solid particles and oil droplets) according to Allen and Raabe (1982) as follows:

$$C_c = 1 + Kn \cdot (\alpha + \beta \cdot e^{-\frac{\gamma}{Kn}}) \quad (3.48)$$

where  $Kn = 2\lambda/d_p$  is the Knudsen number,  $\lambda$  is the mean free path of the particles,  $\alpha = 1.142$ ,  $\beta = 0.558$  and  $\gamma = 0.999$ . In the aerodynamic lens of the AMS the Knudsen number is  $Kn \gg 1$ , which indicates free molecular flow regime conditions. Therefore  $C_c$  can be simplified to:

$$C_c \approx Kn \cdot (\alpha + \beta) = \frac{(\alpha + \beta) \cdot \lambda}{d_p} \quad (3.49)$$

Combining Equations (3.47) and (3.49) the drag force  $F_D$  can be expressed as:

$$F_D \approx \frac{3\pi \cdot \eta_{air} \cdot \Delta v \cdot d_p}{\frac{(\alpha + \beta) \cdot \lambda}{d_p}} = \frac{3\pi \cdot \eta_{air} \cdot \Delta v \cdot d_p^2}{(\alpha + \beta) \cdot \lambda} \propto d_p^2 \quad (3.50)$$

The mass  $m$  of a (spherical) particle is:

$$m = \frac{\pi}{6} \cdot \rho_p \cdot d_p^3 \propto d_p^3 \quad (3.51)$$

and therefore the acceleration inside the lens is given as:

$$a = \frac{F_D}{m} \propto \frac{d_p^2}{d_p^3} = \frac{1}{d_p} \quad (3.52)$$

Assuming that  $\Delta v$  does not change during the acceleration, this results in a particle velocity of:

$$v_p = a \cdot t \quad (3.53)$$

with  $t$  the time spent in the acceleration region:

$$t = \sqrt{2 \frac{l}{a}} \quad (3.54)$$

where  $l$  is the length of the acceleration region.

Combining Equations (3.52), (3.53) and (3.54),  $v_p$  is given as:

$$v_p = a \cdot \sqrt{2 \frac{l}{a}} = \sqrt{2la} \Rightarrow v_p \propto \frac{1}{\sqrt{d_p}} \quad (3.55)$$

In this simplified approach the particle velocity in the AMS is proportional to the reciprocal of the square root of the particle diameter. In reality, the relationship has been empirically found to follow Equation (3.56) (Allan et al., 2003a):

$$v_p = v_l + \frac{v_g - v_l}{1 + \left( \frac{d_{va}}{D^*} \right)^b} \quad (3.56)$$

where  $v_l$  and  $v_g$  are the asymptotic velocities for  $d_{va} \rightarrow \infty$  and  $d_{va} \rightarrow 0$  (in  $\text{m s}^{-1}$ ), respectively,  $D^*$  is an effective scaling diameter (in nm), and  $b$  is a dimensionless slope parameter typically in the order of 0.5. The velocities  $v_l$  and  $v_g$  can also be seen as the gas velocities inside the lens and after the nozzle expansion, respectively, because large particles cannot be slower than the velocity of the gas in the lens<sup>1</sup>, and the small particles cannot be faster than the expanding gas behind the nozzle.

During a particle size or PToF calibration, particles of known sizes are introduced into the instrument and their flight times are measured. The particle velocities  $v_p$  in the ToF-AMS (in  $\text{m s}^{-1}$ ) are calculated from the particle flight times  $t_p$  (in s) and the particle flight path  $l_c$  (i.e. the distance between the particle chopper and the vaporiser, in m), and plotted against their calculated vacuum-aerodynamic diameters  $d_{va}$ . The function given in Equation (3.56) is then fitted to the points (here using the Levenberg-Marquardt non-linear least squares

---

<sup>1</sup> This is true as long as the stopping distance of the particle is shorter than the distance between two apertures in the lens. This will be discussed later in this section.

optimisation (see Press et al. (1992) for details), which is included in IGOR). As calibration particles usually polystyrene latex (PSL) spheres (e.g. Duke Scientific Corporation, Palo Alto, CA, USA) are used. They are particle size standards of known and certified size, are spherical and have a density near unity ( $\rho_{PSL} = 1.05 \text{ g cm}^{-3}$ ). However, the range of PSL particle sizes is limited and it is not possible to extend the calibration to small particle sizes. For this reason, ammonium nitrate ( $\text{NH}_4\text{NO}_3$ ) or dioctyl phthalate (DOP) particles, size-selected with a DMA, are often used for size calibrations.

The relationship between the vacuum-aerodynamic diameter  $d_{va}$  and the electrical mobility diameter  $d_{mob}$  of the particles is given by Equation (3.57) (DeCarlo et al., 2004).

$$\begin{aligned} d_{va} &= \frac{\rho_{eff}}{\rho_0} \cdot d_{mob} \\ \rho_{eff} &= \rho_p \cdot \frac{1}{\chi_t \cdot \chi_v} \cdot \frac{C_c(d_{ve})}{C_c(d_{va})} = \rho_m \cdot S \end{aligned} \quad (3.57)$$

where  $\rho_{eff}$  is the effective density of the particle as defined above,  $\rho_0$  is the unit density ( $1 \text{ g cm}^{-3}$ ),  $\rho_p$  is the actual particle density,  $\rho_m$  is the bulk density of the particle material (which might be different to  $\rho_p$  due to for example internal voids),  $\chi_v$  and  $\chi_t$  are the dynamic shape factor in the free molecular and the transition regime, respectively,  $C_c$  is the Cunningham slip correction factor and  $S$  is the so-called Jayne shape factor.

The  $d_{va}$  can therefore be calculated from the  $d_{mob}$  of the calibration particles, the particle material density and the Jayne shape factor as follows:

$$d_{va} = \frac{\rho_m}{\rho_0} \cdot S \cdot d_{mob} \quad (3.58)$$

The Jayne shape factor  $S$  corrects for non-sphericity of the calibration particles ( $\chi_t$  and  $\chi_v$ ) and for differences in the particle density ( $\rho_p$ ) compared to the material density and can be determined during calibrations with PSL reference particles. For DOP particles the Jayne shape factor is  $S = 1$ , for ammonium nitrate particles it is  $S = 0.8$ , even though ammonium nitrate particles are supposed to be spherical. The value of  $S = 0.8$  can be explained by 20 % void volume in the particles, which means that only 80 % of the particles are solid.

Calibration Species	$\rho_m$ in $\text{g cm}^{-3}$	$S$	$p_{amb}$ in hPa	Diameter Range in nm	Calibration Points
PSL	1.05	1	998	300-800	4
DOP	0.98	1	1010	50-600	17
$\text{NH}_4\text{NO}_3$	1.72	0.8	1002	50-600	19

Table 3.2: Parameters for three different PToF calibrations performed with the ToF-AMS.  $\rho_m$  is the particle material density,  $S$  the Jayne shape factor,  $p_{amb}$  the ambient pressure during the calibration. The diameters are electrical mobility diameters in nm. The calibrations with PSL and  $\text{NH}_4\text{NO}_3$  were performed at the same day, the calibration with DOP three days later.

For a size calibration, calibration particles are generated with a Constant Output Atomizer (TSI Inc., Model 3076) and dried with a diffusion dryer (TSI Inc., Model 3062) filled with silica gel. In case of PSL, the particles are directly guided into the ToF-AMS and a CPC (TSI Inc., Model 3025) in parallel, in case of DOP and NH<sub>4</sub>NO<sub>3</sub> the particles are first size-selected with an Electrostatic Classifier (TSI Inc., Model 3080). The CPC is only used to check the particle number concentrations. From the various size calibrations which have been performed during this work, three performed with different calibration species, will be used for further characterisation (Table 3.2).

### Uncertainties of the Size Calibration

The uncertainties of the size calibration arise from uncertainties in the determination of the vacuum-aerodynamic diameter of the calibration particles and from uncertainties in the determination of the particle velocities. In the following, the main uncertainties are described:

- Uncertainty in the determination of  $d_{va}$ :

- Variability in PSL reference particle size

The variability in the size of the PSL particles is given by the manufacturer. It lies between  $\pm 1\%$  and  $\pm 2\%$  for the standards used here.

- Uncertainty in NH<sub>4</sub>NO<sub>3</sub> particle size

Due to the fact that for the calculation of the  $d_{va}$  of the NH<sub>4</sub>NO<sub>3</sub> calibration particles the Jayne shape factor is determined with the help of reference particles, the uncertainty in the  $d_{va}$  of NH<sub>4</sub>NO<sub>3</sub> particles is only determined by the uncertainty in the size of the reference particles. Here, DOP particles will be used as reference.

- Uncertainty in DOP particle size

The DOP particles are size-selected with a DMA. As already discussed in the IE calibration section of this chapter, the uncertainty in the selected diameter is estimated to be  $\Delta d_{va} / d_{va} = \pm 3\%$ .

- Uncertainty in the determination of  $v_p$ :

- Uncertainty in the flight path length  $l_c$

The length of the flight path of the particles depends on the position where the particles impact on the vaporiser (because the vaporiser has an inverse conical shape). In the worst case it is  $\Delta l_c = \pm 0.01\text{ m}$ .

- Uncertainty in the measured particle flight time  $t_p$

This uncertainty is due to the uncertainties in the start and end times,  $t_p(0)$  and  $t_p(\text{end})$  of the time-of-flight measurement:

The uncertainty in  $t_p(0)$  is caused by the width of the chopper slits, which covers 1 % of the chopper area. At a chopper frequency of 115 Hz and the assumption that the chopper is infinitely thin and the particles are infinitely small, this uncertainty is  $\Delta t_p(0) = \pm 4.4 \cdot 10^{-5}\text{ s}$ .

The fact that the chopper is not infinitely thin causes the chopper slits to be effectively smaller than 1 %, because the particles need some time to fly through the slit. With a chopper thickness of 0.2 mm and a particle velocity of  $v_p = 200\text{ m s}^{-1}$ , a particle needs 1  $\mu\text{s}$  to fly through the chopper, which makes the slit effectively 1.15

% smaller. In addition, the slit is effectively smaller by the diameter of the particles that fly through it, because the particle can only pass through when the chopper edges around the slit are not in the way of the particle. For this reason the chopper is only ‘open’ for the particle when the slit has moved out of the beam for exactly the particle radius, and it is already ‘closed’ when the slit is still out of the beam for exactly the particle radius. Therefore, the chopper slit is additionally 0.03 % smaller. This will reduce the uncertainty in  $t_p(0)$  to  $\Delta t_p(0) = \pm 4.3 \cdot 10^{-5}$  s.

The uncertainty in  $t_p(\text{end})$  is caused by the uncertainties in the evaporation time of the particles, the velocity distribution of the ions in the mass spectrometer and the resolution of the flight time measurement.

The width (FWHM) of a PToF distribution of an individual particle is approximately 30  $\mu\text{s}$  independent on the particle size (Jayne et al., 2000). This means that the uncertainty in the evaporation time is  $\Delta t_{p,\text{evap}} = \pm 1.5 \cdot 10^{-5}$  s.

The velocity of the ions during the transport to the mass spectrometer  $v_{ion}$  is dependent on the ion chamber voltage  $U_{ion}$ . Because of the voltage bias  $U_{HB}$  that is applied to the vaporiser, the electric field inside the ionisation chamber is inhomogeneous, causing the ions to experience different potentials dependent on their position in the field. With  $U_{ion} = 47.5$  eV and  $U_{HB} = 40$  eV the uncertainty in the potential the ions experience is at most  $\pm 3.75$  eV. The uncertainty in  $t_{p,ion}$  is dependent on the  $m/z$  of the ions. At  $m/z$  300 it is  $\Delta t_{p,ion} = \pm 1.2 \cdot 10^{-6}$  s (worst case).

The uncertainty caused by the digitalisation of the measured flight time is at a pulsing time  $T_{pulse} = 13 \cdot \mu\text{s}$  and with co-adding of two adjacent mass spectra  $\Delta t_{p,digi} = \pm 1.3 \cdot 10^{-5}$  s.

The overall uncertainty in  $t_p(\text{end})$  is therefore  $\Delta t_p(\text{end}) = \pm 2.0 \cdot 10^{-5}$  s.

The overall uncertainty in the measured particle flight time  $t_p$  is herewith  $\Delta t_p = \pm 4.8 \cdot 10^{-5}$  s. With the particle flight times typically measured with the ToF-AMS (2-5 ms, dependent on the particle size), this results in an uncertainty in the measured particle velocity of  $\Delta v_p / v_p < \pm 4$  %.

## Results

The results from the three size calibrations described in Table 3.2 are shown in Figure 3.21. The markers represent the measurements, the solid lines are the fits (Equation (3.56)) through the points with all four parameters fitted without constraints.

Figure 3.21 shows that the DOP calibration agrees well with the PSL calibration points. Only for  $d_{va} > 800$  nm, where there are no DOP calibration points, it slightly deviates from the calibration with PSL particles. Therefore the combination of the DOP and the PSL calibrations can be used as reference calibration for the determination of the Jayne shape factor for other calibration species. After applying a Jayne shape factor of  $S = 0.8$  to the  $\text{NH}_4\text{NO}_3$  calibration, it almost perfectly agrees with the DOP calibration curve. Only for large vacuum aerodynamic diameters ( $d_{va} > 800$  nm) it slightly deviates from the DOP calibration curve, but agrees well with the PSL calibration. The parameters resulting from fitting Equation (3.56) to the points are shown in the first row of Table 3.3 for the  $\text{NH}_4\text{NO}_3$  calibration and of Table 3.4 for the DOP calibration. The given errors of the parameters are the standard deviations estimated from the residuals. This assumes that the errors are normally distributed with zero mean and constant variance and that the fit function is a good

description of the data (Wavemetrics Inc., 2005). When fitting all four parameters without constraints, the resulting errors are quite large.

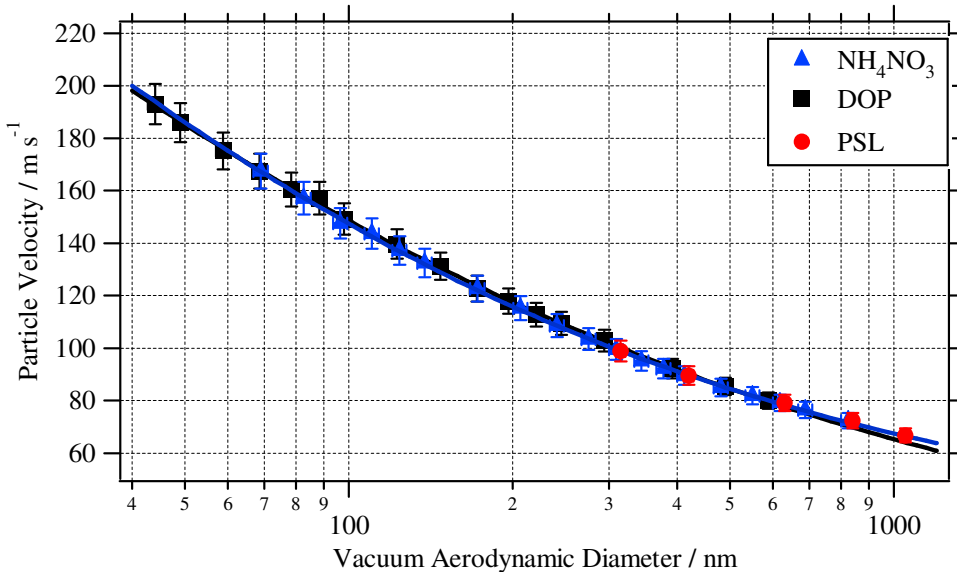


Figure 3.21: Particle size calibration performed with three different types of calibration particles (see Table 3.2). The solid lines are the fits through the data points (Equation (3.56)). Error bars are calculated according to the uncertainties described above.

In order to obtain more robust results the fit was repeated fitting only three of the parameters without constraints and holding one parameter constant. For this purpose, the values of  $v_l$ ,  $v_g$  and  $b$  need to be estimated:

- $b$ , slope parameter: in the simplified approach above it was shown that  $v_p \propto 1/\sqrt{d_p}$ . Therefore the slope parameter can be estimated to  $b = 0.5$ .
- $v_g$ , asymptotic velocity for  $d_p \rightarrow 0$ : this can be estimated as the gas velocity after the nozzle expansion, as small particles cannot go faster than the expanding gas behind the nozzle. It can be determined from the PToF distributions of the gas phase signals. Because different gases are accelerated to different velocities, the estimate of  $v_g$  results in different values dependent on the  $m/z$  used. Here,  $m/z$  28 ( $\text{N}_2^+$ ) is used, resulting in  $v_g = 694 \text{ m s}^{-1}$ .
- $v_l$ , asymptotic velocity for  $d_p \rightarrow \infty$ : this can be estimated as the gas velocity inside the lens, which again is difficult to estimate as the gas undergoes various accelerations and decelerations within the aerodynamic lens. The gas velocity in front of the nozzle (last lens aperture) was calculated to  $v_l = 20 \text{ m s}^{-1}$  (using an inlet flow rate of  $Q_{in} = 1.4 \text{ cm}^3 \text{s}^{-1}$  and a lens pressure of  $p_{lens} = 180 \text{ Pa}$ ). In addition, this assumption can only be used as long as the stopping distance  $SD$  of the particles inside the lens is shorter than the distance between two lens apertures, because otherwise the particles would not obtain the same velocity as the gas. The stopping distance  $SD$  is given by Equation (3.59):

$$SD = \frac{\rho_p d_p}{\rho_g} \left[ Re_0^{\frac{1}{3}} - \sqrt{6} \arctan \left( \frac{Re_0^{\frac{1}{3}}}{\sqrt{6}} \right) \right] \quad (3.59)$$

where  $\rho_p$  and  $\rho_g$  are the particle and the gas density,  $d_p$  is the particle diameter and  $Re_0$  is the Reynolds number as given in Equation (3.60) (Hinds, 1999).

$$Re_0 = \frac{\rho_g v_{p,ini} d_p}{\eta_g} \quad (3.60)$$

with  $\eta_g$  the viscosity of the gas and  $v_{p,ini}$  the initial particle velocity relative to the gas velocity. The latter is assumed to be the difference between the gas velocities in the fifth aperture of the lens (4 mm diameter) and in the lens tube (10 mm diameter). With this approach  $v_{p,ini}$  is calculated to  $104 \text{ m s}^{-1}$ . The resulting stopping distances  $SD$  for particles with  $\rho_p = 1 \text{ g cm}^{-3}$  and diameters between 40 nm and 1  $\mu\text{m}$  are shown in Figure 3.22. As the temperature inside the lens is not known, the stopping distance was calculated for three different temperatures  $T$  (200 K, 273 K and 293 K).

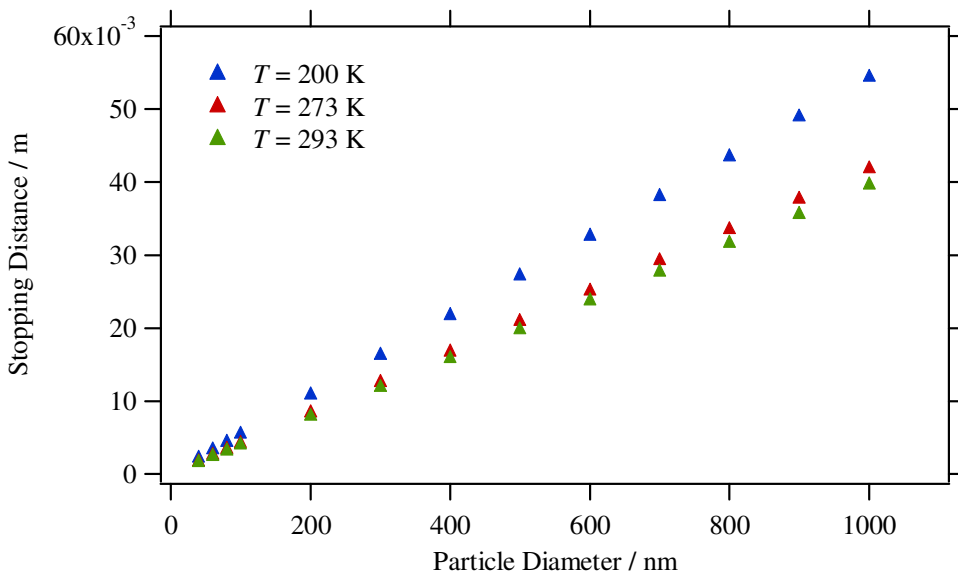


Figure 3.22: Stopping distance  $SD$  inside the aerodynamic lens according to Equation (3.59) as a function of particle diameter  $d_p$  and for three different temperatures  $T$ .

The calculated stopping distances are shorter than 5.5 cm for  $T = 200 \text{ K}$ , shorter than 4.3 cm for  $T = 273 \text{ K}$  and shorter than 3.9 cm for  $T = 293 \text{ K}$  for all relevant particle sizes. The distance between the last aperture and the nozzle of the lens is approximately 5 cm, which means that at a lens pressure of 1.8 hPa  $v_l$  can still be approximated by the gas velocity inside the lens, because inside the lens all particles should have the same velocity as the gas. Nevertheless, due to the large uncertainties in this approach, this should only be done if the range of the calibration data points does not cover the very large particle diameters. In addition, it needs to be taken into account that the stopping distance of the particles becomes larger with decreasing lens pressure (and therefore with decreasing ambient pressure) and the assumption becomes unrealistic.

The results from fitting only three parameters without constraints are also given in Table 3.3 and Table 3.4 for the  $\text{NH}_4\text{NO}_3$  and the DOP calibration, respectively. The resulting

calibration curves are almost identical to the ones resulting from fitting all parameters without constraints for both  $\text{NH}_4\text{NO}_3$  and DOP, and the resulting parameters are very similar to each other for the  $\text{NH}_4\text{NO}_3$  calibration, with the errors being obviously smaller. In case of the DOP calibration, the errors also become smaller when only fitting three parameters independently, but the resulting parameters differ much more from each other than in the  $\text{NH}_4\text{NO}_3$  calibration. In addition, in all cases, at least one of the DOP calibration parameters is significantly different from its estimated value (see initial values given above), and it was only possible to make the DOP calibration curve agree with the PSL calibration points for large  $d_{va}$  in the case of holding  $v_l = 20 \text{ m s}^{-1}$ .

Parameters	$v_l$	$v_g$	$D^*$	$b$
w/o constraints	$21.47 \pm 18.20$	$695 \pm 743$	$5.16 \pm 18.10$	$0.50 \pm 0.18$
$b = 0.5$	$22.01 \pm 2.08$	$686 \pm 78$	$5.41 \pm 1.74$	$0.50 \pm 0.00$
$v_l = 20 \text{ m s}^{-1}$	$20.00 \pm 0.00$	$691 \pm 162$	$5.16 \pm 3.77$	$0.49 \pm 0.02$
$v_g = 694 \text{ m s}^{-1}$	$21.60 \pm 4.00$	$694 \pm 0$	$5.20 \pm 0.28$	$0.50 \pm 0.02$

Table 3.3: Fit parameters resulting from the  $\text{NH}_4\text{NO}_3$  size calibration for various constraints to the fit parameters.

Parameters	$v_l$	$v_g$	$D^*$	$b$
w/o constraints	$3.03 \pm 32.00$	$638 \pm 508$	$6.18 \pm 18.80$	$0.44 \pm 0.18$
$b = 0.5$	$13.21 \pm 2.77$	$504 \pm 25$	$14.52 \pm 2.74$	$0.50 \pm 0.00$
$v_l = 20 \text{ m s}^{-1}$	$20.00 \pm 0.00$	$446 \pm 37$	$21.60 \pm 6.20$	$0.55 \pm 0.02$
$v_g = 694 \text{ m s}^{-1}$	$-0.10 \pm 6.61$	$694 \pm 0$	$4.47 \pm 0.12$	$0.42 \pm 0.02$

Table 3.4: Same as Table 3.3, but for the size calibration with DOP.

In summary, a size calibration should always be performed covering the whole range of particle vacuum aerodynamic diameters of interest. If the calibration particles cover the range of sizes of particles that will be encountered during a measurement and the fitting function adequately reflects the calibration data, the individual values of the fit parameters are not important for the inversion of the data and  $v_g$  and  $v_l$  need not to be estimated. However, if the range of calibration points does not cover all the sizes expected, the calibration curve needs to be extrapolated and the values of  $v_g$  and  $v_l$  may become important for sizing of small and large particles, respectively. In this case,  $v_g$  and  $v_l$  should be estimated as described above.

### 3.3.2 Pressure-dependency of the Size Calibration

As mentioned before, in the AMS the particles obtain a size-dependent velocity due to the gas expansion while exiting the aerodynamic lens. The strength of the acceleration is dependent on the pressure inside the aerodynamic lens. The pressure inside the lens,  $p_{lens}$ , is dependent on the ambient pressure; it is approximately 180 Pa at 1000 hPa ambient pressure and decreases with decreasing ambient pressure. This means that the particle velocity for a certain particle size varies with varying ambient pressure and it is necessary to perform a size calibration at exactly the pressure one wants to do the measurements (e.g. measurements

at elevated sites or aircraft measurements). A pressure-dependent size calibration, where the calibration parameters are determined as a function of the ambient pressure, becomes important for the analysis of aircraft measurements, so that the particle diameters can be calculated correctly for every ambient pressure occurring during the measurements. For this purpose, the same calibration set-up is used as described for the standard size calibration with the difference that a needle valve is installed upstream the ToF-AMS inlet to control the upstream pressure (i.e. to simulate various ambient pressures). The upstream or ambient pressure  $p_{up}$  is determined with a Baratron pressure gauge. A schematic of the calibration set-up is shown in Figure 3.23. This set-up is a further development of the experiments described in Henseler (2003).

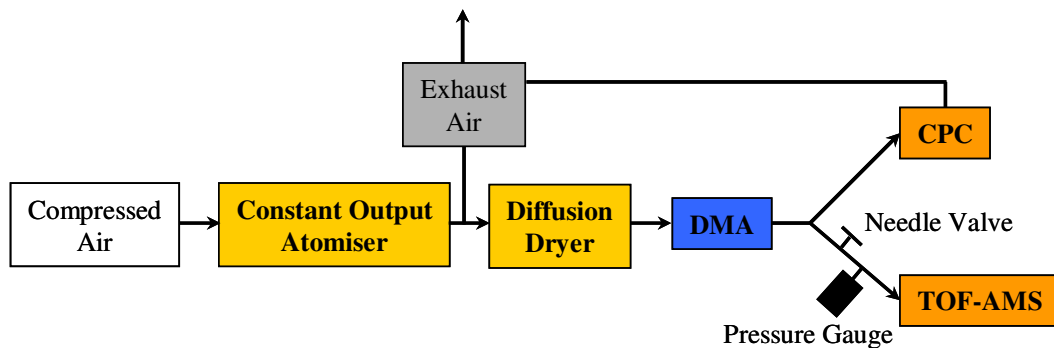


Figure 3.23: Schematic of the set-up for the pressure-dependent size calibration.

The pressure-dependent size calibration is performed in the same way as described for the standard size calibration, with ammonium nitrate particles, electrical mobility diameters between 50 and 600 nm and for 11 different ambient pressures between 200 and 1000 hPa. The results are shown in Figure 3.24 and Figure 3.25, and in Table 3.5.

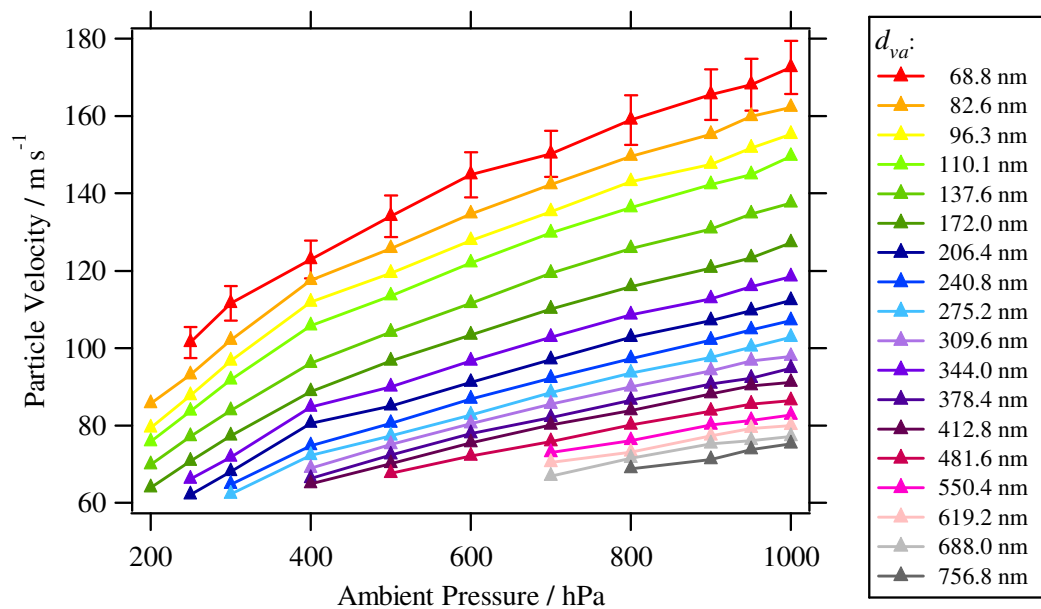


Figure 3.24: Results from the pressure-dependent particle size calibration. Shown is the measured particle velocity for all particle diameters used during the calibration as a function of the ambient pressure  $p_{up}$ . Error bars are shown for measurement at  $d_{va} = 68.8$  nm only, but are of similar size for the other measurements.

In Figure 3.24 the particle velocity as a function of ambient pressure for various vacuum-aerodynamic diameters is shown. The particle velocity (for one particular  $d_{va}$ ) increases with increasing ambient pressure, because the pressure inside the aerodynamic lens increases. Another way of presenting the results from this calibration is plotting the particle velocity as a function of vacuum aerodynamic diameter for each ambient pressure the calibration was performed, resulting in a single calibration curve for each ambient pressure (Figure 3.25).

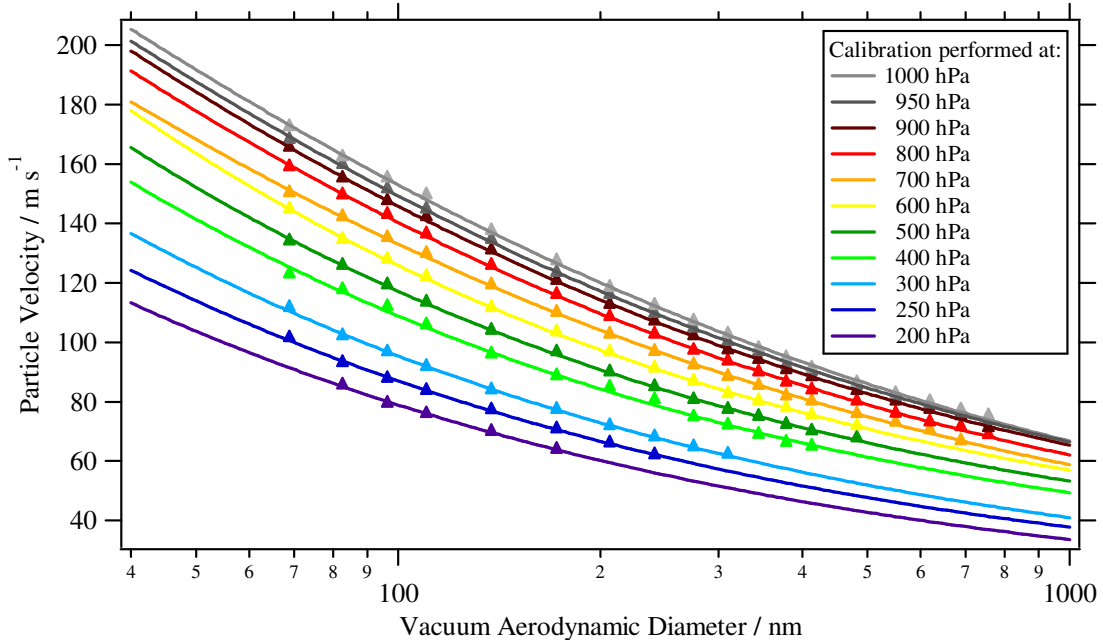


Figure 3.25: Results of the pressure-dependent size calibration. Shown is the measured particle velocity as a function of vacuum aerodynamic diameter, the solid lines are the fits (Equation (3.56)) through the calibration points. Each curve represents a size calibration for one individual ambient pressure.

The solid lines in Figure 3.25 again represent the results from fitting Equation (3.56) to the calibration points. The four parameters were fitted independently when possible, but for a few ambient pressures (especially  $p_{up} < 400$  hPa) it was necessary to hold  $b = 0.5$  and to estimate  $v_g$ , as there were only few calibration points available. The resulting parameters of the fits and their errors are given in Table 3.5. The quite large errors again show the sensitivity of the used fit algorithm to the boundary conditions.

At all ambient pressures the slope parameter  $b$  is always close to 0.5 and a systematic pressure-dependency could not be found;  $v_g$  and  $D^*$  show a linear dependency on the ambient pressure, while  $v_l$  can be approximated by a power law function. Parameterisations for the measured pressure-dependencies of the individual parameters are given in Equations (3.61) - (3.63).

$$v_l = (-171.85 \pm 483) + (110.48 \pm 441) \cdot p_{amb}^{(0.079 \pm 0.002)} \quad (3.61)$$

$$v_g = (231.47 \pm 10.70) + (0.48 \pm 0.0163) \cdot p_{amb} \quad (3.62)$$

$$D^* = (13.92 \pm 0.70) - (0.009 \pm 0.001) \cdot p_{amb} \quad (3.63)$$

$v_l$  and  $v_g$  are given in  $\text{m s}^{-1}$ ,  $D^*$  in nm and  $p_{amb}$  in hPa. The fit parameters as a function of the ambient pressure are shown in Figure 3.26.

Ambient Pressure	$v_l$	$v_g$	$D^*$	$b$
1000	$18.73 \pm 0.83$	$696.88 \pm 913.00$	$5.47 \pm 25.60$	$0.46 \pm 0.23$
950	$13.21 \pm 21.40$	$696.03 \pm 712.00$	$5.17 \pm 18.30$	$0.47 \pm 0.18$
900	$18.36 \pm 15.40$	$650.23 \pm 515.00$	$6.29 \pm 16.50$	$0.50 \pm 0.15$
800	$16.29 \pm 1.64$	$610.49 \pm 47.80$	$6.95 \pm 1.59$	$0.50 \pm 0.00$
700	$14.68 \pm 2.17$	$554.09 \pm 53.40$	$7.90 \pm 2.29$	$0.50 \pm 0.00$
600	$28.08 \pm 13.00$	$530.83 \pm 417.00$	$9.15 \pm 20.50$	$0.60 \pm 0.18$
500	$25.04 \pm 15.30$	$475.79 \pm 433.00$	$9.93 \pm 26.20$	$0.59 \pm 0.22$
400	$3.38 \pm 97.60$	$421.34 \pm 0.01$	$10.57 \pm 118.00$	$0.48 \pm 0.86$
300	$2.36 \pm 1.80$	$400.00 \pm 0.00$	$9.40 \pm 0.42$	$0.50 \pm 0.00$
250	$0.45 \pm 2.17$	$350.00 \pm 0.00$	$10.92 \pm 0.60$	$0.50 \pm 0.00$
200	$-3.84 \pm 4.12$	$300.00 \pm 0.00$	$14.06 \pm 1.47$	$0.50 \pm 0.00$

Table 3.5: Fit parameters  $v_l$ ,  $v_g$ ,  $D^*$  and  $b$  (Equation (3.56)) resulting from size calibrations performed at various ambient pressures.

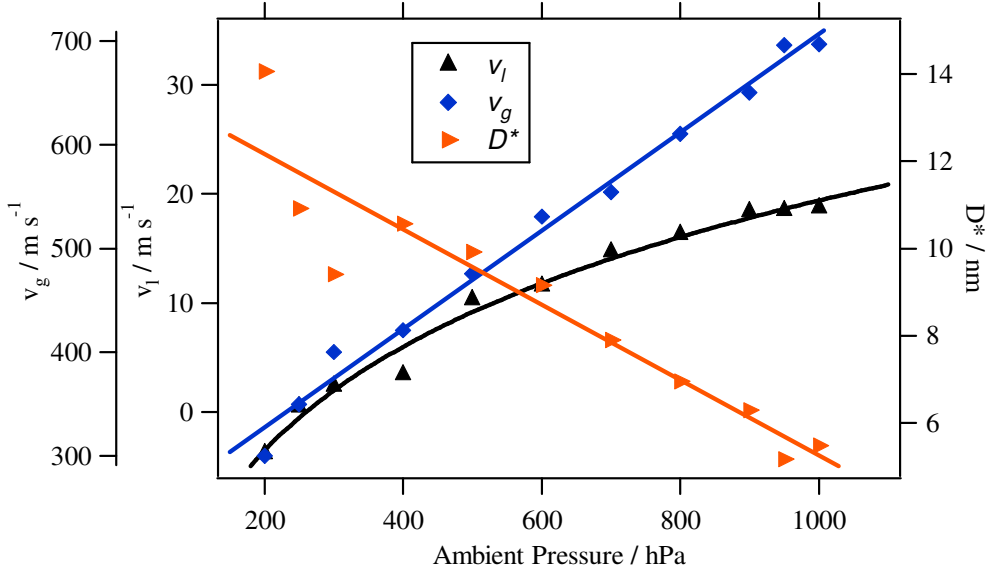


Figure 3.26: Fit parameters  $v_l$  (black),  $v_g$  (blue) and  $D^*$  (orange) as a function of ambient pressure. The solid lines represent linear fits in case of  $v_g$  and  $D^*$  and a power law fit in case of  $v_l$ . The resulting pressure-dependencies are given in Equations (3.61) to (3.63).

The most difficult part of a pressure-dependent size calibration is to find the pressure-dependency of the fit parameters. The resulting values strongly vary with the initial values of the fit and it is not always possible to make the fit converge properly. In addition, the lower the pressure, the more difficult it is to do the calibration with small and large particle sizes. In order to extend the size range of those calibrations and to stabilise the fit it is necessary to estimate  $v_g$  from the airbeam signal measured during the calibration as shown above. Unfortunately, it is not possible to estimate  $v_l$  properly, as at low pressures the stopping

distance of the particles becomes too large to guarantee that the particle velocity is equal to the gas velocity inside the lens (see above). It was found during this work that – at least for the instrument used here – holding  $b = 0.5$  during the fit is a good approach to stabilise the fit for large particle sizes.

As already said before, a pressure-dependent size calibration is most important when doing aircraft measurements to be able to convert particle flight times into particle sizes for all conditions. In addition, it also needs to be taken into account that a pressure change due to normal weather situation changes also changes the size calibration of the instrument. However, a pressure change between 980 and 1020 hPa results in a change of the calculated vacuum aerodynamic diameter of only a few %, which is about the same magnitude as the uncertainties of the size calibration itself.

After having converted the measured particle flight time into the vacuum aerodynamic diameter of the particles the PToF distributions have the format of species-related signal in ions  $s^{-1}$  as a function of  $d_{va}$ . Equal to the MS data, the signal of the PToF distributions is converted into mass concentrations according to Equation (3.32) and dividing it through the collection efficiency  $CE$  of the particles. Finally, the size distributions are converted into  $dM/d\log d_{va}$  as a function of  $d_{va}$ , resulting in individual mass distributions for the different species.

### 3.3.3 Dependency on Vaporiser Temperature

In this last section about the characterisation of PToF distributions the influence of the vaporiser temperature on the characteristics of the size distributions will be investigated. If the vaporiser temperature is too low, particles hitting the vaporiser will only slowly evaporate, resulting in a broadening of the size distributions, as well as in a shift of the position of the distribution maximum (which is dependent on the width of the distribution). In order to measure the dependency of the distribution width and the distribution maximum on the vaporiser temperature, laboratory-generated monodisperse aerosol was introduced into the ToF-AMS and PToF distributions were measured for vaporiser temperatures between 200 and 820 °C. This was done for three different types of aerosol particles: for ammonium nitrate and ammonium sulphate with an electrical mobility diameter of  $d_{mob} = 350$  nm and for PSL with a diameter of  $d_p = 400$  nm. The resulting size distributions for PSL particles are shown in Figure 3.27.

The position of the distribution maxima and the distribution widths (FWHM) was determined by fitting Gaussian distributions to each measured size distribution. The resulting distribution widths and maxima as a function of the vaporiser temperature are shown in Figure 3.28. For all species, a decrease in the distribution width as well as a shift of the position of the distribution maximum with increasing vaporiser temperature can be seen. Reaching a certain temperature which is different for the different species, both the width and the position of the distribution maximum “level off” and are no longer dependent on the vaporiser temperature. Ammonium nitrate shows the weakest dependency on the vaporiser temperature with the position of the distribution maximum varying only slightly with increasing vaporiser temperature and the peak width staying almost constant for temperatures of 350 °C and more. This shows that ammonium nitrate flash-evaporates at quite low vaporiser temperatures. The width of the sulphate distributions decreases rapidly with increasing temperature up to 350 °C, while at the same time the position of the peak maximum shifts to shorter particle flight times. Both vary only slightly with further

increasing temperature, showing that ammonium sulphate also evaporates at quite low temperatures. As PSL particles do not evaporate easily at low temperatures it was not possible to determine the maximum and width of the PSL size distributions up to a vaporiser temperature of 700 °C. Above this temperature the width of the PSL size distribution decreases rapidly and the position of the maximum also shifts to shorter flight times, meaning that PSL flash-evaporates at a vaporiser temperature of 750 °C and above.

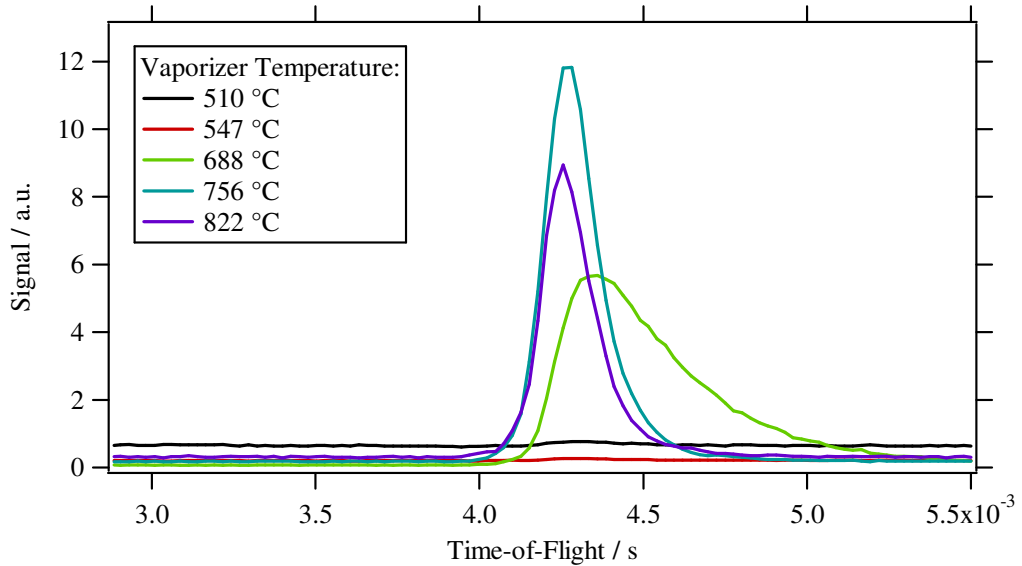


Figure 3.27: Measured PToF distributions of laboratory-generated PSL particles ( $d_{mob} = 400$  nm) at various vaporiser temperatures.

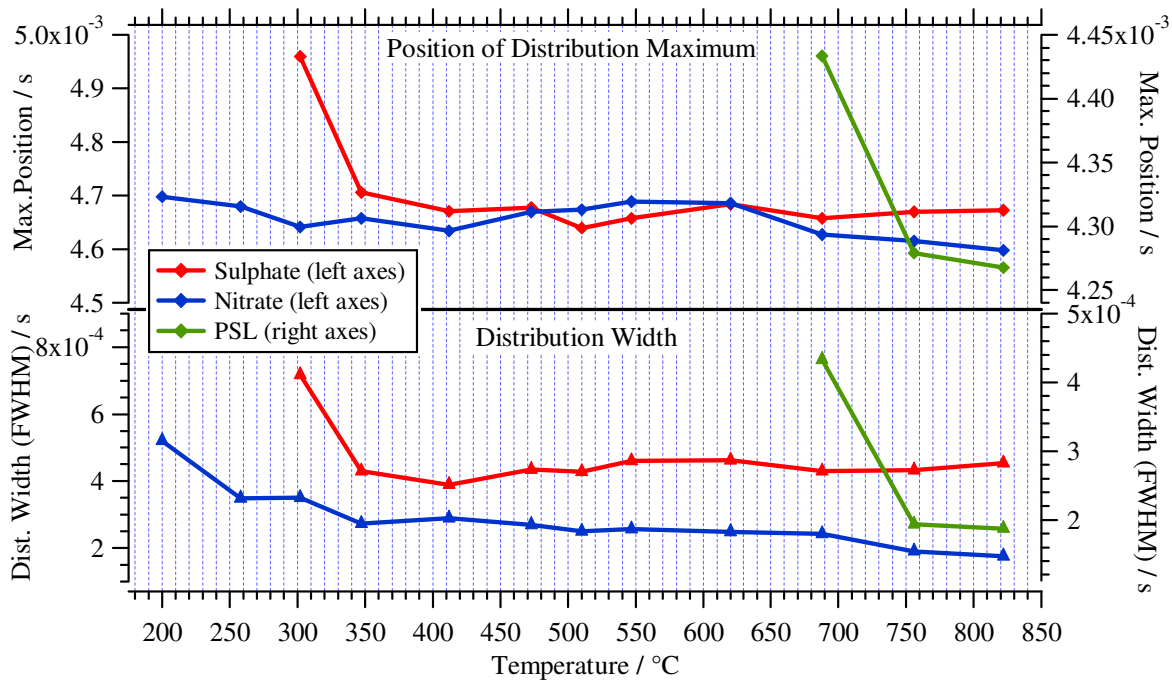


Figure 3.28: Position of the distribution maximum and distribution widths of laboratory-generated monodisperse ammonium nitrate, ammonium sulphate and PSL aerosol as a function of the vaporiser temperature.

In summary these experiments show that it is important not to do measurements at a too low vaporiser temperature, depending on the chemical composition of the measured aerosol.

---

When measuring with a vaporiser temperature higher than the one needed to flash-evaporate the species, no further reduction of the distribution width can be achieved by increasing the vaporiser temperature. In this case, the width of the size distribution is not increased by slow evaporation anymore. The operating temperature of AMS instruments in the field is always an compromise between fast evaporation for exact size measurements (high temperature is needed) and low fragmentation of organic compounds (low temperature is needed). It is approximately 600 °C, as most chemicals found in the atmosphere flash-evaporate at this vaporiser temperature, and to make measurements from different AMS instruments comparable to each other.

The ToF-AMS data analysis and characterisation processes that had an impact on this analysis are completely discussed now. In the last section of this chapter, more characterisation of the instrument and investigation of further capabilities will be described.

## 3.4 Mass Concentration Detection Limits

In the following section, results of systematic laboratory experiments for the determination of nitrate, sulphate, ammonium, chloride and organics mass concentration detection limits for both, a Q-AMS and a ToF-AMS under various measurement conditions are described. They are also subject to a forthcoming publication (Hings et al., 2006).

### 3.4.1 Definition

For the chemical analysis at trace levels it is important to know the smallest concentration or amount of analyte that can be detected. The problem in general is to differentiate between the response given by a blank and that given by a sample with a small concentration of the analyte, or in other words, detecting a weak signal in the presence of background signal and noise. Measurements are subject to random errors, which produce a normal distributed error curve. Therefore the distributions of replicate blank and sample measurements will overlap each other as the two average signals approach each other in magnitude, and at some point the chance of mistakenly identifying the analyte as present when it is not or vice versa reaches an unacceptable level. For this reason, the limit of detection (*LOD*) must be defined in statistical terms and be related to the probability of making a wrong decision. In other words, the limit of detection is the concentration of analyte which produces a signal that can be distinguished from the blank signal with a certain statistical confidence. By convention (e.g. Kellner et al., 2004), it is defined as

$$LOD = \mu_b + 3 \cdot \sigma_b \quad (3.64)$$

with  $\mu_b$  the arithmetic mean and  $\sigma_b$  the standard deviation of a set of blank measurements. For this definition it is assumed that the measurement of the analyte concentration at *LOD* level is sufficiently close to the measurement at zero concentration (blank), so that both measurements generate error curves with almost identical standard deviations  $\sigma_b$ . With the centre points of both distributions being three standard deviations apart from each other the probability for a wrong decision (in either way) is only 0.3 %.

### 3.4.2 Measurement of AMS Detection Limits

In the specific case of the AMS MS mode the analyte measurement is the aerosol beam measurement while the background measurement with the aerosol beam blocked can be identified as the blank measurement. As described above, in the MS mode of the AMS for each single aerosol beam measurement also the background signal  $I_b$  is determined. The aerosol concentrations are extracted from the difference of aerosol beam measurement and background measurement, performed during the same averaging interval. Therefore, the *LOD* of mass concentrations obtained from the AMS can be experimentally determined from a set of consecutive measurements under identical conditions and is given by

$$LOD_{AMS} = LOD_{exp} = 3 \cdot \sigma(I_b) \quad (3.65)$$

with  $\sigma(I_b)$  the standard deviation of the background signal  $I_b$ , where  $I_b$  and  $LOD_{AMS}$  are given in the same units (e.g. in  $\mu\text{g m}^{-3}$ ). These  $LOD_{exp}$  will be used here to experimentally determine detection limits for individual species under various measurement conditions.

There are various contributions to the observed variations in the background signal. Limited counting statistics due to the small number of ions reaching the detector per unit time at the individual  $m/z$  is one of the major contributions. Additional variation is produced by the distribution of detector signal intensities (i.e. the detector current output) from individual ions reaching the detector. Further factors are real fluctuations in background ion concentration, ionisation electron flux or electronic noise. While the experimental determination of the  $LOD_{exp}$  according to Equation (3.65) accounts for all these contributions, an estimate of  $LOD$  levels can be obtained by an approach introduced by Allan et al. (2003a and b) that only accounts for counting statistics and single ion signal intensity distribution: The distribution of the number of detected ions can be modelled as a Poisson distribution. For calculation of the error of the measured signal it must also be taken into account that the signal of a single ion is not a constant but arises from a Gaussian distribution of pulse areas or intensities. In this simplified approach the distribution width of single ion intensities is accounted for by multiplying the width of the Poisson distribution with a constant factor of  $\alpha = 1.2$ , which was determined from single-ion measurements with the Q-AMS (Allan et al., 2003a). Therefore, the (statistical) error of any signal  $I$ , in ions per second, is given by Equation (3.66).

$$\Delta I = \alpha \cdot \frac{\sqrt{I}}{\sqrt{t_s}} \quad (3.66)$$

with  $t_s$  the total time in seconds spent sampling the particular  $m/z$ , associated with signal  $I$ , during the data acquisition interval. For each individual  $m/z$  signal in the Q-AMS  $t_s$  is equal to the time spent measuring the background signal in MS mode, divided by the total number of  $m/z$  scanned (typically 300) and multiplied by the fraction of the peak area that is used to determine signal intensity (0.4); for the ToF-AMS  $t_s$  is equal to the time spent measuring the background signal in MS mode multiplied by the duty cycle of ion extraction of the TOFMS (Drewnick et al., 2005).

In accordance with the standard definition of the  $LOD$  (Equations (3.64) and (3.65)) we define the detection limit  $LOD_{stat}$  determined from this approach as:

$$LOD_{stat} = 3 \cdot \alpha \cdot \frac{\sqrt{I_b}}{\sqrt{t_s}} \quad (3.67)$$

with  $I_b$  the signal obtained from a background measurement with the AMS.  $I_b$  can either be the signal intensity of an individual  $m/z$  or the accumulated signal intensity of all fragments of a certain species. The  $LOD_{stat}$  obtained from Equation (3.67) are given in  $\text{ions s}^{-1}$ . They are converted into mass concentrations in the same way as the signal intensities of the raw spectra (Equation (3.32)). This detection limit is similar to the one defined by Allan et al. (2003a and b). However, since their  $LOD_{stat}$  accounts for the uncertainty of the background as well as of the aerosol measurement, it is at least by a factor of  $\sqrt{2}$  larger than with our definition which is based on the common standard definition of detection limits.

In order to measure and characterise the AMS detection limits for different species and a variety of measurement conditions, three different kinds of measurements have been performed:

- 1) Measurements of filtered air to determine the minimum possible detection limits for nitrate, sulphate, ammonium, chloride and organics. The duration of the filter measurements was 2 hours, with an averaging interval of 30 seconds. The chopper open-to-closed ratio was 50 %, i.e. the instrument background (aerosol beam blocked) was measured during half of the time.
- 2) Measurements with various constant mass concentrations of laboratory-generated ammonium nitrate ( $0.3, 7, 20$  and  $80 \mu\text{g m}^{-3}$  nitrate mass concentration) and ammonium sulphate ( $4, 20$  and  $50 \mu\text{g m}^{-3}$  sulphate mass concentration). The duration of each measurement was 1 hour, the averaging interval was again 30 seconds. This was done to determine the dependency of the individual detection limits on the aerosol mass loading and to investigate whether the detection limit of one species is dependent on the mass loading of another species (cross-sensitivity).
- 3) “Background perturbation experiments”, where a filter measurement according to 1) was performed directly after a high mass concentration of a species was measured. These experiments were done with ammonium nitrate ( $90$  and  $150 \mu\text{g m}^{-3}$  nitrate), ammonium sulphate ( $100 \mu\text{g m}^{-3}$  sulphate) and with polystyrene latex spheres (PSL,  $200 \mu\text{g m}^{-3}$  organics), in order to determine the self-cleaning time constants of the instruments (i.e. the time after which the detection limit has decreased to  $1/e$  of the detection limit at the high mass concentration).

All experiments except of the filter measurements were performed using the following set-up: The aerosol was generated using a Constant Output Atomizer (TSI Inc., Model 3076). For measurements where a nitrate mass concentration is given in the text, a solution of ammonium nitrate in water was used, for sulphate measurements a solution of ammonium sulphate in water was used, and for organics measurements a dispersion of PSL particles in water ( $d_p = 300 \pm 6 \text{ nm}$ ) was used. The generated aerosol was then directed through a diffusion dryer (TSI Inc., Model 3062) filled with silica gel in order to dry the particles before they were guided into the AMS and a CPC (TSI Inc., Model 3025) in parallel. The CPC was used to verify the performance of the atomizer, i.e. the temporal stability of the generated particle concentrations.

### 3.4.3 Filter Measurements

While measuring filtered air, the AMS instrument background and the background variations reach their minimum levels. The detection limits determined from these measurements are therefore the best possible detection limits which can be achieved with the AMS under regular operation conditions.

The results from the filter measurements are shown in Table 3.6. The experimentally determined detection limits ( $LOD_{exp}$ , Equation (3.65)) are given together with those estimated from ion counting statistics ( $LOD_{stat}$ , Equation (3.67)) for nitrate, sulphate, ammonium, chloride and organics. The Q-AMS  $LOD_{exp}$  lie between  $0.016 \mu\text{g m}^{-3}$  (nitrate) and  $0.309 \mu\text{g m}^{-3}$  (organics), while the ToF-AMS  $LOD_{exp}$  are on average lower by a factor of 9 (range  $1.5 - 17$ ) and lie between  $0.002 \mu\text{g m}^{-3}$  (nitrate) and  $0.022 \mu\text{g m}^{-3}$  (ammonium). For both instruments the lowest  $LOD_{exp}$  are observed for nitrate, sulphate and chloride, which

produce only a few fragments with good signal-to-noise ratios. The highest  $LOD_{exp}$  are found for ammonium, which has fragments at  $m/z$  with large contributions from other (noise-adding) species like air and water, and for organics which fragments on a large number of  $m/z$ , causing low signal-to-noise ratios at the individual  $m/z$ . The observed differences between the ToF-AMS and Q-AMS  $LOD_{exp}$  can largely be explained by the different ion duty cycles  $D_{ion}$  (see section 3.2.1) of the two mass spectrometers. In the Q-AMS MS Mode the complete mass spectrum ( $300 m/z$ ) is scanned by the quadrupole mass spectrometer, using only 0.4 mass units per  $m/z$  for ion signal determination. The duty cycle of the chopper is 50 %. The Q-AMS ion transmission duty cycle in MS Mode is therefore given by Equation (3.68).

$$D_{ion,Q-AMS,MS} = \frac{0.4}{300} \cdot 50\% = 0.067\% \quad (3.68)$$

The ion duty cycle of the ToF-AMS  $D_{ion,ToF-AMS}$  is  $m/z$ -dependent (see Chapter 3.2.1). For  $m/z$  28 it is in MS mode at a chopper ratio of 50 %:

$$D_{ion,ToF-AMS,MS} = 50\% \cdot D_{ion,overfill} = 8.7\% \quad (3.69)$$

Because the  $LOD$  is inversely proportional to the square root of the sample time  $t_s$  of an individual  $m/z$  and therefore inversely proportional to the square root of the duty cycle of a  $m/z$ , the relationship between the Q-AMS and ToF-AMS  $LOD$  due to differences in duty cycle is given by

$$LOD_{Q-AMS} = \sqrt{\frac{D_{ion,ToF-AMS}}{D_{ion,Q-AMS}}} \cdot LOD_{TOF-AMS} \approx 11 \cdot LOD_{TOF-AMS} \quad (3.70)$$

The difference is lower for species which fragment into  $m/z < 28$  (because of the reduced ToF-AMS duty cycle) and higher for species which fragment into  $m/z > 28$  (because of the higher duty cycle of the ToF-AMS and the high contribution by electronic noise in the Q-AMS).

Species	$LOD_{exp}, \mu\text{g}/\text{m}^3$		$LOD_{stat}, \mu\text{g}/\text{m}^3$	
	Q-AMS	TOF-AMS	Q-AMS	TOF-AMS
Nitrate	0.016	0.002	0.017	0.004
Sulphate	0.024	0.002	0.014	0.001
Ammonium	0.097	0.022	0.069	0.042
Chloride	0.02	0.013	0.028	0.013
Organics	0.309	0.018	0.153	0.02

Table 3.6: Limits of Detection ( $LOD$ ) of Q-AMS and ToF-AMS, derived from measurements of filtered air.  $LOD_{exp}$  are experimentally determined,  $LOD_{stat}$  are estimated from ion counting statistics. In both cases, the detection limits are calculated for 30 seconds saving intervals.

Additionally, it needs to be taken into account that the Q-AMS used here has a larger critical orifice ( $130\text{ }\mu\text{m}$ ) than the ToF-AMS ( $100\text{ }\mu\text{m}$ ). Therefore, the volumetric flow rate into the Q-AMS ( $2.0\text{ cm}^3\text{s}^{-1}$ ) is higher than the flow rate into the ToF-AMS ( $1.4\text{ cm}^3\text{s}^{-1}$ ), causing 43 % more aerosol mass per time to reach the vaporiser. This results in improved counting statistics which in turn results in about 20 % lower detection limits. In other words, if the Q-AMS was also operated with a  $100\text{ }\mu\text{m}$  critical orifice, the  $LOD_{exp}$  would be about 20 % higher than the  $LOD_{exp}$  determined with the  $130\text{ }\mu\text{m}$  critical orifice. The Q-AMS  $LOD_{exp}$  would then on average be larger by a factor of 11 rather than by a factor of 9, exactly the factor that was calculated by only accounting for the differences in ion duty cycle.

Even though this is only an approximation which only takes the major effects contributing to the ion transmission efficiency into account, it gives a reasonable explanation for the differences in the determined Q-AMS and ToF-AMS  $LOD_{exp}$ .

As shown in the previous paragraphs, an estimate of  $LOD$  levels can also be obtained by accounting for variations in the background signal that are caused by counting statistics and single ion signal intensity distribution only. The  $LOD_{stat}$  given in Table 3.6 have been calculated using this approach (Equation (3.67)). As the  $LOD_{stat}$  do not account for all effects which contribute to the background variation (see before), they are expected to be lower than (or equal to) the  $LOD_{exp}$ . For the Q-AMS  $LOD_{stat}$  this is the case for sulphate, ammonium, organics and nitrate, whereas the  $LOD_{stat}$  for chloride is slightly higher than the  $LOD_{exp}$  but still within the uncertainty of the calculation. The ToF-AMS  $LOD_{stat}$  are almost equal for sulphate, chloride, nitrate and organics. Only the  $LOD_{stat}$  for ammonium are higher than the  $LOD_{exp}$ .

In summary, the  $LOD_{stat}$  are a good estimate of the minimum possible detection limits (e.g. during a field campaign), as long as one is aware that reduced ion counting statistics are not the only contribution to instrument background variation and that the real detection limits might be slightly higher than the  $LOD_{stat}$ .

While the mass concentrations of the various species are calculated from the sum of the associated  $m/z$  (see Equation (3.32)), the  $LOD$  of the individual  $m/z$  contribute non-linearly to the total  $LOD$  of the species. In order to find out to which extent the individual  $m/z$  contribute to the detection limits of the different species,  $LOD$  values for every  $m/z$  resulting in ‘mass spectra’ of detection limits have been calculated from the filter measurements (shown in Figure 3.29).

As already expected from the  $LOD_{exp}$  of the various species given before, the ToF-AMS  $LOD$  are much lower than the Q-AMS  $LOD$ . This difference becomes larger with increasing  $m/z$ . While the ToF-AMS  $LOD$  on average decrease with increasing  $m/z$ , the Q-AMS  $LOD$  stay more or less constant (except from the peaks with high background intensity). This behaviour has two main reasons: As explained above the ToF-AMS duty cycle increases with increasing  $m/z$ , favouring reduced detection limits. In addition, the ToF-AMS effectively reduces electronic noise by rejecting all signals below a certain threshold value. This is not the case for the Q-AMS such that the influence of electronic noise dominates more and more the total noise as ion signal intensities decrease with increasing  $m/z$ . The highest  $LOD$  values for both instruments are found at  $m/z$  with typically high background signal intensities, resulting in larger background variations. Those are fragments for example from water (e.g.  $m/z$  16, 17, 18), air (e.g.  $m/z$  28, 32, 40, 44) and potassium ( $m/z$  39 and 41). The high  $LOD$  values at  $m/z$  182, 183, 184 and 186 can be attributed to tungsten which is constantly emitted from the vaporiser and always contributes to the background signal.

The *LOD* ‘mass spectra’ derived from the measurements with filtered air again show that species which fragment at  $m/z$  with typically high background signal intensities have high detection limits (e.g. ammonium which fragments on  $m/z$  with high background from air and water). Species which fragment on a large number of  $m/z$  also have high detection limits, because the *LOD* of the individual  $m/z$  all contribute to the species’ *LOD* (e.g. organics). This effect is even larger for the Q-AMS detection limits, as the *LOD* do not decrease with increasing  $m/z$ .

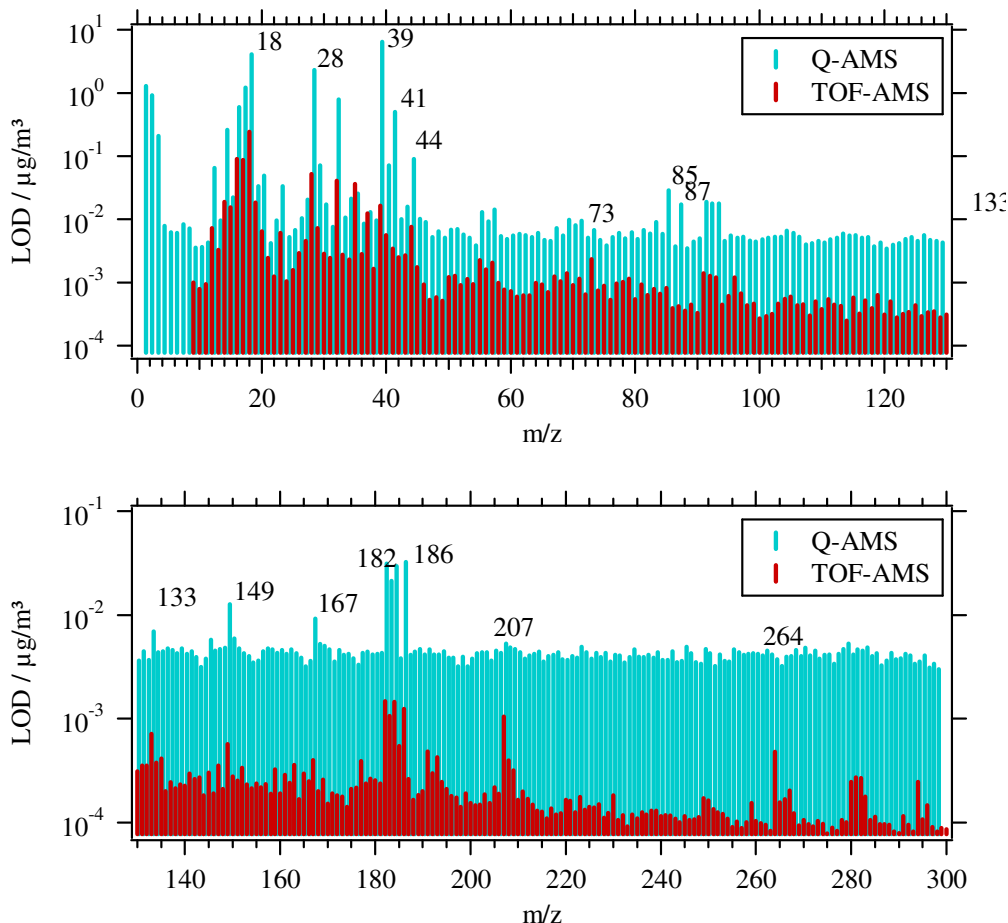


Figure 3.29: Detection limits of individual  $m/z$ , experimentally determined from 30 seconds blank measurements for Q-AMS (blue) and ToF-AMS (red). The  $m/z$  with the highest detection limits are labelled. Note, that the detection limits for the different species (as given in Table 3.6) are calculated from the background variation of that species and are not simply the sum of the *LOD* of the corresponding  $m/z$ .

### Variation of aerosol beam-to-background measurement ratio

The chopper open-to-blocked ratio  $CR$ , which determines the fraction of the total measuring time that is spent measuring the aerosol beam, is set typically to 50 %. In other words, the time spent measuring the aerosol beam signal  $I_o$  is equal to the time spent measuring the instrument background signal  $I_b$ . As mentioned before, in this case the standard deviations of the two signals,  $\sigma_o$  and  $\sigma_b$ , are equal and the detection limit can be determined as three times the standard deviation of the background signal  $I_b$ . The question is if it is possible to lower the instrument *LOD* by variation of the chopper open-to-closed ratio, for example by

spending more time (more than 50 %) measuring the aerosol beam. These considerations were carried out only with the ToF-AMS since its data acquisition software allows an easy change of the *CR*. However, the discussion here also holds for Q-AMS instruments.

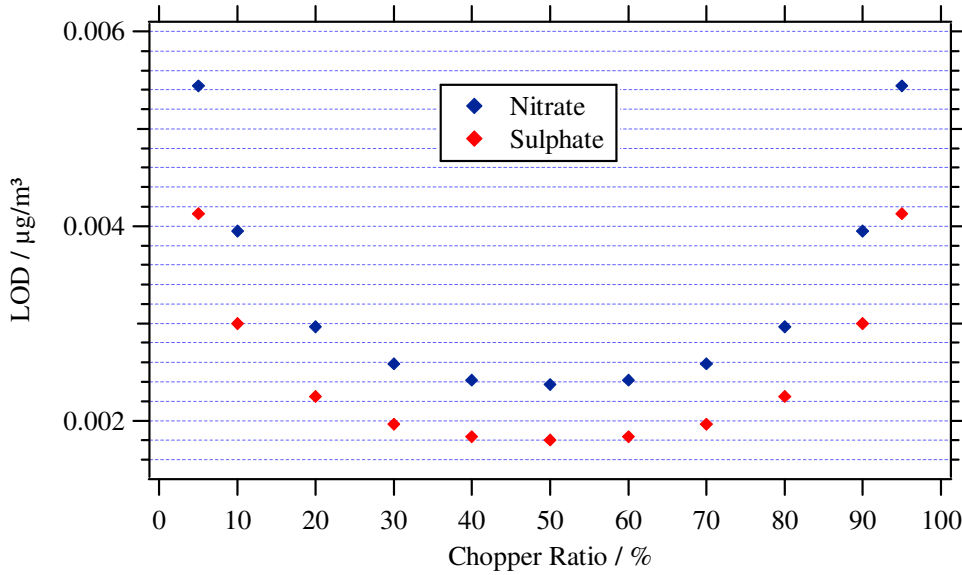


Figure 3.30: ToF-AMS nitrate and sulphate detection limits which would result from measurements with  $CR \neq 50\%$  as calculated from the  $LOD_{exp}$  measured at  $CR = 50$ .

Measuring with a *CR* other than 50 % means that the time  $t_{s,b}$  spent measuring  $I_b$  is no longer equal to the time  $t_{s,o}$  spent measuring  $I_o$ . Since the dominating source of noise for these measurements, counting statistics, scales with  $1/\sqrt{t_s}$ , the standard deviations of the two measurements  $\sigma_o$  and  $\sigma_b$  will no longer be equal and the standard deviation  $\sigma$  which determines the detection limit needs to be calculated as the geometric mean of  $\sigma_o$  and  $\sigma_b$  (Equation (3.71))

$$\sigma = \sqrt{\frac{\sigma_o^2 + \sigma_b^2}{2}} \quad (3.71)$$

When measuring for example at a *CR* of 80 % (80 % of the time spent measuring the aerosol beam, 20 % spent measuring the background),  $\sigma_o$  will be decreased and  $\sigma_b$  will be increased with respect to the standard deviation  $\sigma$  at *CR* = 50 %:

$$\begin{aligned} \sigma_o &= \sigma(CR = 80\%) = \sigma(CR = 50\%) \cdot \sqrt{\frac{50}{80}} \\ \sigma_b &= \sigma(CR = 20\%) = \sigma(CR = 50\%) \cdot \sqrt{\frac{50}{20}} \end{aligned} \quad (3.72)$$

In other words, the detection limits which result from a measurement with  $CR \neq 50\%$  can be calculated from the  $LOD_{exp}$  which were measured at  $CR = 50\%$ . This was done for the ToF-AMS filter data and the results for nitrate and sulphate are given in Figure 3.30. The *LOD* increase symmetrically around  $CR = 50\%$ . The increase lies between 2 % at  $CR = 60$  and 40 % and 130 % at  $CR = 95$  and 5 %. The absolute values are still quite small, but nevertheless

these results show that the lowest  $LOD$  is achieved at a chopper open-to-blocked ratio  $CR$  of 50 %, and any deviation from this ratio results in an increase in detection limit. The resulting decrease in the aerosol measurement uncertainty obtained by spending more time measuring the aerosol beam is more than compensated by the increased uncertainty of the blank measurement due to the shorter time spent measuring the instrument background.

### 3.4.4 Measurement at Elevated Mass Concentrations

Measurements of detection limits were performed also at elevated mass concentrations of ammonium nitrate and ammonium sulphate to investigate the influence of the mass loading of a certain species on the  $LOD$  of this species and of other species (cross-sensitivity).

The results from the measurements with constant elevated ammonium nitrate mass concentrations are given in Table 3.7 and Figure 3.31. In order to simplify matters, only the nitrate mass concentrations are specified. Additionally to the experimentally determined Q-AMS and ToF-AMS detection limits ( $LOD_{exp}$ ) also the detection limits estimated from ion counting statistics ( $LOD_{stat}$ ) are given in Table 3.7.

Nitrate Mass Concentration	$LOD_{exp}, \mu\text{g}/\text{m}^3$									
	Nitrate		Sulphate		Ammonium		Chloride		Organics	
	Q-AMS	TOF-AMS	Q-AMS	TOF-AMS	Q-AMS	TOF-AMS	Q-AMS	TOF-AMS	Q-AMS	TOF-AMS
0.3 $\mu\text{g}/\text{m}^3$	0.018	0.003	0.024	0.004	0.114	0.026	0.026	0.01	0.333	0.034
7 $\mu\text{g}/\text{m}^3$	0.053	0.004	0.045	0.005	0.143	0.025	0.044	0.005	0.448	0.03
20 $\mu\text{g}/\text{m}^3$	0.076	0.018	0.054	0.009	0.151	0.047	0.049	0.008	0.456	0.081
80 $\mu\text{g}/\text{m}^3$	0.123	0.087	0.058	0.095	0.117	0.51	0.062	0.025	0.54	0.16

Nitrate Mass Concentration	$LOD_{stat}, \mu\text{g}/\text{m}^3$									
	Nitrate		Sulphate		Ammonium		Chloride		Organics	
	Q-AMS	TOF-AMS	Q-AMS	TOF-AMS	Q-AMS	TOF-AMS	Q-AMS	TOF-AMS	Q-AMS	TOF-AMS
0.3 $\mu\text{g}/\text{m}^3$	0.022	0.004	0.02	0.002	0.087	0.036	0.028	0.01	0.178	0.023
7 $\mu\text{g}/\text{m}^3$	0.056	0.004	0.037	0.004	0.137	0.039	0.056	0.009	0.305	0.023
20 $\mu\text{g}/\text{m}^3$	0.078	0.006	0.042	0.005	0.123	0.048	0.06	0.009	0.314	0.024
80 $\mu\text{g}/\text{m}^3$	0.12	0.011	0.049	0.013	0.131	0.064	0.068	0.011	0.343	0.029

Table 3.7: Limits of Detection ( $LOD$ ) of Q-AMS and ToF-AMS, derived from measurements with different constant concentrations of ammonium nitrate. Only the nitrate mass concentration is given in the table. The  $LOD_{exp}$  are also shown in Figure 3.31.

As expected, the  $LOD_{exp}$  of nitrate and ammonium increase with increasing ammonium nitrate mass concentrations for both Q-AMS and ToF-AMS. The fact that the experimentally determined detection limits  $LOD_{exp}$  increase with increasing ammonium nitrate mass concentrations for all species and in both instruments shows that detection limits determined via measurements with filtered air are the minimum possible detection limits which are only realistic for a clean instrument background. Also noticeable is that not only the  $LOD_{exp}$  of ammonium and nitrate increase with increasing ammonium nitrate mass concentrations, but also the  $LOD_{exp}$  of the other species, which shows that there is a certain cross-sensitivity

between the different species. This means that increasing the mass concentration of one species does not only affect its own *LOD* but also the *LOD* of other species. This effect can be explained by the contribution of fragments of one species to fragmentation peaks of another species, resulting in increased background variation of these peaks. As a consequence also the *LOD* of the other species will increase.

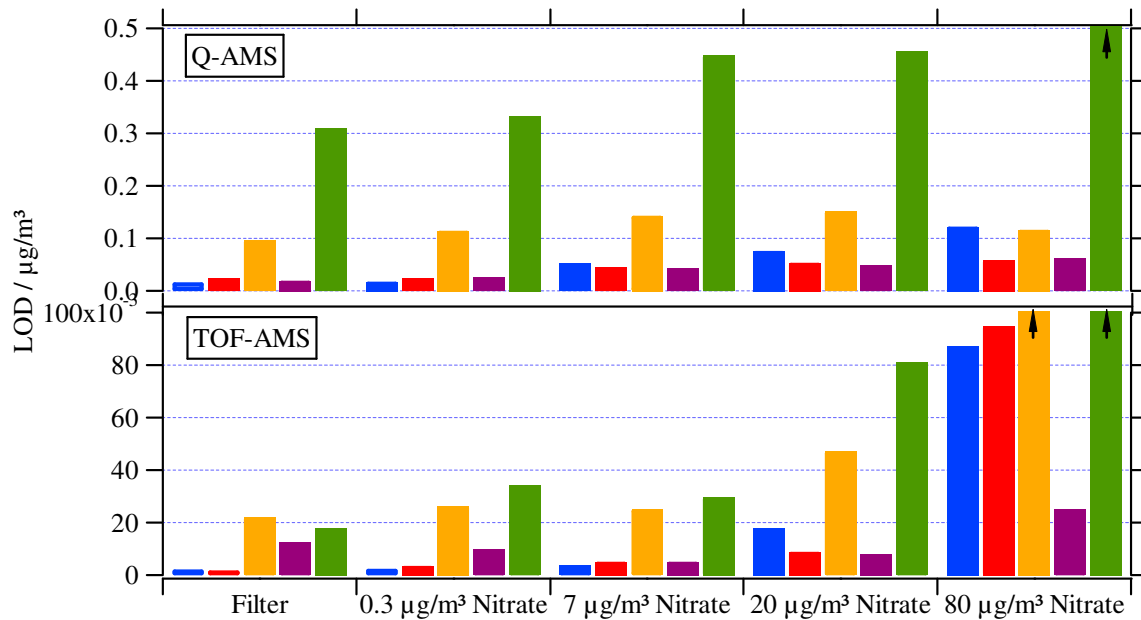


Figure 3.31: Limits of Detection ( $LOD_{exp}$ ) of Q-AMS and ToF-AMS, derived from measurements with different constant concentrations of ammonium nitrate. Only the nitrate mass concentration is given in the axis label. Detection limits are shown in green for organics, in yellow for ammonium, in purple for chloride, in red for sulphate and in blue for nitrate.

In order to quantify the increase in  $LOD_{exp}$ , a linear relationship between the  $LOD_{exp}$  and the aerosol mass concentration was assumed, where the  $LOD$  at zero aerosol mass concentration is equal to the  $LOD_{exp}$  determined from filter measurements. Based on this assumption the absolute (in  $\text{ng m}^{-3}$ ) and relative (in %) increase in  $LOD_{exp}$  per  $\mu\text{g m}^{-3}$  increase in aerosol mass concentration was calculated for all species (Table 3.8). For nitrate, sulphate, chloride and organics  $LOD$  the increase in nitrate mass concentrations was used for this calculation, whereas for the ammonium  $LOD$  the increase in ammonium concentrations was used.

The relative increase in the ToF-AMS  $LOD_{exp}$  (per  $\mu\text{g m}^{-3}$  increase in aerosol mass concentration) is 44 % for nitrate, 86 % for ammonium, 8 % for chloride, 10 % for organics and 61 % for sulphate. This indicates a significant cross-sensitivity between nitrate and sulphate, which is caused by the contribution of a nitrate fragment to a major sulphate fragment ( $m/z$  48). Chloride and organics show only minor cross-sensitivities to nitrate. Nevertheless, as the absolute increase in the ToF-AMS detection limits due to increased mass concentrations is very low ( $0.1 - 19 \text{ ng m}^{-3}/\mu\text{g m}^{-3}$ ), this will not have a limiting effect on measurements at ambient conditions. However, during certain conditions (e.g. in laboratory measurements) this could be the case.

	absolute ( $\text{ng m}^{-3}/\mu\text{g m}^{-3}$ )		relative (%/ $\mu\text{g m}^{-3}$ )	
	Q-AMS	TOF-AMS	Q-AMS	TOF-AMS
<b>Nitrate</b>	2	1	9	44
<b>Sulphate</b>	1	1	2	61
<b>Ammonium</b>	2	19	2	86
<b>Chloride</b>	1	0.1	3	8
<b>Organics</b>	5	2	1.4	10

Table 3.8: Absolute and relative increase in  $LOD_{exp}$  per  $\mu\text{g m}^{-3}$  increase in ammonium aerosol mass concentration. The absolute increase is given in  $\text{ng m}^{-3}$ , the relative increase is given in % per  $\mu\text{g m}^{-3}$ .

While the measured absolute increases in the Q-AMS  $LOD_{exp}$  ( $1 - 5 \text{ ng m}^{-3}/\mu\text{g m}^{-3}$ ) are in the same order of magnitude as those measured for the ToF-AMS, the relative increases are much lower due to the approximately 10 times higher  $LOD$  levels in the Q-AMS, compared to the ToF-AMS. The relative increase in the Q-AMS  $LOD_{exp}$  per  $\mu\text{g m}^{-3}$  increase in the aerosol mass concentrations is 9 % for nitrate, 2 % for ammonium, 2 % for sulphate, 3 % for chloride and 1 % for organics, which is significantly lower than for the ToF-AMS and shows no indication of significant cross-sensitivities between the LOD of a species and the aerosol mass concentration of other species. Therefore cross-sensitivity and resulting  $LOD$  increase as a consequence of high aerosol concentrations of other species can typically be neglected for the Q-AMS.

The detection limits  $LOD_{stat}$  estimated from ion counting statistics are given in the lower panel of Table 3.7 for the measurements with elevated ammonium nitrate mass concentrations. While the Q-AMS  $LOD_{stat}$  agree quite well with the corresponding  $LOD_{exp}$  (with the exception of the organics  $LOD_{stat}$  which is by a factor of approximately 2 lower), the ToF-AMS  $LOD_{stat}$  do not reflect the increase in the detection limits which can be seen in the  $LOD_{exp}$ , especially not for the  $80 \mu\text{g m}^{-3}$  concentration. One of the reasons for this can be found in the calculation of the  $LOD_{stat}$  which are determined from the calculated average species' signal intensities and not from the variation of the whole  $m/z$  ion signal. Therefore cross-sensitivities between the different species are not included in the  $LOD_{stat}$ . For the Q-AMS, where there are no significant cross-sensitivities, the  $LOD_{stat}$  fit very well to the  $LOD_{exp}$ . In summary, the  $LOD_{stat}$  are a good estimate of detection limits during 'real world' measurements, where mass concentrations will not show extreme concentration ratios (i.e. a very high concentration of one species and at the same time a very low concentration of another species), such that cross-sensitivity does not play a significant role. On the other hand, during laboratory measurements with very high mass concentrations of one species and at the same time very low mass concentrations of another species, the  $LOD_{stat}$  should not be used to determine detection limits.

In addition to the measurements with ammonium nitrate, measurements of detection limits at elevated ammonium sulphate concentrations have also been performed. The results from these measurements are shown in Table 3.9 and Figure 3.32. Here only the sulphate mass concentrations are specified in order to simplify matters.

The  $LOD_{exp}$  of sulphate and ammonium increase with increasing ammonium sulphate mass concentrations. As already seen for the ammonium nitrate measurements, the  $LOD_{exp}$  of most of the other species also increase with increasing sulphate mass concentration. The absolute and relative increase in  $LOD_{exp}$  are given in Table 3.10. The relative increase in the ToF-

AMS  $LOD_{exp}$  (per  $\mu\text{g m}^{-3}$  increase in aerosol mass concentration) is ~390 % for sulphate, 9 % for ammonium, 1.5 % for nitrate and 33 % for organics. Significant cross-sensitivity can only be seen between sulphate and organics, which is caused by the contribution of almost all sulphate fragments to the organics fragments at the same  $m/z$ . Chloride and nitrate do not show any significant cross-sensitivities to sulphate. Here again, the absolute increase in the ToF-AMS detection limits is very low ( $0.04 - 7 \text{ ng m}^{-3}/\mu\text{g m}^{-3}$ ).

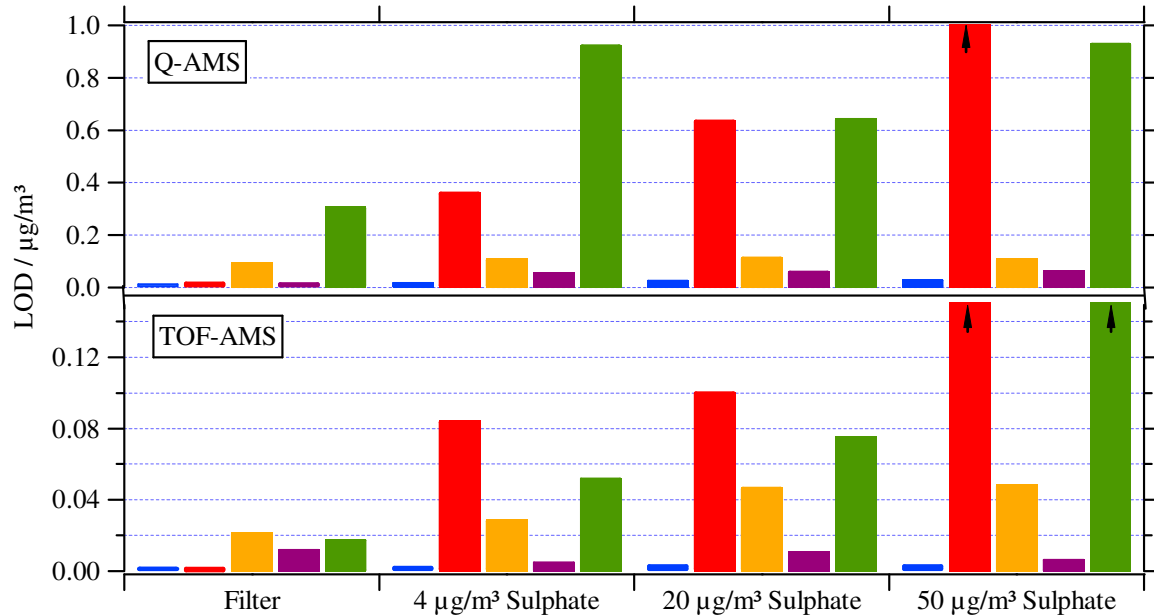


Figure 3.32: The same as Figure 3.31, but derived from measurements with different constant concentrations of ammonium sulphate. Only the sulphate mass concentration is given in the axis label.

Sulphate Mass Concentration	$LOD_{exp}, \mu\text{g/m}^3$									
	Nitrate		Sulphate		Ammonium		Chloride		Organics	
	Q-AMS	TOF-AMS	Q-AMS	TOF-AMS	Q-AMS	TOF-AMS	Q-AMS	TOF-AMS	Q-AMS	TOF-AMS
4 $\mu\text{g/m}^3$	0.021	0.003	0.366	0.085	0.112	0.029	0.058	0.006	0.928	0.053
20 $\mu\text{g/m}^3$	0.029	0.004	0.64	0.101	0.118	0.047	0.063	0.012	0.647	0.076
50 $\mu\text{g/m}^3$	0.031	0.004	1.761	0.361	0.113	0.049	0.066	0.007	0.934	0.337

Sulphate Mass Concentration	$LOD_{stat}, \mu\text{g/m}^3$									
	Nitrate		Sulphate		Ammonium		Chloride		Organics	
	Q-AMS	TOF-AMS	Q-AMS	TOF-AMS	Q-AMS	TOF-AMS	Q-AMS	TOF-AMS	Q-AMS	TOF-AMS
4 $\mu\text{g/m}^3$	0.023	0.004	0.207	0.012	0.082	0.04	0.055	0.008	0.192	0.021
20 $\mu\text{g/m}^3$	0.034	0.004	0.426	0.024	0.109	0.043	0.081	0.01	0.327	0.023
50 $\mu\text{g/m}^3$	0.046	0.005	0.857	0.044	0.155	0.051	0.071	0.01	0.49	0.024

Table 3.9: Limits of Detection ( $LOD$ ) of Q-AMS and ToF-AMS, derived from measurements with different constant concentrations of ammonium sulphate. Only the sulphate mass concentration is given in the table. The results for  $LOD_{exp}$  are also shown in Figure 3.32.

The relative increase in the Q-AMS  $LOD_{exp}$  per  $\mu\text{g m}^{-3}$  increase in the sulphate mass concentrations is 145 % for sulphate, 1 % for ammonium, 2 % for nitrate, 6 % for chloride and 4 % for organics. No significant cross-sensitivities between any other species and the sulphate or ammonium mass concentration can be found. Again, the ToF-AMS  $LOD_{exp}$  are more sensitive to changes in mass concentration than the Q-AMS  $LOD_{exp}$ . Similar to the  $LOD_{stat}$  determined from the ammonium nitrate measurements, the Q-AMS and ToF-AMS  $LOD_{stat}$  fit quite well, as long as effects other than limited counting statistics (like cross-sensitivity) do not play a significant role. The  $LOD_{stat}$  are too low for Q-AMS and ToF-AMS sulphate and organics and fit well for the other species.

	absolute ( $\text{ng m}^{-3}/\mu\text{g m}^{-3}$ )		relative (%/ $\mu\text{g m}^{-3}$ )	
	Q-AMS	TOF-AMS	Q-AMS	TOF-AMS
<b>Nitrate</b>	0.4	0.04	2	1.5
<b>Sulphate</b>	35	7	145	387
<b>Ammonium</b>	1	2	1	9
<b>Chloride</b>	1	-	6	-
<b>Organics</b>	13	6	4	33

Table 3.10: Absolute and relative increase in  $LOD_{exp}$  per  $\mu\text{g m}^{-3}$  increase in aerosol mass concentration. The absolute increase is given in  $\mu\text{g m}^{-3}$ , the relative increase is given in % per  $\mu\text{g m}^{-3}$ .

### 3.4.5 Background Perturbation Experiments

For the background perturbation experiments a high mass concentration of ammonium nitrate, ammonium sulphate or PSL aerosol was introduced into the AMS in order to increase the instrument background. Abruptly thereafter filtered air was measured and the detection limits were determined as a function of time. The calculation of the  $LOD_{exp}$  is not as straight forward as for the measurements with constant aerosol mass concentration, as in addition to the natural background variation a decrease in the background signal level is given because of the change from high aerosol mass concentrations to filter measurements. The detection limit  $LOD^*$  determined from the standard deviation in a sliding window of 5 minutes background measurements (10 measurements at 30 second averaging time) is therefore biased towards higher values due to the background level change within this time window. The real  $LOD_{exp}$  for every time step  $t$  can be approached from  $LOD^*$  using the following relationship:

$$LOD_{exp}(t) = N \cdot LOD^*(t) - \sum_{i=t+1}^{t+N} LOD(i) \quad (3.73)$$

with  $N$  the number of background measurements from which the  $LOD^*$  was calculated. This equation can be solved iteratively backwards from the end of the measurement, assuming that at this time (after 1.5 hours) the  $LOD^*$  equals the  $LOD_{exp}$ , because no further change of background signal intensity is observed anymore. Figure 3.33 shows the time series of  $LOD_{exp}$  of ToF-AMS sulphate determined from the PSL perturbation experiment.

From the determined decrease in the  $LOD_{exp}$  the time in seconds after which the  $LOD_{exp}$  had decreased to 1/e of the  $LOD_{exp}$  at the high mass concentration was calculated by fitting an

exponential function to the  $LOD_{exp}$  time series. Since this time constant  $\tau_s$  is a measure how fast the instrument background is reduced by removal of the background ion signal it will be called the ‘self-cleaning’ time constant for the detection limits. The self-cleaning time constants extracted from these measurements are given in Table 3.11. Where no values are given, it was not possible to fit an exponential function to the  $LOD_{exp}$  time series either because of an only slow decrease in the  $LOD_{exp}$  with time (because it did not increase significantly while measuring at the high mass concentration), or because of very high noise in the  $LOD_{exp}$  time series. For the Q-AMS it was only possible to obtain values for the  $150 \mu\text{g m}^{-3}$  nitrate and the  $100 \mu\text{g/m}^3$  sulphate experiment. The nitrate  $LOD_{exp}$  has the smallest self-cleaning time constants with 11 seconds in the nitrate experiment and 16 seconds in the sulphate experiment; with 304 seconds the highest time constant was found for organics during the nitrate experiment.

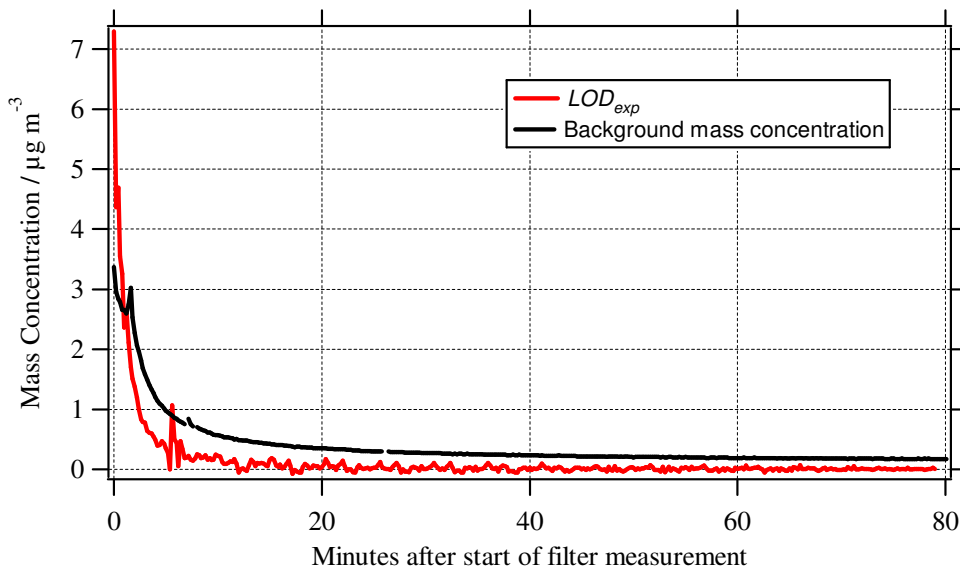


Figure 3.33: Time series of the ToF-AMS sulphate limit of detection, derived from the background perturbation experiment with  $200 \mu\text{g m}^{-3}$  polystyrene latex.

The other self-cleaning time constants which could be determined lie between 30 seconds and 2 minutes. The highest self-cleaning time constants in the ToF-AMS could be found for ammonium (109 – 133 seconds) in the nitrate experiments. The other values lie with 20 – 82 seconds in a similar range as those for the Q-AMS.

The major conclusion that can be made from the available data is that the self-cleaning time constants of all species are small compared to those of typical changes of aerosol mass concentrations during ambient aerosol measurements. Since these changes mostly occur on timescales of tens of minutes to several hours, instrument history (expressing itself in increased background concentrations) will not have limiting effects on measurement detection limits. However, caution needs to be exercised under measurement conditions where rapidly changing air masses are probed as in aircraft or car chasing measurements. In addition, from the data in Table 3.11 the tendency of self-cleaning time constants to increase with increasing molecular weight of the species can be found. An exception from this tendency is ammonium, which largely depends on the self-cleaning time constants of the relatively sticky water molecules.

Mass Concentration / $\mu\text{g m}^{-3}$	Self-cleaning Time Constants, seconds									
	Nitrate		Sulphate		Ammonium		Chloride		Organics	
	Q-AMS	TOF-AMS	Q-AMS	TOF-AMS	Q-AMS	TOF-AMS	Q-AMS	TOF-AMS	Q-AMS	TOF-AMS
90 (Nitrate)	-	78	-	82	-	133	-	-	-	45
150 (Nitrate)	11	-	130	42	-	109	-	-	304	21
100 (Sulphate)	16	-	58	-	28	-	28	-	67	-
200 (Organics)	-	18	-	77	-	191	-	73	-	20

Table 3.11: Self-cleaning time constants (time after which the detection limit has decreased to 1/e of the detection limit at a high mass concentration of ammonium nitrate, ammonium sulphate, or PSL) of Q-AMS and ToF-AMS  $LOD_{exp}$ . Only the mass concentrations of nitrate, sulphate or organics are given.

### 3.4.6 Reduction of the Organics-related Detection Limits

As shown above the organics  $LOD$  are much higher than those related to the individual inorganic species. This is due to the large number of mass fragments contributing ion signals and also noise to the total organics signal. In order to investigate whether it is possible to reduce the organics  $LOD$  by using only a selection of mass fragments and correcting for the omitted fraction, the following tests have been performed with the ToF-AMS and Q-AMS filter data.

The organics  $LOD$  was calculated from the filter test data presented above using only different selections of mass fragments instead of all fragments. To determine the selection of these fragments, the  $m/z$  were first sorted in order of decreasing organics signal and decreasing organics signal-to-noise. Then increasing numbers of mass fragments were used for calculating the  $LOD$ , starting with only the mass fragment with the most intense signal, then the first two most intense signals and so on, until all organics mass fragments were used for this calculation. The same was made for the sorted signal-to-noise ratios and for the unsorted  $m/z$  (using the first organics-related peak, using the first two peaks and so on). For sorting of  $m/z$  the peak intensity and signal-to-noise information was taken from an average mass spectrum of semi-urban aerosol from a field campaign performed with the ToF-AMS. For individual applications of this method to improve organics  $LOD$  the average mass spectrum of the actual measurement has to be used to get information on how the ion signals should be sorted.

For each of the ion peak selections the  $LOD$  was calculated from the filter test data. These  $LOD$  were then multiplied by the ratio of the total organics ion current to the ion current of the selected peaks in order to account for omitted ion signals and to obtain total organics concentration. In Figure 3.34 the results for all these calculations are summarized. One can see that for different selections of mass fragments different  $LOD$  were obtained. The largest reduction in  $LOD$  was found when the mass fragments were sorted in order of decreasing signal-to-noise ratios and if the mass fragments with the 25 and the 24 most intensive signal-to-noise ratios were used for the  $LOD$  calculation of ToF-AMS and Q-AMS organics, respectively. For this selection a correction factor of 1.25 for the ToF-AMS and of 1.31 for the Q-AMS is needed to obtain total organics. This minimum achievable  $LOD$  is  $10.8 \text{ ng m}^{-3}$  for the ToF-AMS compared to a  $LOD$  of  $17.9 \text{ ng m}^{-3}$  when all ion signals are used and  $150 \text{ ng m}^{-3}$  compared to  $309 \text{ ng m}^{-3}$  for the Q-AMS. Thus a reduction of organics  $LOD$  by almost

a factor of two is possible for the ToF-AMS and by a factor of even more than 2 for the Q-AMS, using only a selection of ion signals to calculate total organics.

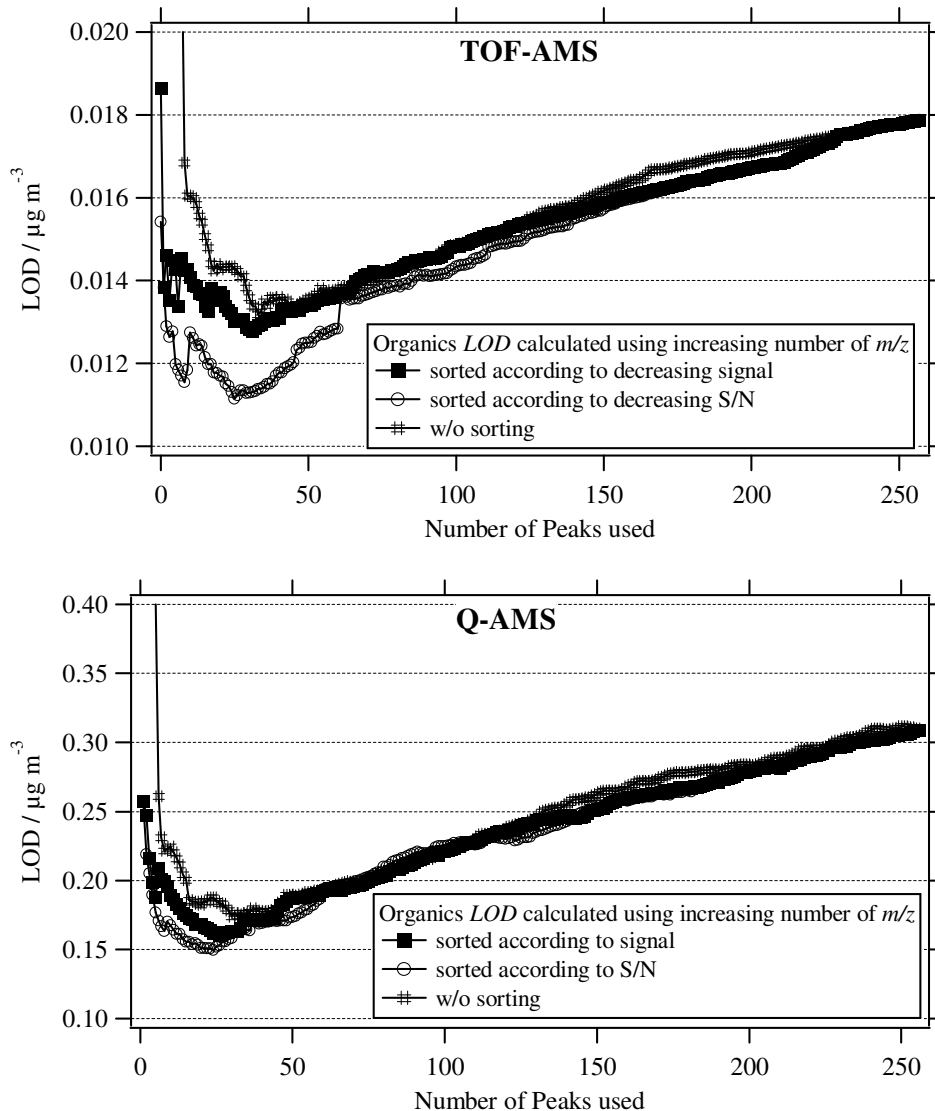


Figure 3.34: ToF-AMS (upper panel) and Q-AMS (lower panel) organics  $LOD_{exp}$  from filter data, calculated using an increasing number of selected  $m/z$ . In two cases (black squares and circles) the  $m/z$  were first sorted according to decreasing organics signal and decreasing signal-to-noise ratio, respectively. The lowest  $LOD$  is achieved using the first (25 for the ToF-AMS and 24 for the Q-AMS) peaks with highest signal-to-noise ratio.

Generally the detection limits of both analysers can be improved by increasing the measurement time  $t_s$ , because the dominating source of noise, counting statistics, scales with  $1/\sqrt{t_s}$ . The values given here were determined for  $t_s = 30$  s. Under typical field measurement conditions the AMS operates alternately in MS mode and P-ToF mode, measuring mass concentrations and species-resolved size distributions, respectively. Thus, for 5 or 10-minute saving intervals  $t_s$  increases to 150 or 300 s, resulting in  $LOD$  values that are lower by  $^{1/2}_{2.2}$  or  $^{1/3}_{3.2}$ , respectively. For one-hour time intervals  $LOD$  values would decrease by a factor of approximately 7.7. When time resolution should not be reduced, the only method of increasing  $t_s$  is increasing the ion duty cycle for the  $m/z$  that are most critical

for the measurement. In the Q-AMS this can be done by measuring the ion signal only at a selection of  $m/z$  that are the most prominent fragments of the species in question. A measurement mode that supports this is called ‘jump ms mode’ and is implemented in the current Q-AMS data acquisition software. In the ToF-AMS the ion duty cycle could be further increased by pulsing the mass spectrometer with higher frequency such that a larger fraction of the low  $m/z$  ions is extracted into the mass spectrometer. However, this has the consequence that the maximum  $m/z$  measured in the mass spectra is reduced. Therefore in both cases a reduction in  $LOD$  is only possible by giving up a fraction of the information in the mass spectra. Another way to reduce detection limits is by increasing the mass flow rate into the instrument by using a larger critical orifice. This again results in better counting statistics and therefore lower detection limits. Nevertheless, changing the size of the critical orifice might also alter the focusing abilities of the aerodynamic lens and therefore change the particle transmission efficiency (that is a function of particle size) into the instrument.

To summarise, all detection limits experimentally determined with the ToF-AMS are given in Table 3.12.

	Nitrate	Sulphate	Ammonium	Chloride	Organics
Filter	0.002	0.002	0.022	0.013	0.018
<b>Elevated Nitrate Mass Concentration</b>					
<b>0.3 <math>\mu\text{g}/\text{m}^3</math></b>	0.003	0.004	0.026	0.01	0.034
<b>7 <math>\mu\text{g}/\text{m}^3</math></b>	0.004	0.005	0.025	0.005	0.03
<b>20 <math>\mu\text{g}/\text{m}^3</math></b>	0.018	0.009	0.047	0.008	0.081
<b>80 <math>\mu\text{g}/\text{m}^3</math></b>	0.087	0.095	0.51	0.025	0.16
<b>Elevated Sulphate Mass Concentration</b>					
<b>4 <math>\mu\text{g}/\text{m}^3</math></b>	0.003	0.085	0.029	0.006	0.053
<b>20 <math>\mu\text{g}/\text{m}^3</math></b>	0.004	0.101	0.047	0.012	0.076
<b>50 <math>\mu\text{g}/\text{m}^3</math></b>	0.004	0.361	0.049	0.007	0.337

Table 3.12: Summary of the experimentally determined detection limits (30-sec averaging interval) for the ToF-AMS. Values are given in  $\mu\text{g m}^{-3}$ .

In order to exceed for example the minimum detection limit of nitrate (ammonium), the mass concentration provided by 3 (1100) ammonium nitrate particles of 100 nm diameter would be sufficient.

### 3.5 Size-dependent Mass Spectra

A unique feature of the ToF-AMS compared to the Q-AMS is its capability to provide size-dependent information for all  $m/z$  simultaneously. It is not only possible to extract mass size distributions of several species, but also whole mass spectra for every individual size bin in a PToF distribution (hereafter referred to as “size-dependent mass spectra”).

To demonstrate and further investigate this feature of the ToF-AMS, an external mixture of a polydisperse ammonium sulphate and a monodisperse ammonium nitrate aerosol has been generated in the laboratory as follows: One solution of ammonium nitrate in water and one solution of ammonium sulphate in water were each nebulised by an individual Constant Output Atomizer (TSI Inc., Model 3076) and the generated particles were subsequently dried with a diffusion dryer (TSI Inc., Model 3062). The ammonium nitrate particles were then size-classified by an Electrostatic Classifier (TSI Inc., Model 3080), whereas the ammonium sulphate aerosol remained polydisperse. Then the two aerosol flows were merged and introduced into the ToF-AMS and a CPC in parallel. The ToF-AMS was set to a general alternation mode, switching between MS and PToF mode every 10 seconds. The resulting size distributions for nitrate, sulphate, ammonium, chloride and organics, as measured in the PToF mode, are shown in Figure 3.35.

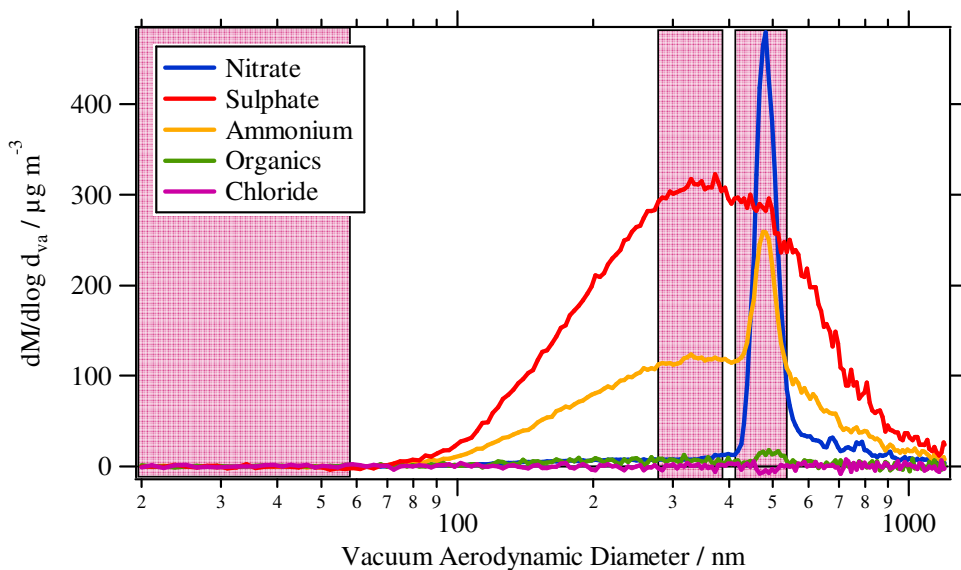


Figure 3.35: Mass size distributions of nitrate, sulphate, ammonium, chloride and organics of a laboratory-generated external mixture of polydisperse ammonium sulphate and monodisperse ammonium nitrate ( $d_{mob} = 350$  nm) aerosol.

As expected, the size distributions of chloride and organics are zero for almost all particle diameters. The exception of the organics size distribution for  $d_{va} = 480$  nm will be discussed later. The measured sulphate size distribution mirrors the polydisperse size distribution as generated by the atomiser, while in the ammonium size distribution the contribution from the monodisperse ammonium nitrate and the polydisperse ammonium sulphate aerosol can clearly be recognised. Finally, nitrate shows a monodisperse size distribution with a mode diameter of approximately  $d_{va} = 480$  nm, which corresponds to an electrical mobility

diameter of 350 nm. The shaded areas in Figure 3.35 represent three different diameter ranges with three different chemical compositions of the particles. For these diameter ranges, size-dependent mass spectra were calculated to give the chemical composition of the particles covering the specific size range.

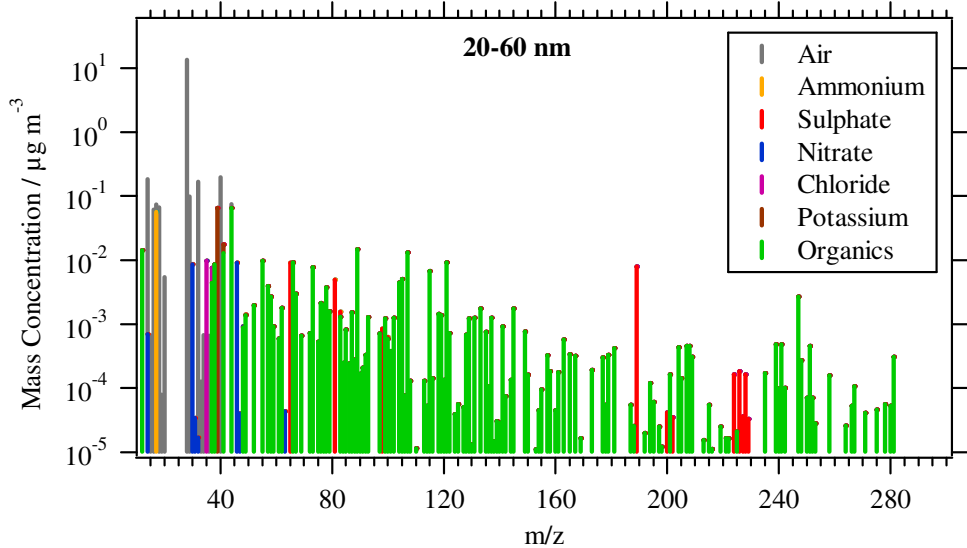


Figure 3.36: Average mass spectrum of the laboratory-generated aerosol for the size range 20-60 nm.

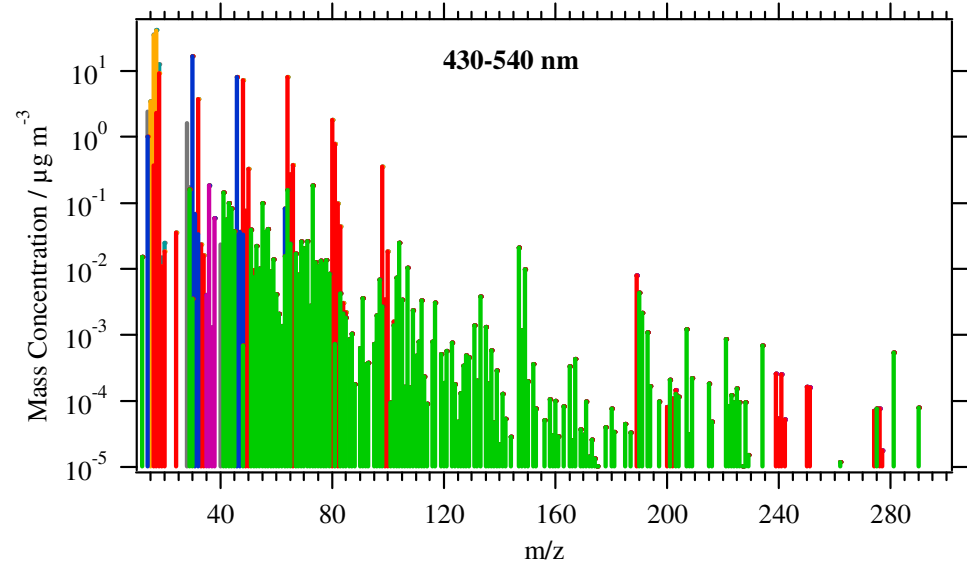


Figure 3.37: Average mass spectrum of the laboratory-generated aerosol for the size range 430-540 nm.

The resulting mass spectra for the size range 20-60 nm, where no particle signal was measured, and for the size range 430-540 nm, where a fraction of the ammonium sulphate and the whole ammonium nitrate distribution were measured, are shown in Figure 3.36 and Figure 3.37, respectively. They reflect very well the expected chemical composition of the generated aerosol and the differences in the different particle size ranges.

From these size-dependent mass spectra the amount of nitrate, sulphate, chloride and organics in the different size ranges was calculated. The results are shown in Figure 3.38.

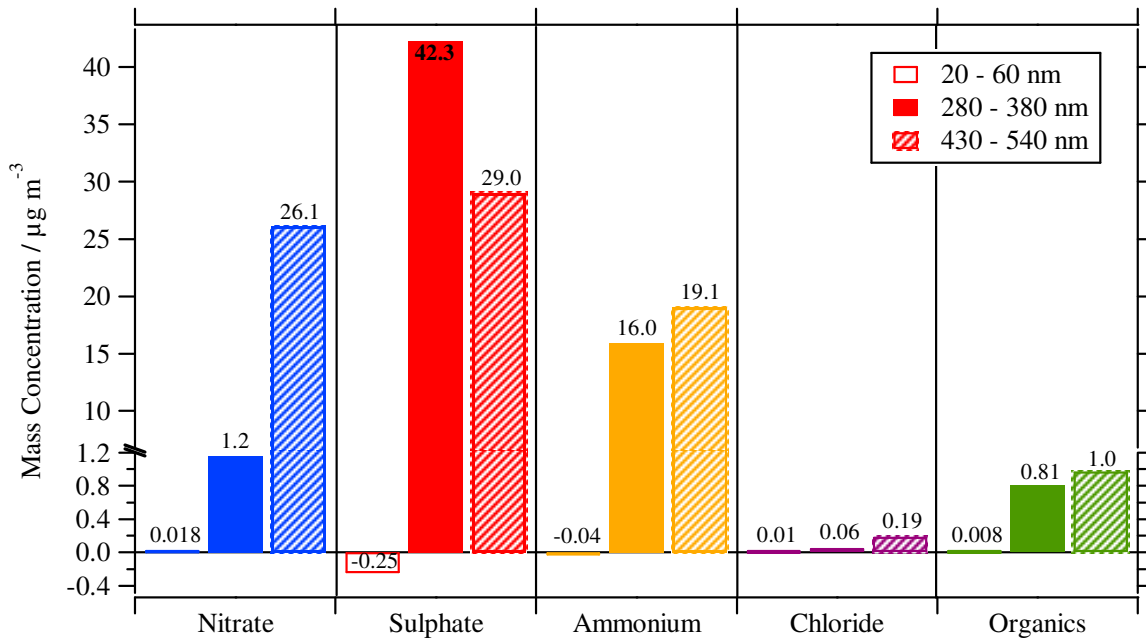


Figure 3.38: Mass concentrations of nitrate, sulphate, ammonium, chloride and organics in the three different size ranges (see Figure 3.35) of the laboratory-generated aerosol.

The mass concentrations are as expected, with almost zero concentration of all species in the small particles ( $d_{va} = 20-60 \text{ nm}$ ), almost only sulphate and ammonium in the intermediate size range ( $d_{va} = 280-380 \text{ nm}$ ) and an additional contribution of nitrate together with an increased fraction of ammonium in the large particles ( $d_{va} = 430-540 \text{ nm}$ ). Although there should not be a contribution of other species to the mass concentration of the aerosol, the mass concentrations of chloride and organics show maxima around the particle diameters where large nitrate and sulphate signal is found. This effect can be seen even more clearly in Figure 3.39, where the organics mass size distribution is shown on a better suited scale than in Figure 3.35. The organics distribution clearly follows the size distribution of the mixed ammonium nitrate/ammonium sulphate aerosol. The reason for this effect is that the PToF raw spectra were integrated by the data acquisition software without subtracting the mass spectrum baseline (see chapter 3.1.3), which varies with varying signal intensity of the peaks. The average difference raw spectrum of the generated aerosol is shown in Figure 3.40. This demonstrates that the MS baseline is not constant over the whole mass range but increases with increasing signal intensity. If this increased MS baseline is not subtracted when integrating the raw mass spectrum, the resulting signal of the affected  $m/z$  will be overestimated. As can also be seen in Figure 3.40, this affects not only the signal at  $m/z$  which cause the increase in baseline, but also at a few following  $m/z$ . For this reason, the mass concentrations of species not present in the aerosol might be overestimated and the detection limits of these species will be increased (see section 3.4.4 for details).

The effect does only play a minor role for the aerosol generated here and will even be less for ambient aerosol composition and mass concentrations, as the ratio of mass concentrations and therefore of the signal intensities at different species will be lower than here and the baseline influence will be only of minor importance.

However, it is currently worked on a procedure to reanalyse the PToF raw data and include an MS baseline subtraction in order to avoid such artefacts.

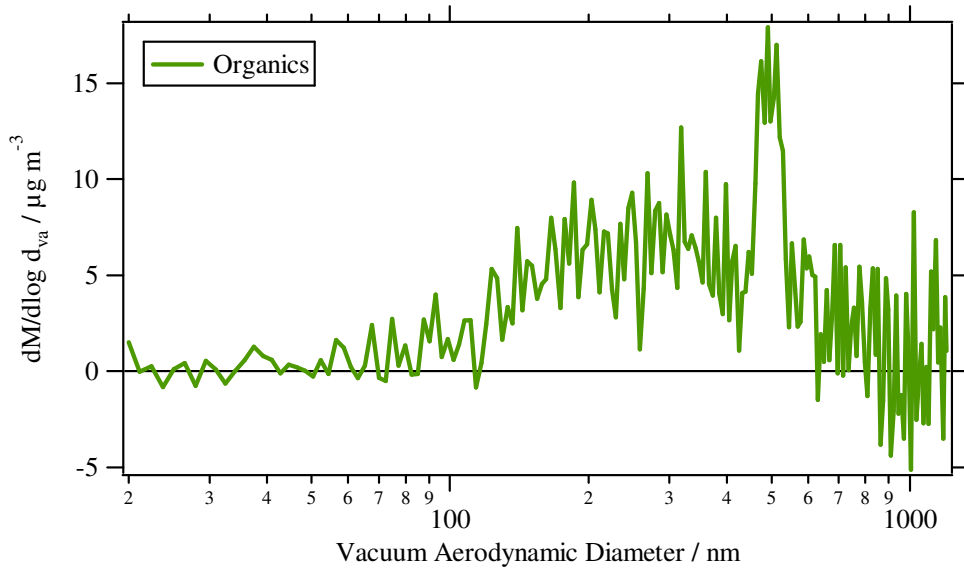


Figure 3.39: Mass size distribution measured for organics; even though the generated aerosol did not contain organics a small artificial organics signal is extracted from the mass spectra.

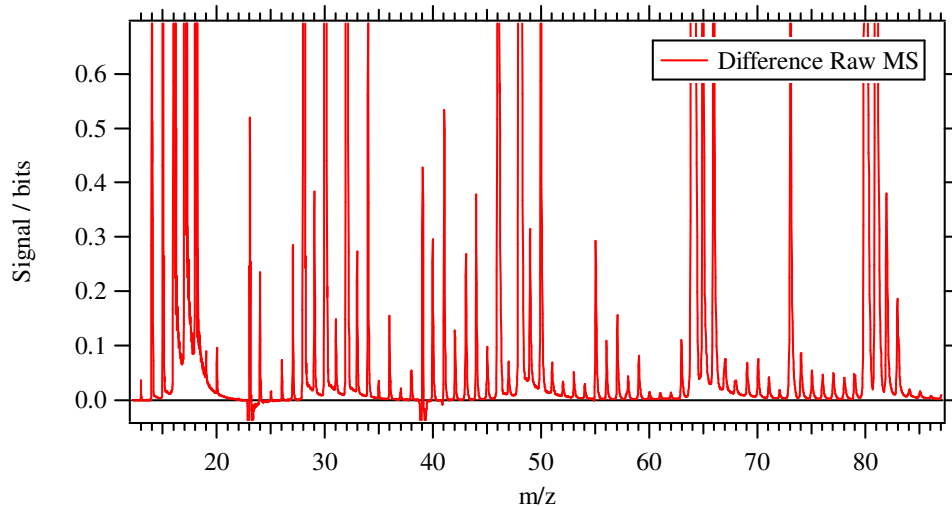


Figure 3.40: Average raw spectrum of the laboratory-generated aerosol (zooming around the baseline). The MS baseline is not of a constant level, but varies with varying peak signal intensities.

### 3.6 Data Analysis Software

As previously mentioned, the ToF-AMS used during this work was the prototype of the instrument, for which data analysis strategies or software did not exist when this work was started. The data analysis procedures and algorithms described in this chapter (0-3.3) were either developed or adopted from similar procedures for the Q-AMS and optimised for ToF-AMS data analysis within this thesis work. Even though large parts of the ToF-AMS analysis are similar to Q-AMS data analysis, it was not possible to use the existing data analysis toolkit developed by James Allan (Allan et al., 2003a; Allan et al., 2003b; Allan, 2004). For this reason, and because other groups started to use ToF-AMS instruments, it was soon necessary to write a data analysis software package capable of automated and systematic ToF-AMS data analysis and correction. The development of this data analysis software and implementation of the data processing and correction algorithm developed within this work (see Chapter 3) was a major part of this thesis.

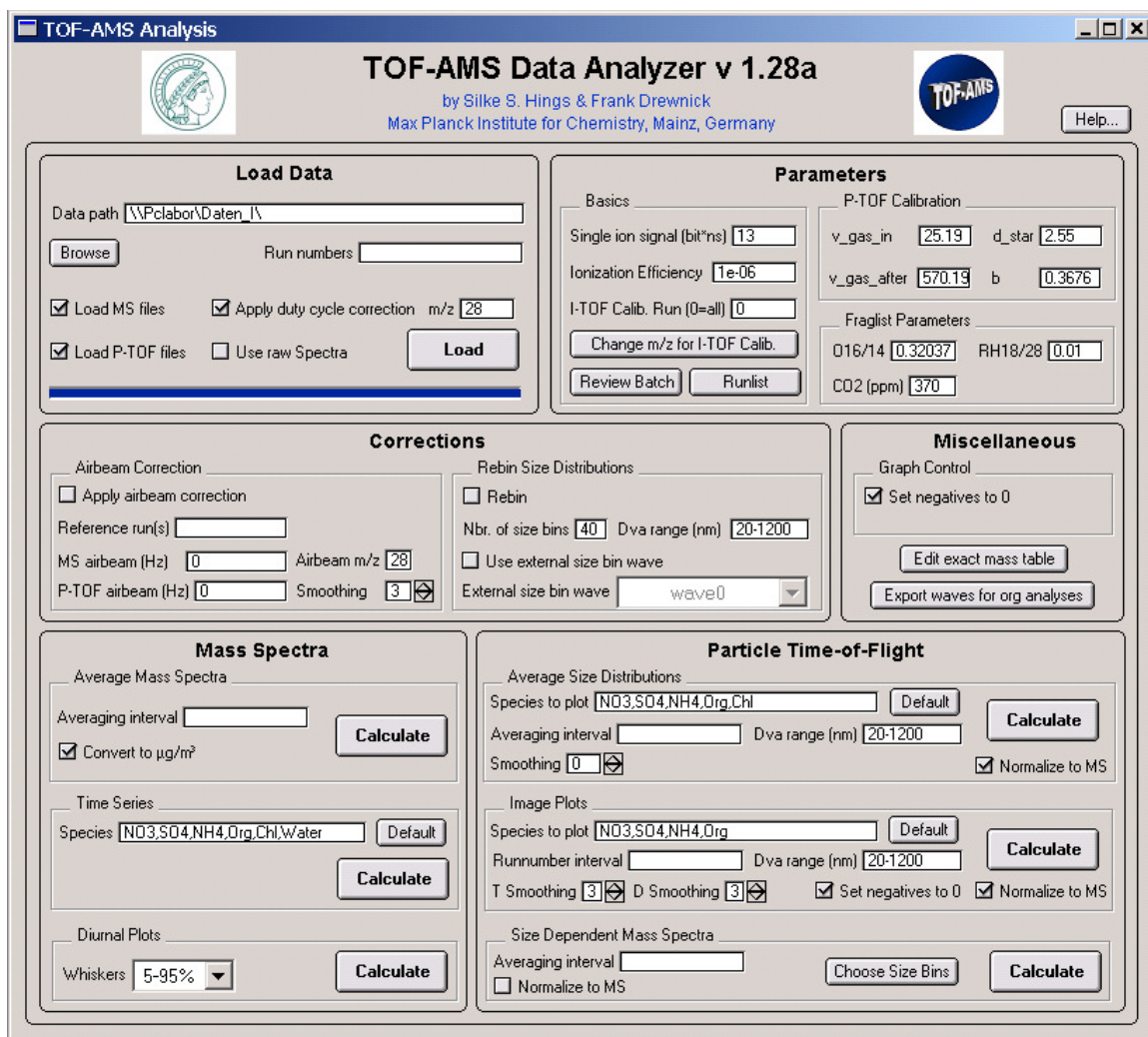


Figure 3.41: Screenshot of the ToF-AMS data analysis software panel developed during this work.

As up to now all AMS analysis has been performed using IGOR Pro (Wavemetrics Inc., Lake Oswego, OR, USA), all the analysis code developed here has also used this program as

platform. The analysis software produced can be used for processing of ambient field data as well as for laboratory studies. It automatically processes the raw data according to the analysis strategies presented in the previous sections of this chapter and applies any necessary calibration data and corrections. In addition, it displays the results in high quality graphs. However, it has also been designed around user customisation, so the corrections and application of techniques are user-definable, keeping it as flexible as possible. Figure 3.41 shows a screenshot of the developed ToF-AMS data analysis software panel.

The latest version of the code is posted together with a short manual on the internet and can be found at <http://cires.colorado.edu/jimenez-group/ToFAMSResources/>.

One of the major improvements of the ToF-AMS compared to the Q-AMS is its capability to provide size-dependent data for all  $m/z$ . This, however, means that the amount of data produced is enormous. For this reason, the ToF-AMS data acquisition and logging software was overworked to be capable of saving the data in HDF5 format (for information about HDF5 see <http://hdf.ncsa.uiuc.edu/HDF5/>). This data format allows to access raw data directly from the hard drive instead of loading everything into the memory. Therefore it is possible to process data for example of a whole campaign within one single IGOR experiment, which would not be possible using files in IGOR text file (itx) format as up to now.

The existing data analysis software developed during this work and described above only works for itx files and it was therefore necessary to develop a new data analysis toolkit. This is done in cooperation of groups from the University of Manchester, the University of Colorado at Boulder, Aerodyne Research Inc. and the Max Planck Institute for Chemistry in Mainz. This software tool combines (and extends) the data processing strategies and algorithms of the data analysis tool developed within this work with HDF5-based data handling and is not part of this work.



## 4 Field Deployment of the ToF-AMS

One of the main objectives of this work was to validate the ToF-AMS as a tool for quantitative measurements of the chemical composition as well as chemically resolved size distributions of the atmospheric aerosol. The ToF-AMS was deployed during various field campaigns since its first set-up in 2004. In this chapter, the first three of these campaigns are described. Since the main focus of this work is placed on engineering aspects of the ToF-AMS hardware and software and their characterisation, the field campaigns served the purpose of feasibility test. Therefore the meteorological situations of the campaigns will not be addressed in detail.

### 4.1 PMTACS-NY 2004 – First ToF-AMS Field Deployment

The PM<sub>2.5</sub> Technology Assessment and Characterisation Study – New York 2004 (PMTACS-NY 2004) was one of several US EPA “Supersites”, intended to provide enhanced measurement data on chemical and physical properties of particulate matter and its associated precursors. One of the primary objectives of this study was to test and evaluate recently developed aerosol measurement technologies like the ToF-AMS. It took place on the campus of Queens College in Queens, New York (40.74° N, 73.82° W, altitude ~25 m a.m.s.l.) from January 8<sup>th</sup>, 2004 until February 6<sup>th</sup>, 2004. The measurement site was located in a one-storey building next to parking lot #6 (shown in Figure 4.1).



Figure 4.1: Measurement site of the PMTACS-NY 2004 campaign. The inlet used by the aerosol mass spectrometers is indicated by the arrow.

The ToF-AMS was located in a room together with a Q-AMS, and both instruments shared a common inlet line. The inlet was at a height of 6.50 m above ground level, 1.50 m above the

roof of the building. The aerosol was pumped through a PM<sub>2.5</sub> cyclone (URG-2000-30EN) and 14 mm ID copper tubing at a flow rate of 10 l min<sup>-1</sup>. Inside the building the inlet line was covered with 2 cm thick foam tube insulation to reduce heating of the sample before extraction into the instruments. First the Q-AMS extracted its inlet flow (0.1 l min<sup>-1</sup>) from the total flow and several cm downstream of this sampling point the ToF-AMS extracted its inlet flow (also 0.1 l min<sup>-1</sup>). The total inlet line length from the cyclone to the inlet of the ToF-AMS was 7.60 m. Diffusion, settling and inertial losses of particles in the size range 25 nm up to 1 µm were estimated to be below 3 % for any size for this inlet line.

During the PMTACS-NY 2004 campaign the ToF-AMS was used for ambient aerosol measurements for the first time and a first version of the data acquisition software was written just before and improved during the campaign. Data processing software did not exist at this time and it was started to develop data analysis strategies during the campaign. Figure 4.2 shows a picture of the preliminary set-up of the ToF-AMS during the campaign, with the vacuum system and the mass spectrometer separated from the electronics rack.

The data collected by the ToF-AMS consists of many short-term time period fragments and calibration routines were not mature yet, resulting in relatively large uncertainties in the measured mass concentrations. However, the data clearly demonstrate the instruments' ability for sensitive aerosol composition and size distribution measurements.

During most of the campaign the instrument was controlled and the data were collected by a first version of a custom data acquisition software (written in C++), which controlled the movement of the chopper, the operation of the data acquisition board, the data transfer to the memory, first processing of the raw data, and the saving of the processed data to disk. The voltages of the ioniser and the TOFMS were set manually in a separate control software developed by Tofwerk (Thun, Switzerland). The filament current was set to 3.5 A, producing an electron emission current of approximately 2 mA, the pulsing time of the TOFMS was set to 12 µs and the particle chopper chopped the beam at a rate of approximately 125 Hz.

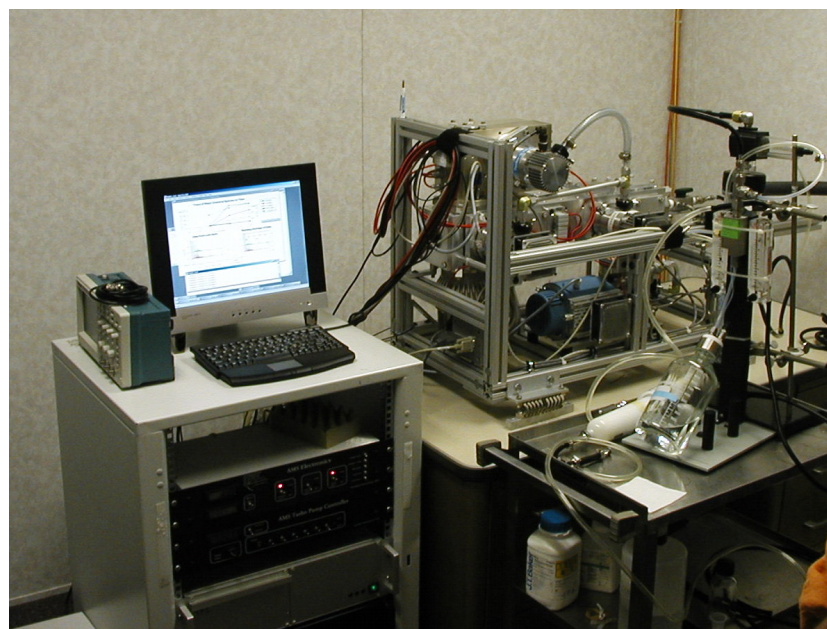


Figure 4.2: A Picture of the ToF-AMS set-up during PMTACS-NY 2004. As this was a preliminary set-up, the vacuum system and mass spectrometer (right) are separated from the electronics rack (left).

During the campaign a total of about 50 hours of only PToF mode data were collected, producing almost 7 GB of data. More than 112 hours of only MS mode data resulted in 0.16 GB of data, while measuring more than 65 hours in general alternation mode (switching between MS and PToF mode) resulted in 6.6 GB of data. In addition, single particle data were collected for 23,143 chopper cycles during 63 minutes of data collection, spread over five days of the campaign. These data represent a total measuring time of about 190 seconds, producing 2.4 GB of data.

In order to be able to convert the measured signals into mass concentrations and size distributions, a PToF calibration, an inlet flow calibration and an IE calibration were performed during the campaign. As it was not possible to average the CPC readings automatically during the IE calibration, this was done manually using a pocket calculator and averaging as many readings as possible within the averaging time interval of 5 minutes. Therefore the total uncertainty in the determined  $IE_{NO_3}$  is with more than 20 % quite high.

The data collected in the different modes of operation were processed separately according to the data analysis procedures described in chapter 3. The processing of and findings from the data collected in SPToF mode are described in Drewnick et al. (2005) and will not be discussed in detail here, as the characterisation and processing of ToF-AMS single particle data is subject of a forthcoming thesis and is therefore not part of this work. Here only a short summary of the results from the single particle data obtained during PMTACS-NY 2004 will be given. In addition, an extensive discussion of the measured mass concentrations and species-resolved size distributions from the co-located Q-AMS, and their association with sources can be found in Weimer et al. (2006).

## Results

The MS mode data were processed and converted into time series of mass concentrations. A direct comparison of ToF-AMS data with measurements performed with the co-located Q-AMS were performed to validate the capability of the ToF-AMS to measure aerosol mass concentrations and size distributions. For this comparison, the ToF-AMS mass concentration time series need to be divided into four different time periods:

- period #1: 13/01 22:03 – 15/01 11:04
- period #2: 17/01 00:02 – 21/01 10:07
- period #3: 28/01 09:25 – 31/01 11:30
- period #4: 31/01 14:13 – 01/02 08:33

An IE calibration was performed at the end of period #3.

After application of all corrections, the resulting mass concentrations in the four periods compare differently to the Q-AMS mass concentrations in the various intervals. Those differences are probably caused by the following reasons: At the end of period #1 the instrument needed to be disassembled for exchange of the vaporiser which did not reach the standard operating temperature (~600 °C). After period #2 the data acquisition software was changed, while during period #4 the co-located Q-AMS did not work properly.

Since a valid IE calibration does only exist for period #3, periods #1, #2 and #4 are excluded from further analysis and only data from period #3 will be discussed.

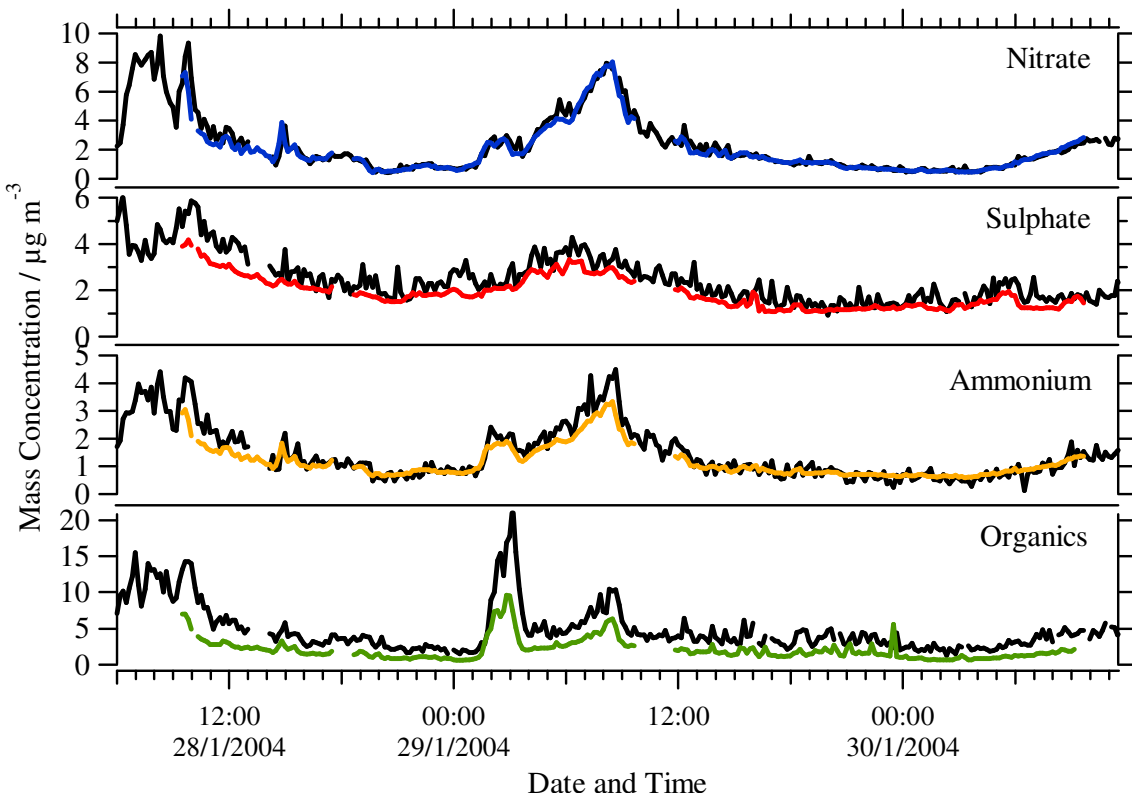


Figure 4.3: Mass concentration time series of non-refractory nitrate, sulphate, ammonium and total non-refractory organics measured with the ToF-AMS (blue, red, yellow, green) and the Q-AMS (black) for the same time interval during measurement period #3 of the ToF-AMS.

Figure 4.3 shows the mass concentration time series of nitrate, sulphate, ammonium and organics for both ToF-AMS and Q-AMS for period #3. For the same period, scatter plots of mass concentrations measured with the ToF-AMS plotted versus Q-AMS mass concentrations are shown for nitrate, sulphate, ammonium and organics in Figure 4.4. In Table 4.1 the parameters of the correlations and linear regressions are shown for each species individually. The tightness of the correlations between the two instruments for this period is very good for nitrate and ammonium with  $R^2$  values around 0.95. The correlations for sulphate and organics are slightly broader, but still good with  $R^2$  of 0.84 and 0.80, respectively. The slopes of the linear regressions lie between 0.46 and 0.88 with positive intercepts ranging from 0.06 to 0.32  $\mu\text{g m}^{-3}$ . With the regression line forced through origin the resulting slopes are larger lying between 0.47 and 0.91, meaning that for the inorganic species approximately 80 to 90 % of the mass concentrations of the individual species measured with the Q-AMS were detected with the ToF-AMS. For organics only 50 % of the Q-AMS mass concentrations were measured with the ToF-AMS. While the measured mass concentrations of nitrate, ammonium and sulphate agree well within the uncertainties of the performed IE calibration, significantly lower concentrations were measured for organics in the ToF-AMS. Only a small fraction (< 3 %) of this difference can be explained by transport losses of particles in the sampling line between Q-AMS and ToF-AMS, while another small part (~5 %) of the low organics mass concentrations is due to the fact that ToF-AMS organics here is the sum of signal measured up to  $m/z$  206, while in the Q-AMS the ion signals up to  $m/z$  300 are used to calculate organics mass concentrations. Another small part of the difference can be explained by small differences in vaporiser temperature and electron

energy in the two instruments. In addition, subsequent laboratory characterisation of the ToF-AMS has shown that several of the ioniser and TOFMS voltages were not tuned optimally during PMTACS-NY 2004. This resulted in a decrease in ion transmission with increasing  $m/z$ , thus reducing the total signal for those species which have higher  $m/z$  ions associated with them: organics and to a smaller extent sulphate. Also, the ToF-AMS threshold which rejects signals that are smaller than this threshold, might have been set too high, which can also explain the difference in the mass concentrations of ToF-AMS and Q-AMS. This will be further discussed in the next section.

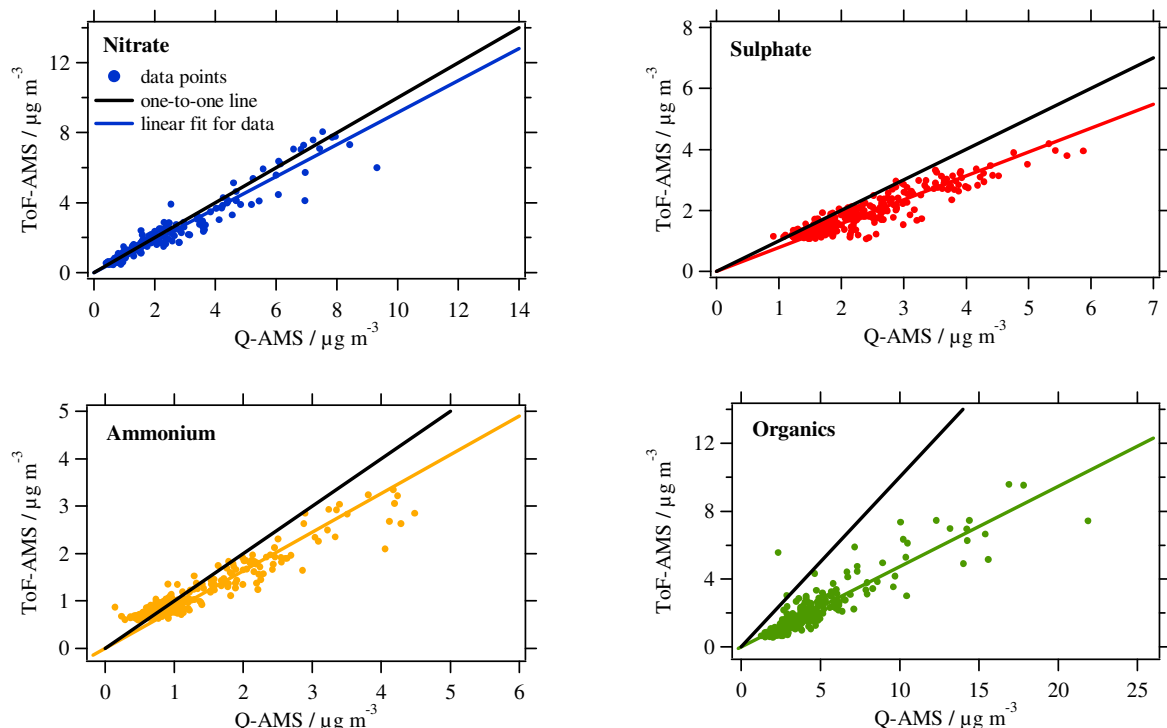


Figure 4.4: Comparison of the mass concentrations measured with the ToF-AMS and the Q-AMS for period # 3. The dots represent the measurements, the solid coloured lines are the linear fits through the data points, and the black solid lines are the 1:1 correlation lines.

Species	Slope	Intercept / $\mu\text{g m}^{-3}$	Recovery	$R^2$
Nitrate	0.88	0.11	0.91	0.93
Sulphate	0.68	0.29	0.78	0.84
Ammonium	0.64	0.32	0.82	0.95
Organics	0.46	0.06	0.47	0.8

Table 4.1: Parameters of the correlations between the TOF-AMS and Q-AMS mass concentration data for nitrate, sulphate, ammonium and organics calculated for period # 3.

However, despite the deviation from the 1:1 lines, both ToF-AMS organics and sulphate correlate well with the same species measured in the Q-AMS, suggesting that there are no further issues affecting the detection of these species.

The PToF mode data were processed to generate 5-min averages of the size distributions for nitrate, sulphate, ammonium and organics. As an example, in Figure 4.5 the temporal evolution of the nitrate size distribution is shown as image plot for a period of 10 hours for ToF-AMS and Q-AMS. The data shown in this Figure are 5-min averages in case of the ToF-AMS and 10-min averages in case of the Q-AMS, both without any smoothing of the data.

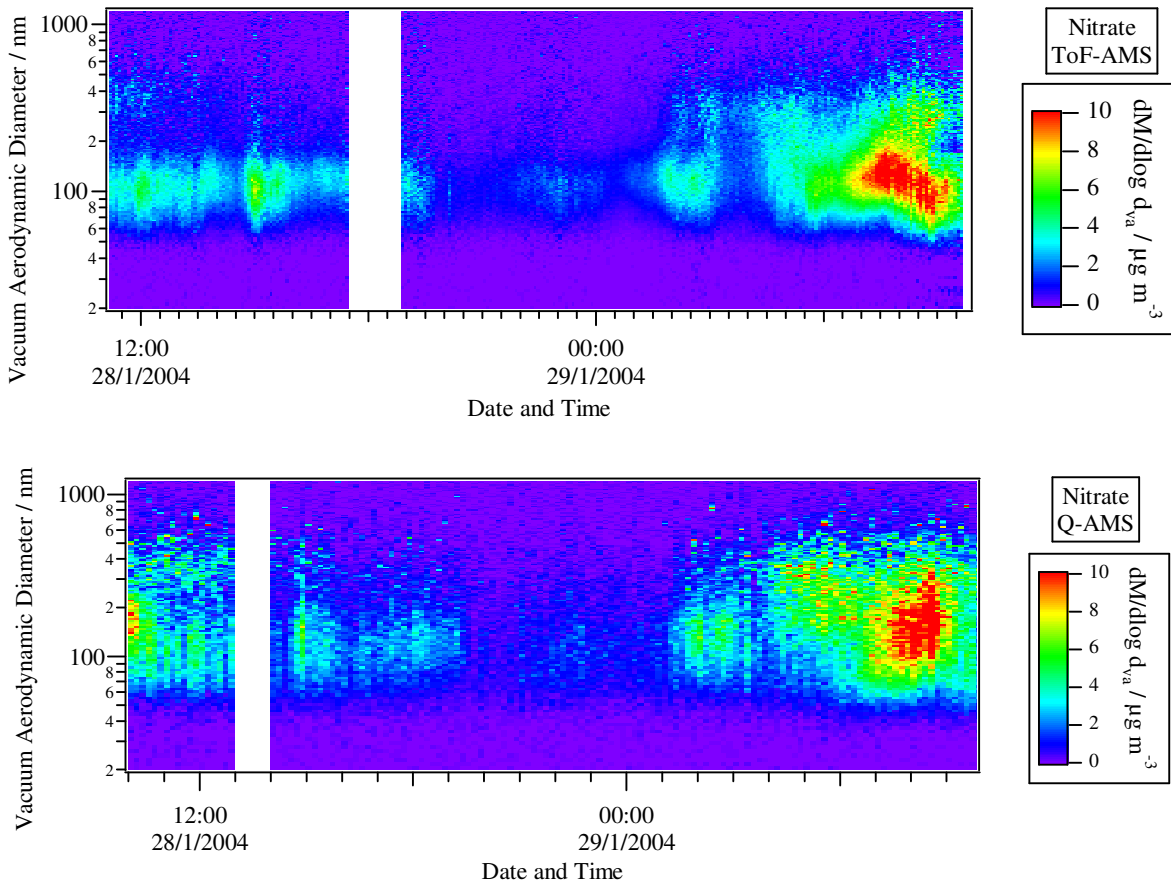


Figure 4.5: Temporal evolution of the nitrate size distribution measured with the ToF-AMS (top) and Q-AMS (bottom), shown for the time interval 28/01 10:20 until 29/01 09:45. The intensity of the signal bins is colour-coded as shown in the legend. The ToF-AMS data shown in this Figure are 5-minute averages; the Q-AMS data are 10-min averages. All data are shown without any smoothing.

Apart from differences of detail, the data from both instruments agree well in the temporal evolution of the size distributions, the absolute sizes of the particle modes, as well as in the absolute intensity of the modes. Despite the fact that the Q-AMS data are averages over 10 minutes while the ToF-AMS data are averages over 5 minutes, the size distribution time series generated from the ToF-AMS data shows significantly less noise and is much smoother than the Q-AMS image plot. This results in a better resolution of the characteristics within time as well as within size. Several characteristics that are blurred in the Q-AMS size distribution time series can be clearly seen in the size distributions of the ToF-AMS. This reduction of noise is mainly due to significantly improved duty cycle (see chapter 3.2.1) in the ToF-AMS size distribution measurements: While in the Q-AMS a size distribution for

only a single  $m/z$  is measured at a time, in the ToF-AMS all  $m/z$  size distributions are measured simultaneously.

Figure 4.6 shows average size distributions for nitrate, sulphate, ammonium and organics for the last six days of the ToF-AMS deployment during PMTACS-NY 2004. The species-resolved size distributions suggest – with the exception of 27/01 – a partial external mixture of nitrate and sulphate particles, as for the days of 28/01 to 01/02 the main part of the nitrate size distribution is found at significantly smaller particle diameters than the sulphate size distribution. In addition, the nitrate size distribution shows a small second mode located at the same particle size as the sulphate mode, which might be due to a subpopulation of the nitrate that is internally mixed in the sulphate particles. The ammonium size distributions are in all cases a combination of the nitrate and sulphate size distributions, with two more or less separate modes, while the organics size distributions are broader than the nitrate or sulphate distributions. They seem to be more associated with the sulphate size distributions. The single particle data confirm what is suggested here: Internal mixture of nitrate, sulphate and organics on 27/01, and partial external mixture of these species during the other days of single particle data collection.

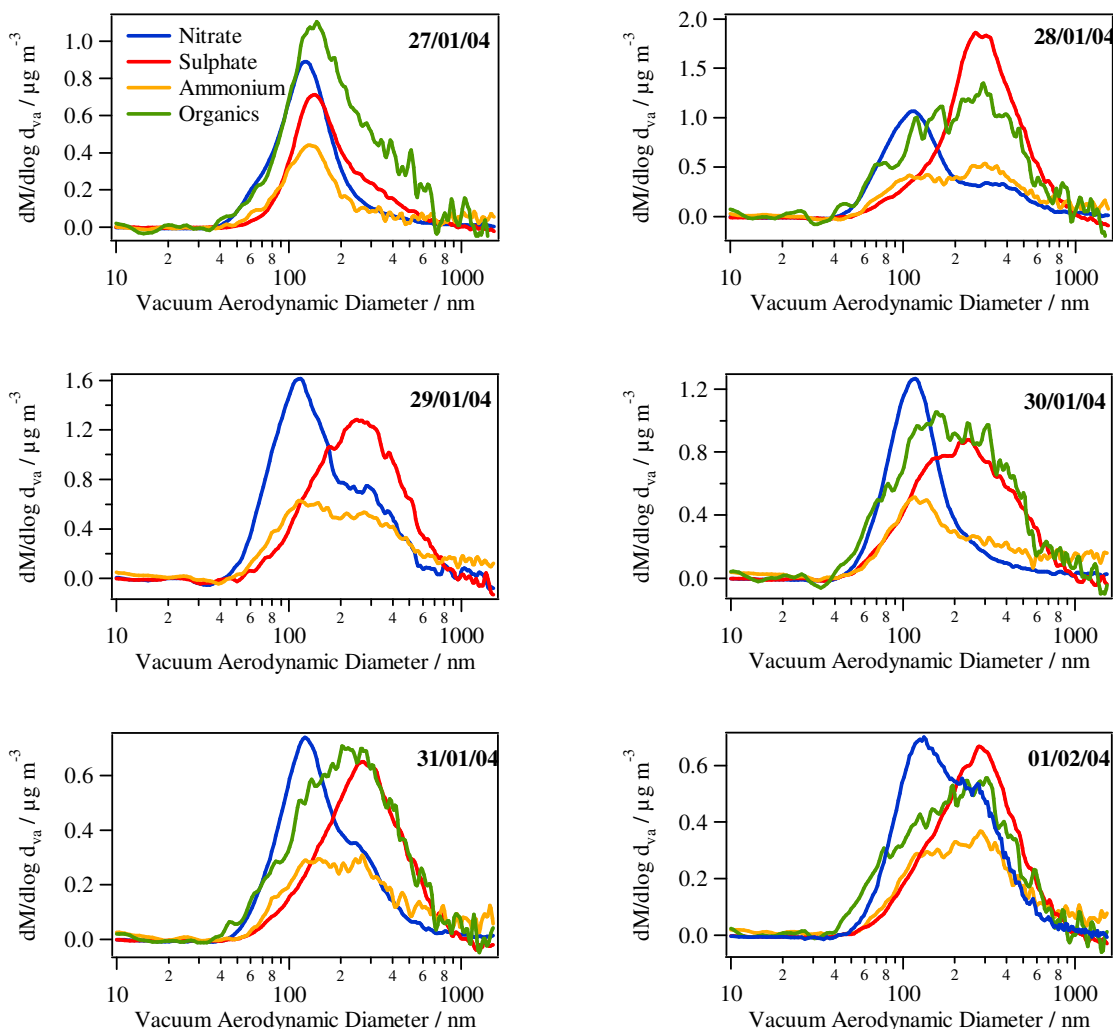


Figure 4.6: Average size distributions for the last six days of the ToF-AMS deployment, shown for nitrate, sulphate, ammonium and organics. The size distributions are plotted as traces of  $dM/d\log d_{va}$  versus particle vacuum aerodynamic diameter.

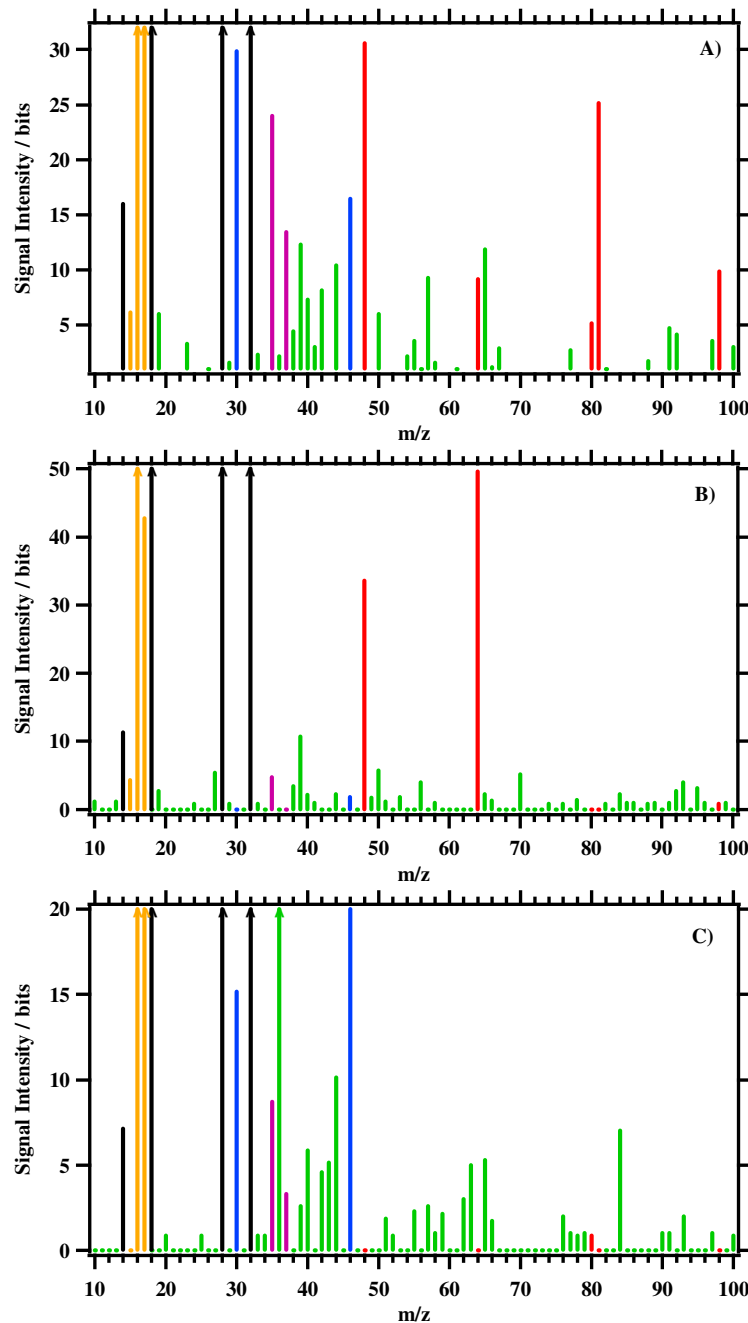


Figure 4.7: Examples of averaged single particle event mass spectra. A) Internally mixed ammonium nitrate/ammonium sulphate particle with organics and chloride ( $d_{va} = 405$  nm); B) “Pure” ammonium sulphate particle ( $d_{va} = 315$  nm); C) Ammonium nitrate particle with some organics and chloride ( $d_{va} = 190$  nm). The signal of the individual  $m/z$  is coloured according to the species they belong mainly to: air beam components (black), ammonium (yellow), nitrate (blue), sulphate (red), chloride (purple), and organics (green).

The single particle data acquired during the PMTACS-NY 2004 campaign showed that typical single particle events are 2-5 consecutive spectra (48-120  $\mu$ s) “wide” (corresponding to 2-5 subsequent extractions of the TOFMS) in a PToF cycle, which is consistent with what is observed in the Q-AMS (Jayne et al., 2000). The occurrence of significant ions in such a

row of spectra together is called “single particle event”. A single particle mass spectrum is calculated by adding the associated mass spectra of such an event.

Three examples of single particle mass spectra are shown in Figure 4.7. A) shows an internally mixed ammonium nitrate/ammonium sulphate particle with some organics and chloride, with a particle diameter  $d_{va} = 405$  nm; B) shows a “pure” ammonium sulphate particle with  $d_{va} = 315$  nm; and C) shows an ammonium nitrate particle, internally mixed with organics and some chloride.

The top panel of Figure 4.8 shows the total particle-related ion signal in the individual single particle mass spectra, plotted versus the particle diameter at which the single particles were found together with a line proportional to  $d_{va}^3$ . The markers are shaded according to the relative organics content in the particles, showing that most of the particles (that were identified as such) contain a significant amount of inorganic species. Most of the particles with  $d_{va} > 150$  nm follow the  $d_{va}^3$  line, while the levelling off for particles with  $d_{va} < 150$  nm reflects single particle ion intensities biased by single particle threshold rejection of smaller ion signals. The size distribution calculated by adding the total particle ion signal of each single particle event is shown in the lower panel together with the average total PToF mode size distribution for the days of SPToF mode measurements. Both size distributions agree well for particle diameters  $d_{va} > 150$  nm, again indicating that for particles with  $d_{va} > 150$  nm the detection in the SPToF mode works reliably. During the PMTACS-NY 2004 campaign smaller particles were detected less efficiently.

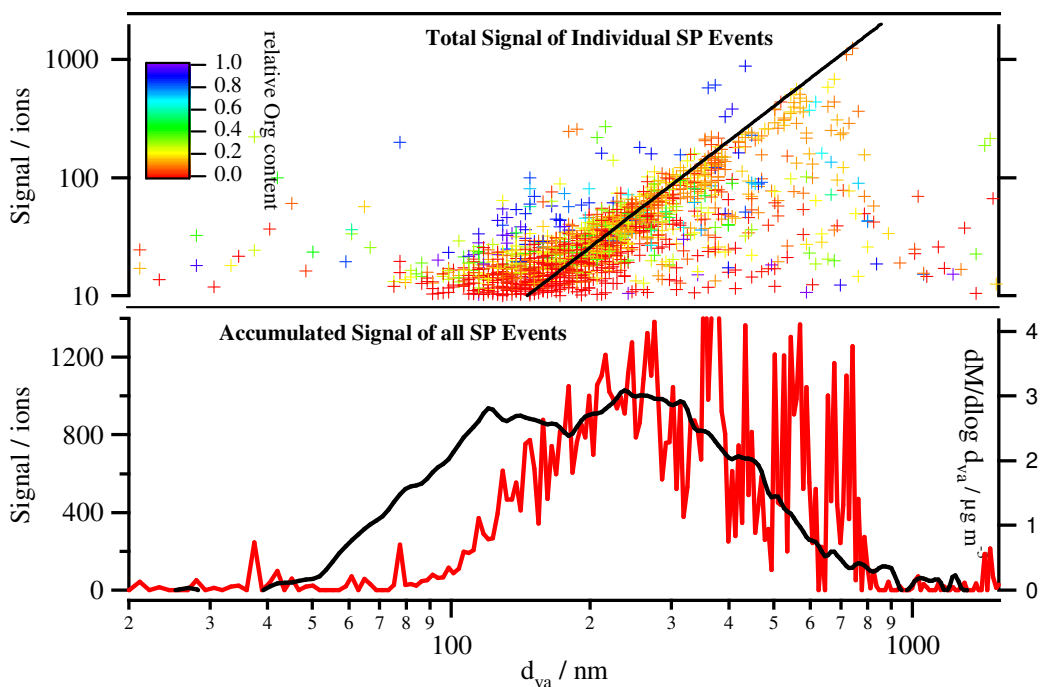


Figure 4.8: Top panel: Total particle-related ion signal versus particle diameter  $d_{va}$  for all extracted single particle events. The markers are coloured according to the relative organics content of the particles. Lower panel: Average size distribution calculated from the total ion signal of all single particle events (red line) and average P-ToF size distribution for the days of SPToF measurements (black line).

The increased noise of the size distribution calculated from the single particle data compared to the PToF mode size distribution is due to the significantly lower particle statistics (~3 minutes of single particle measurements compared to 5 days in PToF mode).

Summarising the results from the PMTACS-NY 2004 campaign – which was the first field deployment of a ToF-AMS instrument – the data clearly demonstrates the instruments' ability for sensitive aerosol composition and size distribution measurements. Nevertheless, it also needs to be said that further characterisation of the ToF-AMS as well as the development of data acquisition and analysis software was crucial in order to be able to perform reliable measurements in the future.

## 4.2 FACE-2004

The Feldberg Aerosol Characterization Experiment 2004 (FACE-2004) took place on the “Kleiner Feldberg” in the Taunus from July 13<sup>th</sup> to August 17<sup>th</sup> 2004. The measurements were performed at the Taunus Observatory (Kleiner Feldberg, 825 m a.m.s.l., 50°13'25''N, 8°26'56''E) near Frankfurt/Main in central Germany. One of the major objectives of the FACE campaign was the test and comparison of new and established measurement technologies. In this context, it was used to better understand and characterise the ToF-AMS under ambient atmospheric conditions during typical ground-based campaign operation. The measurement site consisted of two sets of two stacked containers with a stairway in between and a platform on top. The ToF-AMS and a Q-AMS were deployed in one of the lower containers using a common inlet that separated into the two flows just in front of the instrument inlets. As inlet size selector a PM<sub>1.0</sub> cyclone (URG-2000-30EHB) was used. The inlet system had a total length of 6.6 m 1/2" stainless steel tubing (ID = 12.7 mm) and 0.3 m 1/8" stainless steel tubing (ID = 3.2 mm), a horizontal length of 0.6 m 1/2" tubing and 0.25 m 1/8" tubing and a total angle of curvature of 350° (1/2") and 75° (1/8"). The height of the inlet above ground was 7.5 m. The volumetric flow rate through the 1/2" inlet was 16.7 l min<sup>-1</sup> and 0.1 l min<sup>-1</sup> through the 1/8" inlet. The particle losses in the inlet system have been estimated to be less than 4 % for particles between 50 nm and 1.3 µm diameter, and less than 2 % for particles with diameters between 100 nm and 900 nm. For the two AMS instrument the particle losses should be virtually identical.

During the FACE-2004 campaign both instruments were set to an alternate mode, switching between MS and PToF mode every 10 seconds. For both instruments the chopper frequency and vaporiser temperature were set to 115 Hz and 600 °C, respectively. Average mass spectra and size distributions were saved to disk every 6 min for the Q-AMS and every 5 minutes for the ToF-AMS<sup>1</sup>. For the Q-AMS the following fragments were chosen to be measured in PToF mode: for nitrate *m/z* 30 (NO<sup>+</sup>) and 46 (NO<sub>2</sub><sup>+</sup>), for sulphate *m/z* 48 (SO<sup>+</sup>) and 64 (SO<sub>2</sub><sup>+</sup>), for ammonium *m/z* 15 (NH<sup>+</sup>), 16 (NH<sub>2</sub><sup>+</sup>), and 17 (NH<sub>3</sub><sup>+</sup>), for organics *m/z* 41, 43, 55, 57, 69, 71 (C<sub>n</sub>H<sub>2n+1</sub> and C<sub>n</sub>H<sub>2n-1</sub>), and *m/z* 44 (CO<sub>2</sub><sup>+</sup>), and additionally *m/z* 18 (H<sub>2</sub>O<sup>+</sup>) and *m/z* 28 (N<sub>2</sub><sup>+</sup>).

For quality assurance several calibrations have been performed before and during the campaign: for the ToF-AMS an ionisation efficiency (IE) calibration was performed in the MPI laboratory directly before the campaign, as it was not possible to do this during the campaign with the used preliminary data acquisition software. For the Q-AMS an equivalent calibration was performed during the campaign on July 15<sup>th</sup>. A particle size calibration was performed at the beginning of the campaign at the Taunus Observatory, on July 14<sup>th</sup>, for both instruments simultaneously.

In the following, the datasets obtained by the ToF-AMS and the co-located Q-AMS will be compared to each other.

### Results

The mass concentrations of nitrate, sulphate, ammonium and total organics measured during FACE-2004 with both ToF-AMS and Q-AMS are plotted as time series in Figure 4.9. In

<sup>1</sup> Due to the early-stage data acquisition software that was used for the ToF-AMS, it was not possible to set the ToF-AMS averaging interval to 6 min, which was the time used for all other co-located instruments.

addition, the total non-refractory mass concentrations – the sum of these four species – are displayed. Both instruments show very similar trends with high and low mass concentration episodes, with the organics dominating the total aerosol most of the time.

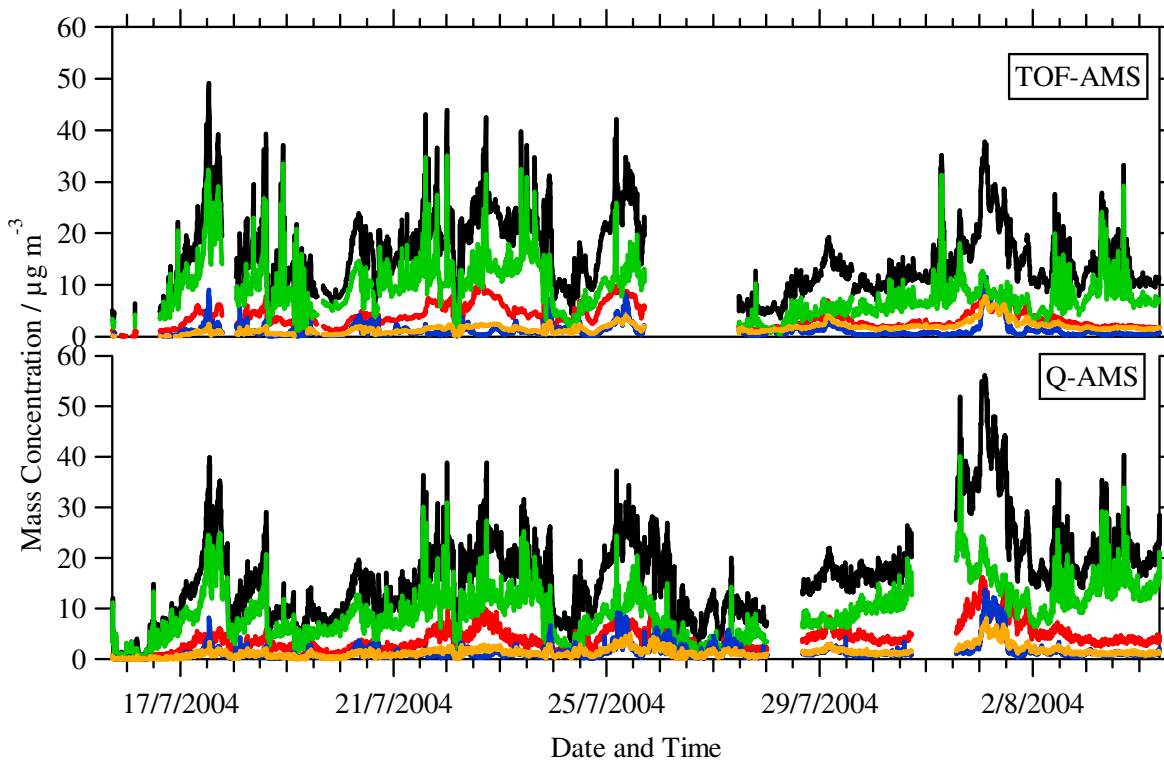


Figure 4.9: Time series of non-refractory nitrate (blue), sulphate (red), ammonium (yellow), total organics (green) and total non-refractory mass concentrations (black), measured with ToF-AMS (upper panel) and Q-AMS (lower panel).

While during the first 10 days both instruments agree well, after a failure of one of the ToF-AMS turbo molecular pumps July 25<sup>th</sup> the ToF-AMS mass concentrations are significantly different to the Q-AMS mass concentrations. Therefore two different periods of the campaign were classified: period I covers the time span before the pump failure (until July 25 17:00 h), period II covers the time span after the pump failure. In order to better compare ToF- and Q-AMS mass concentrations, correlations of 30-min averages have been calculated for nitrate, sulphate, ammonium, and total organics mass concentrations as shown in Figure 4.10 (data from period I in blue, data from period II in green). The red and black solid lines are linear regressions to the data of the periods before and after the ToF-AMS pump failure, period I and period II, respectively, the black dashed line is the 1:1 line. The parameters of the linear regressions are given in Table 4.2, with ‘recovery’ meaning the resulting slope of the linear regression when the intercept is forced to be zero. During period I the two aerosol mass spectrometers show very good correlations for all species with slopes between 0.93 and 1.07 and correlation coefficients  $R^2$  between 0.69 and 0.83. Only the intercept of the linear regression for the organics is somewhat larger ( $1.14 \mu\text{g m}^{-3}$ ). Calculating the ‘recoveries’ for direct comparison of the two instruments results in slightly larger slopes, lying between 1.01 and 1.21. This comparison of the two Aerosol Mass Spectrometers is significantly better than the one performed during the PMTACS-NY 2004 campaign. It shows that the two instruments agree within the uncertainties of the measurements in the order of 10-20%. The

lower correlation coefficient of the organics (compared to the other species) as well as the large intercept of this correlation are mainly due to the higher organic mass concentrations observed with the ToF-AMS but not with the Q-AMS late on July 18. Looking more closely at this time period, the unaveraged 1-min ToF-AMS data frequently show peaks of high organic mass concentrations which are only one to two minutes wide and are mainly caused by contributions of organics at  $m/z$  57 (which is a marker for hydrogenated organic aerosol). The fact that the high organic mass concentration peaks are of only short duration points to a source nearby that was generating very large particles composed of hydrocarbon-like organics, like for example a pump of one of the other instruments that was not working properly and generating an oil mist. This would also explain why the Q-AMS does not show the increased organics mass concentrations: If the organic aerosol mass of one of the peaks measured with the ToF-AMS was caused by only one large particle that at the same time only contained hydrogenated organic aerosol (which has major fragments only at a few  $m/z$ ), the Q-AMS has a large chance to ‘miss’ this particle, because it is not scanning the ‘correct’  $m/z$  (where the organic mass appeared) at the short time interval ( $\sim <100\ \mu\text{s}$ ) the particle was vaporized. Unfortunately, this theory cannot be verified with the help of size distribution measurements, since those were not measured during this time due to a ToF-AMS data acquisition software problem.

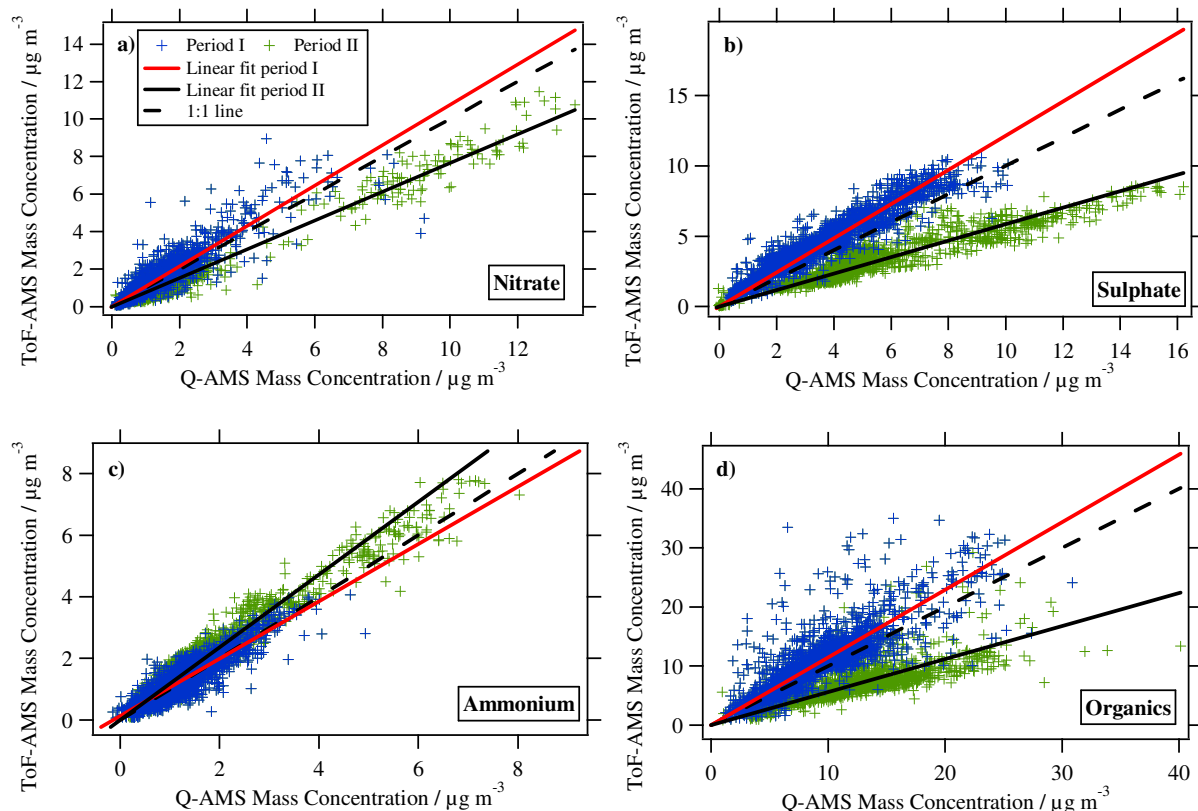


Figure 4.10: Correlations of ToF-AMS and Q-AMS mass concentrations for a) nitrate, b) sulphate, c) ammonium and d) organics. Blue markers indicate data from period I, green markers from period II. The red and black solid lines are linear fits for period I and II, respectively, the black dashed line is the 1:1 line.

The linear fits for period II have similar good correlation coefficients  $r^2$ , lying between 0.64 and 0.97, but the ToF-AMS concentrations are very low compared to those of the Q-AMS especially for sulphate and organics. The pump failure on 25/07 seems to have caused a significant reduction in the MCP detector performance due to excessive ion current onto the detector during the failure, causing the detector gain and therefore the single ion signal intensity to be significantly reduced. The differences in loss in aerosol mass concentrations that are seen for the different species are likely due to the influence of the ion detection threshold of the data acquisition system, which was – after the pump failure – well above its ideal value with respect to the magnitude of the single ion signal. As a too high threshold setting primarily affects small ion events where only a small number of ions reach the detector at the same time, and because the single ion signal intensity distribution is different for different  $m/z$ , the effect of signal loss due to a too high threshold is different for different  $m/z$ .

During FACE-2004 the smallest losses of ToF-AMS signal compared to the Q-AMS mass concentrations were found for nitrate and sulphate (Table 4.2), for which the total signal is located in only few relative intense  $m/z$ . This means that a relative large fraction of the nitrate and sulphate signal is located in large ion events where a large number of ions reach the detector at the same time. These ion events are larger than the threshold and are therefore not affected by the threshold-related ion losses. The larger loss in the organics mass concentrations can be explained by the larger fraction of the total signal that is distributed over many  $m/z$  with only low signal intensity. This means that a larger fraction of the signal is found in single ion events, which are easily lost due to a too high threshold, and that the organics signal is more sensitive to large threshold settings than nitrate and sulphate. Other than for nitrate, sulphate and organics, the ToF-AMS ammonium mass concentrations show an increase relative to the Q-AMS mass concentrations after the pump failure. This can be explained by the way the ammonium mass concentration is calculated from the ammonium-related  $m/z$ : Before calculating the ammonium concentration from  $m/z$  15, 16 and 17, these are corrected for contributions of water, nitrogen and oxygen gas-phase signals, which in turn are calculated from other  $m/z$  that are related to these species (e.g.  $m/z$  18 for water or  $m/z$  28 for nitrogen). Since the gas-phase signals – even though their absolute intensity is high – are mainly distributed in small ion events, they are very sensitive to threshold-related losses. For this reason, a much too high threshold leads to a too low correction due to gas-phase signals, leaving a too high signal intensity that is associated with ammonium.

The explanations given above could be verified by modelling the threshold-related loss of the species' mass concentrations for the measured aerosol conditions during this campaign (Drewnick, 2006).

	Period I				Period II			
	Intercept	Slope	R <sup>2</sup>	Recovery	Intercept	Slope	R <sup>2</sup>	Recovery
<b>Nitrate</b>	0.05 ± 0.02	1.05 ± 0.01	0.83	1.08	-0.06 ± 0.01	0.80 ± 0.01	0.97	0.77
<b>Sulphate</b>	0.68 ± 0.03	1.07 ± 0.01	0.91	1.21	0.37 ± 0.03	0.53 ± 0.01	0.87	0.56
<b>Ammonium</b>	0.12 ± 0.01	0.93 ± 0.01	0.82	1.01	0.49 ± 0.01	1.00 ± 0.01	0.95	1.12
<b>Organics</b>	1.14 ± 0.16	1.04 ± 0.02	0.69	1.15	1.02 ± 0.14	0.49 ± 0.02	0.64	0.42

Table 4.2: Parameters from the linear regressions in Figure 4.10.

Figure 4.11 and Figure 4.12 show average size distributions of nitrate, sulphate, ammonium and organics, measured with ToF-AMS and Q-AMS for two different episodes during period I. Shown in Figure 4.11 is the average size distribution for 20/07/04, 0:00-12:00 h, in Figure 4.12 the average for 21/07/04, 0:00-14:00 h. Those episodes were chosen because both ToF-AMS and Q-AMS were measuring PToF data during this time. Due to the used preliminary data acquisition software it was not possible to measure PToF data with the ToF-AMS during the whole campaign.

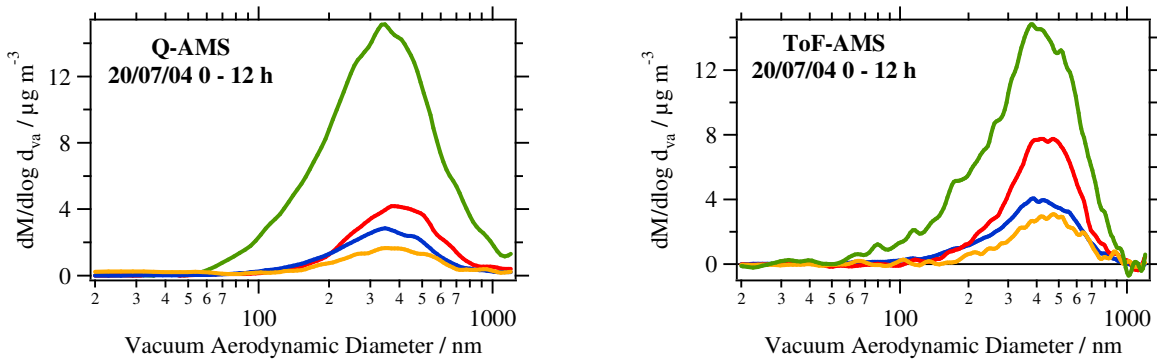


Figure 4.11: Average size distributions of nitrate (blue), sulphate (red), ammonium (yellow), and organics (green), measured with Q-AMS (left) and ToF-AMS (right) for the time period 20/07/04 0:00-12:00 h.

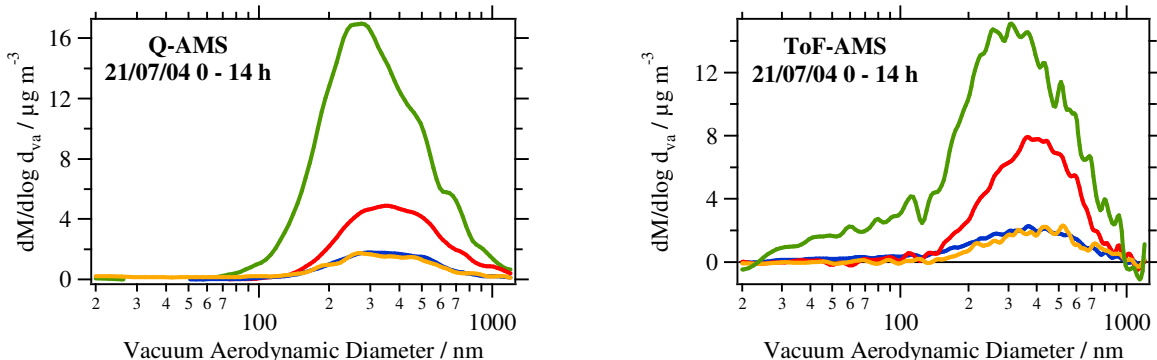


Figure 4.12: The same as Figure 4.11, but for the time period 21/07/04 0:00-14:00 h.

Parameters resulting from fitting monomodal log-normal distributions to the average size distributions are given in Table 4.3. On both days the size distributions of both instruments are quantitatively very similar to each other, only the sulphate distribution is more intense in the ToF-AMS. The ToF-AMS mode diameters calculated from the log-normal fits are always slightly larger than the Q-AMS mode diameters (difference between 13 nm and 82 nm). The ToF-AMS organics size distributions extend to smaller particle sizes than the Q-AMS organics size distributions. As the size distributions for both ToF-AMS and Q-AMS are normalised to the mass concentrations obtained in MS mode of each instrument, this causes the ToF-AMS organics size distribution to be less intense than the Q-AMS organics size distribution. In addition, the higher sensitivity of the ToF-AMS for small particles causes the size distributions to be skewed towards smaller particles. This can be seen particularly in the organics size distributions and results in a shift of the maximum of the log-normal fits towards larger particles. In contrast to the calculated values in Table 4.3, the

actual distribution maxima of the ToF-AMS and Q-AMS size distributions are very similar to each other and agree within their uncertainty of typically 20-30 nm.

To summarise, the size distributions of both instruments agree reasonably well and indicate small particles ( $d_{va} < 150$  nm) containing mostly organics.

		20/07/04		21/07/04	
		TOF-AMS	Q-AMS	TOF-AMS	Q-AMS
Nitrate	mode	412	342	356	343
	width	1.62	1.86	1.67	1.69
Sulphate	mode	428	384	381	366
	width	1.63	1.64	1.66	1.6
Ammonium	mode	441	359	400	335
	width	1.59	1.83	1.66	1.73
Organics	mode	408	332	319	279
	width	1.42	1.85	1.94	1.94

Table 4.3: Parameters of the average species-resolved size distributions, obtained by log-normal fits. Mode diameter values are given in nm, distribution widths are given as GSD.

During the FACE-2004 campaign it could be shown that the data obtained by the ToF-AMS quantitatively agree with those obtained by a Q-AMS when both instruments operate under well-calibrated conditions. However, setting the ToF-AMS threshold too high results in signal loss that is different for different species and that can therefore not be corrected for. Further characterisation and analysis of how to set the data acquisition threshold properly is done by the Jimenez group at the University of Colorado at Boulder.

## 4.3 HNY 2005

Measurements of aerosol associated with New Year's fireworks are an excellent test of instrumentation with high time resolution, as the emissions of those fireworks are large and occur at a well-defined point in time in the absence of complex sunlight driven photochemistry. Very few measurements of fireworks aerosol with high time resolution are described in the literature. These cover for example particle size distribution measurements (Wehner et al., 2000), single particle mass spectrometry (Liu et al., 1997), and black carbon concentration measurements (Babu and Moorthy, 2001). However, most of these measurements were performed far away from the centres of the activities, resulting in a measurement of the advected smoke cloud.

The Happy New Year 2005 campaign (HNY 2005) was realised from December 28<sup>th</sup> 2004 to January 4<sup>th</sup> 2005 in the centre of the fireworks activities on the south bank of the Rhine River in Mainz, a city (population: 190000) in central Germany (50°N, 8°E).

The instruments used in this study – a condensation particle counter (Grimm CPC 5.403; Grimm Aerosoltechnik GmbH & Co. KG, Ainring, Germany), a proton transfer reaction mass spectrometer (PTR-MS) and a ToF-AMS – were housed in a maintenance garage within one of the supports of the Theodor Heuss bridge, which crosses the Rhine river close to the centre of Mainz. The findings from this campaign are subjects to two publications: Williams et al. (2005) and Drewnick et al. (2006). Here, only the aerosol measurements will be presented, as presenting the results from the gas phase measurements are beyond the scope of this work.

The aerosol inlet was located at a height of approximately 1.5 m above ground level on the side of the bridge between a busy street running parallel to the river and the Rhine promenade, each within a distance of 5-10 m. The distance to the river was about 20 m. Due to the vicinity of the measurement site to the street, a significant influence from local traffic is expected. The time resolutions of the CPC and the ToF-AMS were 1 s and 5 min, respectively, the ToF-AMS was set to a general alternation mode, switching between MS and PToF mode every 10 s.

### Identification of Fireworks Components

As described in chapter 3, a deconvolution algorithm is applied to the ToF-AMS mass spectra, in order to extract the individual contributions from different species at a given  $m/z$ . This algorithm is based – in addition to known isotope ratios and measured fragmentation patterns – on several assumptions concerning the assignment of certain  $m/z$  to individual species. Those assumptions are based on the experience of aerosol measurements in the ambient atmosphere. These assumptions may not be applicable to aerosol measurements during fireworks events, as additional, more “exotic” species can be expected in the aerosol at significant levels, causing a change in the assignment of individual  $m/z$  to certain species. For this reason, the assignment of every single  $m/z$  to possible fireworks specific species needed to be examined. Using information about species involved in fireworks chemistry, possible elemental compositions could be identified plotting the time series of the signal measured for each  $m/z$  from 5 to 120 over the measurement interval. The relative signal intensity during and outside the time of the firework activity, together with volatility information of the individual compounds relevant in fireworks chemistry, resulted in a quite robust overall picture of the assignment of the various  $m/z$  signals to individual species.

Many of the potential firework generated species could be excluded, either because they cannot be measured with the ToF-AMS as they are refractory, or because the time series of the particular  $m/z$  did not show any fireworks signature. A summary of the resulting “unusual” assignments of  $m/z$  to individual species for the fireworks aerosol is given in Table 4.4. Several of the  $m/z$  listed in Table 4.4 are usually used to calculate the total organics mass concentration from ToF-AMS mass spectra. Therefore the deconvolution algorithm for the calculation of organics needed to be adapted in order to account for the different assignment of these  $m/z$  to other species during the measurement of the fireworks aerosol. For this reason, an adapted version of the ToF-AMS data analysis software was written.

Since the relative ionisation efficiency  $RIE$  is not known for most of the additional species found in the fireworks aerosol, absolute mass concentrations could not be calculated for these compounds.

$m/z$	Compound	Comment
7	Lithium	Weak but clear fireworks contribution
19	Fluorine	Weak but clear fireworks contribution
23	Sodium	Very intense fireworks contribution
24	NaH	Significant fireworks contribution
32	S (in addition to O <sub>2</sub> )	Very intense fireworks contribution
36	H <sup>35</sup> Cl	Very intense fireworks contribution
38	H <sup>37</sup> Cl	Very intense fireworks contribution
39	<sup>39</sup> K (mainly)	Extremely intense fireworks contribution
41	<sup>41</sup> K, Organics	Very intense fireworks contribution
74	K <sup>35</sup> Cl, Organics	Likely mainly KCl
76	K <sup>37</sup> Cl, Organics	KCl and Organics

Table 4.4: Unusual assignments of certain  $m/z$  in the aerosol mass spectra to individual species for the fireworks aerosol.

### Quantification of Aerosol Potassium

The composition of aerosol influenced by fireworks is very different to the one observed for typical ambient aerosol. For example potassium is one of the major components in firework related aerosol (Dutcher et al., 1999; Liu et al., 1997; Kulshresta et al., 2004; Perry, 1999) while it is not part of the suite of non-refractory species typically determined with the ToF-

AMS. However, it is observed as contaminant in the instrument and the mass spectra are corrected for its contributions at  $m/z$  39 and 41. Potassium generates ions by thermal ionisation on the hot vaporiser (surface ionisation) with relatively high efficiency. However, due to the fact that it is not quantified during typical ambient measurements with the ToF-AMS, measurements of the *RIE* of potassium do not exist so far.

An approach to obtain a rough estimate of the *RIE* for aerosol potassium can be made using the analysis of a relatively undisturbed fireworks aerosol by Dutcher et al. (1999). Dutcher and co-workers used PIXE (proton induced x-ray emission) analysis to determine the elemental composition of a firework-generated aerosol during a baseball game in the Houston Astrodome. They found an elemental concentration ratio of potassium to sulphur (K/S) virtually identical to the ratio of these elements in black powder (2.76:1), which is the major component of most fireworks. Assuming that during the Mainz' fireworks the sampled aerosol was dominated by firework generated material, and that during the fireworks the same K/S ratio of 2.76 is present in our aerosol samples, the measurement of aerosol S can be used for a rough estimate of the aerosol potassium content.

In the aerosol, S is mainly found as sulphate or sulphuric acid, both summarised as ToF-AMS sulphate. In the fireworks dominated aerosol the average sulphate concentration measured with the ToF-AMS was  $36.2 \mu\text{g m}^{-3}$ , resulting in an average S concentration of  $12.1 \mu\text{g m}^{-3}$ . Assuming an average K/S ratio of 2.76 the average potassium concentration in the fireworks aerosol is  $33.2 \mu\text{g m}^{-3}$ . The average nitrate-equivalent mass concentration (see chapter 3) of potassium measured with the ToF-AMS is  $48.1 \mu\text{g m}^{-3}$ . Applying a *CE* factor of 0.5 (assuming internal mixture of the firework-related aerosol components), an average potassium concentration of  $96.2 \mu\text{g m}^{-3}$  is obtained. In order to get a potassium concentration of  $33.2 \mu\text{g m}^{-3}$  in agreement with the K/S ratio reported by Dutcher et al. (1999), a relative ionisation efficiency for potassium of  $RIE_K = 2.9$  needs to be applied. This *RIE* for potassium is subject to substantial uncertainty due to the assumptions made for its estimation. Nevertheless, as it is the first and only estimate for a *RIE* for ToF-AMS potassium measurements, it will be used to determine ambient aerosol potassium mass concentrations from these measurements.

## Results

Mass concentration time series of nitrate, sulphate, ammonium, chloride, organics and potassium are shown in Figure 4.13 for the whole campaign. The ordinate is clipped at  $30 \mu\text{g m}^{-3}$  to make sure that the variations in ambient aerosol concentrations are still visible. The variation in the ambient aerosol concentrations is episodic rather than diurnal, and suggests to be more associated to airmass advection than to local emissions. Three different periods can be distinguished from the time series in Figure 4.13:

- “background interval 1”: 29/12/04 18:30 h – 02/01/05 03:00 h  
(with exception of the “fireworks aerosol”)  
This episode is dominated by relatively high mass concentrations.
- “background interval 2”: 02/01/05 03:00 h – 04/01/05 12:00 h  
In the beginning of this time period the particle concentrations decreased to very low values, and slowly increased again over the next few days.

- “fireworks aerosol”: 31/12/04 23:45 h – 01/01/05 08:00 h

Average aerosol mass concentrations and the relative composition of the aerosol measured with the ToF-AMS during the three different periods are given in Table 4.5 and Figure 4.14, respectively. The aerosol mass concentrations during background interval 2 are about one-third of the concentrations during background period 1, nevertheless the relative composition of both aerosols is very similar. During the fireworks and especially during the period of maximum firework intensity, the mass concentrations of most aerosol species are much higher than during the background measurements, and the relative composition of the aerosol is very different from the background composition, highlighting the main contributions from the fireworks. Due to the rapidly changing magnitude of the species’ mass concentrations, the self-cleaning times of the ToF-AMS might be longer than the timescales of the changes in the mass concentrations. However, the exact values of the mass concentrations do not play a role for the purpose of this work.

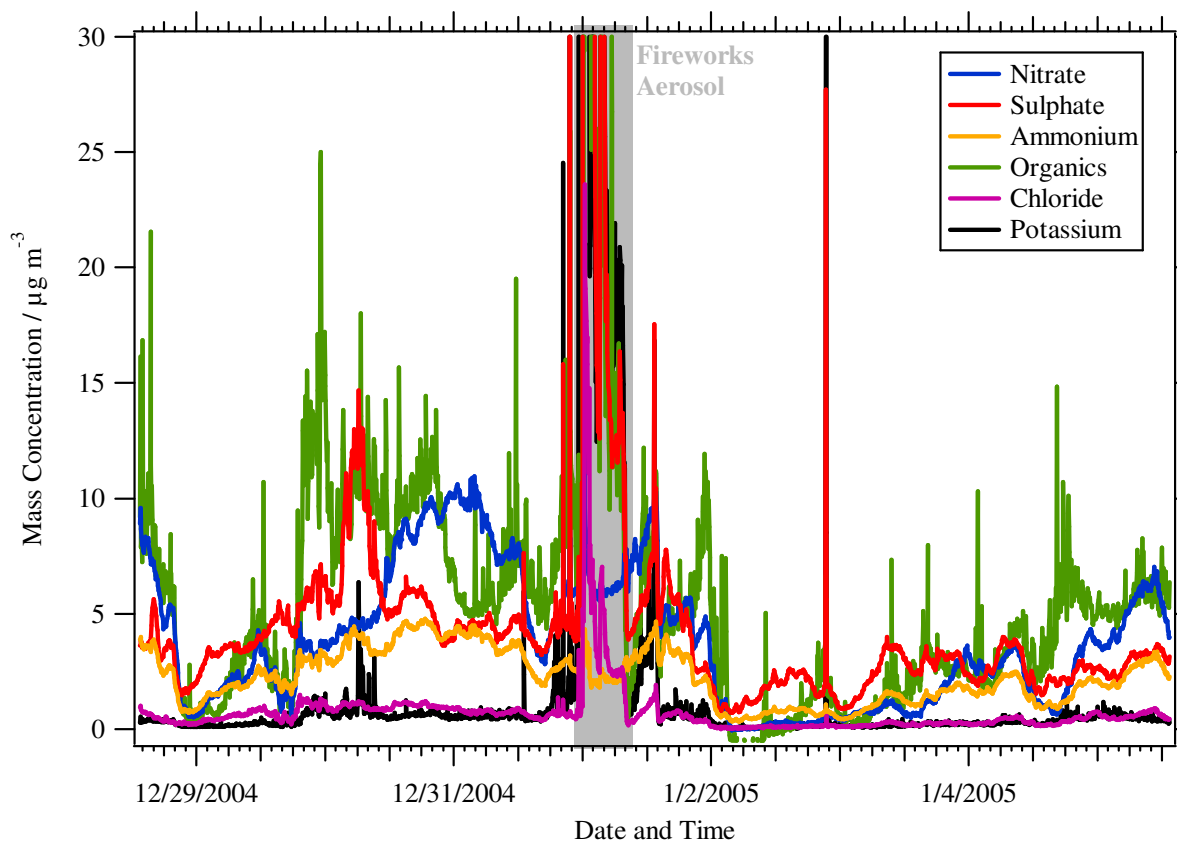


Figure 4.13: Time series of the non-refractory aerosol components, measured with the ToF-AMS during the whole campaign.

It is obvious that neither aerosol phase nitrate nor ammonium is generated in the fireworks in significant amounts, as the average mass concentration of both species are similar during the fireworks and during background interval 1, into which the fireworks aerosol is “embedded”. Since nitrates are a major component of fireworks, it is remarkable that the nitrate concentration does not increase during the fireworks at all. This suggests that all the nitrates in fireworks crackers are quantitatively converted into gas phase  $\text{NO}_x$ , which has been found previously to increase during fireworks (Mandal et al., 1997; Wehner et al., 2000; Ravindra et al., 2003).

Species	Background 1	Background 2	Fireworks mean	Fireworks max
Nitrate	6.17 (25.1%)	1.94 (21.1%)	6.48 (5.8%)	12.63 (2.1%)
Sulphate	5.26 (21.4%)	2.43 (26.5%)	36.17 (32.5%)	209.03 (34.2%)
Ammonium	3.30 (13.5%)	1.42 (15.5%)	2.39 (2.1%)	4.32 (0.7%)
Chloride	0.78 (3.2%)	0.29 (3.2%)	5.13 (4.6%)	23.61 (3.9%)
Organics	7.86 (32.0%)	2.76 (30.0%)	28.03 (25.2%)	127.40 (20.8%)
Potassium	1.18 (4.8%)	0.34 (3.7%)	33.15 (29.8%)	234.12 (38.3%)
Total ToF-AMS	24.55 (100%)	9.18 (100%)	111.35 (100%)	611.11 (100%)

Table 4.5: Absolute (in  $\mu\text{g m}^{-3}$ ) and relative (in % of the total mass concentration) concentrations of the background and fireworks aerosol as measured with the ToF-AMS.

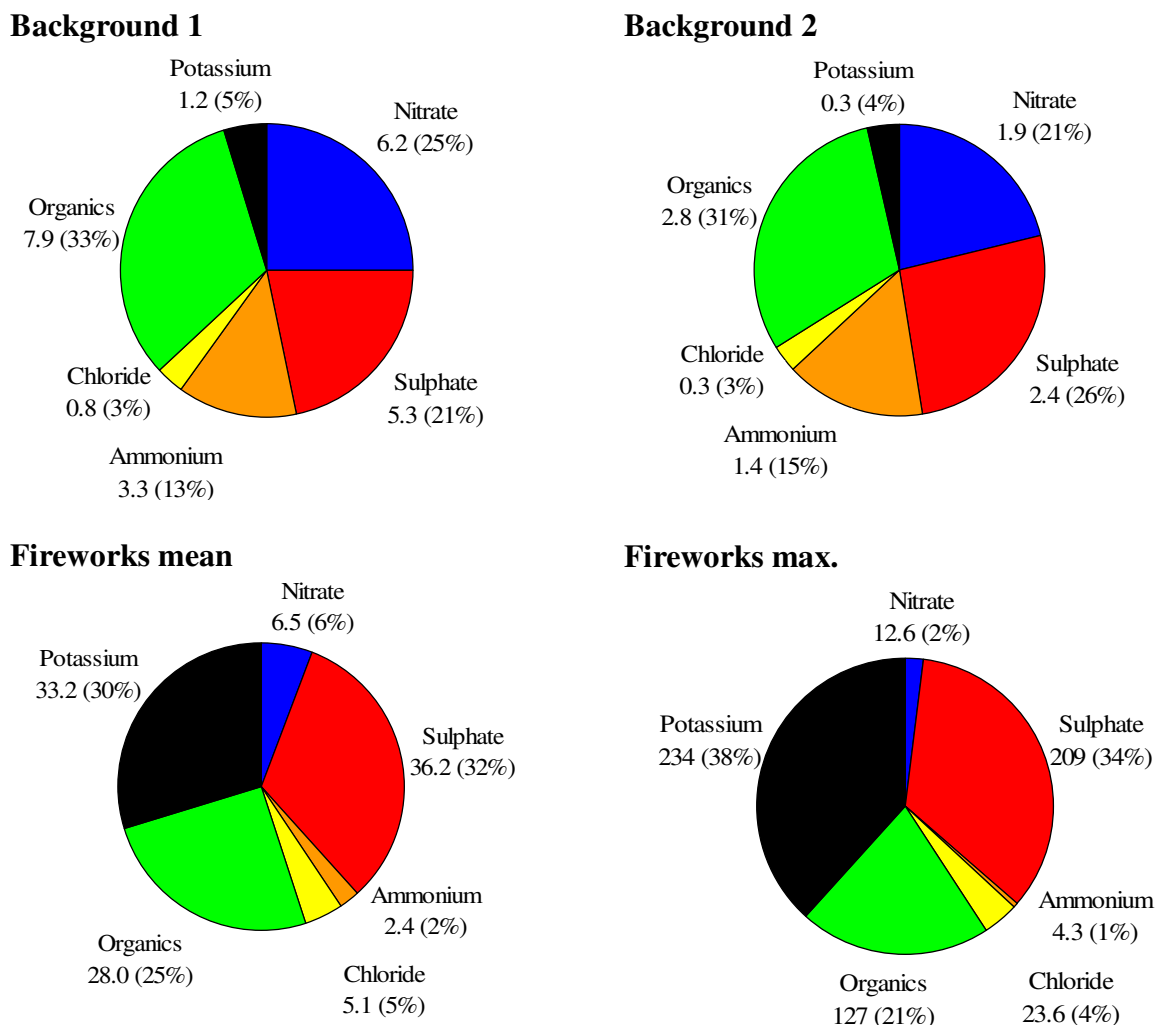


Figure 4.14: Composition of the sub-micron aerosol as measured with the ToF-AMS during background intervals 1 (left top) and 2 (right top) and during the fireworks aerosol (left bottom). The composition of the aerosol during the maximum concentrations in the fireworks is also shown (right bottom).

The most intense contributions of the fireworks to the aerosol composition can be found in sulphate, organics and potassium, resulting in large increases in the mass concentrations of these species.

The increase in the various species' mass concentrations of the fireworks aerosol relative to background interval 1 is shown in Table 4.6. The large increase in the potassium concentrations shows the low abundance of this element in regular ambient aerosol.

Species	Average of Firework	Maximum during Firework
Sulphate	7-fold	40-fold
Organics	3.5-fold	16-fold
Potassium	28-fold	200-fold
Chloride	7-fold	30-fold

Table 4.6: Relative increase in species' mass concentrations of the fireworks aerosol compared to background interval 1.

More insight into the composition of the organic aerosol can be derived by having a closer look at the average fireworks and background mass spectra and the time series for the individual  $m/z$  signals. Investigations of the organic fraction have shown that for typical urban aerosol the total organics can be separated into two major components: hydrocarbon-like organic aerosol (HOA) and oxygenated organic aerosol (OOA) (Zhang et al., 2005), which make up most of the measured organic signal. The major peaks of the HOA and OOA mass spectra,  $m/z$  57 and  $m/z$  44, respectively, can be used as tracers for these aerosol types. The time series of these  $m/z$  signals show that contributions of HOA cannot be associated with the fireworks aerosol, while the  $m/z$  associated with OOA show a large fireworks peak. Apparently, the major part of the increased total organics during the fireworks aerosol is due to oxidised organic species. On the other hand, a distinct diurnal pattern is found for the HOA-related  $m/z$  that reflects the diurnal traffic pattern at the site outside the time of the fireworks.

Size distributions of  $m/z$  44 (OOA) and  $m/z$  57 (HOA) are shown in Figure 4.15 for the time interval of the fireworks aerosol, showing that the differences in the size distribution of these two aerosol components are very distinct. The traffic-related HOA aerosol size distribution is bimodal with a small particle mode at 70 nm, extending down to a few tens of nm and an accumulation mode at 250 nm. The OOA-related size distribution is monomodal with a mode diameter at approximately 400 nm, very similar to the size distributions for sulphate and chloride measured during the fireworks and shown in Figure 4.16.

The average total mass concentration measured with the ToF-AMS during the whole day of January 1<sup>st</sup> was  $51 \mu\text{g m}^{-3}$ , lying above the EU particle standard according to the EU *Framework Directive on Ambient Air Quality for PM<sub>10</sub>*:  $50 \mu\text{g m}^{-3}$ , which is not to be exceeded more than 35 days per year. As the aerosol measurement with the ToF-AMS is not only limited to non-refractory aerosol components, but also to particle sizes below  $\sim 1 \mu\text{m}$  ( $\sim \text{PM}_{1.0}$ ), the PM<sub>10</sub> concentration during this day was likely even much larger than the concentration measured with the ToF-AMS.

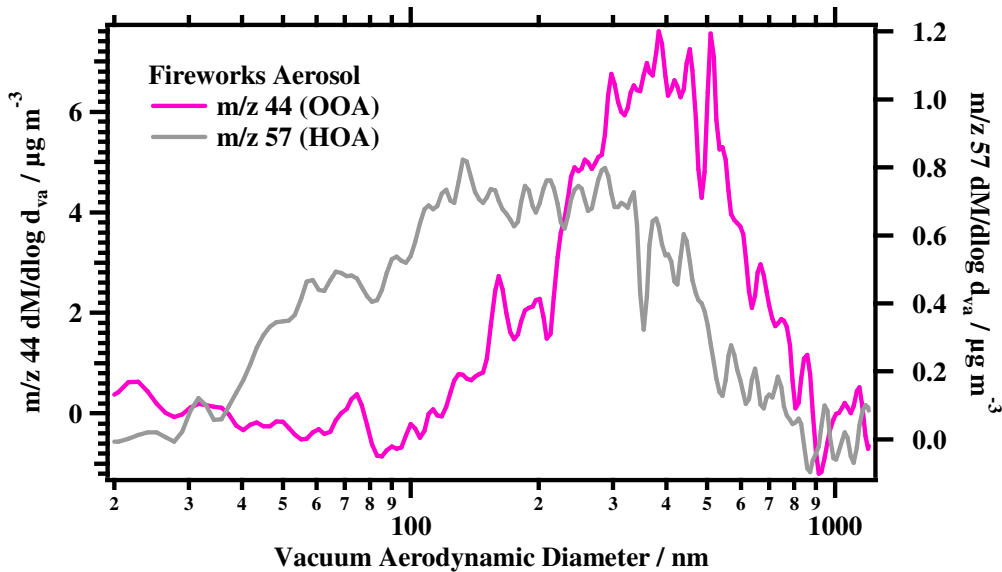


Figure 4.15: Average size distribution for  $m/z$  44 (marker for OOA) and  $m/z$  57 (marker for HOA) during the fireworks aerosol.

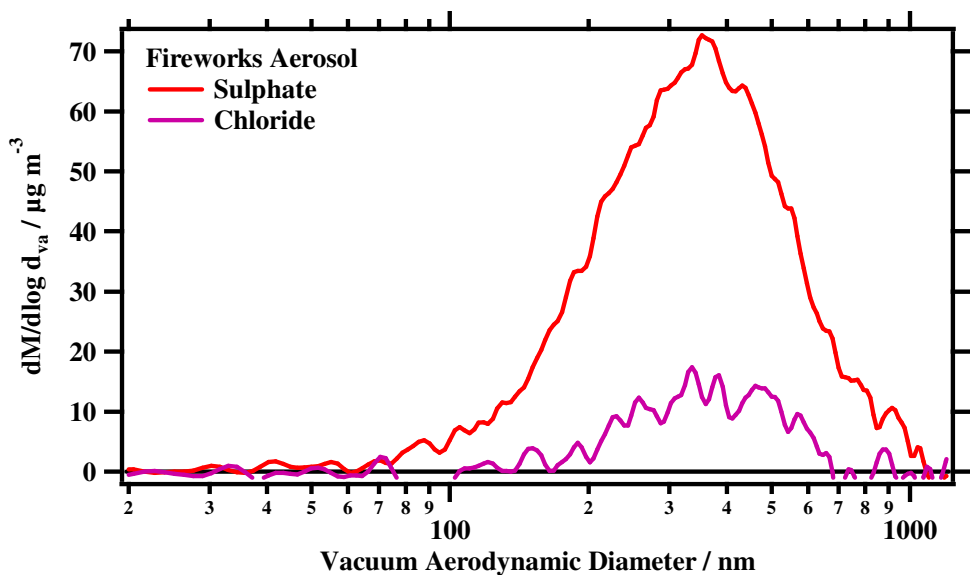


Figure 4.16: Average size distribution for sulphate and chloride during the fireworks aerosol.

The time series of several selected aerosol species (sulphate, potassium, organics, chloride) are shown together with the time series of the particle number concentrations for the time period of the fireworks in Figure 4.17. A sharp peak in the mass concentrations of all aerosol species and in the particle number concentrations is observed exactly at midnight. Interestingly, a short depression is found that starts a few minutes after midnight and lasts about 10-15 minutes. Their maximum concentrations are reached within several minutes after this depression, which might be caused by people pausing to release fireworks in order to toast the onset of the New Year. Accordingly, this short depression in concentrations is be called the “champagne dip”. Changes in meteorological conditions are not likely to be the reason for the champagne dip, as the average wind speed was very low ( $< 0.6 \text{ m s}^{-1}$ ) during the whole time of the fireworks. The wind direction changed between southerly and northerly directions, advecting air parcels from along the promenade which can be regarded

as a linear source of firework aerosol. However, it cannot be completely excluded that changes in the advection and dilution of the air may have caused the champagne dip pattern as well.

After reaching their peak concentrations around 00:20 h – 00:25 h, aerosol concentrations decay gradually within the following hours, and reach pre-fireworks levels around 08:00 h in the morning.

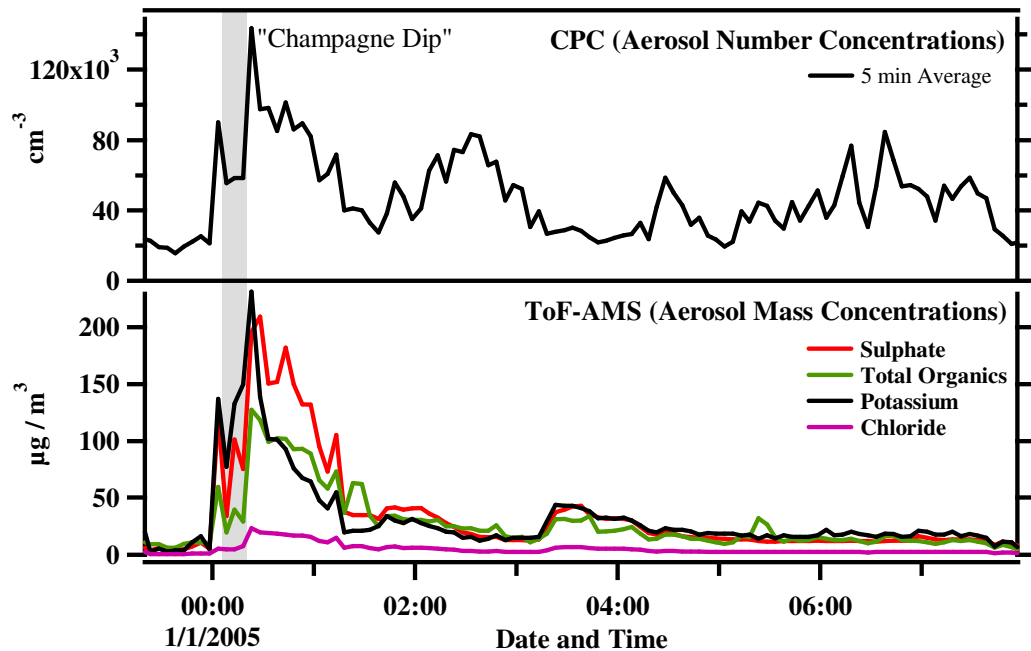


Figure 4.17: Time series of aerosol particle number concentrations (upper panel) and aerosol species mass concentrations (lower panel) for the fireworks time interval. The marked time interval is the “champagne dip”.

## 5 Conclusions and Future Work

The Aerodyne Time-of-Flight Aerosol Mass Spectrometer (ToF-AMS) is a further development of the Aerodyne Aerosol Mass Spectrometer (Q-AMS), which is well-characterised and used by research groups all over the world. Both instruments utilise an aerodynamic lens, differential pumping, aerodynamic particle sizing, thermal vaporisation and electron impact ionisation. Instead of a quadrupole mass spectrometer the ToF-AMS uses an orthogonal extraction time-of-flight mass spectrometer to analyse the ions.

Within this work, laboratory and in-field characterisation of the ToF-AMS have demonstrated that the ToF-AMS is capable of providing quantitative information on the chemical composition of the sub-micron non-refractory fraction of aerosol particles with high size and time resolution.

Since the ToF-AMS was set up for the first time during the first weeks of this PhD work, a data processing software did not exist. Therefore a major objective of this work was to develop a complete data processing scheme to obtain quantitative and useful results from the raw data acquired from ambient as well as laboratory sampling based on the unique needs of this instrument's data structure and on the instrument characterisation experiment results. This scheme includes corrections that need to be applied and calibrations that need to be performed in order to extract reliable results from the raw data. In addition, considerable work has been performed to write a reliable, user-friendly data analysis software which is capable of automated and systematic ToF-AMS data analysis and correction and delivers accurate and repeatable results.

Comparisons with co-located Q-AMS instruments during field campaigns have shown that it is crucial to perform ToF-AMS measurements under well-calibrated and well-tuned conditions. Especially the data acquisition threshold that rejects small signals needs to be set carefully, so that only signals due to noise are rejected. If the instrument is tuned and calibrated correctly and if the data processing is done properly, the ToF-AMS is a powerful tool for quantitative measurement of the chemical composition as well as chemically-resolved size distributions of the atmospheric aerosol. One major improvement compared to the Q-AMS is its capability of measuring all  $m/z$  simultaneously, leading to an improved ion duty cycle, resulting in approximately ten times lower mass concentration detection limits. In addition, the deconvolution algorithm that is applied to the MS mode data to derive aerosol species' mass concentrations can be used for PToF mode data as well and size-dependent information on the chemical composition of the aerosol can therefore be obtained (size-dependent mass spectra, chapter 3.5). Also, the possibility of obtaining complete chemical information on single particles and therefore on internal and external mixture of the particles is given. Other improvements are the increased mass resolving power (up to 900) and the reduced bulk of the instrument due to the use of a compact TOFMS.

Limitations of the instrument are mostly not specific to the ToF-AMS, but are given for all Aerodyne AMS instruments and for similar other aerosol mass spectrometers. Due to the used aerodynamic lens assembly, only sub-micron aerosol particles can be analysed, with a 100 % transmission efficiency for particles with diameters between approximately 40 and 600 nm. As the particles are vaporised by thermal desorption, only non-refractory aerosol

components will vaporise at the vaporiser temperature of ~600 °C, and other refractory species like sea salt, metals, crustal material or soot cannot be analysed. The ionisation of the vapour molecules by electron impact results in intensive fragmentation of the parent molecules, especially making the analysis of the organic components very difficult. The collection efficiency of the AMS is most of the time below 100 %, mainly caused by particle bounce, but also by losses due to the inlet and by the shape of the particles. Therefore, external measurement of the collection efficiency by comparison with a co-located quantitative instrument is required for quantitative measurements.

During this work, the following characterisation experiments have been performed:

- Pressure-dependent inlet flow calibration
- Ionisation efficiency calibrations in MS mode
- Size calibrations with various chemical species
- Pressure-dependent size calibrations
- Experiments to characterise the capability of obtaining size-dependent mass spectra
- Measurement of size distributions for various species at different vaporiser temperatures
- Experiments to measure mass concentration detection limits under various measurement conditions

In addition, much work has been done to develop data processing strategies and to implement those into a data analysis software package:

- Development and implementation of the I-ToF calibration procedure
- Further development and implementation of the peak integration procedure
- Implementation of the ion duty cycle correction
- Further development of the inlet flow and airbeam correction
- Development of a correction for doubly-charged particles occurring during IE calibrations in MS mode

Finally, the ToF-AMS has been deployed and validated during three field campaigns under different atmospheric conditions.

### Ongoing and Future Work

Due to the large amount of data produced by the ToF-AMS there is a strong need for a data analysis software that includes improved data management to be able for example to process data from a whole field campaign in a single IGOR experiment file. For this purpose, the data acquisition software was revised to be capable of saving data in HDF5 file format, and a new analysis software is under development that makes use of these data and the advantages of this format. This is done in cooperation between groups from the University of Manchester, the University of Colorado at Boulder, Aerodyne Research Inc. and the Max Planck Institute for Chemistry in Mainz.

There will always be room for improvement of the data acquisition software, which is developed by the Jimenez group of the University of Colorado at Boulder. For example, it is

currently worked on automated calibration procedures included in the data acquisition software. An improved IE calibration procedure which can be performed without the need of an external particle counter, will be very helpful.

The capability of the ToF-AMS to measure the chemical composition of single particles needs to be characterised and single particle data analysis strategies need to be developed. This is subject of a PhD work currently undertaken at the MPI for chemistry in Mainz.

In order to be able to differentiate between different species which have the same nominal mass but different elemental composition, an increased mass resolving power is needed. A ToF-AMS instrument employing a high resolution time-of-flight mass spectrometer instead of the compact TOFMS is already available and shows promising results (DeCarlo et al., 2006). Its mass resolving power in the order of 4000 makes it possible to directly separate most ions from inorganic and organic species at the same nominal  $m/z$ , the quantification of several types of organic fragments independently ( $C_xH_y$ ,  $C_xH_yO_z$ ,  $C_xH_yN_p$ ,  $C_xH_yO_zN_p$ ), and the direct identification of organic nitrogen and organosulfur content. This opens new possibilities that need adequate characterisation experiments in order to reach its full performance.

One challenge that is related to all types of Aerodyne AMS instrument operation and analysis relates to the problem of collection efficiency. It would be desirable to have a more direct and reliable way of determining it rather than being dependent on the comparison with external measurements or just applying a  $CE$  of 0.5 to all datasets. The installation of a light scattering probe in the particle time-of-flight region of the instrument may help to directly probe the  $CE$  due to particle bounce, as this would count all the particles prior to the detection region. In addition, a change in the design or construction of the vaporiser may help to reduce the losses due to particle bounce.

Although electron impact ionisation has many advantages like for example the possibility of universal detection of all vaporised molecules with similar sensitivity, it also has limitations. For example, it causes extensive fragmentation resulting in complex mass spectra which do not allow to identify specific organic compounds. Accurate classification of organic compounds can therefore be improved by reducing the fragmentation of organic molecules when they are ionised. This can be achieved by employing ionisation methods that are softer than 70 eV electron impact ionisation. One soft ionisation method which has recently been demonstrated by Aerodyne Research Inc., uses VUV light from a krypton discharge lamp to ionise the vapour molecules. In this method, a VUV resonance lamp is integrated into the AMS vaporisation/ionisation region and used in alternation with the standard EI ion source to optimise quantitative information. A second soft ionisation technique under development for AMS deployment is  $Li^+$  attachment. This method has the advantage that it generally occurs without fragmentation or the occurrence of side reactions. Therefore, it almost only results in the formation of quasi-molecular  $Li(M)^+$  adduct ions, and the resulting mass spectra are relatively simple to interpret. A third soft ionisation technique, dissociative electron attachment, takes advantage of low energy electrons that are present during the EI process. These electrons attach to other molecules resulting in negatively charged species. In order to be able to detect those negative ions, the TOFMS needs to be tuned accordingly.

A direct comparison of mass spectra obtained using the different ionisation methods described above is given in Canagaratna et al., 2006.

In addition to the technical developments described in the last sections, there are many scientific aspects the ToF-AMS can contribute to. For example, its reduced mass concentration detection limits compared to those of the Q-AMS make the ToF-AMS even more suitable for measurements at sites where only low mass concentrations are found. Examples are aircraft measurements in the upper troposphere or measurements at the high alpine research station Jungfraujoch.

The fact that AMS type instruments provide information only on non-refractory aerosol components can be addressed by the simultaneous deployment of an AMS and a laser type aerosol mass spectrometer. The complementary nature of these instruments gives the possibility to derive size-resolved and chemical information on both, particles containing non-refractory and refractory components.

## 6 Appendix

### 6.1 ToF-AMS Data Analysis Software

Name of Function	Purpose
Airbeam_Correction_MS	Apply airbeam correction to MS mode data
Airbeam_Correction_PToF	Apply airbeam correction to PToF mode data
Airbeam_MS	Make timeseries of MS airbeam ( $m/z$ 28 and 32) signals
Airbeam_PToF	Make timeseries of PToF airbeam ( $m/z$ 28 and 32) signals
Baseline_ToF	Subtract PToF baseline from PToF distributions
check_use_raw_data	Keep raw data in memory
Color_Traces	Colorise traces according to 'AMS colors'
Create_Waves	Create the most important waves before loading data
Diurnal_plots	Make diurnal plots
dMdlogdva	Convert size distributions into $dM/d\log d_{va}$
Do_Parameter_Control_Panel	Create window with parameter values as they will be loaded
Dutycycle_correction_MS	Apply duty cycle correction to MS mode data
Dutycycle_correction_PToF	Apply duty cycle correction to PToF mode data
Edit_Ion_ToF_calib_masses	Give possibility to edit the $m/z$ for IToF calibration
Edit_masstable	Give possibility to edit the list of exact $m/z$
Export_waves	Export organics waves for HOA/OOA analysis
Get_DirectoryInfo	Get information about the data directory
Get_Parameters	Read important parameters from parameter and info files
Get_SaveTime	Read the saving time from the info files and create time axis
Globals	Set global variables
load_browse	Give possibility to browse for data directory
Load_Infofiles	Subfunction to load info and parameter files if available
Load_load	Read runnumbers to be loaded, load and preprocess files
Load_Msfiles	Subfunction to load MS files
Load_progress_upd	Update progress bar on panel
Load_PToFfiles	Subfunction to load PToF files
Make_dva	Make diameter wave
Make_Image_Waves	Make waves needed for image plots
Make_MSDiff	Calculate difference mass spectra from open and closed spectra
Make_PToF	Write PToF data into 3D wave
Make_SizeDist	Calculate species' size distribution arrays
Make_TimeSeries	Calculate species' mass concentration time series

Name of Function	Purpose
Make_ugmatrices	Apply deconvolution algorithm to 3D arrays
Make_ugwaves	Apply deconvolution algorithm to 2D arrays
Mass_Calibration	Apply IToF calibration to MS mode raw data
MS_average_calc	Calculate and display average mass spectrum for selected run interval
MS_default	Set time series species selection to default
MS_Sticks	Integrate raw mass spectra
MS_timeseries_calc	Display mass concentration time series for selected species
NO3_equivalent_MS	Convert signal into nitrate-equivalent mass concentration
Normalize_to_MS	Normalise average size distribution to MS mode data
Normalize_to_MS_image	Normalise image plots to MS mode data
panel_batch	Display AMS batch file that is used
panel_button_help	Open browser and go to ToF-AMS web page
PToF_avg_calc	Calculate and display average size distributions for selected species and run interval
PToF_avg_default	Set size distribution species selection to default
PToF_im_calc	Calculate and display image plots for selected species
PToF_im_default	Set image plot species selection to default
PToF_MS_calc	Calculate and display size-dependent mass spectra for selected run interval and diameter ranges
PToF_MS_choose	Open table to insert diameter ranges
Set_reference	Set airbeam reference value to average from selected run numbers
Show_runlist	Show list of run numbers and corresponding saving time
Smooth_image	Smooth image plots as selected
Stack_Sticks	Apply deconvolution algorithm to waves

Table 6.1: Functions written for the ToF-AMS data analysis software package and their purpose.

## 6.2 List of Figures

- Figure 1.1: Illustration of number, surface area and volume distributions of a typical urban model aerosol (Seinfeld and Pandis, 1998).
- Figure 1.2: Conceptual schematic of an online aerosol mass spectrometer (after Jimenez, 2002)
- Figure 1.3: Schematic of a linear time-of-flight mass spectrometer.
- Figure 1.4: Schematic of a reflectron time-of-flight mass spectrometer.
- Figure 2.1: A picture of the mobile Time-of-Flight Aerosol Mass Spectrometer (ToF-AMS) used during this work in its configuration for field deployment.
- Figure 2.2: Schematic of the Time-of-Flight Aerosol Mass Spectrometer (ToF-AMS).
- Figure 2.3: FLUENT simulation results illustrating the particle trajectories of 100 nm diameter spheres inside the aerodynamic lens (Jayne et al., 2000). The critical orifice is in upstream the first aperture.
- Figure 2.4: Size-dependent transmission efficiency of the aerodynamic lens (Worsnop, 2003).
- Figure 2.5: Schematic of the evaporation and ionisation sub-chamber (Aerodyne Research, Inc.).
- Figure 3.1: Flow chart of ToF-AMS data analysis and processing. For details see text.
- Figure 3.2: Averaged raw mass spectrum as it is acquired with the ToF-AMS.
- Figure 3.3: PToF distribution as it is acquired in PToF mode. Shown is one column of the 2-dimensional PToF array, containing the measured signal as a function of particle flight time for one specific ion flight time (1742 ns, corresponding to  $m/z$  28).
- Figure 3.4: Mass resolving power  $R$  of the time-of-flight mass spectrometer used during this work as a function of  $m/z$ . The inserts show two different peaks in the beginning and in the end of the raw mass spectrum (black) and the resulting Gaussian fits (green).
- Figure 3.5: Illustration of the peak integration process. The MS baseline (green line) is calculated by linearly interpolating between the averages of the baseline areas before (Baseline Area 1) and after the peak (Baseline Area 2) and subtracted from every point within the integration interval. The total signal corresponding to a particular  $m/z$  is given as the sum of all points within the integration interval (Peak Integration Area).
- Figure 3.6: Unit resolution spectrum of laboratory-generated PSL particles in ions  $s^{-1}$  as a function of  $m/z$ . The height of the sticks corresponds to the total integrated signal intensity of the individual  $m/z$ .
- Figure 3.7: Illustration of the PToF baseline subtraction for an individual  $m/z$ . The baseline (green line) is calculated as the linear interpolation between the averages of the two baseline areas (Baseline Area 1 in the beginning of the PToF cycle; Baseline Area 2 in the end of the PToF cycle). The dotted and solid curves

show the PToF distribution before and after PToF baseline subtraction, respectively.

Figure 3.8: Overall ion duty cycle  $D_{ion,overall,MS}$  of the ToF-AMS in MS mode according to Equation (3.15).

Figure 3.9: Overall ion duty cycle  $D_{ion,overall,PToF}$  of the ToF-AMS in PToF mode according to Equation (3.15).

Figure 3.10: A picture of the inlet flow calibration set-up.

Figure 3.11: Schematical set-up of the pressure-dependent inlet flow calibration.

Figure 3.12: The measured pressure inside the aerodynamic lens as a function of the upstream pressure in front of the critical orifice (dotted). The solid line represents a linear regression through the points above 300 hPa upstream pressure.

Figure 3.13: Volumetric (blue) and mass (red) flow rate into the ToF-AMS as a function of the upstream pressure in front of the critical orifice. The measured values are indicated by the dotted lines, the solid lines represent the linear regression through the measured values down to 300 hPa  $p_{up}$ .

Figure 3.14: Volumetric (blue) and mass (red) flow rate into the ToF-AMS as a function of the lens pressure. The measured values are indicated by the dotted lines, the solid line represents the linear regression through the measured values down to 0.7 hPa  $p_{lens}$ .

Figure 3.15: Illustration of the signal correction to account for a decay in the MCP detector performance and clogging of the critical orifice. See text for details.

Figure 3.16: PToF distribution measured during an IE calibration using ammonium nitrate particles with  $d_{mob} = 250$  nm. The part of the distribution that corresponds to doubly-charged particles is drawn in red, the grey shaded area gives the signal that corresponds to singly-charged particles. Note, that there is still non-zero signal from singly-charged particles at high  $d_{va}$  due to slow evaporation of the particles.

Figure 3.17: IE calibration with ammonium nitrate particles ( $d_{mob} = 250$  nm), without (black) and with (blue) correction for doubly-charged particles. The solid lines represent linear regressions through the measured values, the error bars are calculated from the uncertainties given in the last section.

Figure 3.18: IE calibration with ammonium nitrate particles ( $d_{mob} = 350$  nm), without (black) and with (blue) correction for doubly-charged particles. The solid lines represent linear regressions through the measured values, the error bars are calculated from the uncertainties given in the last section.

Figure 3.19: IE calibration with ammonium nitrate particles ( $d_{mob} = 400$  nm). A correction for doubly-charged particles was not necessary. The solid line represents a linear regression through the measured values, the error bars are calculated from the uncertainties given in the last section.

- Figure 3.20: Particle size calibration performed with three different types of calibration particles (see Table 3.2). The solid lines are the fits through the data points (Equation (3.53)). Error bars are calculated according to the uncertainties described above.
- Figure 3.21: Stopping distance  $SD$  inside the aerodynamic lens according to Equation 0 as a function of particle diameter  $d_p$  and for three different temperatures  $T$ .
- Figure 3.22: Schematic of the set-up for the pressure-dependent size calibration.
- Figure 3.23: Results from the pressure-dependent particle size calibration. Shown is the measured particle velocity for all particle diameters used during the calibration as a function of the ambient pressure  $p_{up}$ . Error bars are shown for measurement at  $d_{va} = 68.8$  nm only, but are of similar size for the other measurements.
- Figure 3.24: Results of the pressure-dependent size calibration. Shown is the measured particle velocity as a function of vacuum aerodynamic diameter, the solid lines are the fits (Equation (3.53)) through the calibration points. Each curve represents a size calibration for one individual ambient pressure.
- Figure 3.25: Fit parameters  $v_l$  (black),  $v_g$  (blue) and  $D^*$  (orange) as a function of ambient pressure. The solid lines represent linear fits in case of  $v_g$  and  $D^*$  and a power law fit in case of  $v_l$ . The resulting pressure-dependencies are given in Equations 0 to 0.
- Figure 3.26: Measured PToF distributions of laboratory-generated PSL particles ( $d_{mob} = 400$  nm) at various vaporiser temperatures.
- Figure 3.27: Position of the distribution maximum and distribution widths of laboratory-generated monodisperse ammonium nitrate, ammonium sulphate and PSL aerosol as a function of the vaporiser temperature.
- Figure 3.28: Detection limits of individual  $m/z$ , experimentally determined from 30 seconds blank measurements for Q-AMS (blue) and ToF-AMS (red). The  $m/z$  with the highest detection limits are labelled. Note, that the detection limits for the different species (as given in Table 3.6) are calculated from the background variation of that species and are not simply the sum of the  $LOD$  of the corresponding  $m/z$ .
- Figure 3.29: ToF-AMS nitrate and sulphate detection limits which would result from measurements with  $CR \neq 50\%$  as calculated from the  $LOD_{exp}$  measured at  $CR = 50$ .
- Figure 3.30: Limits of Detection ( $LOD_{exp}$ ) of Q-AMS and ToF-AMS, derived from measurements with different constant concentrations of ammonium nitrate. Only the nitrate mass concentration is given in the axis label. Detection limits are shown in green for organics, in yellow for ammonium, in purple for chloride, in red for sulphate and in blue for nitrate.
- Figure 3.31: The same as Figure 3.30, but derived from measurements with different constant concentrations of ammonium sulphate. Only the sulphate mass concentration is given in the axis label.

- Figure 3.32: Time series of the ToF-AMS sulphate limit of detection, derived from the background perturbation experiment with  $200 \mu\text{g m}^{-3}$  polystyrene latex.
- Figure 3.33: ToF-AMS (upper panel) and Q-AMS (lower panel) organics  $LOD_{exp}$  from filter data, calculated using an increasing number of selected  $m/z$ . In two cases (black squares and circles) the  $m/z$  were first sorted according to decreasing organics signal and decreasing signal-to-noise ratio, respectively. The lowest  $LOD$  is achieved using the first (25 for the ToF-AMS and 24 for the Q-AMS) peaks with highest signal-to-noise ratio.
- Figure 3.34: Mass size distributions of nitrate, sulphate, ammonium, chloride and organics of a laboratory-generated external mixture of polydisperse ammonium sulphate and monodisperse ammonium nitrate ( $d_{mob} = 350 \text{ nm}$ ) aerosol.
- Figure 3.35: Average mass spectrum of the laboratory-generated aerosol for the size range 20-60 nm.
- Figure 3.36: Average mass spectrum of the laboratory-generated aerosol for the size range 430-540 nm.
- Figure 3.37: Mass concentrations of nitrate, sulphate, ammonium, chloride and organics in the three different size ranges (see Figure 3.34) of the laboratory-generated aerosol.
- Figure 3.38: Mass size distribution measured for organics; even though the generated aerosol did not contain organics a small artificial organics signal is extracted from the mass spectra.
- Figure 3.39: Average raw spectrum of the laboratory-generated aerosol (zooming around the baseline). The MS baseline is not of a constant level, but varies with varying peak signal intensities.
- Figure 3.40: Screenshot of the ToF-AMS data analysis software panel developed during this work.
- Figure 4.1: Measurement site of the PMTACS-NY 2004 campaign. The inlet used by the aerosol mass spectrometers is indicated by the arrow.
- Figure 4.2: A Picture of the ToF-AMS set-up during PMTACS-NY 2004. As this was a preliminary set-up, the vacuum system and mass spectrometer (right) are separated from the electronics rack (left).
- Figure 4.3: Mass concentration time series of non-refractory nitrate, sulphate, ammonium and total non-refractory organics measured with the ToF-AMS (blue, red, yellow, green) and the Q-AMS (black) for the same time interval during measurement period # 3 of the ToF-AMS.
- Figure 4.4: Comparison of the mass concentrations measured with the ToF-AMS and the Q-AMS for period # 3. The dots represent the measurements, the solid coloured lines are the linear fits through the data points, and the black solid lines are the 1:1 correlation lines.
- Figure 4.5: Temporal evolution of the nitrate size distribution measured with the ToF-AMS (top) and Q-AMS (bottom), shown for the time interval 28/01 10:20 until

- 29/01 09:45. The intensity of the signal bins is colour-coded as shown in the legend. The ToF-AMS data shown in this Figure are 5-minute averages; the Q-AMS data are 10-min averages. All data are shown without any smoothing.
- Figure 4.6: Average size distributions for the last six days of the ToF-AMS deployment, shown for nitrate, sulphate, ammonium and organics. The size distributions are plotted as traces of  $dM/d\log d_{va}$  versus particle vacuum aerodynamic diameter.
- Figure 4.7: Examples of averaged single particle event mass spectra. A) Internally mixed ammonium nitrate/ammonium sulphate particle with organics and chloride ( $d_{va} = 405$  nm); B) “Pure” ammonium sulphate particle ( $d_{va} = 315$  nm); C) Ammonium nitrate particle with some organics and chloride ( $d_{va} = 190$  nm). The signal of the individual  $m/z$  is coloured according to the species they belong mainly to: air beam components (black), ammonium (yellow), nitrate (blue), sulphate (red), chloride (purple), and organics (green).
- Figure 4.8: Top panel: Total particle-related ion signal versus particle diameter  $d_{va}$  for all extracted single particle events. The markers are coloured according to the relative organics content of the particles. Lower panel: Average size distribution calculated from the total ion signal of all single particle events (red line) and average P-ToF size distribution for the days of SPToF measurements (black line).
- Figure 4.9: Time series of non-refractory nitrate (blue), sulphate (red), ammonium (yellow), total organics (green) and total non-refractory mass concentrations (black), measured with ToF-AMS (upper panel) and Q-AMS (lower panel).
- Figure 4.10: Correlations of ToF-AMS and Q-AMS mass concentrations for a) nitrate, b) sulphate, c) ammonium and d) organics. Blue markers indicate data from period I, green markers from period II. The red and black solid lines are linear fits for period I and II, respectively, the black dashed line is the 1:1 line.
- Figure 4.11: Average size distributions of nitrate (blue), sulphate (red), ammonium (yellow), and organics (green), measured with Q-AMS (left) and ToF-AMS (right) for the time period 20/07/4 0:00-12:00 h.
- Figure 4.12: The same as Figure 4.11, but for the time period 21/07/04 0:00-14:00 h.
- Figure 4.13: Time series of the non-refractory aerosol components, measured with the ToF-AMS during the whole campaign.
- Figure 4.14: Composition of the sub-micron aerosol as measured with the ToF-AMS during background intervals 1 (left top) and 2 (right top) and during the fireworks aerosol (left bottom). The composition of the aerosol during the maximum concentrations in the fireworks is also shown (right bottom).
- Figure 4.15: Average size distribution for  $m/z$  44 (marker for OOA) and  $m/z$  57 (marker for HOA) during the fireworks aerosol.
- Figure 4.16: Average size distribution for sulphate and chloride during the fireworks aerosol.

Figure 4.17: Time series of aerosol particle number concentrations (upper panel) and aerosol species mass concentrations (lower panel) for the fireworks time interval. The marked time interval is the “champagne dip”.

## 6.3 List of Tables

- Table 3.1:  $IE_{NO_3}$  values derived from calibrations with ammonium nitrate particles of three different mobility diameters  $d_{mob}$ .
- Table 3.2: Parameters for three different PToF calibrations performed with the ToF-AMS.  $\rho_m$  is the particle material density,  $S$  the Jayne shape factor,  $p_{amb}$  the ambient pressure during the calibration. The diameters are electrical mobility diameters in nm. The calibrations with PSL and  $NH_4NO_3$  were performed at the same day, the calibration with DOP three days later.
- Table 3.3: Fit parameters resulting from the  $NH_4NO_3$  size calibration for various constraints to the fit parameters.
- Table 3.4: Same as Table 3.3, but for the size calibration with DOP.
- Table 3.5: Fit parameters  $v_l$ ,  $v_g$ ,  $D^*$  and  $b$  (Equation (3.53)) resulting from size calibrations performed at various ambient pressures.
- Table 3.6: Limits of Detection ( $LOD$ ) of Q-AMS and ToF-AMS, derived from measurements of filtered air.  $LOD_{exp}$  are experimentally determined,  $LOD_{stat}$  are estimated from ion counting statistics. In both cases, the detection limits are calculated for 30 seconds saving intervals.
- Table 3.7: Limits of Detection ( $LOD$ ) of Q-AMS and ToF-AMS, derived from measurements with different constant concentrations of ammonium nitrate. Only the nitrate mass concentration is given in the table. The  $LOD_{exp}$  are also shown in Figure 3.30.
- Table 3.8: Absolute and relative increase in  $LOD_{exp}$  per  $\mu g m^{-3}$  increase in ammonium aerosol mass concentration. The absolute increase is given in  $ng m^{-3}$ , the relative increase is given in % per  $\mu g m^{-3}$ .
- Table 3.9: Limits of Detection ( $LOD$ ) of Q-AMS and ToF-AMS, derived from measurements with different constant concentrations of ammonium sulphate. Only the sulphate mass concentration is given in the table. The results for  $LOD_{exp}$  are also shown in Figure 3.31.
- Table 3.10: Absolute and relative increase in  $LOD_{exp}$  per  $\mu g m^{-3}$  increase in aerosol mass concentration. The absolute increase is given in  $\mu g m^{-3}$ , the relative increase is given in % per  $\mu g m^{-3}$ .
- Table 3.11: Self-cleaning time constants (time after which the detection limit has decreased to 1/e of the detection limit at a high mass concentration of ammonium nitrate, ammonium sulphate, or PSL) of Q-AMS and ToF-AMS  $LOD_{exp}$ . Only the mass concentrations of nitrate, sulphate or organics are given.
- Table 3.12: Summary of the experimentally determined detection limits (30-sec averaging interval) for the ToF-AMS. Values are given in  $\mu g m^{-3}$ .
- Table 4.1: Parameters of the correlations between the TOF-AMS and Q-AMS mass concentration data for nitrate, sulphate, ammonium and organics calculated for period # 3.

- Table 4.2: Parameters from the linear regressions in Figure 4.10.
- Table 4.3: Parameters of the average species-resolved size distributions, obtained by log-normal fits. Mode diameter values are given in nm, distribution widths are given as GSD.
- Table 4.4: Unusual assignments of certain  $m/z$  in the aerosol mass spectra to individual species for the fireworks aerosol.
- Table 4.5: Absolute (in  $\mu\text{g m}^{-3}$ ) and relative (in % of the total mass concentration) concentrations of the background and fireworks aerosol as measured with the ToF-AMS.
- Table 4.6: Relative increase in species' mass concentrations of the fireworks aerosol compared to background interval 1.
- Table 6.1: Functions written for the ToF-AMS data analysis software package and their purpose.
- Table 6.2: List of symbols used in this work.
- Table 6.3: List of abbreviations used in this work.

## 6.4 List of Symbols

Symbol	Description	Unit/Value
$A$	Orifice area	$\text{m}^2$
$a$	Calibration parameter for inlet flow calibration	$\text{cm}^3 \text{s}^{-1} \text{hPa}^{-1}$
$a$	Calibration parameter for IToF calibration	$\text{ns}^{-1}$
$a$	Acceleration	$\text{m s}^{-2}$
$AB$	Airbeam signal intensity	$\text{ions s}^{-1}$
$b$	Calibration parameter for inlet flow calibration	$\text{cm}^3 \text{s}^{-1}$
$b$	Slope parameter for size calibration	
$b_h$	Upper peak integration border	in terms of $m/z$
$b_l$	Lower peak integration border	in terms of $m/z$
$C$	Mass concentration	$\mu\text{g m}^{-3}$
$C_c$	Cunningham slip correction factor	
$C_{CPC}$	Mass concentration of particles measured with the CPC	$\mu\text{g m}^{-3}$
$CE$	Collection efficiency correction factor	
$C_{NO_3}$	Mass concentration of nitrate	$\mu\text{g m}^{-3}$
$Corr_I$	Doubly-charged particle correction factor for signal I	
$Corr_N$	Doubly-charged particle correction factor for concentration N	
$CR$	Chopper open-to-closed ratio	%
$C_s$	Mass concentration of species s	$\mu\text{g m}^{-3}$
$D^*$	Effective scaling diameter of size calibration	$\text{nm}$
$D_{chopper}$	Chopper duty cycle	%
$D_{ion}$	Ion duty cycle	%
$D_{ion,MS}$	Ion duty cycle in MS mode	%
$D_{ion,overshoot}$	Ion duty cycle due to overshooting	%
$D_{ion,PToF}$	Ion duty cycle in PToF mode	%
$d_m$	Slope parameter (parameterisation of mass resolving power)	
$d_{mob}$	Electrical mobility diameter	$\text{nm}$
$d_p$	Particle diameter	$\text{nm}$
$d_{va}$	Vacuum aerodynamic diameter	$\text{nm}$
$d_{ve}$	Volume-equivalent diameter	$\text{nm}$
$e$	Elementary charge	$1.602176 \cdot 10^{-19} \text{ C}$
$E_{kin}$	Kinetic energy	$\text{J / eV}$

Symbol	Description	Unit/Value
$E_{el}$	Electrical energy	J / eV
$f_{chopper}$	Particle chopper frequency	Hz
$F_D$	Drag force	N
$f_{NO_3}$	Fraction of $NO_3$ in $NH_4NO_3$	0.775
$GSD$	Geometric standard deviation	
$I$	Signal intensity	bits or ions $s^{-1}$
$I_b$	Signal intensity measured in beam blocked position	bits or ions $s^{-1}$
$I_{corr}$	Corrected signal intensity	bits or ions $s^{-1}$
$IE_{NO_3}$	Ionisation efficiency of $NO_3$	
$I_o$	Signal intensity measured in beam open position	bits or ions $s^{-1}$
$IPP$	Ions per particle	
$I_s$	Signal intensity of species s	ions $s^{-1}$
$ID$	Inner diameter	m
$I_{df}$	"Difference" signal intensity of species s	
$k_d$	Discharge coefficient	
$Kn$	Knudsen number	
$l$	Length of the acceleration region	m
$l_c$	Chamber length	m
$LOD$	Limit of detection	$\mu g m^{-3}$
$LOD^*$	Biased limit of detection (perturbation experiments)	$\mu g m^{-3}$
$LOD_{exp}$	Limit of detection, experimentally determined	$\mu g m^{-3}$
$LOD_{stat}$	Limit of detection, determined from statistical considerations	$\mu g m^{-3}$ or ions $s^{-1}$
$m/z$	Mass-to-charge ratio of the ion	
$m_0$	$m/z$ at which $R$ is equal to $R_0/2$	
$M_{air}$	Molecular weight of air	$kg mol^{-1}$
$m_{in}$	Inlet mass flow rate	$kg s^{-1}$
$m_{ion}$	Ion mass	kg
$m_p$	Peak maximum	in terms of $m/z$
$MPP$	Molecules per particle	
$MW_{NO_3}$	Molecular weight of $NO_3$	$62 g mol^{-1}$
$N$	Number concentration	$cm^{-3}$
$N_A$	Avogadro's number	$6.022142 \cdot 10^{23} mol^{-1}$
$n_{coadds}$	Number of co-adds	
$N_{CPC}$	Number concentration measured with CPC	$cm^{-3}$

Symbol	Description	Unit/Value
$p_{amb}$	Ambient pressure	hPa
$p_{lens}$	Pressure inside aerodynamic lens	Pa
$p_{up}$	Pressure upstream the critical orifice	Pa
$q$	Electric charge of the ion	C
$Q_{in}$	Volumetric inlet flow rate	$\text{cm}^3 \text{s}^{-1}$
$Q_{meas}$	Measured volumetric inlet flow rate	$\text{cm}^3 \text{s}^{-1}$
$R$	Correlation coefficient of linear regressions	
$R$	Mass resolving power	
$R$	Universal gas constant	$8.314472 \text{ J mol}^{-1}\text{K}^{-1}$
$R_0$	Nominal mass resolving power	
$Re$	Reynolds number	
$RIE_s$	Relative ionisation efficiency of species s	
$s$	Species	
$S$	Jayne shape factor	
$SD$	Stopping distance	m
$SI$	Single ion signal intensity	bits·ns
$s_{ion}$	Ion flight path	m
$t$	Time	s
$T$	Temperature	K
$T_{air}$	Air temperature	K
$t_{ed}$	Ion time-of-flight from extractor to detector	s
$t_{ion}$	Ion time-of-flight	s
$t_p$	Particle time-of-flight	s
$T_{pulse}$	time between two extraction pulses of the TOFMS	s
$t_s$	Total time spent sampling a particular $m/z$	s
$U$	Voltage	V
$U_{HB}$	Heater bias voltage	V
$U_{ion}$	Ion chamber voltage	V
$v_g$	Asymptotic velocity for $d_{va} \rightarrow 0$	$\text{m s}^{-1}$
$v_{ion}$	Ion velocity	$\text{m s}^{-1}$
$v_l$	Asymptotic velocity for $d_{va} \rightarrow \infty$	$\text{m s}^{-1}$
$v_p$	Particle velocity	$\text{m s}^{-1}$
$v_{p,ini}$	Initial particle velocity	$\text{m s}^{-1}$
$x_e$	Extraction length	m

Symbol	Description	Unit/Value
$x_{ed}$	Distance between extractor and detector	m
$x_{ion}$	Distance travelled by ion during $T_{pulse}$	m
$z$	Number of elementary charges in the ion	
$\alpha$	Factor for calculation of $LOD_{stat}$	1.2
$\alpha$	Coefficient for parameterisation of $C_c$	1.142
$\beta$	Coefficient for parameterisation of $C_c$	0.558
$\chi_t$	Dynamic shape factor in transition regime limit	
$\chi_v$	Dynamic shape factor in free molecular regime limit	
$\Delta m/z$	FWHM of peak at $m/z$	in terms of $m/z$
$\Delta v$	Relative velocity between gas and particle	$m\ s^{-1}$
$\gamma$	Ratio of specific heats	1.4
$\gamma$	Coefficient	0.999
$\eta_{air}$	Air viscosity	$\text{Pa}\cdot\text{s}$
$\eta_g$	Gas viscosity	$\text{Pa}\cdot\text{s}$
$\lambda$	Mean free path of the particles	m
$\mu_b$	Arithmetic mean of set of blank measurements	$\mu\text{g m}^{-3}$
$\rho_0$	Unit density	$1\ \text{g cm}^{-3}$
$\rho_{air}$	Density of air	$\text{g cm}^{-3}$
$\rho_{eff}$	Effective particle density	$\text{g cm}^{-3}$
$\rho_m$	Material density	$\text{g cm}^{-3}$
$\rho_p$	Particle density	$\text{g cm}^{-3}$
$\sigma$	Width parameter of Gaussian fit	
$\sigma_b$	Standard deviation of set of blank measurements	$\mu\text{g m}^{-3}$ or $\text{ions s}^{-1}$
$\sigma_o$	Standard deviation of set of aerosol measurements	$\mu\text{g m}^{-3}$ or $\text{ions s}^{-1}$
$\tau$	Self cleaning time constant	s

Table 6.2 List of symbols.

## 6.5 List of Abbreviations

Abbreviation	Meaning
AB	Airbeam signal, $m/z$ 28 or $m/z$ 32
AMS	Aerosol Mass Spectrometer
APCI-MS	Atmospheric Pressure Chemical Ionisation Mass Spectrometry
ATOFMS	Aerosol Time-Of-Flight Mass Spectrometer
CAART	Chemical Analysis of Aerosols in Real Time
CE	Collection Efficiency
CPC	Condensation Particle Counter
DMA	Differential Mobility Analyser
DOP	Dioctyl Phthalate
EI	Electron Impact Ionisation
EU	European Union
FACE-2004	Feldberg Aerosol Characterisation Experiments 2004
FWHM	Full Width at Half Maximum
GSD	Geometric Standard Deviation
HDF5	Hierarchical Data Format 5
HN Y 2005	Happy New Year Campaign 2005
HOA	Hydrocarbon-like Organic Aerosol
IE	Ionisation Efficiency
IPP	Ions per particle
IToF	Ion time-of-flight
Itx	IGOR Text File
LDI	Laser Desorption/Ionisation
LOD	Limit of Detection
MCP	Microchannel Plate
MPI	Max Planck Institute
MPP	Molecules per Particle
MS baseline	Baseline of Mass Spectrum
MS mode	Mass Spectrum Mode
OOA	Oxygenated Organic Aerosol
PALMS	Particle Analysis by Laser Mass Spectrometry
PAMS	Particle Analysis by Quadrupole Mass Spectrometry

<b>Abbreviation</b>	<b>Meaning</b>
PIXE	Proton Induced X-Ray Emission
PMTACS-NY 2004	PM2.5 Technology Assessment and Characterization Study-New York
PSL	Polystyrene Latex
PToF	Particle Time-of-Flight
PToF baseline	Baseline of PToF distribution
PToF mode	Particle Time-of-Flight mode
PTR-MS	Proton Transfer Mass Spectrometer
Q-AMS	Quadrupole Aerosol Mass Spectrometer
QMS	Quadrupole Mass Spectrometer
Recovery	Slope of linear regression when fit is forced through zero
RIE	Relative Ionisation Efficiency
RSMS	Rapid Single Particle Mass Spectrometry
S/N	Signal-to-Noise Ratio
SOA	Secondary Organic Aerosol
SPToF mode	Single Particle Time-of-Flight mode
US EPA	United States Environmental Protection Agency
TDPBMS	Thermal Desorption Particle Beam Mass Spectrometer
ToF-AMS	Time-of-Flight Aerosol Mass Spectrometer
TOFMS	Time-of-Flight Mass Spectrometer
VOC	Volatile Organic Compounds

Table 6.3: List of abbreviations.

## 6.6 Publications Originating from this Work

### Peer Reviewed

Drewnick, F., **S.S. Hings**, P.F. DeCarlo, J.T. Jayne, M. Gonin, K. Fuhrer, S. Weimer, J.L. Jimenez, K.L. Demerjian, S. Borrmann, D.R. Worsnop. *A New Time-of-Flight Aerosol Mass Spectrometer (ToF-AMS) - Instrument Description and First Field Deployment.* *Aerosol Science and Technology* 39, 637-658, 2005.

Drewnick, F., **S.S. Hings**, J. Curtius, G. Eerdekens, J. Williams. *Measurement of fine particulate and gas-phase species during the New Year's Fireworks 2005 in Mainz, Germany.* *Atmospheric Environment* 40, 4316-4326, 2006.

Dusek, U., G.P. Frank, L. Hildebrandt, J. Curtius, J. Schneider, S. Walter, D. Chand, F. Drewnick, **S.S. Hings**, D. Jung, S. Borrmann, M.O. Andreae. *Size Matters More Than Chemistry for Cloud-Nucleating Ability of Aerosol Particles.* *Science* 312, 1375-1378, 2006.

**Hings, S.S.**, S. Walter, F. Drewnick, J. Schneider, S. Borrmann. *Comparison of a Quadrupole and a Time-of-Flight Aerosol Mass Spectrometer during the Feldberg Aerosol Characterization Experiment 2004.* *Aerosol Science and Technology*, submitted, 2006.

**Hings, S.S.**, M.R. Alfarra, A.S.H. Prevot, S. Borrmann, F. Drewnick. *Characterisation of Aerodyne Aerosol Mass Spectrometer Mass Concentration Detection Limits. Part I: LOD of the Analyzers.* *Aerosol Science and Technology*, submitted, 2006.

Williams, J., F. Drewnick, **S.S. Hings**, J. Curtius, G. Eerdekens, T. Klüpfel, T. Wagner. *Firework Emissions for Satellite Validation?* *Environmental Chemistry* 2, 94–95, 2005.

### Conference Presentations

Drewnick, F., G.P. Frank, D. Chand, J. Curtius, U. Dusek, A. Hoffer, S. Metzger, O. Schmid, J. Schneider, H.-J. Vössing, L. Hildebrandt, D. Jung, N. Jürgens, **S.S. Hings**, K. Kandler, A. Kürten, B. Nillius, L. Silva, S. Walter, R. Weigel, B. Winterholler, H. Bingemer, S. Borrmann, M.O. Andreae. *The Feldberg Aerosol Characterization Experiment (FACE) 2004 – Overview.* Poster Presentation at the EGU General Assembly, Vienna, Austria, April 2005.

Drewnick, F., **S.S. Hings**, S. Borrmann, P.F. DeCarlo, J.L. Jimenez, M. Gonin, J.T. Jayne, D.R. Worsnop. *Ambient Aerosol Measurements with the Time-of-Flight Aerosol Mass Spectrometer (ToF-AMS) during the PMTACS-NY 2004 Winter Campaign.* Poster Presentation at the AAAR Fall Meeting, Atlanta, GA, USA, October 2004.

**Hings, S.S.**, S. Walter, J. Schneider, S. Borrmann, F. Drewnick. *Laboratory and In-Field Characterization of the Time-of-Flight Aerosol Mass Spectrometer (TOF-AMS).* Poster Presentation at the International Aerosol Conference, St. Paul, MN, USA, September 2006.

**Hings, S.S.**, F. Drewnick, S. Borrmann. *A Thermal Desorption Electron Impact Time-of-Flight Aerosol Mass Spectrometer – The Aerodyne TOF-AMS*. Oral presentation at the Workshop on European Particle Mass Spectrometry, Ispra, Italy, November 2005.

**Hings, S.S.**, S. Walter, F. Drewnick, J. Schneider, J. Curtius, D. Jung, A. Kürten, D. Chand, G.P. Frank, M.O. Andreae, S. Borrmann. *Intercomparison of two Aerosol Mass Spectrometers during the FACE-2004 Campaign*. Poster presentation at the European Aerosol Conference, Ghent, Belgium, August 2005.

**Hings, S.S.**, F. Drewnick, J. Curtius, G. Eerdekens, T. Klüpfel, J. Williams. *Measurement of Aerosol Chemical Composition and Species-resolved Size Distributions at the Mainz New Year's Eve Fireworks 2004/05*. Poster presentation at the European Aerosol Conference, Ghent, Belgium, August 2005.

**Hings, S.S.**, S. Walter, F. Drewnick, J. Schneider, J. Curtius, D. Jung, A. Kürten, D. Chand, G.P. Frank, S. Borrmann. *Intercomparison of two Aerosol Mass Spectrometers during the FACE-2004 Campaign*. Poster presentation at the EGU General Assembly, Vienna, Austria, April 2005.

**Hings, S.S.**, F. Drewnick, S. Borrmann, P. DeCarlo, J.L. Jimenez, M. Gonin, J.T. Jayne, D.R. Worsnop. *Characterization and Performance Evaluation of the Time-of-Flight Aerosol Mass Spectrometer (ToF AMS)*. Poster presentation at the AAAR Fall Meeting, Atlanta, GA, USA, October 2004.

## 7 References

- Aerodyne Research, Inc. *ARI Aerosol Mass Spectrometer Operation Manual*. Aerodyne Research, Inc., Billerica, MA, USA, 2005.
- Alfarra, M.R., H. Coe, J.D. Allan, K.N. Bower, H. Boudries, M.R. Canagaratna, J.L. Jimenez, J.T. Jayne, A. Garforth, S.M. Li, D.R. Worsnop. *Characterization of Urban and Regional Organic Aerosols In the Lower Fraser Valley Using Two Aerodyne Aerosol Mass Spectrometers*. *Atmospheric Environment* 38, 5745–5758, 2004.
- Allan, J.D., J.L. Jimenez, H. Coe, K.N. Bower, P.I. Williams, D.R. Worsnop. *Quantitative Sampling Using an Aerodyne Aerosol Mass Spectrometer. Part 1: Techniques of Data Interpretation and Error Analysis*. *Journal of Geophysical Research – Atmospheres* 108, 4090, 2003a.
- Allan, J.D., H. Coe, K.N. Bower, P.I. Williams, M.W. Gallagher, M.R. Alfarra, J.L. Jimenez, D.R. Worsnop, J.T. Jayne, M.R. Canagaratna, E. Nemitz, A.G. McDonald. *Quantitative Sampling Using an Aerodyne Aerosol Mass Spectrometer. Part 2: Measurements of Fine Particulate Chemical Composition in Two UK Cities*. *Journal of Geophysical Research – Atmospheres* 108, 4091, 2003b.
- Allan, J.D., H. Coe, K.N. Bower, M.R. Alfarra, A.E. Delia, J.L. Jimenez, A.M. Middlebrook, F. Drewnick, T.B. Onasch, M.R. Canagaratna, J.T. Jayne, D.R. Worsnop. *Technical note: Extraction of chemically resolved mass spectra from Aerodyne aerosol mass spectrometer data*. *Journal of Aerosol Science* 35, 909–922, 2004.
- Allan, J.D. *An Aerosol Mass Spectrometer: Instrument Development, Data Analysis Techniques and Quantitative Atmospheric Particulate Measurements*. PhD thesis, University of Manchester, UK, 2004.
- Allen, J. and R.K. Gould. *Mass-Spectrometric Analyzer for Individual Aerosol-Particles*. *Review of Scientific Instruments*, 52, 804-809, 1981.
- Allen, J.O., D.P. Fergenson, E.E. Gard, L.S. Hughes, B.D. Morrical, M.J. Kleeman, D.S. Gross, M.E. Gälli, K.A. Prather, G.R. Cass. *Particle Detection Efficiencies of Aerosol Time of Flight Mass Spectrometers under Ambient Sampling Conditions*. *Environmental Science & Technology* 34, 211-217, 2000.
- Allen, M.D., O.G. Raabe. *Re-Evaluation of Millikan Oil Drop Data for the Motion of Small Particles in Air*. *Journal of Aerosol Science* 13, 537-547, 1982.
- Aschmann, S.M., R. Atkinson, J. Arey. *Products of Reaction of OH Radicals with  $\alpha$ -Pinene*. *Journal of Geophysical Research* 107, 4191, 2002.

- Babu, S.S. and K.K. Moorthy. *Anthropogenic impact on aerosol black carbon mass concentration at a tropical coastal station: A case study.* Current Science 81, 1208-1214, 2001.
- Baron, P.A., K. Willeke. *Aerosol Measurement – Principles, Techniques and Applications.* Second Edition, John Wiley & Sons, Inc. Toronto, 2001.
- Cabalo, J., A. Zelenyuk, T. Baer, R.E. Miller. *Two-Color Laser Induced Evaporation Dynamics of Liquid Aerosols Probed by Time-of-Flight Mass Spectrometry.* Aerosol Science and Technology 33, 3-19, 2000.
- Canagaratna, M.R., J.T. Jayne, J.L. Jimenez, J.D. Allan, M.R. Alfarra, Q. Zhang, T.B. Onasch, F. Drewnick, H. Cue, A. Middlebrook, A. Delia, L.R. Williams, A.M. Trimborn, M.J. Northway, C.E. Kolb, P. Davidovits, D.R. Worsnop. *Chemical and Microphysical Characterization of Ambient Aerosols with the Aerodyne Aerosol Mass Spectrometer.* Mass Spectrometry Reviews, accepted, 2006.
- Carson, P.G., K.R. Neubauer, M.V. Johnston, A.S. Wexler. *Online Chemical-Analysis of Aerosols by Rapid Single-Particle Mass-Spectrometry.* Journal of Aerosol Science, 26, 535-545, 1995.
- Carson, P.G., M.V. Johnston, A.S. Wexler. *Laser desorption/ionization of ultrafine aerosol particles.* Rapid Communications in Mass Spectrometry 11, 993-996, 1997.
- Charlson, R.J., S.E. Schwartz, J.M. Hales, R.D. Cess, J.A. Coakley, J.E. Hansen, D.J. Hofmann. *Climate Forcing by Anthropogenic Aerosols.* Science 255, 423-430, 1992.
- Chow, J.C. *Measurement Methods to Determine Compliance with Ambient Air-Quality Standards for Suspended Particles.* Journal of the Air & Waste Management Association 45, 320-382, 1995.
- Davidsson, K.O., K. Engvall, M. Hagström, J.G. Korsgren, B. Lönn, and J.B.C. Pettersson. *A Surface Ionization Instrument for On-Line Measurements of Alkali Metal Components in Combustion: Instrument Description and Applications.* Energy & Fuels 16, 1369-1377, 2002.
- Davis, W. D. *Surface Ionization Mass Spectroscopy of Airborne Particulates.* Journal of Vacuum Science and Technology 10, 278, 1973.
- DeCarlo, P., J.G. Slowik, D.R. Worsnop, P. Davidovits, J.L. Jimenez. *Particle Morphology and Density Characterization by Combined Mobility and Aerodynamic Diameter Measurements. Part 1: Theory.* Aerosol Science and Technology 38, 1185-1205, 2004.
- DeCarlo, P.F., J.R. Kimmel, A. Trimborn, J.T. Jayne, A.C. Aiken, M. Gonin, K. Fuhrer, T. Horvath, K. Docherty, D.R. Worsnop, J.L. Jimenez. *A Field-Deployable High-Resolution Time-of-Flight Aerosol Mass Spectrometer.* Analytical Chemistry, in press, 2006.
- Dempster, A.J. *A New Method of Positive Ray Analysis.* Physical Review 11, 316-325, 1918.

- Dockery, D.W., C.A. Pope, X. Xu, J.D. Spengler, J.H. Ware, M.E. Fay, B.G. Ferris, F.E. Speizer. *An Association between Air Pollution and Mortality in Six U.S. Cities.* The New England Journal of Medicine 329, 1753-1759, 1993.
- Drewnick, F. *Aerosolmesstechnik II - Moderne Methoden der Aerosolmesstechnik.* Lecture Course, University of Mainz, 2003.
- Drewnick, F., S.S. Hings, P.F. DeCarlo, J.T. Jayne, M. Gonin, K. Fuhrer, S. Weimer, J.L. Jimenez, K.L. Demerjian, S. Borrmann, D.R. Worsnop. *A New Time-of-Flight Aerosol Mass Spectrometer (ToF-AMS) - Instrument Description and First Field Deployment.* Aerosol Science and Technology 39, 637-658, 2005.
- Drewnick, F., S.S. Hings, J. Curtius, G. Eerdekens, J. Williams. *Measurement of fine particulate and gas-phase species during the New Year's fireworks 2005 in Mainz, Germany.* Atmospheric Environment 40, 4316-4327, 2006.
- Drewnick, F. *Personal Communication.* 2006.
- Dutcher, D.D., K.D. Perry, T.A. Cahill, S.A. Copeland. *Effects of Indoor Pyrotechnic Displays on the Air Quality in the Houston Astrodome.* Journal of the Air & Waste Management Association 49, 156-160, 1999.
- Ettner-Mahl, M. *Entwicklung und Charakterisierung eines Laserablationsmassenspektrometers zur chemischen Analyse von atmosphärischen Aerosolpartikeln.* PhD Thesis, Max Planck Institute for Chemistry, Mainz, Germany, 2006.
- Fenger, J. *Urban Air Quality.* Atmospheric Environment 33, 4877-4900, 1999.
- Finlayson-Pitts, B.J. and J.N. Pitts. *Chemistry of the Upper and Lower Atmosphere: Theory, Experiments and Applications.* Academic Press, San Diego, California, London, 2000.
- Fritschi, S. *Aufbau und Charakterisierung eines Aerosolerzeugungssystems.* Diploma thesis, University of Mainz and Max-Planck-Institute for Chemistry Mainz, 2006.
- Fuchs, N. *On the Stationary Charge Distribution on Aerosol Particles in a Bipolar Ionic Atmosphere.* Geofisica pura e applicata 56, 185-193, 1963.
- Gard, E., J.E. Mayer, B.D. Morrical, T. Dienes, D.P. Fergenson, K.A. Prather. *Real-Time Analysis of Individual Atmospheric Aerosol Particles: Design and Performance of a Portable ATOFMS.* Analytical Chemistry 69, 4083-4091, 1997.
- Gross, D.S., M.E. Gälli, P.J. Silva, K.A. Prather. *Relative Sensitivity Factors for Alkali Metal and Ammonium Cations in Single Particle Aerosol Time-of-Flight Mass Spectra.* Analytical Chemistry 72, 416-422, 2000.
- Harrison, R.M. and J.X. Yin. *Particulate Matter in the Atmosphere: Which Particle Properties Are Important for Its Effects on Health?* Science of the Total Environment 249, 85-101, 2000.

- Henseler, S.S. *Charakterisierung des Einlasssystems des Aerodyne Aerosolmassenspektrometers AMS*. Diploma thesis, University of Mainz and Max Planck Institute for Chemistry, Mainz, Germany, 2003.
- Hinds, W.C. *Aerosol Technology – Properties, Behavior, and Measurement of Airborne Particles*. Second Edition, John Wiley & Sons, Inc. Toronto, 1999.
- Hings, S.S., M.R. Alfarra, A.S.H. Prevot, S. Borrmann, F. Drewnick. *Characterisation of Aerodyne Aerosol Mass Spectrometer Mass Concentration Detection Limits – Part I: LOD of the Analysers*. Aerosol Science and Technology, submitted, 2006.
- Hinz, K.P., R. Kaufmann, B. Spengler. *Simultaneous detection of positive and negative ions from single airborne particles by real-time laser mass spectrometry*. Aerosol Science and Technology 24, 233-242, 1996.
- Hoffmann, T., J.R. Odum, F. Bowman, D. Collins, D. Klockow, R.C. Flagan, J.H. Seinfeld. *Formation of Organic Aerosols from the Oxidation of Biogenic Hydrocarbons*. Journal of Atmospheric Chemistry 26, 189-222, 1997.
- Hoffmann, T., R. Bandur, S. Hoffmann, B. Warscheid. *On-line characterization of gaseous and particulate organic analytes using atmospheric pressure chemical ionization mass spectrometry*. Spectrochimica Acta Part B-Atomic Spectroscopy 57, 1635-1647, 2002.
- Hogrefe O., F. Drewnick, G.G. Lala, J.J. Schwab, K.L. Demerjian. *Development, Operation and Applications of an Aerosol Generation, Calibration and Research Facility*. Aerosol Science and Technology 38, 196-214, 2004.
- Huffman, J.A., J.T. Jayne, F. Drewnick, A.C. Aiken, T. Onasch, D.R. Worsnop, J.L. Jimenez. *Design, Modeling, Optimization, and Experimental Tests of a Particle Beam Width Probe for the Aerodyne Aerosol Mass Spectrometer*. Aerosol Science and Technology 39, 1143–1163, 2005.
- Hussin, A., H.G. Scheibel, K.H. Becker, J. Porstendorfer. *Bipolar Diffusion Charging of Aerosol Particles-I: Experimental Results within the Diameter Range 4-30 nm*. Journal of Aerosol Science 14, 671-677, 1983.
- Jäglid, U., J.G. Olsson, J.B.C. Pettersson. *Detection of sodium and potassium salt particles using surface ionization at atmospheric pressure*. Journal of Aerosol Science 27, 967-977, 1996.
- Jayne, J.T., D.C. Leard, X. Zhang, P. Davidovits, K.A. Smith, C.E. Kolb, D.R. Worsnop. *Development of an Aerosol Mass Spectrometer for Size and Composition Analysis of Submicron Particles*. Aerosol Science and Technology 33, 49-70, 2000.
- Jimenez, J.L. *Aerosol Mass Spectrometry: Instrumentation & Applications*. Graduate Course on Mass Spectrometry & Chromatography, University of Colorado at Boulder, 2002.
- Jimenez, J.L., J.T. Jayne, Q. Shi, C.E. Kolb, D.R. Worsnop, I. Yourshaw, J.H. Seinfeld, R.C. Flagan, X. Zhang, K.A. Smith, J.W. Morris, P. Davidovits. *Ambient Aerosol Sampling*

- Using the Aerodyne Aerosol Mass Spectrometer.* Journal of Geophysical Research - Atmospheres 108, 8425, 2003a.
- Jimenez, J.L., R. Bahreini, D.R. Cocker, H. Zhuang, V. Varutbangkul, R.C. Flagan, J.H. Seinfeld, C.D. O'Dowd, T. Hoffmann. *New Particle Formation from Photooxidation of Diiodomethane ( $CH_2I_2$ ).* Journal of Geophysical Research - Atmospheres 108, 4318, 2003b.
- Johnston, M.V. *Sampling and Analysis of Individual Particles by Aerosol Mass Spectrometry.* Journal of Mass Spectrometry 35, 585-595, 2000.
- Kamens, R., M. Jang, C. Chien, K. Leach. *Aerosol Formation from the Reaction of  $\alpha$ -Pinene and Ozone Using a Gas-Phase Kinetics-Aerosol Partitioning Model.* Environmental Science & Technology 33, 1430-1438, 1999.
- Kamens, R.M. and M. Jaoui. *Modeling Aerosol Formation from  $\alpha$ -Pinene + NO<sub>x</sub> in the Presence of Natural Sunlight Using Gas-Phase Kinetics and Gas-Particle Partitioning Theory.* Environmental Science & Technology 35, 1394-1405, 2001.
- Kane, D.B. and M.V. Johnston. *Size and Composition Biases on the Detection of Individual Ultrafine Particles by Aerosol Mass Spectrometry.* Environmental Science & Technology 34, 4887-4893, 2000.
- Kellner, R., J.-M. Mermet, M. Otto, M. Valcarcel, H.M. Widmer (Eds.). *Analytical Chemistry - A Modern Approach to Analytical Science.* Second Edition, WILEY-VCH Verlag GmbH & Co. KgaA, Weinheim, 2004.
- Kleindienst, T.E., D. Smith, W. Li, E.O. Edney, D.J. Driscoll, R.E. Speer, W.S. Weathers. *Secondary Organic Aerosol Formation from the Oxidation of Aromatic Hydrocarbons in the Presence of Dry Submicron Ammonium Sulphate Aerosol.* Atmospheric Environment 33, 3669-3681, 1999.
- Kulmala, M., H. Vehkamaki, T. Petajda, M. Dal Maso, A. Lauri, V.M. Kerminen, W. Birmili, P.H. McMurry. *Formation and Growth Rates of Ultrafine Atmospheric Particles: A Review of Observations.* Journal of Aerosol Science 35, 143-176, 2004.
- Kulshrestha, U.C., T. Nageswara Rao, S. Azhaguvvel, M.J. Kulshrestha. *Emissions and accumulation of metals in the atmosphere due to crackers and sparkles during Diwali festival in India.* Atmospheric Environment 38, 4421-4425, 2004.
- Lake, D.A., M.P. Tolocka, M.V. Johnston, A.S. Wexler. *Mass spectrometry of individual particles between 50 and 750 nm in diameter at the Baltimore supersite.* Environmental Science & Technology 37, 3268-3274, 2003.
- Liu, B.Y.H., and D.Y.H. Pui *Electrical Neutralization of Aerosols.* Journal of Aerosol Science 5, 465-472, 1974.

- Liu, P., P.L. Zieman, D.B. Kittelson, P.H. McMurry. *Generating Particle Beams of Controlled Dimensions and Divergence: I. Theory of Particle Motion in Aerodynamic Lenses and Nozzle Expansions*. *Aerosol Science and Technology* 22, 293-313, 1995a.
- Liu, P., P.L. Zieman, D.B. Kittelson, P.H. McMurry. *Generating Particle Beams of Controlled Dimensions and Divergence: II. Experimental Evaluation of Particle Motion in Aerodynamic Lenses and Nozzle Expansions*. *Aerosol Science and Technology* 22, 314-324, 1995b.
- Liu, D.-Y., D. Rutherford, M. Kinsey, K.A. Prather. *Real-Time Monitoring of Pyrotechnically Derived Aerosol Particles in the Troposphere*. *Analytical Chemistry* 69, 1808-1814, 1997.
- Mandal, R., B.K. Sen, S. Sen. *Impact of Fireworks on Our Environment*. *Indian Journal of Environmental Protection* 17, 850-853, 1997.
- Mayer, H. *Air Pollution in Cities*. *Atmospheric Environment* 33, 4029-4037, 1999.
- McLafferty, F.W. and F. Turecek. *Interpretation of Mass Spectra*. Fourth Edition, University Science Books, 1993.
- McKeown, P.J., M.V. Johnston, D.M. Murphy. *Online Single-Particle Analysis by Laser Desorption Mass-Spectrometry*. *Analytical Chemistry* 63, 2069-2073, 1991.
- McMurry, P.H. *A Review of Atmospheric Aerosol Measurements*. *Atmospheric Environment* 34, 1959-1999, 2000.
- Morrical, B.D., D.P. Fergenson, K.A. Prather. *Coupling Two-Step Laser Desorption/Ionization with Aerosol Time-of-Flight Mass Spectrometry for the Analysis of Individual Organic Particles*. *Journal of the American Society for Mass Spectrometry* 9, 1068-1073, 1998.
- Murphy, D.M. and D.S. Thomson. *Laser Ionization Mass-Spectroscopy of Single Aerosol-Particles*. *Aerosol Science and Technology* 22, 237-249, 1995.
- Myers, R.L. and W.L. Fite. *Electrical detection of airborne particulates using surface ionization techniques*. *Environmental Science & Technology* 9, 334-336, 1975.
- Noble, C.A. and K.A. Prather. *Real-Time Single Particle Mass Spectrometry: A Historical Review of a Quarter Century of the Chemical Analysis of Aerosols*. *Mass Spectrometry Reviews* 19, 248-274, 2000.
- O'Dowd, C.D., J.L. Jimenez, R. Bahreini, R.C. Flagan, J.H. Seinfeld, K. Hameri, L. Pirjola, M. Kulmala, S.G. Jennings, T. Hoffmann. *Marine Aerosol Formation from Biogenic Iodine Emissions*. *Nature* 417, 632-636, 2002.
- Odum, J.R., T. Hoffmann, F. Bowman, D. Collins, R.C. Flagan, J.H. Seinfeld. *Gas/Particle Partitioning and Secondary Organic Aerosol Yields*. *Environmental Science & Technology* 30, 2580-2585, 1996.

- Paul, W. and H. Steinwedel. *Ein neues Massenspektrometer ohne Magnetfeld.* Zeitung für Naturforschung 8a, 448-450, 1953.
- Penner, J.E., M. Andreae, H. Annegarn, L. Barrie, J. Feichter, D. Hegg, A. Jayaraman, R. Leaitch, D. Murphy, J. Nganga and G. Pitari. *Aerosols, their Direct and Indirect Effects. Climate Change 2001: The Scientific Basis. Contribution of Working Group I to the Third Assessment Report of the Intergovernmental Panel on Climate Change.* Editor C.A. Johnson, Cambridge University Press, Cambridge, New York, 289-348, 2001.
- Perry, K.D. *Effects of Outdoor Pyrotechnic Displays on the Regional Air Quality of Western Washington State.* Journal of the Air & Waste Management Association 49, 146-155, 1999.
- Prather, K.A., T. Nordmeyer, K. Salt. *Real-Time Characterization of Individual Aerosol-Particles Using Time-of-Flight Mass-Spectrometry.* Analytical Chemistry 66, 1403-1407, 1994.
- Press, W.H., S.A. Teukolsky, W.T. Vetterling, B.P. Flannery. *Numerical Recipes in C.* Second Edition, Cambridge University Press, New York, 1992.
- Ramanathan, V., P.J. Crutzen, J.T. Kiehl, D. Rosenfeld. *Atmosphere - Aerosols, Climate, and the Hydrological Cycle.* Science 294, 2119-2124, 2001.
- Ravindra, K., S. Mor, C.P. Kaushik. *Short-term variation in air quality associated with firework events: A case study.* Journal of Environmental Monitoring 5, 260-264, 2003.
- Ravishankara, A.R. *Heterogeneous and Multiphase Chemistry in the Troposphere.* Science 276, 1058-1065, 1997.
- Reents, W.D., S.W. Downey, A.B. Emerson, A.M. Muisce, A.J. Muller, D.J. Siconolfi, J.D. Sinclair, A.G. Swanson. *Single-Particle Characterization by Time-of-Flight Mass-Spectrometry.* Aerosol Science and Technology 23, 263-270, 1995.
- Reents, W.D. and Z.Z. Ge. *Simultaneous elemental composition and size distributions of submicron particles in real time using laser atomization/ionization mass spectrometry.* Aerosol Science and Technology 33, 122-134, 2000.
- Reents, W.D. and M.J. Schabel. *Measurement of Individual Particle Atomic Composition by Aerosol Mass Spectrometry.* Analytical Chemistry 73, 5403-5414, 2001.
- Reilly, P.T.A., A.C. Lazar, R.A. Gieray, W.B. Whitten, J. M. Ramsey. *The Elucidation of Charge-Transfer-Induced Matrix Effects in Environmental Aerosols Via Real-Time Aerosol Mass Spectral Analysis of Individual Airborne Particles.* Aerosol Science and Technology 33, 135-152, 2000.
- Samet, J.M., F. Dominici, F.C. Curriero, I. Coursac, S.L. Zeger. *Fine Particulate Air Pollution and Mortality in 20 U.S. Cities, 1987-1994.* The New England Journal of Medicine 343, 1742-1749, 2000.

- Seinfeld, J.H. and S.N. Pandis. *Atmospheric Chemistry and Physics: From Air Pollution to Climate Change*. John Wiley & Sons, Chichester, New York, 1998.
- Sinha, M.P., C.E. Giffin, D.D. Norris, T.J. Estes, V.L. Vilker, S.K. Friedlander. *Particle Analysis by Mass-Spectrometry*. Journal of Colloid and Interface Science 87, 140-153, 1982.
- Sinha, M.P. *Laser-Induced Volatilization and Ionization of Microparticles*. Review of Scientific Instruments 55, 886-891, 1984.
- Sipin, M.F., S.A. Guazzotti, K.A. Prather. *Recent Advances and Some Remaining Challenges in Analytical Chemistry of the Atmosphere*. Analytical Chemistry 75, 2929-2940, 2003.
- Spurny, K.R. *Analytical Chemistry of Aerosols*. Lewis Publishers, Boca Raton, London, New York, Washington D.C, 1999.
- Steiner, W.E., B.H. Clowers, K. Fuhrer, M. Gonin, L.M. Matz, W.F. Siems, A.J. Schultz, H.H. Hill, Jr. *Electrospray ionization with ambient pressure ion mobility separation and mass analysis by orthogonal time-of-flight mass spectrometry*. Rapid Communications in Mass Spectrometry 15, 2221-2226, 2001.
- Suess, D.T. and K.A. Prather. *Mass Spectrometry of Aerosols*. Chemical Reviews 99, 3007-3035, 1999.
- Svane, M., M. Hagstrom, J.B.C. Pettersson. *Chemical Analysis of Individual Alkali-Containing Aerosol Particles: Design and Performance of a Surface Ionization Particle Beam Mass Spectrometer*. Aerosol Science and Technology 38, 655-663, 2004.
- Tobias, H.J. and P.J. Ziemann. *Compound identification in organic aerosols using temperature-programmed thermal desorption particle beam mass spectrometry*. Analytical Chemistry 71, 3428-3435, 1999.
- Tobias, H.J., P.M. Kooiman, K.S. Docherty, P.J. Ziemann. *Real-time chemical analysis of organic aerosols using a thermal desorption particle beam mass spectrometer*. Aerosol Science and Technology 33, 170-190, 2000.
- TSI Incorporated. *Model 3025A Ultrafine Condensation Particle Counter Instruction Manual*. TSI, Incorporated, Shoreview, USA, 2002.
- TSI Incorporated. *Model 3076 Constant Output Atomizer Instruction Manual*. TSI Incorporated, Shoreview, USA, 2005.
- TSI Incorporated. *Series 3080 Electrostatic Classifiers Operation and Service Manual*. TSI Incorporated, Shoreview, USA, 2006.
- Thomson, D.S., M.E. Schein, D.M. Murphy. *Particle analysis by laser mass spectrometry WB-57F instrument overview*. Aerosol Science and Technology 33, 153-169, 2000.

- Warneck, P. *Chemistry of the Natural Atmosphere*. International Geophysics Series, Volume 71, Academic Press, 1999.
- Wavemetrics, Inc. *IGOR Pro Manual, Version 5.0*. Wavemetrics, Inc., Lake Oswego, USA, 2005.
- Weimer, S., F. Drewnick, O. Hogrefe, J.J. Schwab, K. Rhoads, D. Orsini, M. Canagaratna, D.R. Worsnop, K.L. Demerjian. *Size-selective non-refractory ambient aerosol measurements during the Particulate Matter Technology Assessment and Characterization Study—New York 2004 Winter Intensive in New York City*. Journal of Geophysical Research – Atmospheres 111, D18305, 2006.
- Wehner, B., A. Wiedensohler, J. Heintzenberg. *Submicrometer Aerosol Size Distributions and Mass Concentration of the Millennium Fireworks 2000 in Leipzig, Germany*. Journal of Aerosol Science 31, 1489-1493, 2000.
- Went, F.W. *Blue Haze in the Atmosphere*. Nature 187, 641-643, 1960.
- Wischmann, H.-E., C. Spix, T. Tuch, G. Wölke, A. Peters, J. Heinrich, W.G. Kreyling, J. Heyder. *Daily Mortality and Fine and Ultrafine Particles in Erfurt, Germany. Part I: Role of Particulate Number and Particle Mass*. Health Effects Institute Research Report 98, 2000.
- Wiedensohler, A. *An Approximation of the Bipolar Charge-Distribution for Particles in the Sub-Micron Size Range*. Journal of Aerosol Science 19, 387-389, 1988.
- Williams, J., F. Drewnick, S.S. Hings, J. Curtius, G. Eerdekens, T. Klüpfel, T. Wagner. *Firework Emissions for Satellite Validation?* Environmental Chemistry 2, 94–95, 2005.
- Wiza, J.L. *Microchannel Plate Detectors*. Nuclear Instruments and Methods 162, 587-601, 1979.
- Worsnop, D.R. *Unpublished Data*. 2003.
- Zhang, X., K.A. Smith, D.R. Worsnop, J.L. Jimenez, J.T. Jayne, C.E. Kolb. *A Numerical Characterization of Particle Beam Collimation by an Aerodynamic Lens-Nozzle System: Part I. An Individual Lens or Nozzle*. Aerosol Science and Technology 36, 617-631, 2002.
- Zhang, X., K.A. Smith, D.R. Worsnop, J.L. Jimenez, J.T. Jayne, C.E. Kolb, J. Morris, P. Davidovits. *Characterization of Particle Beam Collimation: Part II. Integrated Aerodynamic Lens-Nozzle System*. Aerosol Science and Technology 38, 619-638, 2004.
- Zhang, Q., M.R. Alfarra, D.R. Worsnop, J.D. Allan, H. Coe, M.R. Canagaratna, J.L. Jimenez. *Deconvolution and Quantification of Hydrocarbon-like and Oxygenated Organic Aerosols Based on Aerosol Mass Spectrometry*. Environmental Science and Technology 39, 4938-4952, 2005.